Department of Chemical Engineering
Technical University of Denmark

Graduate Schools
Yearbook
2005

Editors:
Kim Dam-Johansen
Martin Bøjer

Address:	Department of Chemical Engineering Søltofts Plads, Building 229 Technical University of Denmark DK-2800 Kgs. Lyngby Denmark
Telephone:	+45 4525 2800
Fax:	+45 4588 2258
E-mail:	kt@kt.dtu.dk
Internet:	http://www.kt.dtu.dk
Print:	Dronninglund Bogtrykkeri A/S Dronninglund, Denmark December 2005
Cover:	Philip W. Brandt – pwb@kt.dtu.dk
Cover photos:	FLSmidth A/S - Klaus Holsting
ISBN:	87-91435-28-5

Contents

Contributions

Preface

This 2005 Chemical Engineering Graduate Schools Yearbook is the third yearbook published on behalf of our graduate students associated to the graduate schools of the department.

In the yearbook the newly matriculated graduate students present the background and the aims that motivate their studies while the graduate students matriculated for longer time present the progress and the status of their research projects. Readers of the yearbooks may thereby follow the progress of the individual graduate students and their studies during the entire enrollment period and read about the numerous high quality research activities at the department.

The present yearbook illustrates the broad spectrum of research activities performed at the department. Our graduate students demonstrate first class and innovative research by mastering the use of chemistry and chemical and biochemical engineering disciplines within major research fields such as: chemical kinetics and catalysis, process simulation and control, process integration and development, reaction engineering, thermodynamics and separation processes, oil and gas technology, combustion technology, polymers science, aerosols physics, mathematical modeling, and our newly established field of chemical, biochemical and pharmaceutical product design.

It is with great pleasure that I present to you:

The Chemical Engineering Graduate Schools Yearbook 2005

Kim Dam-Johansen

Kim Dam-Johansen

Professor, Head of Department

Pavle Andrić
Address: Building 229, room 127
Phone: +45 4525 2842
Fax: +45 4588 2258
e-mail: pan@kt.dtu.dk
www: http://www.chec.kt.dtu.dk

Supervisors: Kim Dam-Johansen
Peter Arendt Jensen

Ph.D. Study
Started: October 2005
To be completed: September 2008

Pre-Treatment and Enzymatic Hydrolysis of Ligno-Cellulose

Abstract

For many years, one of the main research areas at the CHEC research center (Combustion and Harmful Emission Control) at Department of Chemical Engineering, DTU, has been thermal conversion of biomass for the production of heat and electricity. Due to the global increase in interests for liquid fuels, CHEC is, based on past experience, expanding its research to technologies for liquid fuel production. One of the promising liquid fuels is Bio-Ethanol, the ordinary ethanol produced from ligno-cellulosic biomass, which can be used as an alternative to gasoline.

Introduction

The need for introduction of alternative fuels is very obvious. The limitation of the reserves of the fossil-based crude oil and uncertainty of its supplies and constantly rising price; the pronounced green-house-gas effect and increased governmental regulations in respect to the emissions; growing fuel markets in developing countries, have all led to the enormous increase in the interest for the alternative sources of energy.

Ethanol produced from renewable sources such as biomass is emerging as a promising transportation fuel, which can be used as an alternative to the fossil gasoline. Production of ethanol from primary biomass, which can be used as a food or feed, is a well established and known process [1]. However, this process is significantly limited by the high value of this kind of biomass.

An alternative way to produce ethanol is from secondary biomass. Secondary or ligno-cellulosic biomass has low or no value as food. It includes a variety of a relatively cheap agricultural or forestry residues, dedicated crops and different kinds of waste, such as wheat straw, corn stover, wood chips, etc.

Ligno-cellulosic biomass is composed mainly of cellulose, hemi-cellulose and lignin. Ethanol produced from ligno-cellulosic biomass is termed as Bio-Ethanol.

Use of Bio-Ethanol as a renewable transportation fuel could potentially offer many benefits. Some believe that, in the near future, no other sustainable option for production of transportation fuels will be able to match ethanol made from ligno-cellulosic biomass with respect to its environmental, economic, strategic and infrastructural advantages [2].

Compared to fossil fuels, the bio-ethanol contribution to the net emission of CO_2 is low [3]. Blended with gasoline, combustion of ethanol in car engines lowers the emissions of many pollutants such as CO, volatile organic compounds and hydrocarbons [4]. Furthermore, ethanol increases the octane number [5].

Ligno-cellulosic biomass represents a significant domestic source of renewable energy. In the light of growing international fuel markets and the limitation of the crude oil reserves, the Bio-Ethanol could help to meet increased demands for fuels and thus reduce the trade deficit, grow economies and decrease the dependence from crude oil in many countries [2].

The envisaged Bio-Ethanol production process from ligno-cellulosic biomass can be divided into several main steps: biomass transport and handling, biomass pre-treatment, cellulose and hemi-cellulose hydrolysis (often called saccharification), fermentation of sugars and ethanol recovery.

Upon transport to the site of production, biomass is handled using various mechanical operations (separation from dirt and stones, cutting, shredding, milling, conveying, etc.) to facilitate satisfactory heat and mass transfer in the subsequent steps. In the pre-treatment, biomass is usually submitted to rapid conditions such as high temperature and/or use of chemical agents, in order to open the ligno-cellulosic structure and make cellulose and hemi-cellulose susceptible to the hydrolysis. In hydrolysis, cellulose and hemi-cellulose are converted to sugars using enzymes or different acids, while in fermentation these sugars are converted by microorganisms to ethanol. Ethanol is further purified using stripping, distillation, chromatography, pervaporation, etc., to obtain fuel grade. The process also yields a variety of co-products that can be used for electricity and heat generation and feed applications, such as lignin reach residues, proteins, vinasse, bagasse, etc. which are obtained from different operations (screw-pressing, drying, centrifugation, evaporation, combustion, etc.).

The one of the possible process layouts for Bio-Ethanol production is shown on Figure 1.

The enzymatic hydrolysis of ligno-cellulosic biomass is the most promising method for production of Bio-Ethanol. However, it has not yet been demonstrated on a commercial scale [6].

This is mainly because there are still too many obstacles to overcome in Bio-Ethanol production, in order to achieve a competitive price with the gasoline. A key element underlying Bio-Ethanol processing cost reductions is improvement in the pre-treatment and enzymatic hydrolysis technology [2]. Any improvements in these processes could significantly lower the price of producing Bio-Ethanol. In addition, a very interesting possibility that may reduce the production cost is to integrate Bio-Ethanol production with existing combined heat and power plant [3].

To conclude, the Bio-Ethanol production is possibly getting close to commercialization and presently, large resources are employed into solving the bottlenecks of the process [4].

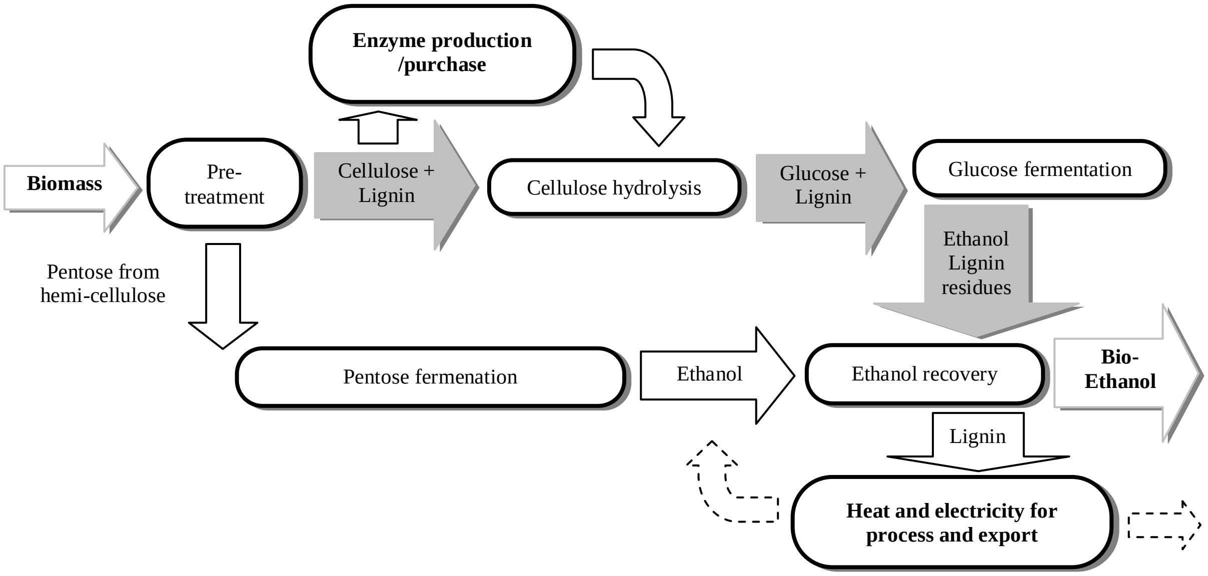

Figure 1: Bio-Ethanol from ligno-cellulosic biomass

Specific objectives

The aim of this project is to investigate the possibilities of commercialization of Bio-Ethanol production from wheat straw, by increasing the efficiency of the separate steps and reducing the processing costs. The main emphasis should be on pre-treatment and enzymatic hydrolysis step, but others steps such as ethanol recovery could be included. The possibilities of integration of the combined heat and power plant with Bio-Ethanol production will be explored. Experimental work will be the part of the project. Co-operation with other departments, institutions and/or companies, will be established.

Acknowledgements

The Ph.D. study is completely sponsored by Danish Technical University.

References

1. J. Zaldivar, J. Nielsen, L. Olsson, Fuel ethanol production from lignocellulose: a challenge for metabolic engineering and process integration, Appl. Microbiol. Biotechnol. 56 (2001) 17–34.
2. C. E. Wyman, Biomass Ethanol: Technical Progress, Opportunities, and Commercial Challenges, Annu. Rev. Energy Environ. 24 (1999) 189-226.
3. M. Galbe, G. Zacchi, A review of the production of ethanol from softwood, Appl. Microbiol. Biotechnol. 59 (2002) 618-628
4. L. Olsson, H. Jørgensen, K. B. R. Krogh, C. Roca, Bioethanol from Lignocellulosic Material. In Polysaccharides: Structural Diversity and Functional Versatility, Second Edition, Marcel Dekker (2004) 957-993.
5. H. L. MacLean, L. B. Lave, Evaluating automobile fuel/propulsion system technologies, Progress in Energy and Combustion Science 29 (2003) 1-69.
6. L.R. Lynd, Overview and evaluation of fuel ethanol from cellulosic biomass: Technology, Economics, the Environment, and Policy, Annu. Rev. Energy Environ. 21 (1996) 403-65.

Niels Bech
Address: Bygning 228, DK-2800 Lyngby
Phone: +45 4525 2851 / +45 2178 4547
Fax: +49 2443 64898
e-mail: nsb@kt.dtu.dk
www: http://www.chec.kt.dtu.dk

Supervisors: Kim Dam-Johansen
Peter A. Jensen

Ph.D. Study
Started: September 2004
To be completed: August 2007

In-Situ Flash Pyrolysis of Straw

Abstract
Energy derived from straw remains a largely untapped energy resource offering a significant potential in the cereal-growing parts of the world. The main barrier for introducing straw to the energy market competitively is its higher cost relative to fossil fuels. The thermochemical process Flash Pyrolysis is capable of converting straw to an attractive liquid fuel. This project focuses on developing an ablative flash pyrolysis process specifically targeted for the production of heavy fuel substitute Bio-oil from straw.

Introduction

Bioenergy in the form of straw represents a significant energy source on a world-wide scale but is today largely unutilized. According to FAO [1], the aggregate world production of cereals including barley, mixed grains, oats, rye sorghum, triticale and wheat amounted to 814 million tons in 2003 of which wheat constituted close to 70%. Geographically, the most significant wheat production areas were Western Europe (17%), North America (16%), India (12%) and the former USSR (12%). Assuming a straw/grain ratio equivalent to the Danish average for 1994-1996 of 40% [2] and straw availability for energy to be 50%, these areas potentially have a virtually untapped energy reserve equivalent to 40 mill. tons (approx. 215 mill. barrels) of heavy fuel originating from wheat. For 2003, this amount of energy corresponded to 8 days of OPEC crude oil production (27 mill. barrels/day) [3] or a market value close to $13 bill. For the net energy importing areas (*i.e.* North America, Western Europe and India), utilization of straw for energy production is thus a CO_2 neutral prospect to gain more independence from the historically less stable oil exporting regions.

Unfortunately, straw does not posses the attractive properties that crude-oil products do such as a relatively high volumetric energy content, good transportability, standardized specifications and simplicity in use. The result is that utilization of straw is only practiced under primitive conditions where it is readily available or where massive public subsidies or regulation warrant it. Apart from the unresolved problems in handling combustion of raw straw, the expense associated with logistics (*e.g.* baling, storage and transport) is the single largest barrier for utilizing straw efficiently in competition with fossil fuels under free market conditions. Access to an uninterrupted supply of fuel is also of importance to energy consumers and accordingly, expenses arising from long-distance transport of straw-derived energy need to be insignificant compared to the value of the fuel itself in order to market the product successfully.

Specific Objectives

Flash pyrolysis is a thermochemical process which under conditions of medium temperature and short residence time converts organic materials to char, tar and gas. Tar, a homogeneous mixture of organics and water commonly referred to as Bio-oil, is a highly compressed energy carrier and may be used in the existing combustors and distribution systems for fossil heavy fuel, while gas can be utilized for process heat.

For straw, the yields of Bio-oil, char and gas are approximately 50, 30 and 20% on dry weight basis [4]. Straw is a relatively inexpensive material provided baling and transportation are not needed. This implies that capital cost is of higher importance for in situ conversion and the development of a high capacity compact reactor system is a cardinal point. Accordingly, the main objective of the project is to identify a suitable reactor system and optimize its performance.

Modelling and Experimental Work

Fluid bed and ablative reactors are the two principal technologies available for flash pyrolysis. In the former, biomaterial is introduced into a bed of hot fluidized inert material, usually sand. Although a well-known technology, fluid beds do have several disadvantages including the requirement for a large flow of inert gas for heat transport and fluidization, a relatively poor capacity/volume ratio and the need for small particle size feed. Therefore, the project focuses on developing and optimizing an ablative process for straw flash pyrolysis.

Figure 1 depicts the reactor which has been specifically developed for this project. Straw in the form of rolled and sieved straw pellets are introduced by a screw feeder into a horizontal heated tube. Here, a three-blade rotor with close clearance to the reactor wall provides rotation to the gas phase and the straw particles.

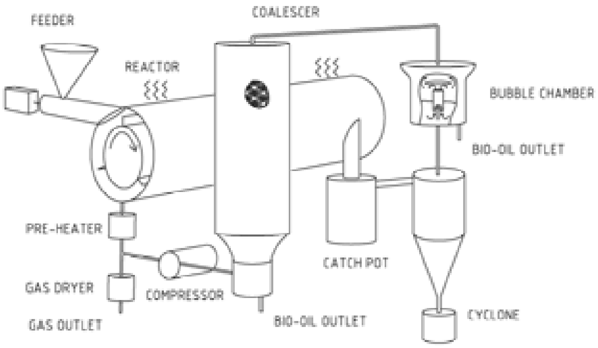

Figure 1: Schematic diagram of the developed ablative pyrolysis bench reactor system.

The residence time in the reactor for the evolved gasses is controlled by means of a recirculation compressor. Liquids are condensed by passing the gasses through a cool pool of tar/water mixture after char particles have been removed in the catch pot and cyclone. Aerosols are collected to large droplets in a coalescer and removed by gravity. Before the gas is metered, it is cooled to ambient temperature in order to remove water. Gas for recirculation is preheated in order to avoid condensation of liquid products within the reactor.

When a particle undergoes pyrolysis in the ablative regime the degradation will take place as a pseudo surface reaction. Under these conditions the energy transported to the surface will balance the requirement for heating the material to the reaction temperature. This phenomenon has been modelled in order to describe the reaction temperature of the particle as a function of reactor parameters (*e.g.* reactor temperature and rotor speed), material properties and particle conversion.

Degradation of the particle is treated as a pseudo-surface reaction even though, strictly speaking, the reaction does not proceed on the surface. For ablative pyrolysis, the steep temperature gradient observed experimentally (*e.g.* [5]) combined with a reaction rate which is strongly dependent on temperature suggest, that reaction is concentrated in a relatively thin shell near the surface. This approach is inspired by the study of Lédé [6] for slab geometry.

An expression for the movement of the surface is obtained by setting up a shell balance for the particle to obtain the differential equation:

$$\frac{d}{dr}\left(r^s v\right) + r^s r_p = 0 \tag{1}$$

Here v is the velocity of the retracting surface and r_p is the rate of reaction. Integration within limits and substituting r_p with the Arrhenius first order expression gives:

$$\frac{dR_{surf}(t)}{dt} = -\frac{1}{R_{surf}^s}\int_0^{R_{surf}} r^s A \exp\left(\frac{-E}{RT(r)}\right) dr \tag{2}$$

The transient temperature distribution in the solid is described with the following partial differential equation [7]:

$$\rho \cdot c_p \frac{\partial T}{\partial t} = \frac{1}{r^s}\frac{\partial}{\partial r}\left(k \cdot r^s \frac{\partial T}{\partial r}\right) \tag{3}$$

where s is the shape factor (s=0 for plate, s=1 for cylinder and s=2 for sphere), ρ is the density, c_p is the specific solid heat capacity and k is the thermal conductivity and since these are considered constant, (3) is rewritten as:

$$\frac{\partial T}{\partial t} = \alpha \frac{1}{r^s}\frac{\partial}{\partial r}\left(r^s \frac{\partial T}{\partial r}\right) \tag{4}$$

where α is the thermal diffusivity ($=k/\rho\, c_p$). The initial and boundary conditions for the system of differential equations (1) and (4) are:

$$\text{IC1}: \ R_{surf}(t=0) = R_0 \tag{5}$$

$$\text{IC2}: \ T(t=0, r) = T_0 \tag{6}$$

$$\text{BC1}: \ k\left.\frac{\partial T}{\partial r}\right|_{r=R_{surf}} = h\left(T^{\infty} - T_{R_{surf}}\right) \tag{7}$$

$$\text{BC2}: \ \left.\frac{\partial T}{\partial r}\right|_{r=0} = 0 \tag{8}$$

IC1 states the initial size of the particle considered, IC2 states that the initial spatial temperature profile is uniform, BC1 states that heat transferred to the external surface by convection is transported into the material by conduction and finally BC2 states that that the particle is symmetric around the particle centre.

The model is made dimensionless by introducing a number of variables selected to fit the system in the best possible way. The dimensionless temperature θ:

$$\theta = \frac{T - T_0}{T_0^{\infty} - T_0} \tag{9}$$

The dimensionless time τ and location x within the particle:

$$\tau = \frac{\alpha\, t}{R_0^2} \qquad \textbf{(10)}$$

$$x = \frac{r}{R_{surf}(t)} \qquad \textbf{(11)}$$

To satisfy the symmetry boundary condition at the center, (8), the variable substitution is used:

$$u = x^2 \qquad \textbf{(12)}$$

To track the position of the surface in time, a dimensionless position, η, is introduced:

$$\eta = \frac{R_{surf}(t)}{R_0} \qquad \textbf{(13)}$$

A dimensionless activation energy, γ, is also introduced based on the initial temperature:

$$\gamma = \frac{E}{R_G T_0} \qquad \textbf{(14)}$$

The dimensionless variables are introduced into the original equations (2) to (8). The conservation of energy in the solid particle becomes:

$$\frac{\partial\theta}{\partial\tau}\eta^2 = 2\left(s+1+u\eta\frac{\partial\eta}{\partial\tau}\right)\frac{\partial\theta}{\partial u} + 4u\frac{\partial^2\theta}{\partial u^2} \qquad \textbf{(15)}$$

with corresponding initial and boundary conditions:

$$\left.\frac{\partial\theta}{\partial u}\right|_{u=1} = \frac{1}{2}\frac{hR_{surf}}{k}\left(\theta^\infty - \theta|_{u=1}\right) = \frac{Bi(R_{surf})}{2}\left(\theta^\infty - \theta|_{u=1}\right)$$

Or

$$\left.\frac{\partial\theta}{\partial u}\right|_{u=1} = \frac{1}{2}\frac{hR_{surf}}{k}\left(\theta^\infty - \theta|_{u=1}\right) = \frac{Bi(R_0)}{2}\eta\left(\theta^\infty - \theta|_{u=1}\right) \qquad \textbf{(16)}$$

$$\theta(t=0,u) = 0 \qquad \textbf{(17)}$$

It is noted that the Biot number, a characteristic dimensionless group in transient heat conduction problems, is introduced. Generally, for non-moving boundaries and for $Bi>10$ particle heating can be assumed to be controlled by internal heat transfer and for $Bi<0.1$ heating is assumed to be controlled by external transfer. However, for moving boundaries caution must be taken when applying this empiricism, as the hot surface of the particle is consumed continuously. Finally, the movement of the surface is made dimensionless yielding:

$$\frac{d\eta}{d\tau} = -\frac{R_0^2 A}{2\alpha}\eta\int_0^1 u^{\frac{s-1}{2}} \exp\left(-\frac{\gamma}{\left(\frac{T_0^\infty}{T_0}-1\right)\theta(u)+1}\right) du \qquad \textbf{(18)}$$

with the initial condition:

$$\eta(\tau=0) = 1 \qquad \textbf{(19)}$$

Discretization by orthogonal collocation is used to approximate the transient temperature profile inside the particle. Integration of the coupled differential equations is performed using the semi-implicit Runge-Kuta integration routine SIRUKE [8]. Equation (18) is solved by Gauss integration.

Results and Discussion

Due to heating the particle is decomposed into a short lifetime Intermediate Liquid Compound (ILC) which forms a film on the cylinder wall [9]. The reaction proceeds according to an irreversible first order reaction [10, 11]:

$$\text{Cellulose} \xrightarrow{r_p} \text{ILC (liquid)} \qquad \textbf{(20)}$$

In subsequent steps, competing reactions lead to the formation of fine char particles and vapours by evaporation and thermal cracking. Following the idea of Diebold and Power [12], heat transfer to the particle is assumed to originate from wall-particle contact (i.e. solid convection) only.

For a rod of cellulose in contact with a rotating disk, the heat transfer coefficient has been experimentally established to be proportional to the contact pressure between rod and disk, provided the relative velocity is above 1.0 to 1.5 m/s [5]. It is assumed that particles of slab cylindrical geometry are indefinite and during conversion slabs are only submitted to wall contact on one side, whereas cylinders and spheres are evenly exposed to the hot surface due to rotation. Also, it is assumed that for cylinders and spheres, the contact pressure between particle and wall can be calculated using the area constituted by the part of the particle submerged in TLC as basis. For slabs, all the surface area of the exposed side is considered to be in intimate contact with the wall. Under these conditions, it can be shown that h is given by:

$$h = \frac{1}{59(s+1)} r\rho g G \qquad \textbf{(21)}$$

where the usual notation is used. Table 1 contains information regarding the kinetic and physical properties used for the subsequent calculations with the exception of heat of reaction which has been ignored due to the insignificance in relation to the latent heat [12]. Particles are assumed to be converted when the characteristic size is reduced to 50 µm which is comparable to the size of the char formed in the later degradation step of ILC.

Table 1 – Physical and chemical parameters used in the simulation.

Parameter	***Value***	***Unit***	***Ref.***
ρ	700	kg/m^3	[13]
A	$2.8 \cdot 10^{19}$	1/s	[11]
E	242	kJ/mol	[11]
c_p	2446	J/kg/K	[13]
k	0.21	W/m/K	[13]
ΔH	~ 0	kJ/kg	[12], [14]
ε	0.70	-	[13]
σ	$5.76 \cdot 10^{-8}$	W/m^2/K^4	-
γ	97.67	-	-
R_0	500	µm	-
R_∞	50	µm	-

Figure 2 depicts modeling results for the surface temperature of a spherical particle undergoing ablative pyrolysis at levels of centrifugal force and reactor wall temperature obtainable in the experimental bench reactor system. Generally, the surface temperature of the reacting particle will increase both by applying a higher reactor temperature and force against the wall of the reactor but remains almost constant for the main part of the conversion. This effect has earlier been demonstrated experimentally for wood by Lédé and co-workers [5]. They found the process to be well described as a melting phenomenon and assigned the “melting temperature” of wood to 466 °C. Due to a higher temperature of their rotating disc and a higher pressure applied to the wood cylinder, the results of the simulation presented here will naturally be lower.

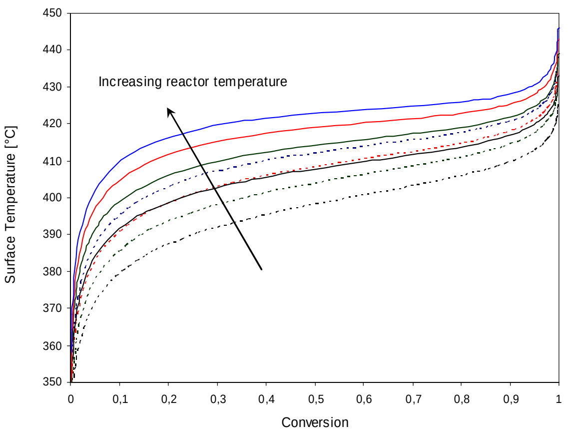

Figure 2: Surface temperature of a spherical particle with an initial temperature of 20°C undergoing ablative pyrolysis at 10,000 (*broken lines*) and 20,000 G’s (*solid lines*). Results for reactor wall temperatures of 500, 550, 600 and 650°C.

The conditions necessary to obtain ablative pyrolysis have by Lédé [6] and Di Blasi [10] suggestively been defined by means of the Biot number, *Bi* and the thermal Thiele modulus, *Th*:

$$\begin{aligned} &Bi \geq 1 \\ &Th >> 1 \end{aligned} \tag{22}$$

The physical interpretation of *Th* is that it gives the ratio between a characteristic time of solid heating and a characteristic time of solid degradation. The ablative envelope is thus characterized by internal control of particle heating and that solid degradation proceeds faster than the inward solid heating rate. As can be seen from Figure 3 the conditions studied in the simulation presented here can by this definition not stringently be characterized as ablative. Therefore, even though the characteristic constant particle surface temperature for ablative pyrolysis is approached, care must be taken when interpreting the future experimental results in relation to the model.

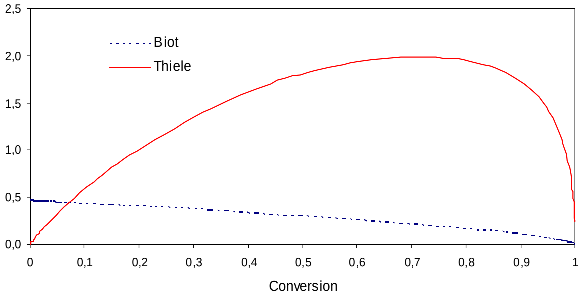

Figure 3: Biot number and Thiele modulus for a spherical particle undergoing pyrolysis (reactor wall temperature 550 C and centrifugal force 10,000 G’s).

Conclusions

A bench reactor system to study the ablative pyrolysis of straw has been constructed and a model to predict the fate of a particle submitted to the environment of the reactor has been developed.

Acknowledgements

The project is partly funded by DTU as part of the Innovation PhD Program and by the Nordic Graduate School in Biofuels Science and Technology.

References

1. FAOSTAT data, last accessed December 2004.
2. Handbook for Farm Management, Landbrugsforlaget, Aarhus, 2003.
3. OPEC Annual Statistical Bulletin 2003, OPEC, Vienna, 2004.
4. Bech, N. In-Situ Flash Pyrolysis of Straw. In: Dam-Johansen, K., Skjøth-Rasmussen (eds.), M.S. Graduate Schools Yearbook 2004, Dept. of Chemical Engineering, DTU, Kgs. Lyngby, 2004, 13-14.
5. Lédé, J., Panagopoulos, J. Li, H.Z., Villermaux, J. Fuel, 64, 1985, 1514-1520.
6. Lédé, J. Biomass and Bioenergy, 7, 1994, 49-60.
7. Bird, R.B., Stewart, W.E., Lightfoot, E.N. Transport Phenomena, 2nd edition, Wiley, New York, 2002.
8. Villadsen, J., Michelsen, M.L. Solution of Differential Equation Models by Polynomial Approximation, Prentice-Hall, New Jersey, 1978.
9. Lédé, J. J. Anal. Appl. Pyrolysis, 70, 2003, 601-618.
10. Di Blasi, C. Chem. Eng. Sci., 51, 1996, 2211-2220.
11. Boutin. O., Ferrer, M., Lédé, J. Chem. Eng. Sci., 57, 2002, 15-25.
12. Diebold, J., Power, A. Engineering aspects of the vortex pyrolysis reactor to produce primary pyrolysis oil vapors for use in resins and adhesives. In: Bridgwater, A.V. (ed.) Research in thermochemical biomass conversion, Elsevier, London, 1988, 609-628.
13. Jensen, P.A., Sander, B., Dam-Johansen, K. Biomass and Bioenergy, 20, 2001, 431-446.
14. Stenseng, M., Jensen, A., Dam-Johansen, K. J. Anal. Appl. Pyrolysis, 58-59, 2001, 767-783.

Søren Prip Beier
Address: Membrane Group / CAPEC, Dept. of Chem. Eng., Building 227, room 110
Technical University of Denmark
Phone: +45 4525 2955
Fax: +45 4588 2258
e-mail: spb@kt.dtu.dk
www: http://www.kt.dtu.dk
Supervisor: Gunnar Jonsson
gj@kt.dtu.dk
Ph.D. Study
Started: September 2005
To be completed: August 2008

Module Design and Performance in Microfiltration, Ultrafiltration and Membrane Contactors

Abstract

When using membranes for separation purposes the flux often decreases to a level much below the clean water flux due to concentration polarization and membrane fouling. Different ways of dealing with this is to be investigated in this project in order to design and test filtration modules with better separation performances. A novel dynamic microfiltration system has been investigated. The decoupling of high cross-flow velocity and high surface shear rate by vibrations of the membrane module leads to the possibility of filtrating at low cross-flow velocity and low transmembrane pressure which reduces the pumping costs and fouling problems.

Introduction

Today membrane processes are mainly used as one or more downstream processes after batch fermentation. However, combining a membrane process directly with a fermentation process the system can be operated either as a fully continuous fermentation process or as a fed batch process, where the products and eventual inhibitants formed during the fermentation can be continuously removed. Thereby the overall productivity of the fermentation can be increased and the formation of byproducts might be reduced as well. One of the main limitations by using membrane processes directly on fermentation broths is the possible clogging of the membrane channels by yeast cells and bacteria and the fouling of the membrane surfaces by proteins and other macromolecules.

Specific Objectives

The possibility of decoupling the driving force of the membrane process and the necessary cross-flow velocity in the membrane feed channels will be investigated in this Ph.D. project. This is done to get a high mass transfer of solutes away from the membrane surface. The decoupling will be investigated by using external force fields such as:

- Very frequent pressure pulsation and back flushing.
- Vibrations and rotations of the membranes or the feed solution.
- Electrical and/or acoustic fields.
- Using spacers and inserts with optimized performance.

For protein separation with ultrafiltration membranes the effects of pH, ionic strength, membrane surface charge and pore size, will be further investigated.

Dynamic Microfiltration

Till now a novel dynamic microfiltration system consisting of a vibrating hollow fiber membrane module has been tested in the filtration of enzyme solutions with and without suspended baker's yeast. The hollow fibers are placed parallel in a module surrounded by the feed stream. The module is vibrated up and down at variable frequency and amplitude and permeate is sucked through the fibers by a progressive pump. The vibrations induce high surface shear rate which is necessary to reduce or avoid membrane fouling. Normally high surface shear rate (and low transmembrane pressure) is induced by high cross-flow velocity along both sides of the membrane. High pumping costs are therefore a consequence of cross-flow microfiltration. In dynamic microfiltration it is possible to operate at low cross-flow velocity because the vibrations induce the necessary surface shear rate. The flux often depends on the surface shear rate as a power function of this type [1,2,3]:

$$J = a \cdot (\gamma_s)^n \qquad (1)$$

The constants *a* and *n* depends on the feed stream composition and can be found by fitting experimental data to Eq. 1. An equation for calculation the periodic surface shear rate γ_s for the membrane module is derived from the Navier-Stokes equation [4]:

$$\gamma_s = v_0 \cdot \sqrt{\frac{\omega}{2\nu}} \cdot [\sin(\omega \cdot t) - \cos(\omega \cdot t)] \qquad (2)$$

V_0 is the velocity amplitude and ω is the angular frequency. An average of the periodic shear rate is used as a value for the surface shear rate. The critical flux concept formulated by Field et al. [5] is used to evaluate the filtration data.

Results and Discussion

Critical fluxes for solutions of the enzyme Fungamyl supplied by Novozymes A/S with and without suspended baker's yeast (5 g/l) have been determined for vibration frequencies between 5 and 25 Hz and amplitudes between 0.2 and 1.175 mm. The critical fluxes vs. the surface shear rate calculated by use of Eq. 2 are depicted in Fig. 1.

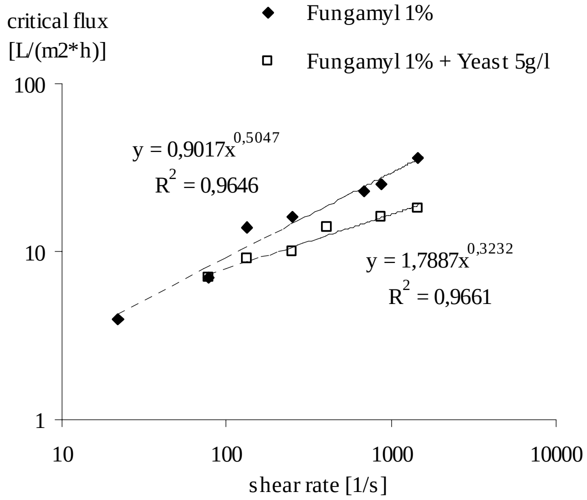

Figure 1: Critical flux vs. average surface shear rate for 1% solutions of Fungamyl with and without suspended baker's yeast (5 g/l).

The expression in Eq. 1 describes the correlation between the critical fluxes and the surface shear rate well. The values of the constants *a* and *n* depend on the feed stream composition. Below the critical flux no severe membrane fouling is observed. High content of macromolecules and particulates in the feed stream decrease the critical flux because of faster membrane fouling. Membrane fouling is a very complex phenomena described extensively in the literature [6]. It seems as if the content of macromolecules (Fungamyl) has a larger impact on the membrane fouling than the yeast cell content. Adsorption and deposition of macromolecules in and on the membrane, and denaturation of macromolecules at the pore entrances probably leads to the formation of a protein gel layer on the membrane surface [7]. Thus the resistance towards mass transport is increased and the enzyme transmission and permeate flux are decreased.

Conclusion and Future Work

The decoupling of the driving force and cross-flow velocity has been investigated in a novel dynamic microfiltration system by use of vibrations of the membrane module. The critical flux depends on the surface shear rate and the feed flow composition described by a power function expression. It was possible to filtrate at low feed flow velocity and low transmembrane pressure resulting in low membrane fouling. In the future filtration of solutions containing other macromolecules has to be investigated as well as performances of other microfiltration, ultrafiltration and membrane contactor module designs have to be investigated. The aim is to reach a better understanding of the membrane fouling in order to reduce the problem and to improve the separation performance in general.

Acknowledgements

I would like to thank Novozymes A/S for delivering enzyme solutions for the experimental work.

References

1. M.Y. Jaffrin, L. Ding, O. Akoum, A. Brou, J. Membr. Sci. 242 (2004) 155-167
2. J. Postlethwaite, S.R. Lamping, G.C. Leach, M.F. Hurwitz, G.J. Lye, J. Membr. Sci. 228 (2004) 89-101
3. O. Al-Akoum, L.H. Ding, M.Y. Jaffrin, Sep. Purif. Technol. 28 (2002) 219-234
4. R.B. Bird, W.E. Stewart, E.N. Lightfoot, Transport Phenomena, Wiley, 2002, p. 120
5. R.W. Field, D. Wu, J.A. Howell, B.B. Gupta, J. Membr. Sci. 100 (1995) 259-272
6. A.D. Marshall, P.A. Munro, G. Trägårdh, Desalination 91 (1993) 65-108
7. G. Jonsson, W. Li, P.L. Johansen, Proceedings of The CEE-Brazil Workshop On Membrane Separation Processes, Commission of European Communities, 3-8 May (1992) 265-276

List of Publications

1. S.P. Beier, G. Jonsson, M. Guerra, A. Garde, Dynamic Microfiltration with a Vibrating Hollow Fiber Membrane Module; Filtration of Yeast Suspensions, J. Membr. Sci. (In preparation)
2. S.P. Beier, G. Jonsson, Separation of Yeast Cells and Enzymes with a Vibrating Hollow Fiber Membrane Module, Sep. Purif. Technol. (In preparation)
3. Oral Presentation for the EUROMEMBRANE 2006 conference, Messina, Italia, Sep. 2006 (In preparation)

Suzan Biran
Address: Department of Chemical Engineering
Søltofts Plads, Building 229
Technical University of Denmark
DK-2800 Kgs. Lyngby
Phone: +45 4525 2920
Fax: +45 4588 2258
e-mail: sb@kt.dtu.dk
www: http://www.chec.kt.dtu.dk

Supervisors: Anker Jensen
Søren Kiil
Poul Bach, Novozymes A/S
Ole Simonsen, Novozymes A/S

Ph.D. Study
Started: September 2003
To be completed: August 2006

Stability of Enzymes in Granular Enzyme Products for Laundry Detergents

Abstract

Enzymes are important constituents in laundry detergents due to their contribution to a more effective and milder washing process (lower energy and water consumption, less wear of fabric). Storage stability of detergent enzymes is a significant quality parameter considered in the development of a new product. The complexity of the detergent matrix implies the presence of a complicated mechanism involved in the inactivation. It is believed that a combination of factors such as humidity, released H_2O_2, autolysis of enzymes, high local pH in the granule, oxygen, defects in granulate structure and other detergent components plays a role in the activity loss. The aim of this project is to investigate the factors responsible for the inactivation of enzymes and propose new formulations and protective components for improved stability.

Introduction

Enzymes are used today in a wide range of industrial processes and in consumer products. The largest application of industrial enzymes is in detergents. The detergent industry absorbs about 45% of enzyme sales in western Europe and more than 25% of the total worldwide enzyme production [1]. After being produced by submerged microbial fermentation, enzymes are recovered and sold as either powder or liquid products for industrial use. In powdered laundry detergents, they are granulated and covered with a protective coating to prevent dust allergies and increase the stability of enzymes.

The main enzyme activity in biological laundry detergents is protease, which acts on organic stains such as grass, blood, egg and human sweat. However, it has become more common in recent years to include a "cocktail" of enzyme activities including lipases and amylases. Lipases are effective on stains resulting from fatty products such as oils and fats, while amylases help remove starchy food deposits. More recently, color enhancing and "anti-bobbling" washing powders have been developed which contain cellulases. The mode of action of such cellulases is to remove detached cellulose fibrils, which cause a progressive dulling of the color as dirt is trapped on the rough surface of the fabric.

Laundry detergents typically consist of a mixture of separate granular materials including surfactants, builders, bleaching agents and enzymes. The surfactants are the main cleaning agent, while the builders provide alkalinity and ionic strength to the wash liquor. Bleaching agents are added to provide a white shine and remove stains on the fabric. A modern bleaching agent is Sodium Percarbonate (SPC), which decomposes in water and releases hydrogen peroxide, being the actual bleaching chemical. In addition to these, powdered laundry detergents contain soil anti-deposition polymers, anti-corrosion agents, perfumes etc.

Enzymes are fragile biomolecules. They can loose their activity in environments, like detergents, where harsh chemicals are present. In practice the enzymes loose a significant part of their activity over a time period of several weeks. To overcome this problem, manufacturers prefer to add more enzyme granules in their products to have satisfactory wash performance. However, this results in an increase in the production cost of the laundry detergent. Partly to obtain a better stability during storage, the enzyme containing particles are typically coated by layers of salts, polymers and/or waxes. This reduces the rate of diffusion of aggressive species into the particles where reaction with the enzymes may cause deactivation. Furthermore, the particles are often formulated with anti-oxidants, such as thiosulfates, to minimize deactivation reactions. For the enzymes in laundry detergents, the deactivation is mainly related to the release of hydrogen peroxide from the bleaching chemicals in a moisture-containing atmosphere. Moreover, humidity, autolysis of enzymes, high local pH in granule, oxygen, defects in granulate structure and other detergent components are some of the factors affecting the granulate stability during storage.

The present understanding of inactivation mechanism of detergent enzymes during storage [2] involves diffusion of water vapor through bleaching particles, where SPC is "activated" and hydrogen peroxide is released. The subsequent diffusion of hydrogen peroxide vapor in the enzyme granule results in oxidation of methionine and tyrosine residues in the enzyme. The sulfur in methionine, found in the active site of Savinase (protease), can be oxidized to sulfoxide by hydrogen peroxide. The fact that enzyme activity is reduced significantly even in non-bleach containing detergents implies that other mechanism(s) are also involved in deactivation of granulates.

Specific Objectives

The objective of this project is to understand the inactivation mechanism of detergent enzymes during storage. It is also aimed to investigate the effect of different detergent ingredients on the granulate stability. According to the new findings, the previously proposed mechanism can be confirmed or modified. In light of the results, new stability-enhancing components or coatings will be proposed and tested for their efficiency in reducing enzyme deactivation in powdered detergents.

Experimental Setup

The set up (Figure 1) provides controlled conditions of H_2O_2 (g) concentration, humidity and temperature. H_2O_2 (g) is generated by bubbling N_2 through a concentrated H_2O_2 solution. Relative humidity (RH) of the gas stream is adjusted by bubbling N_2 through distilled H_2O at appropriate temperature. Further tuning of the H_2O_2 level and moisture is done by a third stream of N_2. Enzyme sample is placed in a column where quartz wool serves as a support material. A gas stream is passed through the column, where freeze-dried Savinase is in direct contact with the flowing gas.

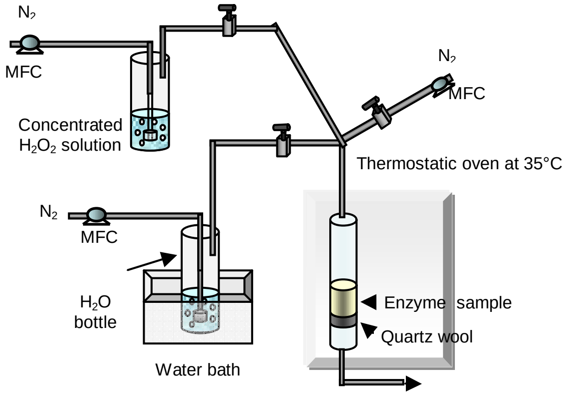

Figure 1: Sketch of the enzyme exposure setup

Results and Discussion

Adsorption

The exposure experiments showed that there is a simultaneous adsorption of moisture and H_2O_2 by the enzyme powder. Isothermal adsorption-desorption investigation of Savinase indicates that significant amount of water was uptaken (Figure 2). However, the absence of hysterisis implies that only physical adsorption is involved and simple drying can remove the uptaken water. H_2O_2 adsorption study, on the other hand, showed that beside physical adsorption chemisorption may also be involved, since 24h-desorption trial of 2-h exposed sample resulted in 74% residual H_2O_2 content.

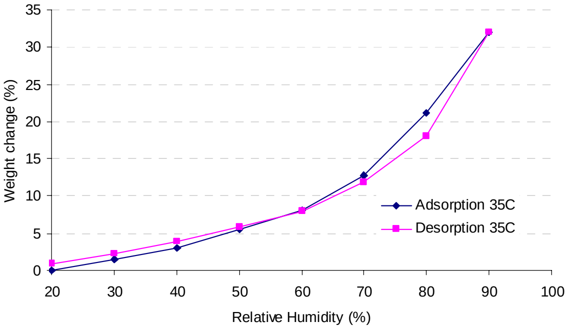

Figure 2: Isothermal adsorption-desorption curve for freeze-dried Savinase at 35°C. No hysterisis was observed.

The effect of RH in the gas stream on the H_2O_2 adsorption was studied. Figure 3 clearly illustrates that amount of H_2O_2 adsorbed by the sample is independent of the moisture in the system.

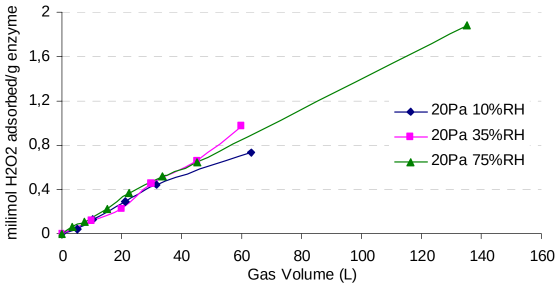

Figure 3: Effect of relative humidity on the hydrogen peroxide adsorption at 35°C. Equal amounts of H_2O_2 were up taken independently of the moisture in the gas stream.

The variation of adsorbed H_2O_2 amount with respect to varying H_2O_2 partial pressures at constant humidity was also determined (Figure 4). As the concentration of H_2O_2 in the gas was increased, the adsorbed H_2O_2 by the enzyme sample also increased. Equilibrium was attained and limit adsorption value was reached provided enough exposure time.

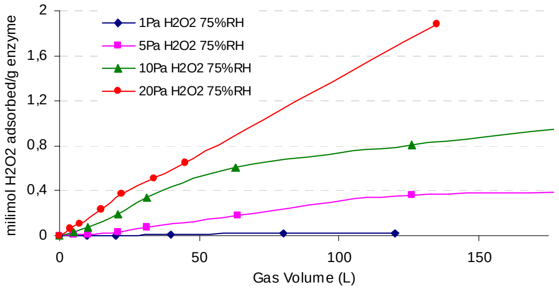

Figure 4: Effect of H_2O_2 (g) concentration on the adsorbed H_2O_2 by the enzyme at 35°C.

Inactivation

The inactivation kinetics of the freeze-dried Savinase was investigated as a function of H_2O_2 (g) concentration and relative humidity.

Effect of H_2O_2 (g) concentration

Stauffer and Etson [3] revealed the oxidation mechanism of a commonly studied protease, subtilisin, by H_2O_2. The enzyme was inactivated by the formation of methionine sulfoxide at position 222. Oxidized enzyme activity towards synthetic substrates decreased relative to native enzyme activity due to the proximity of Met 222 to the active site. Experimental evidence showed that activity decrease of the enzyme was accompanied by the oxidation of just 1 Met residue. Met-sulfoxide formation did not inactivate subtilisin completely but, depending on the substrate, the activity was reduced by 57 to 92%. The authors suggested the following mechanisms responsible for activity loss: a) oxidative modification of Met 222 might result in a conformational change in the protein structure; b) the alteration from a hydrophobic sulfide to a hydrophilic sulfoxide might alter the electronic environment around the active site sufficiently to affect the rate at which individual reaction steps occur; c) the presence of 1 additional oxygen atom might have a conformational interference to the optimum interaction between substrate and enzyme molecules. Other oxidation studies described in the literature also involve utilization of H_2O_2 in a solution [4,5,6]. However, they do not reveal the impact of gaseous hydrogen peroxide released in the detergent box on enzyme stability during storage.

The effect of H_2O_2 (g) on Savinase stability was studied at 10% and 75%RH. On Figure 5, the decrease in % residual activity is illustrated. At 10%RH conditions, the gradual increase in the extent of enzyme inactivation as H_2O_2 (g) concentration went from 0 to 20Pa could be noticed (Figure 5-a). At 75%RH, on the other hand, no matter the concentration, presence of H_2O_2 was enough to cause a drastic reduction in the Savinase activity (Figure 5-b). This implies that at high humidity conditions, enzymes became more susceptible to oxidation.

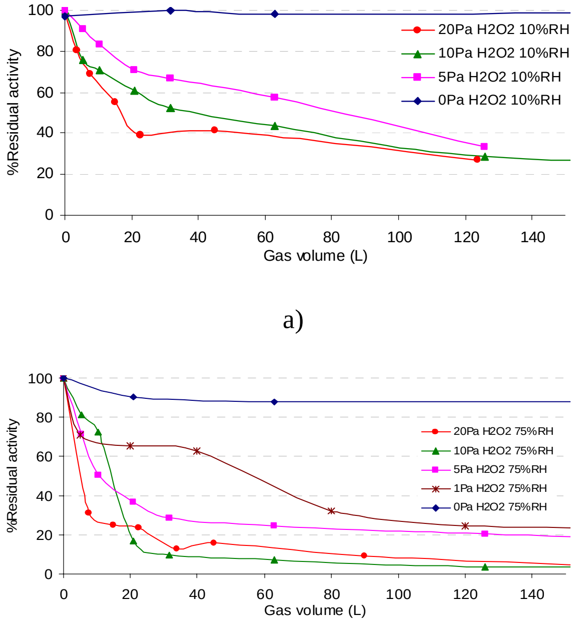

a)

b)

Figure 5: Effect of increasing H_2O_2 (g) concentration on Savinase stability; a) 10%RH; b) 75%RH. At high humidity, presence of H_2O_2 has more detrimental impact on enzyme stability.

Effect of humidity

Dry proteinous products adsorb significant moisture when exposed to humid conditions. Experimental evidence shows that increased residual moisture results in a noticeable reduction in the stability of the product. The detrimental effect of moisture on storage stability is often interpreted in terms of mobility in the solid and reactivity of the protein. Above monolayer levels of water, protein's conformational flexibility is increased and the additional water has ability to mobilize the potential reactants in the amorphous phase. Both effects increase the rate of protein degradation [7]. The negative effect of increasing humidity on enzyme activity was illustrated by exposing the enzymes in the presence of H_2O_2 (g) with constant concentration (20Pa) (Figure 6). The high moisture content in the sample increased the mobility of the enzyme molecules and enhanced the oxidative effect of H_2O_2.

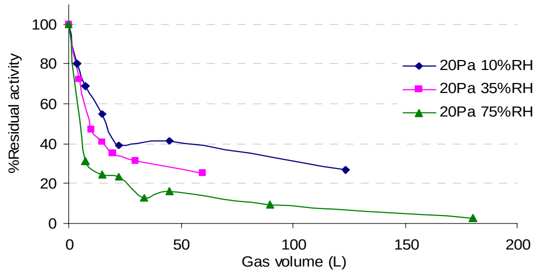

Figure 6: Effect of relative humidity on inactivation extent of the enzyme exposed to 20Pa H_2O_2. As the moisture in the sample increases, the loss of activity becomes more drastic

Moreover, residual activity results of samples exposed to high (75%) and low (10%) relative humidity showed that Savinase may loose part of its initial activity even in the absence of oxidizing agent (Figure 5 a- and b- 0Pa H_2O_2 samples). This was further studied by exposing the freeze-dried Savinase to extreme conditions, i.e. 100%RH. The 80% loss in enzyme activity after exposure for one week (Figure 7) might result from the autoproteolytic activity of Savinase.

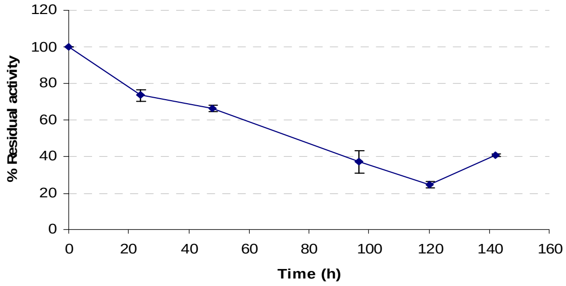

Figure 7: Inactivation curve of Freeze-dried Savinase exposed to 100%RH at 35°C.

Samples were analyzed by sodium dodecylsulfate polyacrylamide gel electrophoresis (SDS-PAGE), where the proteins were unfolded and separated according to their molecular weight (Figure 8). No proteolytic activity was observed in the gel. The main band at 26.7 kDa represents Savinase. The low molecular fragments were already present in the reference sample, so they can be accepted as impurities in the enzyme powder. Moreover, a decrease in the Savinase band could not be detected visually. The dehydration-rehydration studies of subtilisin conducted by De Paz *et al*. [8] also resulted in absence of proteolysis. In fact, Towns [9] stated that self-proteolysis is of minimal concern in solid-state protease formulations, because the inter-molecular reactions require a significant mobility to the segmental portions of the protein backbone. The exposure result of solid-state Savinase to an extreme humidity undoubtedly confirmed this statement.

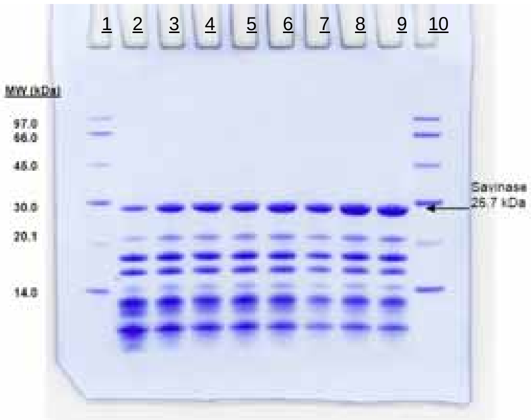

Figure 8: SDS-PAGE gel of freeze dried Savinase exposed to 100% RH. Lines: 1&10- Low molecular weight standards, 2- 0h, 3- 24h, 4- 48h, 5-72h, 6- 96h, 7- 120h, 8- 142h, 9- 142h –exposed samples.

Non-covalent aggregation is another reason for stability decrease in solid-state proteins. It may occur due to an unfavorable conformational change of the protein during its re-hydration in a solution. NATIVE-PAGE separates proteins according to their molecular volumes in a solution.

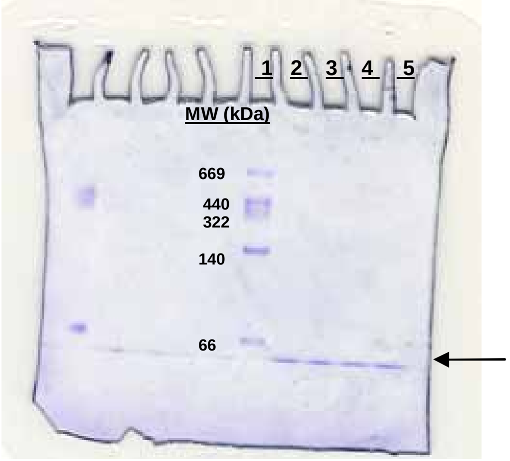

Figure 9: NATIVE-PAGE gel of freeze dried Savinase exposed to 1Pa H_2O_2 and 75%RH. Lines: 1- High molecular weight standard, 2- 0h, 3- 0.6h, 4- 4h, 5-14h –exposed samples.

The single band observed on the NATIVE-PAGE gel implied that no aggregates were formed during the exposure of freeze-dried Savinase to 1Pa H_2O_2 and 75% RH (Figure 9). Further conformation will be achieved by analyzing the samples for their surface charge distribution and molecular conformation by iso-electro focusing (IEF) electrophoresis.

Preliminary Formulation Study

The protective effect of enzyme granulate ingredients on Savinase stability was also examined. Sodium thiosulfate ($Na_2S_2O_3.5H_2O$) and sodium carbonate (Na_2CO_3) were tested. Freeze-dried Savinase powder was mixed with the corresponding salt in 1:1 ratio and the mixture was exposed in a column to 20Pa H_2O_2 and 75%RH. An evident stabilizing effect against oxidation was observed for the both salts (Figure 10). Only 20% and 40% of the initial enzyme activity was lost in the Savinase sample mixed with sodium thiosulfate (STS) and sodium carbonate (SC), respectively, while the column containing pure enzyme powder lost more than 80% of its original activity at the same exposure conditions. The protective nature of STS is based on its anti-oxidative property. It reacts with H_2O_2 and significantly decreases the gas concentration in the column. The decomposition reaction is as follows:

$$Na_2S_2O_3 + 4H_2O_2 \rightarrow Na_2SO_4 + H_2SO_4 + 3H_2O$$

A direct reaction between SC and H_2O_2 is not known, still the presence of the salt resulted in substantially retained activity. The stabilizing effect of SC may be related to the ‘dilution’ it provides when it is mixed with the enzyme powder. Further investigation on the individual effect of the salt on H_2O_2 decomposition is required.

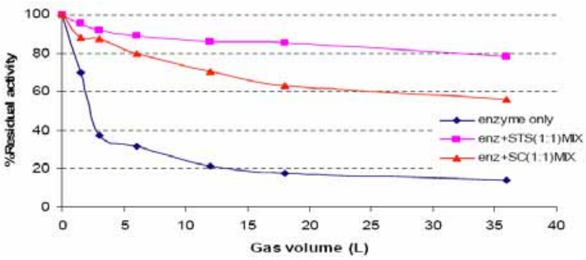

Figure 10: Effect of granule ingredients on enzyme column on residual activity. Mixing Savinase with STS and SC resulted in improved stability. STS had greater protection against oxidation.

Conclusions and Future Work

An accurate method for the generation and measurement of low concentrations of hydrogen peroxide vapor was established. The experimental setup provides controlled conditions for the exposure of freeze-dried enzymes to different concentrations of H_2O_2 vapor and %RH. The effect of these factors is being studied for the determination of the inactivation kinetics of Savinase. The present results indicate that freeze-dried enzyme adsorbs significant amount of moisture and H_2O_2 during exposure. A combined effect of humidity and H_2O_2 is responsible for the inactivation of Savinase. High moisture induces the oxidizing effect of H_2O_2. No proteolytic activity is observed in solid-state enzyme sample. Other mechanisms like deamidation, agglomeration and conformational changes are also studied. The preliminary formulation experiments indicate that STS is an effective protective agent against oxidation. New enzyme formulations will be tested for improved enzyme stability.

Acknowledgements

The Novozymes Bioprocess Academy is acknowledged for the financial support of this project.

References

1. Broze G. (Edr.), Handbook of Detergents, Part A: Properties, Surfactant Science Series Vol. 82, Marcel Dekker, Inc. New York, 1999, p.639.
2. Simonsen O. and Langemo H., 2001, Mechanism of Deactivation of Enzymes and Sodium Percarbonate (SPC) in HDP, *40th International Detergency Conference Proceedings*, 228-231.
3. Stauffer C.E. and Etson D., 1969, The effect on subtilisin activity of oxidizing a methionine residue, *The Journal of Biological Chemistry*, Vol. 244, Iss. 10, 5333- 5338.
4. DePaz R.A., Dale D.A., Barnett C.C., Carpenter J.F., Gaertner A.L., Randolph T.W., 2000, The excluding effects of sucrose on a protein chemical degradation pathway: methionine oxidation in subtilisin, *Archives in Biochemistry and Biophysics*, Vol. 384, No.1, 123-132.
5. Nguyen T.H., Burnier J., Meng W., 1993, The kinetics of relaxin oxidation by hydrogen peroxide, *Pharmaceutical Research*, Vol. 10, No. 11, 1563-1571.
6. Levine R.L., Mosoni L., Berlett B. S., Stadtman E.R., 1996, Methionine residues as endogeneous antioxidants in proteins, *Biochemistry*, Vol. 93, 15036-15040.
7. Pikal M.J., 1994, Freeze-Drying of Proteins: Process, Formulation, and Stability , H*ACS Symposium Series* H, Vol. 567, 120-133.
8. DePaz, R.A., Dale, D.A., Barnett, C.C., Carpenter, J.F., Gaertner, A.L., Randolph, T.W., 2002, Effects of drying methods and additives on the structure, function, and storage stability of subtilisin: role of protein conformation and molecular mobility, *Enzyme and Microbial Technology*, 31, 765-774.
9. Towns J.K., 1995, Moisture content in proteins: its effects and measurement, *Journal of Chromatography A*, 705, 115-127.

Astrid Boisen
Address: Haldor Topsøe A/S
Nymøllevej 55
DK-2800 Lyngby
Phone: +45 4527 2680
Fax: +45 4527 2999
e-mail: asb@topsoe.dk
www: http://www.haldortopsoe.com

Supervisors: Ib Chorkendorff
Søren Dahl, Haldor Topsøe A/S

Ph.D. Study
Started: July 2002
To be completed: June 2006

Ammonia as Storage for Hydrogen

Abstract

Research on ammonia decomposition is strongly related to research on ammonia synthesis. The objective of this work is to investigate whether concepts developed for catalytic ammonia synthesis can be applied to the catalytic ammonia decomposition and help predict the properties of the optimal decomposition catalysts. It is found that knowledge about the ammonia synthesis reaction can be used to accurately describe the ammonia decomposition reaction. However, the optimal catalyst for ammonia decomposition is never the optimal catalyst for ammonia synthesis. The bimetallic nitride Co_3Mo_3N is shown to have significant potential in ammonia decomposition; particularly for use in small mobile units.

Introduction

The current scientific interest in hydrogen as an energy carrier is mainly due to environmental concerns about the harmful emissions from fossil fuels being used today. Furthermore, one of the major attractions of hydrogen as a fuel is its compatibility with fuel cells. Highly efficient conversion of chemical energy into electrical energy makes fuel cells a promising source of power generation that could dramatically improve the efficiency of future energy use.

Industrially, the most important route to hydrogen is steam reforming of hydrocarbons, especially steam methane reforming [1]. One main approach in order to provide the hydrogen for fuel is to produce hydrogen in large production plants and distributing it from there. However, lack of satisfactory hydrogen storage possibilities is a main impediment to the widespread use of hydrogen as a fuel, especially for transportation use. Another main approach is on-site hydrogen production. However, reforming of hydrocarbons produces carbon oxides as by-products. As a means for on-site hydrogen production this presents two problems. Firstly, fuel cells operating at low temperature have a low tolerance for carbon oxides. Only trace amounts of CO in the fuel stream of proton exchange membrane (PEM) fuel cells can poison the catalysts [2]. Removal of carbon oxides from the steam reforming product gas causes this method for on-site generation of pure hydrogen to be complex, sizeable and expensive [3]. Secondly, both CO and CO_2 are greenhouse gases.

Production of hydrogen by ammonia decomposition appears to be an attractive alternative for on-site hydrogen generation without CO_x impurities. In this way ammonia would act as a carbon-free storage molecule for hydrogen. Decomposition of ammonia yields only hydrogen and nitrogen, with nitrogen being essentially benign to the fuel cell. It is a mildly endothermic process, meaning that high temperature shifts the equilibrium towards nitrogen and hydrogen.

$$2NH_3 \rightleftharpoons N_2 + 3H_2 \qquad (1)$$

Ammonia is an excellent material for hydrogen storage. Anhydrous ammonia contains 17.8 wt. % hydrogen; storing 30 % more energy pr. unit volume than liquid hydrogen. The technology for the production, distribution and storage for ammonia is well established. Anhydrous ammonia liquefies at about 8 atm and room temperature, or -33ºC and ambient pressure. Unlike hydrogen gas, ammonia is explosive in air only over a narrow range of concentrations (*i.e.* 16-27 vol. % NH_3 vs. 18.3-59 vol. % H_2 at 0ºC and 1 atm.) with an autoignition temperature of 651ºC compared to 585ºC for hydrogen [4]. Possibly, the main drawback to the use of ammonia as a fuel and hydrogen carrier is its extreme toxicity and harmful health effects. Despite its toxicity ammonia poisoning is very rare probably because of its strong smell which instantly indicates leakages. Furthermore, ammonia decomposition has to be operated at fairly high temperature (above ca. 400ºC) due to equilibrium considerations and kinetics. This may cause longer start-up times while the catalyst beds are being pre-heated.

Ammonia decomposition has recently been used to power alkaline fuel cell (AFC) prototypes by Kordesch and co-workers [5]. Concerns about the effect of unconverted ammonia have however limited its application for PEM fuel cells [6]. Presence of trace amounts of ammonia in the hydrogen gas stream has been reported to decrease fuel cell performance, possibly due to the replacement of H^+ ions by NH_4^+ ions within the anode catalyst layer and by decreasing the membrane conductivity [7]. The ammonia left in the hydrogen gas stream can however, easily be reduced to ppb levels by a simple adsorption [8]. Alternatively, AFCs would require no ammonia absorber. All together, designing catalysts for ammonia decomposition therefore is a very interesting challenge.

Specific Objectives

Traditionally, research on ammonia decomposition is strongly related to research on ammonia synthesis. The catalytic ammonia synthesis reaction has attracted continued technical and scientific interest since it was first discovered almost a century ago. Today, catalytic synthesis of ammonia from the elements is a heterogeneous catalytic reaction for which there has been reached a very detailed understanding [9]. The objective of this work is to investigate whether concepts developed for catalytic ammonia synthesis can be applied to the catalytic ammonia decomposition and help predict the properties of the optimal decomposition catalysts.

Results and Discussion

Supported Fe, Co, Ni, Cu, and Ru catalysts were prepared by incipient wetness impregnation. The $MgAl_2O_4$-support has a BET surface area of 60.4 m^2/g and a pore volume of 433 ml/kg determined by Hg intrusion. The support material (particle size 150-300 μm) was impregnated with an aqueous solution of the metal nitrates. The impregnated supports were dried at 120°C and calcined in a furnace at 2 ºC/min to 450°C and held there for 2 hours. The metal contents were ca. 5wt. % for the lighter metals and ca. 8wt. % for the Ru catalyst giving approximately the same molar metal content in the supported catalysts. The precise metal contents were determined by inductively coupled plasma spectroscopy (ICP) and are given in Table 1. Heating the catalysts to 500°C with 2°C min^{-1} in H_2/He (1:1) for 2 hours prior to activity measurements ensured reduction of the active metal component. After activity measurements the particle size distributions of the metal particles of the supported catalysts were determined by high-angle annular dark-field scanning transmission electron microscopy (HAADF-STEM). This provides Z-contrast imaging where the brightness roughly depends on the square of the atomic number (Z) which makes it particularly suitable for investigating heavy nanoparticles on a light support material. However, as most metals studied here are not much heavier than the $MgAl_2O_4$-support used the determination of the particle size is not optimal. For the Cu and the Co catalyst only an estimate of the average particle size could be obtained. The surface area of the active component is calculated from the average particle size by assuming spherical form of the metal particles.

Unsupported Co_3Mo_3N was prepared by heating $CoMoO_4$ in flowing ammonia with 2ºC min^{-1} to 650ºC and held at that temperature for 8 hours. X-ray powder diffraction (XRPD) showed complete conversion to Co_3Mo_3N with an average crystal size of 490Å (based on D_{400}). The surface area was determined by a single point BET analysis. In order to ensure that the catalyst is completely converted to the nitride it was heated in pure ammonia for 5 hours at 650ºC prior to the activity measurement. The catalysts are described in Table 1.

Table 1. Metal loading and surface area of the catalysts

Catalyst	Metal loading (wt. %)	Average particle size (nm)	Active component surface area (m^2 g^{-1})
Fe, $MgAl_2O_4$	4.61	13	2.9
Co, $MgAl_2O_4$	5.16	20	1.7
Ni, $MgAl_2O_4$	4.96	3	11
Cu, $MgAl_2O_4$	5.39	500	0.067
Ru, $MgAl_2O_4$	7.98	12	10
Co_3Mo_3N	-	490 Å (XRPD)	7 ± 3 (BET)

The decomposition of ammonia was studied in an integral plug flow reactor with flow rates of 75-200 Nml/min and at temperatures varied from 650°C to 300°C. Feed compositions of He/NH_3 (1:1), H_2/NH_3 (1:1) and pure NH_3 were studied. The U-tube quartz reactor with an inner diameter of 4 mm was loaded with ca. 200 mg catalyst (particle size 150-300 μm), resulting in a bed height of approximately 18 mm for the supported catalysts and ca. 6 mm for Co_3Mo_3N. The reaction products were analyzed by mass spectrometry.

In order to be able to compare the reaction rates over the catalysts at given reaction conditions we need to model the experimental rates. A simple kinetic Langmuir-Hinshelwood model can describe the results obtained over all the catalysts investigated. The following reactions have to be considered for describing ammonia decomposition over metals:

$$NH_3 + {}^* \rightleftarrows NH_x{}^* + \frac{3-x}{2} H_2 \qquad (2)$$

$$NH_x{}^* \rightleftarrows N^* + \frac{x}{2} H_2 \qquad (3)$$

$$2N^* \rightarrow N_2 + 2^* \qquad (4)$$

* symbolizes a free surface site or a molecule bound to the surface. In the model it is assumed that desorption of nitrogen is the rate determining step. Assuming that $\theta_N + \theta_{NH_x} \cong 1$, where x = 1 or 2, the rate of the reaction, r, can be described as,

$$r = 2k_4 \left(1 + \frac{p_{H_2}^{x/2}}{K_3} \right)^{-2} (1-\beta)$$

Where k and K is a rate constant and an equilibrium constant respectively, p_x is the partial pressure of component x, and β is the approach to equilibrium. Assuming no atomic hydrogen or free sites present at the catalyst surface is a reasonable assumption at ammonia decomposition conditions, according to a microkinetic model developed for ammonia synthesis with a ruthenium catalyst [10]. However, at very low ammonia concentration the model will break down. Besides site blocking, interactions between adsorbates are not considered. Note that the reaction rate only depends on the hydrogen partial pressure and not the ammonia partial pressure. A high hydrogen pressure inhibits the decomposition reaction by driving the equilibrium of reaction (2) and (3) towards the left. The rate and equilibrium constants are given below:

$$k_4 = a_4 \exp \frac{E_{a,4}}{RT}$$

$$K_3 = A_3 \exp \left(\frac{\Delta H_3}{RT} \right)$$

Where a and A are pre-exponential factors, E_a is the apparent activation energy and ΔH is the heat of reaction.

The reaction rate, r_{NH_3}, is defined as moles NH_3 disappearing per time and volume. For a plug flow reactor (PFR) this is given as,

$$r_{NH_3} = F_{NH_3,0} \frac{dX_{NH_3}}{dV}$$

Where F_{NH_3} is the molar flow rate of NH_3 in moles per time, X_{NH_3} is the conversion of ammonia, and dV is a differential element of catalyst bed volume. Subscript 0 denotes inlet conditions. The catalyst bed volume can be replaced by the catalyst weight, W, by dividing with the packing density (W/V). The reaction rate then becomes,

$$r_{NH_3} = F_{NH_3,0} \frac{dX_{NH_3}}{dW}$$

This allows for the reaction rate to be expressed in $\text{mol/g}_{\text{cat}}^{-1}\text{s}^{-1}$ which can be advantageous when the weight of the catalyst can be more accurately determined than the catalyst bed volume, or when information on the catalyst is desired rather than information on the catalytic reactor.

In ammonia decomposition the total molar flow rate, F_{total}, is a function of the conversion and given as,

$$F_{total} = F_0 \left(1 + X_{NH_3} Y_{NH_3,0} \right)$$

Y_x is the molar fraction of component x. The molar fractions of the gas components can then be calculated,

$$Y_{NH_3} = \frac{F_{NH_3}}{F_{total}} = Y_{NH_3,0} \frac{1 - X_{NH_3}}{1 + X_{NH_3} Y_{NH_3,0}}$$

Similarly,

$$Y_{H_2} = \frac{\frac{3}{2} X_{NH_3} Y_{NH_3,0} + Y_{H_2,0}}{1 + X_{NH_3} Y_{NH_3,0}}$$

$$Y_{N_2} = \frac{\frac{1}{2} X_{NH_3} Y_{NH_3,0} + Y_{N_2,0}}{1 + X_{NH_3} Y_{NH_3,0}}$$

$$Y_{He} = \frac{Y_{He,0}}{1 + X_{NH_3} Y_{NH_3,0}}$$

Furthermore, $p_x = Y_x p_{total}$, where p_{total} is the total pressure. Dividing the catalyst bed into a series of 100 volume elements, allows one to determine X_{NH_3} at the reactor exit by numerical integration.

As shown in Figure 1 excellent descriptions of the observed rates are obtained by fitting the variables a_4, $E_{a,4}$, A_3, and ΔH_3. This suggests that the model is correct at the reaction conditions used. Similar agreement between model and experiment are obtained with all catalysts.

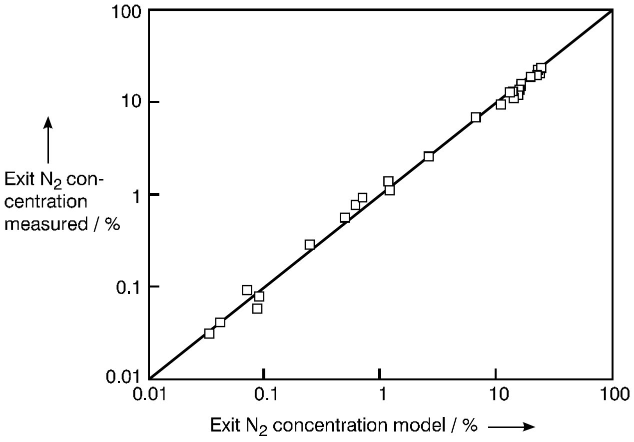

Figure 1. The measured exit N_2 concentration plotted against the exit N_2 concentration described by the kinetic model using the ruthenium catalyst.

The activation energy for the rate determining step in ammonia decomposition, $E_{a,4}$, is fitted to be approximately 160 kJ/mol which corresponds to the activation barrier for dissociation of N_2 in ammonia synthesis minus the binding energy for atomic nitrogen. This is in agreement with available theoretical data [11]. In order to obtain a reliable estimate for the values of a_4, $E_{a,4}$, A_3, and ΔH_3 a more complete set of data would be required. However, this is of no importance in these experiments. Here the Langmuir-Hinshelwood model is used only to compare the reaction rates over the different metals at arbitrary reaction conditions.

Trends in ammonia decomposition activity

It has been shown that a volcano-shaped curve is obtained when the ammonia synthesis activity of a catalyst is plotted against the ability of the catalyst surface to bind to reactants, intermediates or reaction products [12]. The volcano shape can be explained by the principle of Sabatier. According to this principle the optimal catalyst binds adsorbates moderately to the surface. If the adsorbates are bound too weakly the reaction rate will be low due to low coverage of reactants. Conversely, if the catalyst binds adsorbates to strongly it will be difficult to break the bonds again and release the products into the gas phase and consequently the rate will be low due to high coverage of products. For the ammonia synthesis, a more detailed understanding of the reasons underlying the Sabatiers principle has been obtained. A linear relationship between the activation energy for N_2 dissociation, the rate limiting step in ammonia synthesis, and the binding energy of atomic nitrogen on the surface of a series of transition metal catalysts has been shown [13,14]. Such relations, known as the Brøndsted-Evans-Polanyi relation, have long been assumed to be valid [15,16]. In agreement with the Sabatiers principle weaker bonding would require higher activation energy. On the other hand stronger bonding would imply that the adsorbed nitrogen atoms are less willing to participate in subsequent reactions. Furthermore Nørskov and co-workers found that a linear relationship between the activation energy for N_2 dissociation and the binding energy for atomic nitrogen exists, both for close-packed surfaces and for stepped surfaces. The line for the stepped surfaces is shifted to lower activation energies [11].

Thus, both for ammonia decomposition and ammonia synthesis the activity of a metal catalyst can be described by the dissociative adsorption energy of nitrogen onto the surface, actually, onto step-sites. It determines the activation energy of the rate-determining step; N_2 desorption or dissociation, respectively. When plotting the rates of catalytic decomposition of ammonia over supported Fe, Co, Ni, Cu, and Ru catalysts from the experimental findings against the dissociative binding energy of nitrogen onto steps on the metal catalyst surface as determined by DFT calculations [11,14] a volcano-shaped curve is obtained (Figure 2). The reaction rates are given as the number of moles converted per metal surface area in the catalyst used per hour. In principle, the activity should be expressed as the turnover frequency (TOF) with only step sites being active in the reaction as it has been shown for ammonia synthesis. However, this does not influence the overall reactivity trend, which is one of the advantages of studying materials with order of magnitude variations in activity.

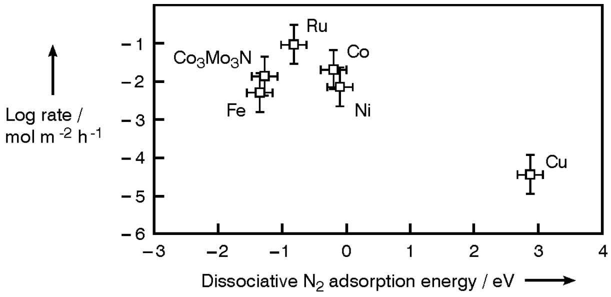

Figure 2. Experimentally observed volcano curve. Rates of ammonia decomposition over various catalysts at 773 K, 1 bar, 3:1 H_2/N_2, and 20% NH_3 plotted against the dissociative N_2 adsorption energy as obtained from DFT calculations.

The accuracy of the DFT calculations is in the order of 0.2 eV [17]. The accuracy of the measured reaction rates is rather good but the conversion of these to the turn over frequency requires an estimate of the catalyst metal surface area (or number of active step sites) which introduces inaccurateness estimated to be a factor of 2.

Co_3Mo_3N is an example of a catalyst that has been designed using the relations described above. By combining a metal with too high adsorption energy and a metal with too low adsorption energy one can obtain a catalyst that is closer to the maximum of the volcano curve. The adsorption energy of nitrogen varies monotonically through the periods in the Periodic Table. The concept of interpolation in the Periodic Table that was used to discover the new Co_3Mo_3N catalyst in ammonia synthesis [18-20] can also be used to rationalize the activity of this new catalyst in ammonia decomposition. Co_3Mo_3N is an interstitial nitride with Co-Mo sites at the surface. In the alloy both Co-rich and Mo-rich step sites occur. The Co-rich sites are the most active for ammonia decomposition and will therefore dominate the reaction. Thus, only the dissociative N_2 adsorption energy for Co-rich sites is being considered. Co_3Mo_3N is shown to have significant potential in ammonia decomposition where the conventional promoted iron catalyst cannot be used due to the severe reaction conditions where iron will form a bulk nitride. Industrially, the density of sites is equally as important as a high turnover frequency. Here, Co_3Mo_3N appears to be an excellent catalyst due to its high density. Particularly, for use in small mobile units it would make an excellent ammonia decomposition catalyst. From the interpolation principle it is actually possible to identify a whole range of new catalyst candidates, e.g., Ru-Co alloys (useful at high ammonia concentrations) and Fe-Co alloys (useful at low ammonia concentrations).

Comparison to trend model for ammonia synthesis

In this section it is examined whether concepts developed for catalytic ammonia synthesis can be applied to the catalytic ammonia decomposition and predicts the properties of the optimal decomposition catalysts. This is done by investigating whether a model describing the trends for catalytic ammonia synthesis activity over transition metals [13] can also describe the measured ammonia decomposition. Because the catalytic ammonia synthesis and decomposition depend only on the binding energy of nitrogen it is possible to establish what the optimal nitrogen binding energy is under given temperature, pressures and gas compositions. The model gives the net ammonia synthesis turnover frequency as a function of the dissociative nitrogen adsorption energy. The net decomposition rate can then be obtained simply by changing sign. In Figure 3 some of the trend predictions (volcano curves) of the model are shown. Actually, the calculated turnover frequencies (TOF) of ammonia synthesis/decomposition at a given set of reaction conditions and various ammonia concentrations are shown as a function of the reaction energy of dissociative N_2 adsorption.

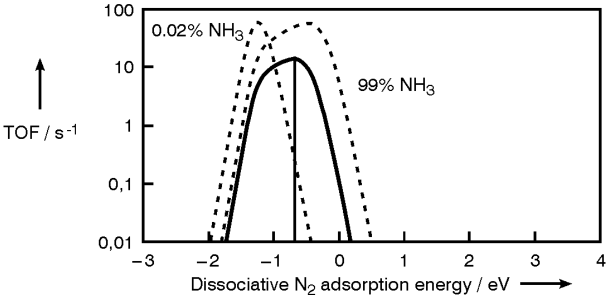

Figure 3. Calculated turnover frequencies (TOF) of ammonia synthesis/decomposition at 773 K, 1 bar, 3:1 H_2/N_2, and 0.02, 20 (solid line), and 99 % NH_3 as a function of the reaction energy of dissociative N_2 adsorption. The vertical line gives the dissociative nitrogen binding energy of the optimal ammonia decomposition catalyst when the ammonia concentration is 20%. At these conditions the gas phase equilibrium NH_3 concentration is 0.13%

The turnover frequency for a ruthenium catalyst (having a dissociative N_2 adsorption energy of -0.82 eV) is 12 s^{-1}. This corresponds to $7.2 * 10^{-20}$ moles ammonia being converted per hour per active site. In the experimentally observed volcano curve in Figure 2 the ammonia decomposition rate of the ruthenium catalysts is 0.091 mol m^{-2} h^{-1}. Dividing the reaction rate by the turnover frequency estimated by the model gives an estimate of the number of active sites per metal surface area. In this case, for the ruthenium catalyst, there are $1.3 * 10^{18}$ active sites per square meter metal surface. Assuming that a ruthenium surface has approximately $1.6 * 10^{19}$ atoms per square meter this correspond to approximately 10% of all surface atoms being active sites for ammonia decomposition.

The position of the experimentally observed volcano curve is in excellent agreement with that predicted from the trend model. Compared to the volcano curve for ammonia synthesis the optimal catalyst for decomposition is one that binds nitrogen less strongly, i.e. the maximum has moved away from iron towards cobalt or nickel. However, as for the ammonia synthesis reaction, the position of the maximum of the volcano curve in ammonia decomposition is also highly dependent on the reaction conditions. This is evident from “the optimal catalyst curve” developed for ammonia synthesis, calculated for an isothermal reactor (Figure 4). The optimal catalyst curve is obtained simply by plotting the position of the maximum for volcano curves calculated at different ammonia concentrations, as illustrated in Figure 3.

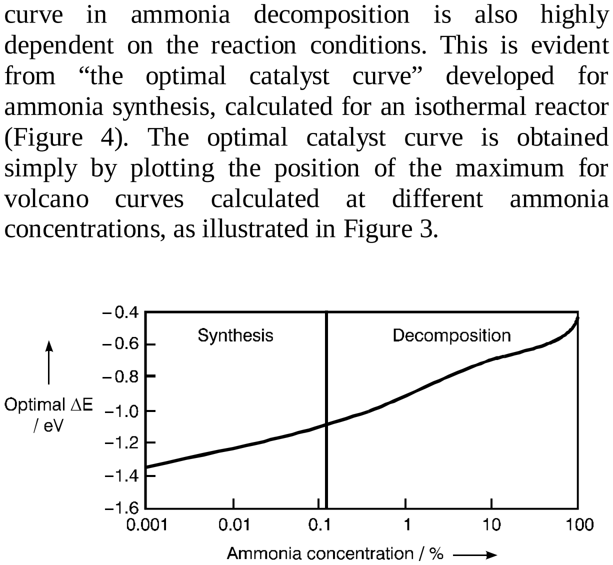

Figure 4. Optimal dissociative N_2 adsorption energy for ammonia synthesis/decomposition at 773 K, 1 bar and 3:1 H_2/N_2. Equilibrium corresponds to ca. 0.13 % ammonia. Calculated for an isothermal reactor

Thus, the optimal catalyst curve shows how the optimal nitrogen binding energy varies when the ammonia concentration is changed at 550ºC, 1 bar and 3:1 H_2/N_2. Figure 4 is applicable to both ammonia synthesis and ammonia decomposition and equilibrium corresponds to 0.13 % ammonia. Interestingly, it is observed that the optimal ammonia synthesis catalyst is *never* the optimal ammonia decomposition catalyst. The widely different reaction conditions in ammonia synthesis and ammonia decomposition results in very different optimal binding energies for the two reactions except, of course, at equilibrium. Furthermore, it can be seen that in the optimal ammonia decomposition process it is necessary to grade the reactor with catalysts having different nitrogen binding energies.

The activity of transition metal catalysts in ammonia synthesis as well as decomposition is significantly improved by adding alkali metals as promoters [21,22]. Industrially, it is therefore essential to use a promoted catalyst in order to obtain the most active catalyst.

Conclusions

Knowledge about the ammonia synthesis reaction can be used to accurately describe the ammonia decomposition reaction. Similarly, both the concept of optimal catalyst curves and the concept of interpolation in the Periodic Table are useful for both reactions. Co_3Mo_3N is shown to have significant potential in ammonia decomposition, particularly for use in small mobile units. Furthermore, it is demonstrated that the optimal catalyst for ammonia decomposition is never the optimal catalyst for ammonia synthesis. Altogether, this suggests that the approach taken for ammonia synthesis could be useful for many other catalyst systems. This should lead to a more rational development of new and improved catalytic processes.

Acknowledgements

This project is supported by The Technical Research Council of Denmark in the context of the program" Towards a Hydrogen based Society".

References

1. F. Joensen, J.R. Rostrup-Nielsen, Journal of Power Sources, 105 (202) 195-201.
2. G.W. Crabtree, M.S. Dresselhaus, M.V. Buchanan, Physics Today, 57 (12) (2004), 39-44.
3. T.V. Coudhary, C. Sivadinarayana, D.W. Goodman, Catalysis Letters, 72 (3-4) (2001) 197-201.
4. A.T. Raissi, Proceedings of the 2002 U.S. DOE Hydrogen Program Review, Report number: NREL/CP-610-32405.
5. M. Cifrain, K.V. Kordesch, Journal of Power Sources, 127 (1-2) (2004) 234-242.
6. A.S. Chellappa, C.M. Fischer, W.J. Thomson, Applied Catalysis A: General, 227 (1-2) (2002) 231-240.
7. F.A. Uribe, S. Gottresfeld, T. Zawodzinski Jr, Journal of the Electrochemical Society, 149 (3) (2002) A293-A296.
8. R.Z. Sørensen, L.J.E. Nielsen, S. Jensen, O. Hansen, T. Johannessen, U. Quaade, C.H. Christensen, Catalysis Communications, 6 (3) (2005) 229-232.
9. M. Boudart, Topics in Catalysis, 1 (3-4) (1994) 405-414.
10. S. Dahl, J. Sehested, J.C.H. Jacobsen, E. Törnqvist, I. Chorkendorff, Journal of Catalysis, 192(2) (2000) 391-399.
11. J.K. Nørskov, T. Bligaard, A. Logadottir, S. Bahn, L.B. Hansen, M. Bollinger, H. Bengaard, B. Hammer, Z. Sljivancanin, M. Mavrikakis, Journal of Catalysis, 209 (2) (2002) 275-278.
12. A. Ozaki, K. Aika, in "Catalysis", J. Anderson, M. Boudart Eds., Vol. 1, p. 87, Springer Verlag, Berlin, 1981.
13. A. Logadottir, T.H. Rod, J.K. Nørskov, B. Hammer, S. Dahl, C.J.H. Jacobsen, Journal of Catalysis, 197 (2) (2001) 229-231.
14. T. Bligaard, J.K. Nørskov, S. Dahl, J. Matthiesen, C.H. Christensen, J. Sehested, Journal of Catalysis, 224(1) (2004) 206-217.
15. M. G. Evans, M. Polanyi, Transactions of the Faraday Society, 34 (1938) 11-24.
16. J.N. Brøndsted, Chemical Reviews, 5 (3) (1928) 231-338.
17. B. Hammer, L.B. Hansen, J.K. Nørskov, Physical Review B, 59 (1999) 7413-7421.
18. C.J.H. Jacobsen, Chemical Communications, 12 (2000) 1057.
19. C.J.H. Jacobsen, S. Dahl, B.S. Clausen, S. Bahn, A. Logadottir, J.K. Nørskov, Journal of the American Chemical Society, 123 (34) (2001) 8404-8405.
20. A. Boisen, S. Dahl, C.J.H. Jacobsen, Journal of Catalysis, 208 (1) (2002) 180-186.
21. D. Szmigiel, W. Rarog-Pilecka, E. Miskiewicz, Z. Kaskur, Z. Kowalczyk, Applied Catalysis A: General, 264 (1) (2004) 59-63.
22. S. Dahl, A. Logadottir, C.J.H. Jacobsen, J.K. Nørskov, Applied Catalysis A: General, 222 (1-2) (2001) 19-29.

List of Publications

1. A. Boisen, S. Dahl, J.K. Nørskov, C.H. Christensen, J. Catal. 230 (2005) 309-312.
2. N. Schumacher, A. Boisen, S. Dahl, A.A. Gokhale, S. Kandoi, L.C. Grabow, J.A. Dumesic, M. Mavrikakis, I. Chorkendorff, J. Catal. 229 (2005) 265-275.
3. A. Boisen, I. Schmidt, A. Carlsson, S. Dahl, M. Brorson, C.J.H. Jacobsen, Chem. Commun. (2003) 958-959
4. C.J.H. Jacobsen, I. Schmidt, M. Brorson, A. Boisen, T.W. Hansen, S. Dahl, Materials Science Forum, 443-444 (2004) 217-222
5. C.J.H. Jacobsen, I. Schmidt, A. Boisen, K. Johannsen: "Katalytisk kemi. Et spørgsmål om miljø og ressourcer" Holte Bogtrykkeri, 2002, ISBN 87-986802-7-7
6. U.G. Nielsen, A. Boisen, M. Brorson, C.J.H. Jacobsen, H.J. Jakobsen, J. Skibsted, Inorg. Chem. 41 (2002) 6432-6439
7. A. Boisen, S. Dahl, C.J H. Jacobsen, J. Catal. 208 (2002) 180-186
8. C.J.H. Jacobsen, S. Dahl, A. Boisen, B.S. Clausen, H. Topsøe, A. Logadottir, J.K. Nørskov, J. Catal., 2005 (2002) 382-387
9. I. Schmidt, A. Boisen, E. Gustavsson, K. Ståhl, S. Persson, A. Carlsson, C.J.H. Jacobsen, Chem. Mater, 13 (2001) 4416-4418
10. A. Boisen, A. Hazell, C.J. McKenzie, Chem. Commun., 2001, 2136-2137

Francesco Castellino
Address: Building 227/132
Phone: +45 4525 2829
Fax: +45 4588 2258
e-mail: frc@kt.dtu.dk
www: http://www.kt.dtu.dk

Supervisors: Anker Degn Jensen
Jan Erik Johnsson
Rasmus Fehrmann

Ph.D. Study
Started: December 2004
To be completed: November 2007

Deactivation of SCR Catalysts by Additives

Abstract
The Danish power companies are obliged to burn biomass at the central power stations. The alkali fraction introduced by biomass into the combustion system is responsible for high rates of deposition and corrosion at the surface of the super-heat exchangers. To minimize these undesired effect, the power companies are planning to mix the biomass burned in their plants some additives, which are able to fix the alkali fraction in harmless compounds. The objective of this Ph.D. project is to evaluate the effect of the selected additives on the commercial catalysts employed in the SCR process.

Introduction

Nitrogen oxides (NO_x) emitted from stationary sources can be efficiently reduced by using the so-called Selective Catalytic Reduction (SCR) process. Ammonia is injected into the flue gas and reacts with the NO fraction according to the following reaction:

$$4\ NH_3 + 4\ NO + O_2 \rightarrow 4\ N_2 + 6\ H_2O$$

The reactor operates at atmospheric pressure and temperature ranging between 300 and 400ºC. The catalysts employed are vanadia-based catalysts. This technology was first developed in Japan in 1970s and is still nowadays the best-developed and worldwide used for fossil fuel combustion processes [1].

However, the application of this technology to the treatment of flue gas from (co)-combustion of secondary fuels such as straw, wood, sewage sludge or meat and bone meal (MBM) is problematic. This is mainly due to the high rates of catalyst deactivation observed and related to compounds (*e.g.* alkali and alkaline earth metals, chlorides, etc.) introduced into the system by these fuels [2,3]. Moreover, these compounds are also responsible for an accelerated deposition on heat transfer surfaces in the boiler and high rates of corrosion.

The use of additives to the fuel is considered by Danish power companies as a promising way to minimize the undesired effects in the combustion chamber caused by biomass combustion. These additives may involve compounds such as phosphates of calcium and aluminum that can (re)-capture the alkali fraction of the flue gas, reducing the concentration of undesired compounds. Their behavior during the combustion process is currently under investigation (PSO project FU-3213). However, it is still unknown whether or not the additives themselves can deactivate the SCR catalyst.

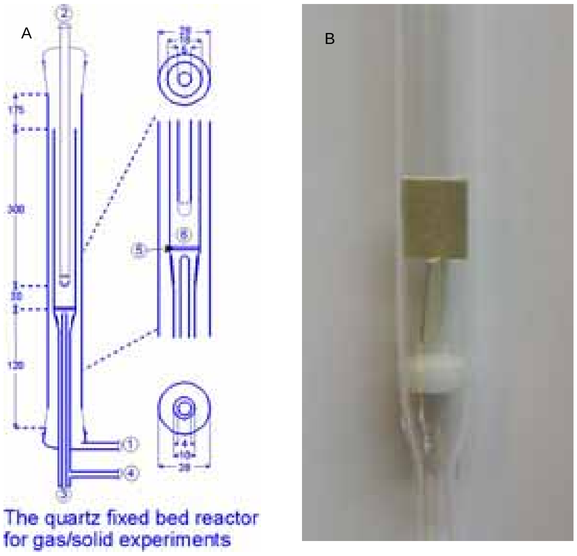

Figure 1: The lab-scale reactor (A). It consists in a quartz tube (B) with a quartz porous plate (5) for supporting the catalyst both as plates and powders. The whole reactor presents two different inlets (1 and 2) which allow keeping the reactants separated while heating to the reaction temperature, avoiding possible side reactions. The temperature in the reacting zone (6) is measured by a thermocouple inserted into (3). The gas finally exits the reactor from (4) and is then analyzed in composition.

Specific Objectives

The purpose of this project is to investigate whether the additives under consideration may cause accelerated deactivation, what the mechanisms of the deactivation are and whether the deactivation can be inhibited or slowed down to an acceptable rate.

The project is part of the biomass strategy of the Danish power company ENERGI E2.

Results and Discussion

The first investigations performed were aimed at evaluating the poisoning strength of the proposed additives by laboratory activity measurements. In particular the degree of deactivation is measured by comparing the activity of a doped catalyst sample with the activity of a fresh one. A sketch of the laboratory reactor used and a photo of some catalyst plates inserted into it are shown in Figure 1. Monolith SCR catalysts used in the power plants are operating in the presence of both external and internal mass transfer limitations. Under these conditions, the rate of reaction is limited by the transport of the reactants into the catalyst and the deactivation by *poisoning* may not be clearly estimated. For this reason, a comprehensive investigation of the activity of Haldor Topsøe A/S DNX catalysts in the SCR reaction has been carried out in our laboratories and reproducible activities for the fresh samples have been obtained. First the reacting conditions which allow neglecting the influence of external mass transfer on the observed rate of reaction have been determined. The tests have involved activity measurements of a catalyst plate sample under increasing values of total flow at different temperatures. From the data obtained, shown in Figure 2, it was concluded that at 350ºC, with a total feed equal to 3 NL/min, the external mass transport has only little influence on the observed rate of reaction (*i.e.* less than 6%). Consequently, when measuring the activity of a plate, the flow is always fixed at this value.

The influence of internal mass transfer limitations has then been evaluated by testing the activity of catalysts, which were crushed and sieved to particle sizes ranging between 106 and 250 µm. According to the results obtained and shown in Figure 3, in order not to have observed rates limited by internal diffusion at temperatures of industrial interests (*i.e.* 350-370ºC) very small particles (106-150 µm) have to be used in the activity tests. Under the same experimental conditions just discussed, samples of catalysts doped by the selected additives are tested. The doping is made according the wet impregnation method. The additives are chosen according to the indications given by ENERGI E2 and the leaders of the project PSO FU-3213. Initial tests are involving mono-calcium phosphate (MCP) and di-calcium phosphate (DCP). Since phosphorus is the main constituent of the additives under investigation, great attention to its chemistry and its behavior in the SCR reaction is paid. Wet impregnation tests by aqueous solutions of phosphoric acid have been performed to estimate the influence of pure phosphorus on the catalyst activity. Doping by MCP is under investigation.

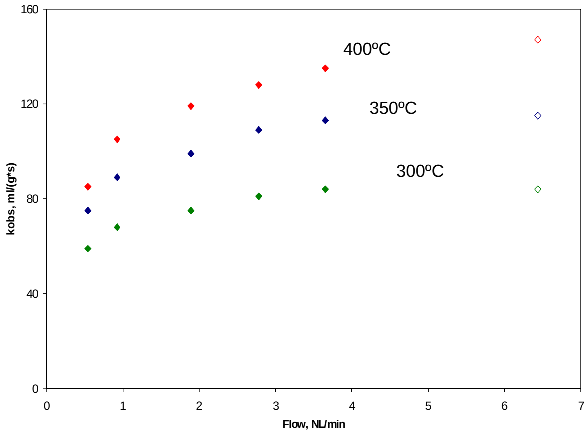

Figure 2: External mass transfer influence on the observed rate of reaction. Feed composition: 500 ppm NO, 600 ppm NH_3, 5% O_2, 5% H_2O, N_2 balance. Catalyst weight: about 0.19 g.

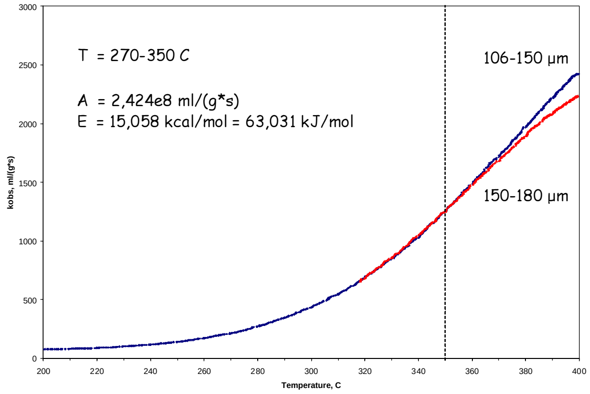

Figure 3: Internal mass transfer influence on the observed rate of reaction at different particle sizes. Feed composition: 500 ppm NO, 600 ppm NH_3, 5% O_2, 5% H_2O, N_2 balance. Catalyst weight: about 0.05 g.

Conclusions

The main objective of this Ph.D. project is to study the effects of the proposed “anti-alkali” additives on the SCR catalysts. Preliminary investigations on the activity of the fresh catalysts have been carried out and indications regarding mass transfer influence on the observed rate of reaction have been obtained. The poisoning strength of the additives is under investigation.

Acknowledgements

This project is supported by the PSO system and the Danish power company ENERGI E2. Supply of the catalyst samples by Haldor Tøpsoe A/S is gratefully acknowledged.

References

1. V.I. Parvulescu, P. Grange, B. Delmon, Catalysis Today 46 (1998) 233-316.
2. Y. Zheng, A.D. Jensen, J.E. Johnsson, Ind. Eng. Chem. Res. 43 (2004) 941-947.
3. R. Khodayari, C.U.I. Odenbrand, Applied Catalysis B: Enviromental 30 (2001) 87-99.

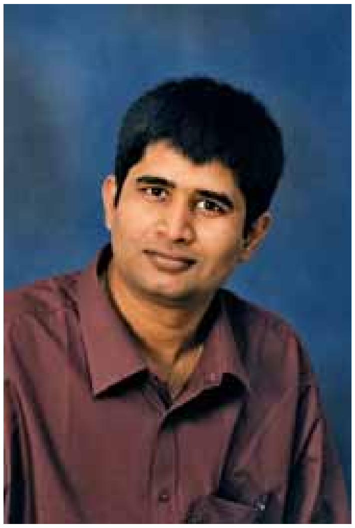

Debasish Chakraborty
Address: Building 312
Technical University of Denmark
Phone: +45 4525 3125
Fax: +45 4593 2399
e-mail: dc@kt.dtu.dk
www: http://www.aerosol.kt.dtu.dk/
Supervisors: Tue Johannessen
Hans Livbjerg
Ib Chorkendorff
Ph.D. Study
Started: April 2003
To be completed: March 2006

Flame Aerosol Synthesis of PtRu Anode Catalysts for Methanol Oxidation in Fuel Cell

Abstract

In this contribution a novel method for preparation of unsupported PtRu catalysts for methanol oxidation is presented. Nanoparticles of PtRu are prepared as aerosol particles by flame spray pyrolysis and subsequently deposited directly on a gas diffusion layer (GDL). The comparison of performance of the flame synthesized PtRu (1:1) unsupported anode with a loading of 1.5 mg/cm^2 with that of PtRu(1:1)/C (10 % metal, loading ~1.5 mg/cm^2) from E-TEK shows that both catalysts have similar onset potential (~210 mV) for methanol oxidation. However, the unsupported flame synthesized anode performs better than the anode prepared form supported E-TEK catalyst. Electrochemical impedance spectroscopy (EIS) has been used to observe the methanol oxidation on the anode catalyst. The EIS reveals that at 50°C and above the rate determining step is the oxidation of the surface adsorbed residues. EIS also shows improvement of methanol oxidation kinetics as the applied anodic potential is increased.

Introduction

The direct methanol fuel cell (DMFC) has the potential to replace the combustion engine in vehicular applications. The device uses a liquid fuel, which means that the existing fuel supply, storage, and delivery systems could be used possibly with a few minor modifications. Methanol can be produced from natural gas, coal or biomass. Compared to the hydrogen fed fuel cell, which is also in consideration as a future energy converting device, direct methanol fuel cell has the advantages of ease of fuel supply and storage [1]. DMFC can be operated at lower temperature than the internal combustion engine (ICE) and this will certainly reduce the polluting nitrogen oxides produced by ICE. DMFC offers another unique advantage for city driving; its efficiency increases as the load on the fuel cell decreases, which is exactly the opposite of the combustion engines.

However, one of the main challenges of making DMFC commercially feasible is to improve the slow reaction kinetics of the methanol oxidation reaction at the anode. There is an initial activation overpotential of some 0.2-0.55 V, depending on the catalyst and operating conditions, required to oxidize methanol anodically at an appreciable rate. At least some of this initiating overpotential is kinetic in nature and could be reduced by suitable catalysts at the anode[2]. Another critical issue of DMFC is the thickness of the anode catalyst layer. A thick catalyst layer increases the ohmic resistance as well as the mass transfer resistance for methanol. Therefore, to improve the DMFC anode performance it is necessary to investigate on new catalytic materials for methanol electroxidation as well as alternative methods for catalyst preparation and membrane electrode assembly (MEA) fabrication.

In DMFC, Pt-Ru is currently the best available catalyst. For improved performance, it is necessary to have a well-mixed Pt-Ru as catalyst. The standard methods of making catalysts are co-impregnation, sequential impregnation, co-precipitation, absorbing alloy colloids or surface organometallic chemistry techniques. However, it could be difficult to achieve the desired close proximity of the active components by the conventional methods as the active components might deposit on different sites on the support. Moreover, all of these processes need several stages for making active catalyst. Flame pyrolysis can be a viable alternative to replace the wet processes with a one step continuous process.

In this study, flame pyrolysis has been successfully applied to produce catalysts [3]. In this process, after dissolving Pt and Ru-precursors in appropriate solvents, the solution is sprayed through a nozzle to produce micron-sized droplets which burns out in a flame resulting in metal atoms and/or metal oxide molecules in the gas phase. Hereafter, clusters immediately nucleate and grow to nano-sized particles by coagulation and/or surface reaction and sintering. The mechanism of the particle formation process in the gas phase ensures intimate mixing of the product components.

The work presented here describes the results of our effort to develop a one step synthesis method of unsupported DMFC anode catalyst in terms of the physical and chemical characterization of the catalysts. The methanol oxidation activity of the synthesized catalyst was also compared with a commercial PtRu/C catalyst.

Experimental

The metal precursors used were ruthenium (III) acetylacetonate (Ru(acac)$_3$, Fluka, purity= 97%) and platinum (II) acetylacetonate (Pt(acac)$_2$, Aldrich Chemical Co., 97% purity). The solvent was a 4 to 1 volume ratio mixture of isooctane (Fluka, purity 99%) and tetrahydrofuran (Sigma, purity 99%). In all the stock solutions, the concentration of Pt(acac)$_2$ was kept constant while the concentration of Ru(acac)$_3$ was varied according to the required catalyst composition. The solution was pumped (figure 1) by using a syringe pump (IVAC P6000) through a gas assisted nozzle to spray the precursor solution to the flame zone as small droplets. The nozzle consisted of a capillary tube of outer diameter 0.9 mm (inner diameter 0.6mm), which is situated in an opening of 1.4 mm diameter creating an annular space of 0.9 mm^2. The design of the nozzle – except for the supporting flames - is similar to the one used by Mädler et al.[5]. The precursor solution was passed through the capillary tube at 30 mL/h and oxygen, as both the dispersion and oxidation gas, was introduced through the annulus at 2.2 L/min. The spray aerosol was contineusly ignited by eight hydrogen-fed supporting flames made by horizontal injection through eight equidistant holes drilled in a hollow metal ring placed around the aerosol jet. Cold air, provided from a water cooled quenching ring was used to quench the aerosol coming out of the flame[6]. The quenching helps decreasing the average particle size by suddenly lowering the temperature and thus decreasing the rate of sintering after the initial particle formation. The product particles were collected directly on the GDL (Toray TGPH090) by withdrawing the nanoparticle aerosol from the flame through it by using a gas-ejector vacuum pump (PIAB Classic). Here, the GDL was, in principle, applied as a catalyst nanoparticle filter.

The deposits have been physically characterized by Scanning Auger Microscopy (SAM) and Scanning Electron Microscopy (SEM). The electrochemical characterization was done by using linear sweep voltammetry (LSV) and electrical impedance spectroscopy (EIS). The experimental details of the electrochemical measurements are given elsewhere [7]. The MEAs were conditioned before taking any measurement. The conditioning of the MEAs was started by flowing overnight humidified H_2 and humidified Ar at the anode and cathode, respectively, at room temperature. Then the cell was run as a H_2/O_2 fuel cell at 90°C for 1 hr with humidified H_2 at the anode[8].

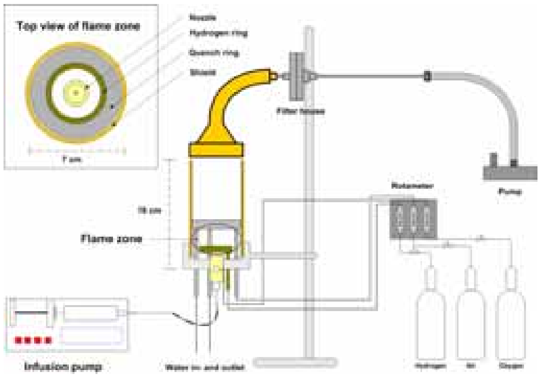

Figure 1: Outline of the flame synthesis equipment

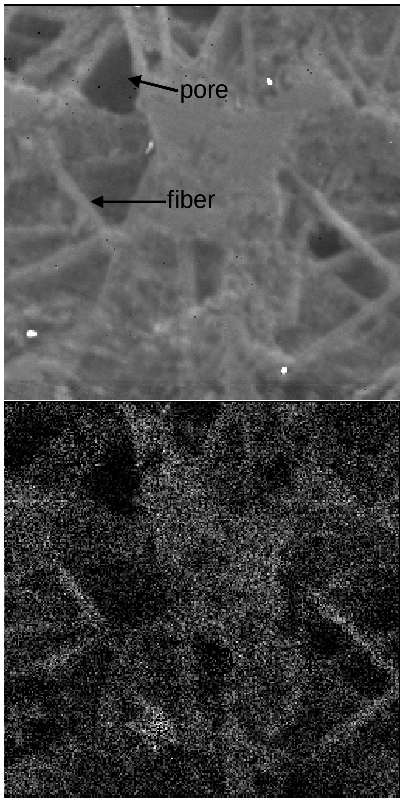

Figure 2. SAM images of bare GDL (top) and GDL with deposits (bottom). The bright spots indicate the presence of Pt. Image scale: 300µm ×300µm

After that H_2 at the anode was replaced with 1.0M methanol and the cell voltage was cycled continuously for 1h between 0 to 0.8 V at a scan rate of 50 mV/sec to finish the conditioning .

Results and Discussion

SAM image of the GDL shows how the individual carbon fibres are woven together to from the whole matrix (figure 2). The macroscopic pores are also visible. When the sample has been scanned for Pt, the bright spots representing the Pt containing regions could be observed mainly on the fibres (figure 2, bottom). The SEM image also confirms that the deposit grows mainly along the fibers (figure 3). The deposit seems to be porous and fluffy. This is possibly the result of the primary particles sticking together rather than sintering to from bigger single particles. The fluffy and porous nature of the deposits is advantageous both for the penetration of reactant to the inside of the agglomerates and exit of the products from inside.

It has been shown in our previous work that the degree of alloying of Pt and Ru obtained from X-ray diffraction (XRD) patterns is rather low compared to the commercial Johnson Matthey unsupported Pt-Ru catalyst. XPS data suggest that a significant fraction of Pt and most of the Ru is present as oxides in the as-prepared Pt1Ru1 catalyst. It has been concluded that the catalyst is a mixture of a crystalline phase consisting predominately of Pt and one or more amorphous phases consisting of mainly Ru as metallic or oxidic states[7]. The average particle size of the crystalline phase of Pt1Ru1 as determined from XRD peak broadening is 10.3±0.3 nm.

A comparison of performance between flame synthesized Pt1Ru1 and 1:1 PtRu/C (10% metal loading) is shown in figure 4. The supported Pt-Ru catalyst has been chosen for comparison because we wanted to observe the difference between a highly alloyed metallic Pt-Ru catalyst and the flame synthesized catalyst. The unsupported Pt-Ru has been reported to have lesser degree of alloying and a significant presence of RuO_2 compared to carbon supported Pt-Ru from E-TEK[9]. The potentials in figure 2 have been corrected for iR losses. Even though the onset potentials are similar, the MEA prepared from the flame synthesized catalyst performs better than the E-TEK catalyst with similar catalyst loading for all higher current densities. At 400 mV, the current density for Pt1Ru1 is ~1.6 times higher than the current density obtained from the MEA with anode made from E-TEK catalyst.

Each of the Nyquist plots at 80°C from the impedance spectroscopy of methanol oxidation at different dc-potentials shows a capacitive loop in the first quadrant and another pseudo-inductive loop in the forth quadrant(figure 5). The capacitive loop arises from the charge transfer resistance of methanol oxidation and the x-axis intercept of the loop represents the magnitude of charge transfer resistance [10-13], whereas it has been postulated that the presence of the pseudo-inductive loop is an indication that the oxidative removal of CO_{ads} is the rate determining step for methanol oxidation on Pt-Ru at DMFC anode[12, 14]. The inductive loop was observed for all impedance spectra taken at 50°C and above[7]. The improvement in the methanol oxidation kinetics with increasing potential is probably because at higher potentials, Pt sites, beside Ru, supplies active oxygen containing species for CO_{ads} oxidation[15].

Even though the as prepared catalyst is mostly unalloyed, during conditioning, when the catalyst was exposed to H_2 and subsequently to CH_3OH at 90°C, the metal oxides could be reduced significantly to metallic state[8]. In fact, we have followed the state of the catalyst during conditioning by EIS and observed that the methanol oxidation capacity of the anode improves significantly. The possible reason for this improvement has been related to the reduction of both Pt and Ru oxides and possible formation of alloys [16].

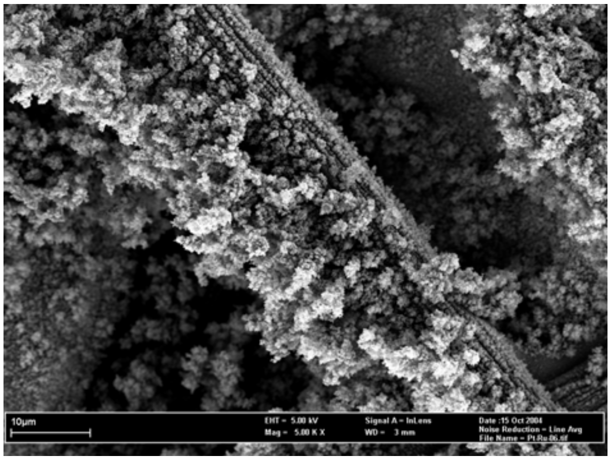

Figure 3. SEM image of the film of PtRu particles on carbon sheet

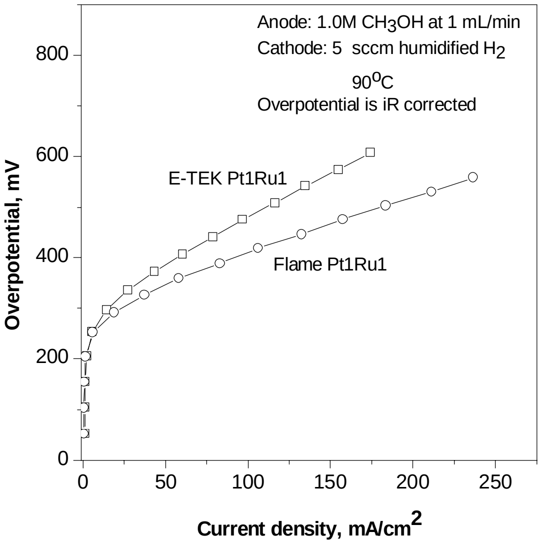

Figure 4 . Comparison of activity between flame-synthesized and E-TEK anode

Conclusion

We have successfully demonstrated a one-step catalyzation method for preparation of the DMFC anodes. The as prepared nanocomposites are a mixture of fcc, mostly unalloyed Pt crystalline phase and an amorphous surface layer, postulated to be a mixture of Pt and Ru oxides. However during conditioning, at least partial reduction of oxides and subsequent alloying occurs. Comparison with commercially available

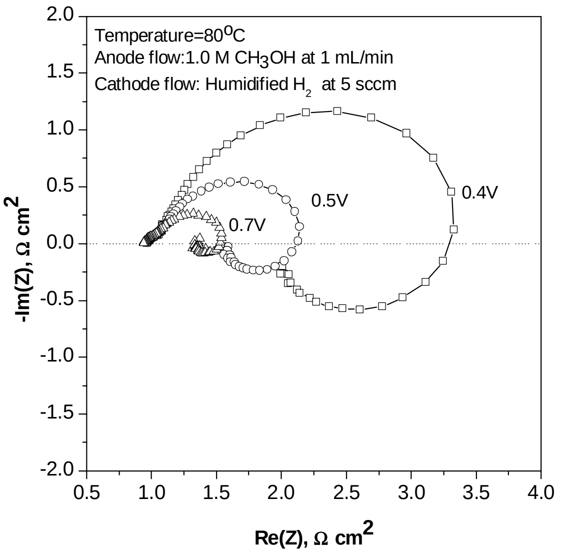

Figure5 Nyquist plots showing the effect of anode potential on methanol oxidation

10%Pt-Ru/C E-TEK catalyst demonstrated that even though the onset potential for methanol oxidation at 90°C on both catalysts are similar (~250 mV), the flame prepared Pt1Ru1 has 60% higher activity at 0.4V

Acknowledgement

This work was supported by PSO (project 5357). The authors wish to thank IRD Fuel Cells A/S for the assistance to the project during start up regarding materials and the design of the fuel cell test unit. The scientific and technical support for the EDS analysis of the DG JRC Institute for Energy, Microstructural Analysis Centre is gratefully acknowledged. Special thanks to Mr. Michael B. Jensen for his involvement in the project as a masters student.

References

[1] B. D. McNicol, D. A. J. Rand and K. R. Williams. Direct methanol-air fuel cells for road transportation. J. Power Sources 83, 15-31. 1999.

[2] G. T. Burstein, C. J. Barnett, A. R. Kucernak and K. R. Williams, Aspects of the anodic oxidation of methanol. Cat. Today 38, 425-437 (1997).

[3] T. Johannessen and S. Koutsopoulos. One-Step Flame Synthesis of an Active Pt/TiO_2 Catalyst for SO_2 Oxidation-A Possible Alternative to Traditional Methods for Parallel Screening. J. Catal. 205[2], 404-408. 2002.

[4] S. E. Pratsinis. Flame Aerosol Synthesis of Ceramic Powders. Prog. Energ. Combust. 24, 197-219. 1998.

[5] L. Mädler, H. K. Kammler, R. Mueller and S. E. Pratsinis. Controlled synthesis of nanostructured particles by flame spray pyrolysis. J. Aerosol Sci. 33, 369-389. 2002.

[6] J. P. Hansen, J. R. Jensen, H. Livbjerg and T. Johannessen. PARTICLE TECHNOLOGY AND FLUIDIZATION - Synthesis of ZnO Particles in a Quench-Cooled Flame Reactor. AICHE J. 47[11], 2413-2418. 2001.

[7] D. Chakraborty, H. Bischoff, I. Chorkendorff and T. Johannessen. Mixed Phase Pt-Ru Catalyst for Direct Methanol Fuel Cell Anode by Flame Aerosol Synthesis. Submitted to J. Electrochem. Soc. (2005) .

[8] H. N. Dinh, X. Ren, F. H. Garzon, P. Zelenay and S. Gottesfeld, Electrocatalysis in direct methanol fuel cells: in-situ probing of PtRu anode catalyst surfaces. J Electroanal. Chem. 491, 222-233 (2000).

[9] A. S. Aricò, A. K. Shukla, K. M. El Khatib, P. Cretì and V. Antonucci, Effect of carbon-supported and unsupported Pt-Ru anodes on the performance of solid-polymer-electrolyte direct methanol fuel cells. J. Appl. Electrochem. 29, 671-676 (1999).

[10] M. Ciureanu, S. D. Mikhailenko and S. Kaliaguine, PEM fuel cells as membrane reactors: kinetic analysis by impedance spectroscopy. Cat. Today 82, 195-206 (2003).

[11] I.-M. Hsing, X. Wang and Y.-J. Leng. Electrochemical Impedance Studies of Methanol Electro-oxidation on Pt/C Thin Film Electrode. J. Electrochem. Soc. 19[5], A615-A621. 2002.

[12] W. Sugimoto, K. Aoyama, T. Kawaguchi, Y. Murakami and Y. Takasu, Kinetics of CH3OH oxidation on PtRu/C studied by impedance and CO stripping voltammetry. J. Electroanal. Chem. In Press, Corrected Proof, (2004).

[13] J. T. Mueller and P. M. Urban. Characterization of direct methanol fuel cells by ac impedance spectroscopy. J. of Power Sources 75[1], 139-143. 9-1-1998.

[14] J. T. Müller, P. M. Urban and W. F. Holderich. Impedance studies on direct methanol fuel cell anodes. J. of Power Sources 84[2], 157-160. 1999.

[15] H. A. Gasteiger, N. Markovic´, P. N. Ross, Jr. and E. J. Cairns. Temperature-Dependent Methanol Electro-Oxidation on Well-Characterized Pt-Ru Alloys. J. Electrochem. Soc. 141[7], 1795-1803. 1994.

[16] D. Chakraborty, I. Chorkendorff and T. Johannessen. Manuscript in preparation

List of Publications:

[1] D. Chakraborty, H. Bischoff, I. Chorkendorff, and T. Johannessen, J. Electrochem. Soc., 152 (12) (2005) A2357-A2363.

[2] D.Chakraborty, M.B. Jensen, I. Chorkendorff, and T. Johannessen, 3rd European Ploymer Electrolyte Fule Cell Forum, 2005, Lucerne, Switzerland.

Henrik Christensen
Address: CHEC, Dept. of Chemical Engineering
Building 229, Office 115
Phone: +45 4525 2853
Fax: +45 4588 2258
e-mail: hc@kt.dtu.dk
www: http://www.chec.kt.dtu.dk
http://www.lundbeck.com
Supervisors: DTU: Søren Kiil & Kim Dam-Johansen
H. Lundbeck A/S: Ole Nielsen & Michael Bech Sommer.

Ph.D. Study
Started: September 2004
To be completed: September 2007

Scale Up of Pharmaceutical Production of Organic Chemical Compounds

Abstract
The design of an efficient reactor system for a chemical reaction requires knowledge on the kinetic data related to the reaction. Kinetics makes it possible to simulate how the reaction is affected by different reaction conditions. This is a discipline, which has not yet been widely used in the pharmaceutical industry. However, due to environmental, economical and quality considerations an increasing interest in this field has appeared. This gives the opportunity for investigating the possibilities for the implementation of new reactor configurations and analysis techniques, which provides a more detailed understanding of the chemical process.

Introduction

The production of Active Pharmaceutical Ingredients (API) is a special area compared to other chemical productions. Typically, the amounts of products produced are rather small, but on the other side the trade prices on the products are high [1]. This has resulted in little focus on process development and optimization from an engineering point of view.

Reactions traditionally take place in batch reactors. These reactors can be used for a range of reactions and in terms of documentation it is convenient to trace errors back to the source. From a scale up point of view batch reactors give rise to a number of challenges: Loss of selectivity and formation of hot spots due to slow mixing and problems with exothermic reactions due to a high volume to surface ratio [2]. This has the consequence that a reaction, which performs satisfying in gram-scale, may fail when it is performed in kg-scale.

Until now the typical way of solving these upscale problems has been to change the critical reaction steps in the synthesis rather than finding a convenient solution by changing from batch reactors to other reactor configurations. This has the drawback that it is time consuming to develop a new synthesis route and it may result in additional synthesis steps or use of an excess of chemicals, which all-together means that the turnover may decrease.

However, a number of changes in the pharmaceutical market have made it relevant to investigate the possibility of optimizing or changing some of the existing production methods. Example given: The competition has increased, due to generic production and more attention on the environmental impact is paid.

An aspect, which until now has also prevented the pharmaceutical industry in process development and implementation of new techniques, is the commitments to the US Food and Drug Administration (FDA). The FDA is responsible for the guidelines that ensure the quality of the pharmaceuticals [3].

Until August 2003 the accepted way of ensuring a product with a given quality was to describe the production method in every detail and finally receive an approval from FDA. From that stage no changes on the approved method are allowed without preapproval from the FDA. This means that even if the production method is inefficient, it is not possible to optimize the process without using precious time on new approvals.

Meanwhile FDA has realized that the lack of optimization has resulted in excessive manufacturing costs. Therefore the FDA has encouraged the pharmaceutical industry to implement new technologies. The new technologies shall ensure a more effective, safe, and affordable production of pharmaceuticals and by that help the consumer to get the pharmaceuticals; they need to improve their health.

These requirements may be met by the implementation of Process Analytical Technology (PAT) [4]. The aim of this technique is to provide a more elaborate understanding of the chemical process. By using modern analysis equipment real time concentration profiles can be recorded for a chemical process. Based on these profiles operating conditions may be changed during the process and the final quality may be improved [5].

To investigate these new possibilities for the manufacturing of pharmaceuticals the Department of Chemical Engineering at the Technical University of Denmark and the pharmaceutical company H. Lundbeck A/S has agreed on a partnership with the main title: "Active Pharmaceutical Ingredients".

Specific Objective

The purpose of this project is to investigate the possibilities for developing a more efficient method for up scaling organic synthesis in pharmaceutical production. This will require:

- Methods to increase the understanding of chemical reaction mechanisms and kinetics, this will also include the efficiency of the analytical methods and apparatus.
- Efficient methods for application of mechanism and kinetic to optimize and scale up organic synthesis to industrial pharmaceutical production.
- Formulate guidelines for future synthesis and scale up problems, which may be met in the pharmaceutical industry.

Chemical Reaction

Mono-substituted aryl piperazines are of great importance in the pharmaceutical production [6]. They can be produced by the Buchwald-Hartwig amination reaction, which was presented in 1995. The reaction in Scheme 1 has been chosen as a model reaction for this project. The products given in Scheme 1 have no connection to an actual pharmaceutical, however, the coupling reaction of the aryl halide and the amine is a very important class of reactions in the pharmaceutical industry.

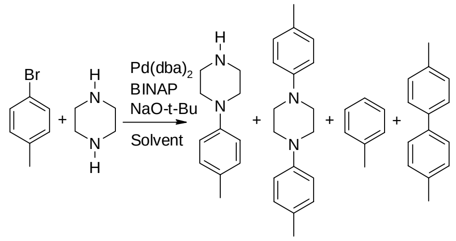

1 2 3 4 5 6

Scheme 1: Formation of aryl piperazine by the Buchwald-Hartwig amination reaction.

The Buchwald-Hartwig amination reaction is the coupling reaction between an aryl halogen (**1**) and a primary or a secondary amine (**2**) in the presence of a homogeneous palladium catalyst and a base. The identified products are: Mono-substituted aryl piperazine (**3**), bi-substituted aryl piperazine (**4**), reduced aryl halogen (**5**) and homo-coupled aryl halogen (**6**). However, it is only **3,** which is desired. **4**, **5** and **6** are unwanted side products.

So far the reaction has been carried out in batch reactors, and the two following strategies have been used in order to avoid formation of **4**: One strategy has been to introduce a protection group, which protects one of the two nitrogen atoms in **2** [7]. Another strategy has been to change the ratio between **1** and **2** [8]. However, from an economic point of view, it will be favorable if the reaction can be carried out without the introduction of protection groups and with equivalent amounts of **1** and **2**, or even better with an excess of **A**.

Chemical Reaction Mechanism

The Buchwald-Hartwig amination reaction is a homogeneously catalyzed reaction, which takes place in the presence of a palladium complex. In the literature it is reported that the formation of the N-aryl amine occurs according to the mechanism given in Figure 1 [9,10]. Figure 1 is dividend into two different areas. The pathway outside the box describes the formation of **3** and **4** and the pathway inside the box describes the formation of **5**.

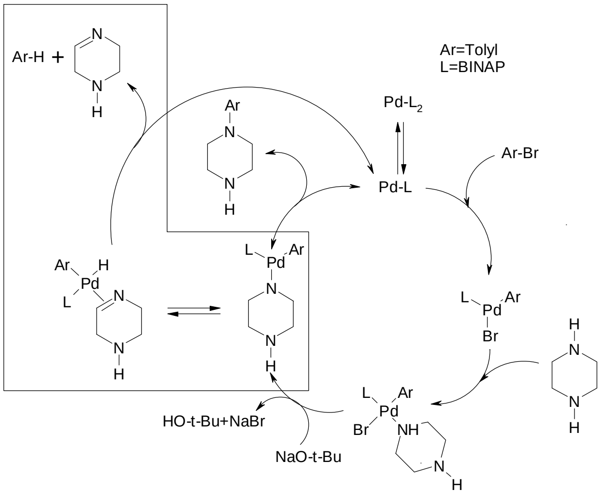

Figure 1: Reaction mechanism for the formation of *N*-aryl amide and the reduction of the aryl halide.

The formation of **3** and **4** can be divided into five intermediate reaction steps:

- Dissociation of the ligand from the palladium complex.
- Oxidative addition of the aryl halide to the palladium complex.
- Coordination of the amine.
- Neutralization of the amine.
- Dissociation of the *N*-arylated amine from the palladium complex.

The formation of the undesired reduced aryl halide adds two additional intermediate reaction steps:

- β-hydride elimination.
- Dissociation of the reduced aryl halide and the oxidized amine.

It has not been possible to find a reaction mechanism, which accounts for the formation of **6**. It is desired to use these mechanisms formulate a kinetic model for the reaction in Scheme 1.

Prior considerations

In the initial phase of the project it was desired to investigate the possibilities for creating a continuously operated reactor configuration for the reaction given in Scheme 1. To obtain a simple reaction system it was attempted to create a homogenous system, where both the reactants and the catalyst were dissolved in a solvent. The classic solvents employed in the Buchwald-Hartwig amination reaction are non-polar aprotic solvents such as *m*-xylene and 1,4-dioxane. However, due to the low polarity of these solvents, it is not possible to dissolve the base NaO-*t*-Bu. Therefore it was decided to change the class of solvent from non-polar aprotic solvents to polar aprotic solvents, because they had a better ability for creating a homogeneous system. Meanwhile, as later described the change of the class of solvent had a significant impact on the product distribution.

Method of Analysis

One of the challenging parts of the project was to develop a method of analysis, which allowed the reactants and products to be detected and quantified. A HPLC method was developed and this gave the possibility for the quantification of the following compounds: **1**, **3**, **4**, **5** and **6**. The primary drawbacks of this method are that it is not able to detect **2**, which is due to the lack of a chromophore group, and that it is invasive. Time has also been devoted to evaluate the possibility for the implementation of online Near-Infrared spectrometry (NIR) as a method of analysis. This method has the advantages that it is able to detect **2,** and that it is noninvasive. However, it was found that the properties of the reaction mixture were not appropriate for NIR measurements. Regarding the method of analysis more work will be done to investigate other analytical techniques. Most attention will be paid to methods that allow noninvasive online measurements.

Experimental Results

The following ratio between the reactants and catalyst has been used in the reactions shown in Figure 2 and 3: 1.0 eq of **1**, 1.1 eq of **2**, 0.05 eq of Pd(dba)$_2$, 0.075 eq of BINAP and 1.5 eq of NaO-*t*-Bu dissolved in a fixed amount of solvent. The temperature is 100 °C and maintained by a microwave source.

In the initial phase of the project the reaction was done in the polar and aprotic solvent 1-methyl-2-pyrrolidone (NMP). However, the data obtained for the product distribution revealed that the selectivity towards the desired product **3** was low. This was due to a high production of the undesired product **5** (Figure 2). The same tendencies were observed for another polar aprotic solvent: *N*,*N*-dimethylacetamide.

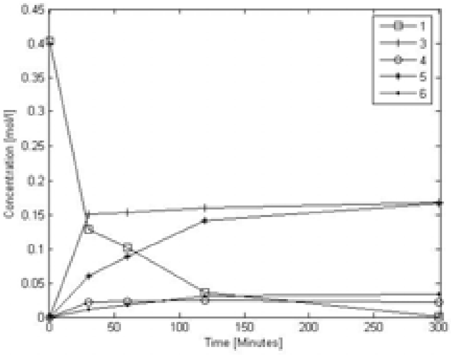

Figure 2: Concentration versus time for the reaction carried out in NMP.

To investigate whether this unexpected high production of **5** was due to the change of the class of solvent (from a nonpolar aprotic to a polar aprotic solvent) the reaction was done in some of the classic solvents for the Buchwald-Hartwig amination reaction i.e. a nonpolar aprotic solvent. The results for the reaction done in 1,4-dioxane are displayed in Figure 3. Figure 3 shows that the formation of 5 is suppressed for reactions performed in 1,4-dioxane compared to the reaction done in NMP. This means that the class of solvent affects the product distribution.

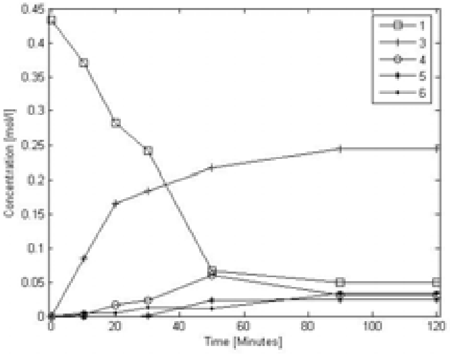

Figure 3: Concentration versus time for the reaction carried out in 1,4-dioxane.

Another observation from figure 3 is that the reaction terminates even though there are still unreacted starting material (**1**) left in the reaction mixture.

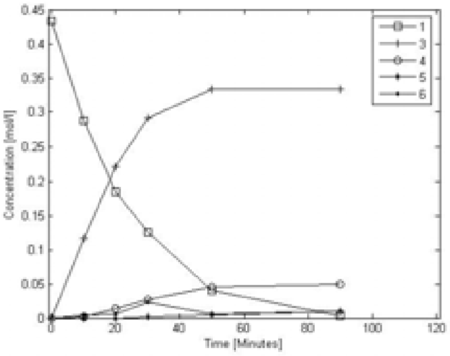

Figure 4: Concentration versus time for the reaction carried out in 1,4-dioxane. 2.2 eq. of 2 were employed.

It was experienced that by applying 2.2 eq of **2** instead of 1.1 of **2**, which are used in Figure 2 and 3, it is possible to obtain full conversion of **1** (Figure 4).

Future Work

- A study of the effect of the different parameters in the reaction (i.e. concentrations and temperature) will be performed.
- Based on available reaction mechanisms in the literature a kinetic model for the reaction in Scheme 1 will be developed.
- New methods of analysis will be evaluated for the reaction. It is also the intention to develop a method, which allows **2** to be detected and quantified.
- An experimental facility will be established at KT/DTU. The facility will consist of an analytical tool and a reactor for liquid phase reactions.

Conclusion

The results obtained for the reaction, has illustrated that the reaction represents a reaction mechanism, which is complex and sensitive towards changes in the class of solvent. The work has also revealed that some of the major challenges, which are connected to a kinetic study, are the development of a reliable method of analysis. For the reaction in this project the huge number of reactants and products that has to be quantified further complicates it. For this project it has the consequence that some of the focus has been moved from reactor design to methods of analysis.

Acknowledgements

This project is performed in close collaboration with H. Lundbeck A/S. H. Lundbeck A/S provides the laboratory facilities and their expertise on organic synthesis.

References

1. Jensen K.F., Chemical Engineering Science, 2001, 56, 293-303.
2. Anderson N.G., Organic Process Research & Development 2001, 5, 621.
3. http://www.fda.gov/opacom/morechoices/mission.html
4. http://www.fda.gov/cder/ops/pat.htm
5. http://www.ptemag.com/pharmtecheurope/article/articleDetail.jsp?id=129539&pageID=1
6. De Prins, L., Psychotropics 2000/2001, 2002, Herman & Fischer A/S, Denmark.
7. Hepperle, M.; Eckert, J.; Gala, D.; Shen, L.; Evans, A.; Goodman, A., Tetrahedron Letters, 2002, 43, 3359-3363.
8. Zhao, S.; Miller, A.; Berger, J.; Flippin, L., Tetrahedron Letters, 1996, 37, 4463-4466.
9. Urgaonkar, S.; Xu, J.; Verkade, J., Journal of Organic Chemistry, 2003, 68, 8416-8423.
10. Wagaw, S.; Rennels, R.A.; Buchwald, S.L., Journal of American Chemical Society, 1997, 119, 8451-8458.

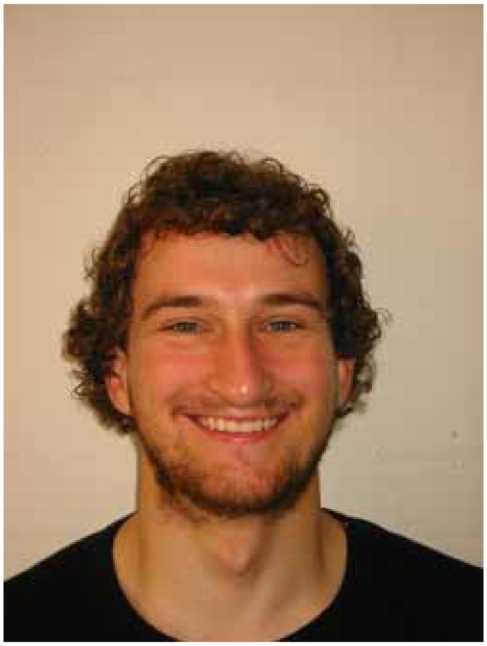

Steen Christensen
Address: CAPEC, Dept. of Chemical Engineering
Building 227, Office 208
Technical University of Denmark
Phone: +45 4525 2912
Fax: +45 4593 2906
e-mail: sch@kt.dtu.dk
www: http://www.capec.dtu.dk

Supervisor: Jens Abildskov

Ph.D. Study
Started: August 2004
To be completed: July 2007

Multi-Scale Modeling of Complex Systems

Abstract
Most chemical systems can only be fully understood based on physical and chemical property data. Property data can not be calculated in a fully rigorous fashion. Normally semi-empirical property prediction models (SEPPs) have been used but they all have weaknesses and limitations concerning size and complexity of the molecules. In a highly competitive climate, chemical engineers are forced to rely increasingly on predicted data. The purpose of this project is to develop a methodology for extracting maximum information from available experimental results. The project will combine SQPP models with molecular modeling to give qualified prediction of pure and mixture behavior of novel compound groups to minimize extensive experimental data generation.

Introduction

Traditionally, process systems engineering (PSE) is concerned with the computer-aided design of products and processes, and the operation and control of these processes throughout their lifecycle. The overwhelming majority of all chemical systems can only be fully understood based on accurate physical and chemical property data. Such property data can not be calculated in a fully rigorous fashion, so chemical engineers have for decades developed numerous semi-empirical property prediction models. Great emphasis has been on models of residual properties of pure components and mixtures and excess property models for liquid mixtures. As the materials of interest to the modern chemical industry become ever more complex, PSE relies on increasingly sophisticated molecular modeling (MM) techniques for the characterization of their properties and behavior. The use of advanced equations of state within mathematical process models is now well established, as is the use of molecular modeling for the derivation of parameters used in these equations, e.g. by generation of “pseudo-experimental” data points to complement real experimental data that are available. During the past fifteen years, theoretical and algorithmic advances along with the revolution in computing technology have made it possible for design questions of practical importance to be addressed by MM. The advances offered by these methods will continue to make inroads in the chemical and related industries in the coming decade.

Methodology

The main objective of this work is to develop a methodology for using molecular modeling results to expand the predictive capabilities of existing SEPP models to new compound groups where there is insufficient experimental data available. The MM simulations are too extensive to use directly in for example a design phase of a purification unit. The SEPP models are preferred in the design phase because of the computational simplicity resulting from their current analytical form. A general approach for handling a new class of chemicals includes five steps:

1. Search literature for all relevant physical property data (liquid densities, vapor pressure data, PVT data, phase diagram data, mixture equilibrium data vapor-liquid-equilibrium (VLE), liquid-liquid-equilibrium (LLE), solid-liquid-equilibrium (SLE), activity coefficients at infinite dilution, excess volumes etc.).

2. Test existing property prediction methods (if available) both for pure compounds and mixtures. Test if it is possible extend the SEPP models (for example UNIFAC) to improve predictions by regression of parameters using experimental data collected.
3. Evaluate if predictive capability for the new class is acceptable.
4. Identify areas with insufficient data. Obtain relevant pseudo-experimental data from molecular modeling. For developing molecular models use known data to establish suitable potentials.
5. Combine experimental and pseudo-experimental data for regression of parameters for SEPP models.

Steps 3 to 5 are made until the predictive capability of the SEPP models have reached an acceptable level of precision and an acceptable range of applicability.

Steps 1 to 2 are the traditional steps taken by engineering researchers when trying to model a new compound group. The first evaluation of the predictive capability is a “stop or go” point because extensive experimental work might be needed. With the methodology proposed in this work it is now possible to proceed to the design phase of a project any “stop or go” decision has to be made. That makes it possible to explore many options qualitatively, before experimental work is required.

How to enable design engineers to accomplish steps 3-4 within established CAPE frameworks is unclear at this point.

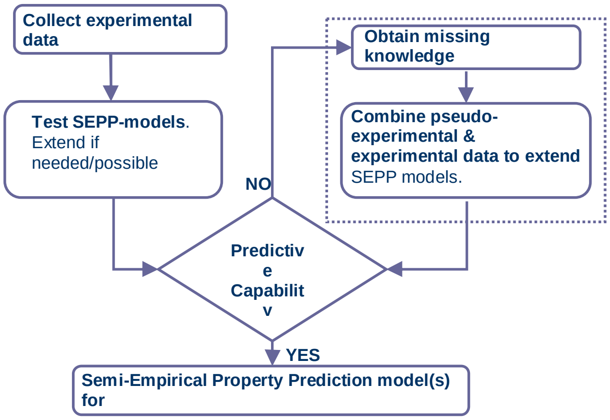

Figure 1: Overview of methodology

Theory

Current theories of interest are related to molecular dynamics (MD) and Gibbs Ensemble Monte Carlo (GEMC) simulations of pure compounds and mixtures.

The GEMC involves has become very popular in recent decades. If one can supply parts of the necessary data, for example vapor pressures, the estimation of activity coefficients becomes the main necessity. That places less demands on the accuracy of the simulations. In that case fluctuation solution theory [1] becomes an alternative. Using that as our basis, we have calculated the derivative of the activity coefficient with respect to composition as shown in Equation 1.

$$\left(\frac{\partial \ln \gamma_1}{\partial x_1}\right)_{T,P,N_2} = \frac{-x_2\left(H_{11}+H_{22}-2H_{12}\right)}{1+x_1x_2\left(H_{11}+H_{22}-2H_{12}\right)}$$

Equation 1

The H_{ij}’s are (spatial) integrals of the radial pair distribution function and x_i’s are the mole fractions at the specific composition. An example of a radial pair distribution function is shown in Figure 2 for an equimolar mixture of benzene (1) and methyl-acetate (2). Where the integral of g(r) is applied using Equation 2.

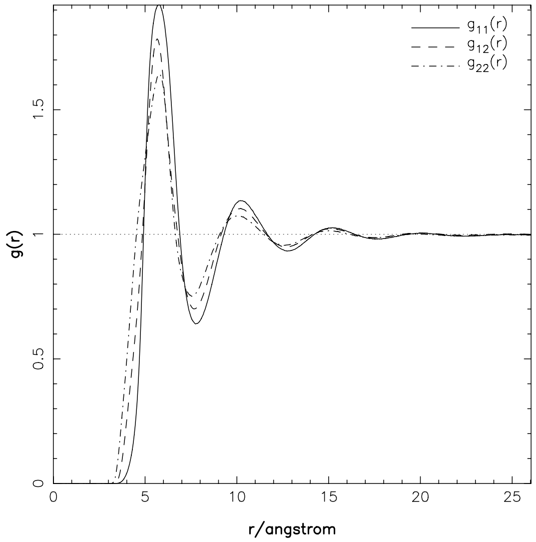

Figure 2: Radial pair distribution functions, $g_{ij}(r)$, for equimolar mixture of benzene (1) and methyl-acetate (2) at 303.15K and 1atm.

As shown in Equation 2 the limits of the integral is from the center of the molecule to infinity. In the actual MD simulations the simulation box is finite therefore the limits of the integral are also finite (0 to r_{max}).

$$H_{ij} = \frac{G_{ij}}{v} = \frac{1}{v}\int_0^\infty 2\pi r^2\left(g_{ij}(r)-1\right)dr$$

Equation 2

The consequence is that the contributions to the integral when r is in the vicinity of r_{max} have to be insignificant. If the contributions are not insignificant the size of the simulation box has to be increased. Because H_{ij} is an integral over volume r^2 is included and the consequence is that errors in g(r) at high values of r are magnified. To ensure that small errors at high radius does not influence the final integral a correlation [2] is applied to the g(r) generated from the MD simulations to ensure that the integral remains finite. When a set of simulations covering the whole composition range have been made, the results can be used to calculate the derivative from Equation 1. The derivatives are used to generate parameters for a Redlich-Kister polynomial and it is now possible to generate activity coefficients for the whole composition range which can be used as input for regression of parameters for a SEPP model.

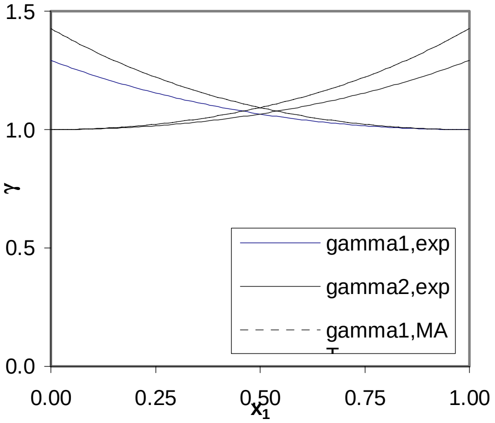

Figure 3: Comparison of activity coefficients as function of composition for a mixture of benzene (1) and methyl-acetate(2) at 303.15K and 1atm. (-) Generated from experimental data. (--) Generated using derivatives of activity coefficient from integration of g(r) from correlation.

MD or MC simulations

In both MD and MC simulations a force potential is calculated on each atom which is used in MD simulation for calculating the acceleration and in MC to find the change in energy related to a certain step. In this project an advanced potential, CHARMM [3], is used which general form is shown in Equation 3.

$$V = V_b + V_\theta + V_\varphi + V_\omega + V_{U-B} + V_{L-J} + V_{coulumb}$$

Equation 3

The first five terms are related to the intramolecular forces. Except V_φ, they only contribute when the conformation deviates from an equilibrium set point. V_b is the contribution from bond length variations; V_θ is related to the bond angle variations; V_ω is the deviation from a dihedral angle plane, V_{U-B} is the contribution the deviation in the equilibrium distance between atom 1 and 3 in a bond angle, where atom 2 is the center atom. V_φ is the contribution from the dihedral angles. The two last contributions in Equation 3 describe intermolecular forces, where V_{L-J} is the Lennard/Jones potential which describes the van der Waals forces and $V_{coulumb}$ describes the interactions between the charges of the atoms. In Equation 4 the bond length force contribution is shown as a summation of all the bonds attached to the atom.

$$V_b = \sum_i k_{b,i} \left(b_i - b_{i,eq} \right)^2$$

Equation 4

One needs to know all the force constants and equilibrium values of all bonds, bonds angles etc. which are relevant to the system. For the Lennard/Jones potential the Lorentz/Berthelot rules of combination are used which reduces the set of parameters to one for each atom type included. However, these can be established with a very limited input of experimental results.

γ- and δ-lactones

γ- and δ-lactones (Figure 4) are internal esters of hydroxy acids. The small lactones are good solvents for industrial cleaning products like paint strippers and deinking and adhesive removers. They also have application as a chemical intermediate in agrichemicals, pharmaceuticals and dyes. The lactones are also known as fragrances naturally occurring in fruits like apricots and peaches. The lactones are purified by distillation. In order to model the fractionation of these compounds it is necessary to have access to physical properties and as these are not commonly known from the literature, prediction is an attractive way to circumvent this problem. The lactones are often formed by lactonization of the corresponding hydroxy acid esters (methyl esters). The hydroxy acids are even more scarcely described in the literature. So the main problem to describe is the ring closure reaction of the hydroxy acids and the equilibrium associated with this process. Analytically it is a problem to determine the purity of the lactones as varying amounts of water may shift the equilibrium towards the open form, i.e. the hydroxy acid. This can partly explain the limited publications of experimental results.

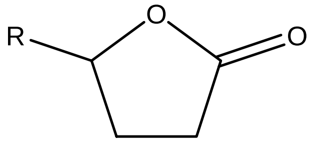

Figure 4: Basic structure of γ-alkyl-γ-lactone.

The work made for the lactone compound group can be divided into two areas, pure compound properties and mixture properties.

Figure 5 shows an example of improving an established group contribution method. The figure shows the boiling point, T_b, plotted against the length of the alkane side chain R (see Figure 4). The first data series shows the experimental data and the second shows the prediction of the Marrero/Gani method [4] with the original parameters, and the third shows the improved results by introducing a new group representing the cyclic ester part of the molecules. The new cyclic ester group has improved the absolute average relative error (AARE) from 6.7% to 1.9% when taking into account all the experimental data available for lactones.

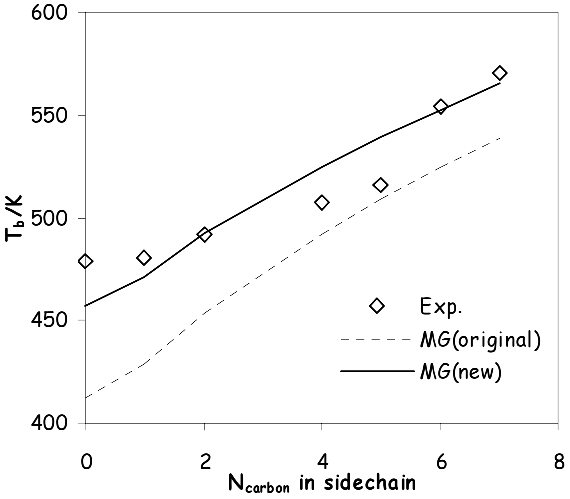

Figure 5: Boiling point, T_b, for γ-lactones as function of the length of alkane side chain R.

Parameters for the cyclic ester group have been determined for prediction of 8 pure compound properties such as T_c P_c ΔH_f etc.

The methodology shown in Figure 1 has also been applied to mixture properties of the lactone compound group. The major group of data is V^E-data which covers mixture with all common compound groups alkanes, alcohols, ethers etc. For a smaller set of data exists for data types normally used in regression of parameters for G^E-models which covers VLE, LLE, SLE, γ^∞ and H^E. The goal is to enable UNIFAC [5] predictions for lactone containing mixtures. Consequently the existing model parameter set was to be tested where the obvious choice was to use the linear ester group in the description of the lactones. Though this step was not need as comparison of mixtures of lactones or equivalent linear ester with key compounds shows very different behavior. Where water and lactones are miscible under normal conditions linear esters mixed with water give liquid-liquid splits. Secondly lactones with alkanes give liquid-liquid splits where alkanes mixed with linear ester are miscible but give azeotrope mixtures. A new UNIFAC group, CCOO(cyc), has been generated on the basis of the data collected. 14 sets of interaction pairs have been determined but the quality of the parameters varies and they need to be improved. The amount of data was sufficient for mixtures with aromatic compounds. Figure 6 shows an example for the mixture between δ-valerolactone (1) and benzene (2) at two temperatures, 298.15K and 313.15K. Together with the experimental data prediction made by UNIFAC using the linear ester group, CCOO, are shown by the dashed lines. The UNIFAC predictions using the new lactone UNIFAC group, CCOO(cyc), are plotted using the full line. It can be seen that the prediction using the linear ester group shows almost ideal behavior while the prediction by the new UNIFAC group describes the data almost perfectly.

As previously mentioned not all the parameter sets have been determined on the basis of an acceptable amount of experimental data. It is in the future scope of the project to generate pseudo-experimental data on which to base the better UNIFAC parameters.

The generation of pseudo data is not a trivial assignment because other parameters are needed to calculate the CHARMM potential from Equation 3. The CHARMM parameters for the internal contributions are generated from *ab initio* quantum mechanical calculations and the interatomic parameters are determined using pure compound properties such as densities, heat capacities, vapor pressures and heats of vaporization. This work is ongoing.

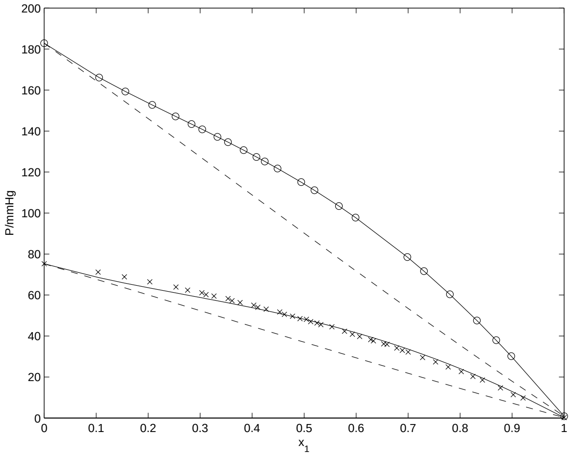

Figure 6 Px-diagram for δ-valerolactone (1) and benzene (2) at 293.15K (x) and 313.15K (o). Full line: UNIFAC using CCOO(cyc) group and dashed line: UNIFAC using CCOO group [6].

It is in the objective of the project to make a database of parameters for common compound groups thereby making it straight forward to generate pseudo data between a new compound group and a well known group. An example could be missing data between the new compound group and alcohols. If CHARMM parameters are available for a list of alcohols it is easy to start generating pseudo data shortly after CHARMM parameters have been generated for the new compound group.

References

1. J.G. Kirkwood, F. Buff, J. Chem. Phys. 19 (1951) 774-777.
2. E. Matteoli, G. Ali Mansoori, J. Chem. Phys. 103 (1995) 4672-4677.
3. A. D. MacKerell et al, J. Phys. Chem. B, 102 (1998) 3586-3616.
4. J. Marrero, R. Gani, Fluid Phase Equilibria 183-184 (2001) 183-208.
5. Aa. Fredenslund, J. Gmehling, P. Rasmussen, (1977), Elsevier, Amstedam.
6. A. Klein, P. Svejda, ELDATA Int. Electron. J. Phys. Chem. Data, 1 (1995) 87-94.

Michelangelo Dall'Ora

Address: DTU Building 229
Phone: +45 4525 2839
Fax: +45 4588 2258
e-mail: mid@kt.dtu.dk
www: http://www.chec.kt.dtu.dk

Supervisors: Anker Degn Jensen
Peter Arendt Jensen

Ph.D. Study
Started: December 2004
To be completed: November 2007

Reactivity and Burnout of Wood Fuels

Abstract

Wood is increasingly used as energy source for heat and power production. In suspension fired boilers wood char oxidation is the slowest step and determines the degree of burnout of the fuel, thus affecting the efficiency of the plant. In order to enable prediction of the burnout and main heat release profile, wood char needs to be characterized, its reactivity to oxygen has to be assessed and kinetic data must be coupled with suitable models accounting for transport processes and char transformation during combustion. This project addresses these issues by means of experimental work at laboratory, pilot and full scale as well as modeling,

Introduction

The large availability of wood, neutrality with respect to CO_2 emissions and the fact that it is a renewable source make it a very attractive solid fuel for combined heat and power plants. A variety of wood species are burned nowadays in power plants, depending on the location of the plant, the wood-related activities in the area (pulp and paper industry, sawmills, etc.) and other economical reasons; wood from conventional forestry, residues from manufacturing of wood based products such as bark, sawdust and off-cuts from sawmills are some of the sources of wood fuel.

The most common techniques for the combustion of wood in combined heat and power plants are grate and suspension firing; this project deals with the latter. Suspension firing has been used for decades to burn pulverized coal; environmental concern and legislation have contributed to the conversion of some of those plants to wood combustion and to the building of new pulverized wood power plants. Today, the world's largest pulverized wood fired power plant in operation is in Denmark.

Wood is usually delivered to the plant as wood pellets (see Figure 1) that are opened by milling prior to entering the boiler; what is fed to the boiler is thus pulverized wood, as is seen in Fig.1.

As soon as the wood particles enter the boiler, they are subjected to very rapid heating and they release volatile matter; this process is known as pyrolysis and leaves a solid residue called char. Pyrolysis significantly affects the overall process of wood combustion by determining yield and influencing morphology, composition and properties of the char.

a b

Figure 1: a) wood pellets, b) pulverized wood

Figure 2 (from [1]) shows two chars from pine wood produced at different conditions. The influence of pyrolysis conditions on char morphology is evident: as the severity of the treatment increases (Fig. 2b), the particle goes through a molten phase and completely loses the typical fiber-like structure of wood. In agreement with this observation, studies on straw showed that straw char produced at high temperatures and high heating rate appears as a spherical shell, with the outer surface that has undergone plastic deformation [2]; however, very little information is available with specific focus on wood char morphology and its dependence on pyrolysis conditions [3].

Wood pyrolysis occurs in a time interval of the order of ms, whereas the subsequent oxidation of the char takes up to several seconds [4]. It is therefore evident that the process of char oxidation is the most relevant when the degree of burnout (conversion) of the fuel is to be calculated. In this perspective, it is vital to assess the reactivity of the char to oxygen. There is a well established awareness that the reactivity of chars from wood is far higher than the reactivity of chars from coal [5]; nevertheless, accurate measurements of wood char reactivity are scarce in literature.

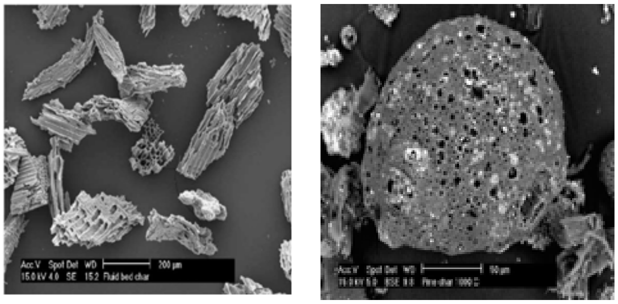

a b

Figure 2: Pine char produced at: a) 1173 K, heating rate 20 K/s, b) 1273 K, heating rate 10^5 K/s [1].

The time required to burn a char particle depends not only on the reactivity of the, but also on its size, density, and the conditions in the furnace.

Specific Objectives

The project aims at enabling a good prediction of wood particles burnout in suspension fired boilers.

The focus will be on:

- Char characterization and investigation of the dependencies of char properties on pyrolysis conditions
- Assessment of char oxidation reactivity
- Modeling of char particle combustion

Experimental

An extensive full-scale experimental campaign was carried out at a Danish power plant. The measurements have included sampling of fuel and ash as well as extraction of particles from the furnace and from the flue gas channel, local inflame measurements and gas composition. The pulverized fuel size distribution was obtained and the majority of the particles (about 65% of the mass) had a size in the interval 125-1000 micron. This is a relatively large particle size when compared to usual sizes for pulverized coal (70-80 wt% below 70 micron [4]); nevertheless, due to the high reactivity of wood char the burnout of the particles during the full scale measurements was very high. The behaviour of wood fuel during co-combustion with natural gas and oil was also investigated during this campaign.

Future work

Currently, pilot scale experimental work is being carried out; char from different wood fuels (bark and pine) is produced at different conditions in an entrained flow reactor in order to investigate the relation between pyrolysis conditions and wood char properties. The char produced will be characterized with respect to composition, particle size, morphology (by SEM microscopy), reactivity (by thermogravimetry).

The experimental results will hopefully help us understand the burning mechanism of a wood char particle and provide us with accurate kinetic data; this will enable us to model char combustion and predict particle burnout from wood fuel and process conditions data.

Acknowledgements

The project is funded by PSO-Elkraft and is carried out at CHEC (Combustion and Harmful Emissions Control) Research Center in cooperation with Energi E2 A/S.

References

1. E. Cetin et al., Fuel 83 (2004) 2139-2150
2. A. Zolin, Reactivity of solid fuels, Ph.D. Thesis, 2001, DTU
3. E. Biagini, C. Fantozzi and L. Tognotti, Combust.Sci. and Tech. 176 (2004) 685-703
4. T. F. Wall in: C.J. Lawn (Ed), Principles of Combustion Engineering for Boilers, Academic Press, UK, 1987
5. M.J. Wornat et al., 26th Symp. on Comb., The Comb. Inst., 1996, 3075-3083

Florin Paul Davidescu
Address: CAPEC, Department of Chemical Engineering
Building 227, room 204
Phone: +45 4525 2811
Fax: +45 4593 2906
e-mail: fpd@kt.dtu.dk

Supervisors: Sten Bay Jørgensen

Ph.D Study
Started: January 2005
To be completed: December 2007

Optimizing Experimental Design Using Grey-Box Modelling

Abstract

An overview of the project is given and some results from current work are presented and discussed. Application of a grey-box stochastic modeling framework for developing stochastic state space models for dynamic systems based on combining first principle models and experimental data is described briefly. The framework is used to develop reliable predictive models for a biochemical reaction network isolated from *E. coli* mutants. The modeling purpose is to use the model to identify the bottlenecks in the reaction network to enable optimizing the production of the desired product through genetic manipulation.

Introduction

There is an increasing interest in producing complex fine chemicals and intermediates in the pharmaceutical industry using biochemical synthesis. Up to now, only one or a few biotransformation steps are involved in complex synthesis problems in industry, although enzymes are widely known as being specific, fast and working under mild conditions. Usually enzymes introduce only minor changes to the substrate. To develop a purely enzymatic synthesis for complex molecules from completely different substrates, large reaction networks are necessary. One way to construct such a functional network is the System of Biotransformations (SBT). The SBT is based on a micro-organism's metabolic network containing the synthesis path including cofactor regeneration reactions down to the desired product which most often is an intermediate in the metabolic network, thus expression of the enzymes catalysing reactions from this intermediate are turned off prior to the extraction i.e the genes are knock-out. Thereby, the SBT is used as cell free extract in the production phase, combining the easy handling of a viable culture with the advantages of *in vitro* biotransformations [2]. The general goal of this study is to identify the bottlenecks of the SBT, to describe them evenly and thereby to optimize the productivity of the selected reaction network. The workhorse of the de-bottlenecking and optimization process is a model describing the biochemical reaction network with good long term prediction properties. Thereby, the SBT contains the relevant reactions of the glycolysis, leading to a system of high dynamics and complexity. Therefore, it is not realistic to develop a "perfect model" from first principle engineering methods. For this reason, in this work a grey-box stochastic model development framework [1] will be used to develop a stochastic state space model. The purpose of this paper is to describe the workflow of the application of the grey-box stochastic modeling framework for development of a kinetic model for a batch reaction network. An initial model structure is developed from first principles. The model parameters and unknown functional dependencies are iteratively estimated as the information in the experimental data are exploited.

Specific Objectives

The main objectives of this project can be summarize at follows. First objective is to develop a systematic methodology for modelling of the reaction pathways for the SBT. The second main objective is to develop a procedure for optimal experimental design for development of an SBT-model for productivity optimization.

Model development for an SBT isolated from *E. coli* mutants

The batch experiments have been conducted by ref [2] and provides two set of measurements: one for glucose and the second for di-hydroxy-acetone-phosphate ($DHAP$). The first step in the model development is model formulation. In order to formulate a model, the existing biochemical reaction network in *E-coli* is presented with focus on the reactions toward the product of interest (DHAP) considering the gene which is knocked out. The simplified biochemical reaction network used for model development is depicted in figure 1. The equilibrium reaction between DHAP and glyrealdehyde-3-phosphate does not take place since the *tpi* gene i.e. responsible for the expression of the enzyme catalyzing the reaction has been knocked-out. For the current version of the model all the reactions from glucose to fructose-1,6-biphosphate were lumped into a single reaction r_1 . The second reaction considered is the reaction from fructose-1,6-biphosphate to glyceraldehide-3-phosphate and di-hydroxy-acetyl-phosphate, r_2 catalyzed by aldolase. The reactions consuming the glyceraldehyde-3-phosphate down to pyruvate in the central carbon metabolism were all lumped into one single reaction r_3. The reaction producing lactate from pyruvate was included as reaction r_4. The reason to include these two reactions is that it is desirable to account for the consumption-production of co-factors ATP and NAD^+. The model consists of dynamic mass balances for all the species involved in the four reactions plus one for each of the two co-factors. The stochastic model equations eq. 1–10 have been completed with the difussion terms as mentioned above.

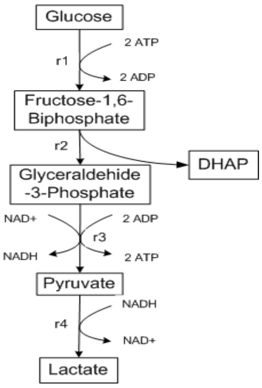

Figure 1 Stochastic grey-box modelling framework, from [1]

In this first model formulation it has been considered that the reaction rates $r_1 - r_4$ are constant and then estimated together with the model parameters and with the initial values of the states and the measurement variances $S_1 - S_2$.

$$\begin{aligned}
dc_{GL} &= -r_1 + \sigma_{11} \cdot dw && (1)\\
dc_{F16B} &= r_1 - r_2 + \sigma_{22} \cdot dw && (2)\\
dc_{DHAP} &= r_2 + \sigma_{33} \cdot dw && (3)\\
dc_{G3P} &= r_2 - r_3 + \sigma_{44} \cdot dw && (4)\\
dc_{PYR} &= r_3 - r_4 + \sigma_{55} \cdot dw && (5)\\
dc_{LAC} &= r_4 + \sigma_{66} \cdot dw && (6)\\
dc_{ATP} &= -2 \cdot r_1 + 2 \cdot r_3 + \sigma_{77} \cdot dw && (7)\\
dc_{NAD} &= -r_3 + r_4 + \sigma_{88} \cdot dw && (8)\\
y_{GLC} &= c_{GL} + e, e \in N\left(0, S_{11}\right) && (9)\\
y_{DHAP} &= c_{DHAP} + e, e \in N\left(0, S_{22}\right) && (10)
\end{aligned}$$

After applying succesively some steps of the grey-box stochastic modelling framework the model have been expanded with two kinetic reaction rate expressions given below (eq. 12). The performance of the model in terms of pure simulation has been improved significantly(not shown), however the model still has a some deficiencies (more details in [3]).

$$\begin{aligned}
r_1 &= r_{1max} \cdot \frac{c_{GLC}}{K_1 + c_{GLC}} && (11)\\
r_2 &= r_{2max} \cdot \frac{c_{F16B} - \frac{c_{DHAP} \cdot c_{G3P}}{K_{eq2}}}{c_{F16B} - \frac{c_{DHAP} \cdot c_{G3P}}{K_{eq2}} + K_{s2}} && (12)
\end{aligned}$$

Conclusions and future work

A stochastic grey-box model for SBT is currently under development and the results seems promising. Statistical tools showed that the model has some deficeincies with the first reaction rate r_1 and the focus is now to improve these deficiencies. Then the focus will move to the experimental design in order to develop the model for the whole reaction network described in figure .

Acknowledgements

The project is part of the European project EUROBIOSYN within the 6^{th} European Framework Programme for Research.

References

[1] Kristensen N. R., Madsen H. and Jørgensen S. B., A method for systematic improvement of stochastic grey-box models, Comp. and Chem. Eng., 28 (2004), 1431-1449.

[2] Schümperli M., Heinemann M., Kümmel A., and Panke S., in preparation, 2005

[3] Davidescu F. P., Madsen H., Schümperli M., Heinemann M., Panke S. and Jørgensen S.B., Stochastic Grey Box Modeling of the enzymatic biochemical reaction network of *E. coli* mutants, submitted to the joint conference ESCAPE 16-PSE, Germany 2006.

Joanna Maria Drews
Address: Building 423, room 206,
Produktionstorvet
Phone: +45 4525 6815
Fax: +45 4588 2161
e-mail: jmd@polymers.dk
www: http://www.polymers.dk,
http://www.risoe.dk/pol

Supervisors: Prof. Søren Hvilsted
Senior Scientist Peter Kingshott, Danish Polymer Centre, Risø National Laboratory

Ph.D. Study
Started: February 2005
To be completed: January 2008

Surface Polymerization Methods for Optimized Adhesion

Abstract
The focus of my project is to surface modify model substrates with the aim of understanding and optimizing adhesion within carbon and glass fibre composite materials. The modification utilizes low power plasma polymerization with specific monomers to provide controlled surface chemistries. The surface characterization part of the project aims at increasing the understanding of the physical and chemical processes taking place in the matrix/fiber interface during the mechanical tests, and provides a supportive understanding of the adhesion mechanisms.

Introduction

The present project is part of a larger STVF Framework Programme on Interface Design of Composite Materials and is carried out as collaboration between the Graduate School of Polymer Science, Technical University of Denmark, and the Danish Polymer Centre, Risø National Laboratory. Additional partners in the project include the Materials Research Department, Risø National Laboratory, where mechanical tests of the fracture toughness of the modified substrates are carried out.

The overall challenge of this project is to improve the mechanical properties of composite materials, which are used for example for wind turbines blades, since existing materials are currently limited in strength. It is known that the macroscopic mechanical properties of fibre composites, such as strength and toughness, are controlled by the fibre/matrix interface. The interface properties are controlled by the fibre sizing. The fibre sizing (or coating) is a material layer that is applied to the fibre surface during fibre manufacturing. The sizing has several functions: to facilitate easy processing, protect the fibres during handling, enable wetting and to create the physico-chemical link to the matrix during the subsequent consolidation of the fibre composite. Until now, however, no coordinated attempts have been made to establish a complete correlation from the nanoscale, i.e. fibre sizing, to the macroscopic properties of the resulting composite materials.

Methods

My Ph.D. project, which is nearing the end of the first year, is focused on using nanoscale surface modification and surface characterisation techniques. The techniques which are currently used in the project are: X-ray Photoelectron Spectroscopy (XPS), Attenuated Total Reflectance Fourier Transform Infrared Spectrometry (ATR-FTIR), and Atom Force Microscopy (AFM). The results are supported by surface derivatisation methods (e.g. Toluidine blue staining) to quantify the number of surface functional groups. From XPS and ATR-FTIR measurements one obtains an understanding of the chemical composition of the polymerized films. The XPS [1] spectra allow for determination of the atomic composition as well as the bonding states of specific atoms. AFM is used to measure the thickness of the modified polymer layer as well as topographical changes [2]. Finally, the Toluidine blue staining method [3] is used to quantify the number of carboxylic acid groups in the volume of the film.

Using surface characterization methods one obtains a better understanding of the physical and chemical properties of materials, and hence such analysis ultimately helps in the design of new and better (e.g. stronger) materials. In this study surfaces will be designed having specific chemical groups, and variable topography. The model systems will develop several interface types, having weak, intermediate and strong bonding, respectively. All bonding experiments are applied on planar model specimens that include glassy carbon substrates (as mimics for carbon fibres) and silicon wafers (as mimics for glass fibres). The substrates have starting surface chemistries very similar to the fibre systems and are atomically smooth, thus allowing for addition of topographical features later in the project.

In order to modify the planar substrates I will use low power 2-phase AC plasma polymerisation [4]. The surface is functionalised with different chemical groups such as amine (from e.g. heptylamine, vinylimidazole, acrylonitrile monomers) and carboxylic acids (e.g. maleic anhydride [5], 1,2-methelenedioxybenzene monomers). During the plasma polymerisation films are created that are covalently bonded to the substrates, which are uniform and stable. The thicknesses of the coatings are regulated by means of varying the time and the power of the plasma polymerisation. With plasma power manipulation it is also possible to change the degree of crossed-linking of the film.

Results

Until now I have focused on glassy carbon as model substrates. Initially, the specimens are cleaned in an ultrasonic bath in the following solvents: (a) chloroform (5 minutes), (b) acetone (10 minutes) and (c) methanol (5 minutes). A high resolution spectrum of clean glassy carbon is shown in Fig. 1. Peak A is due to the C-C, C=C and C-H bonds, while peak B comes from the C-O-C and C-OH bonds. All the smaller peaks owes to the π*-π shake-up, which is given by C=C or the benzene ring.

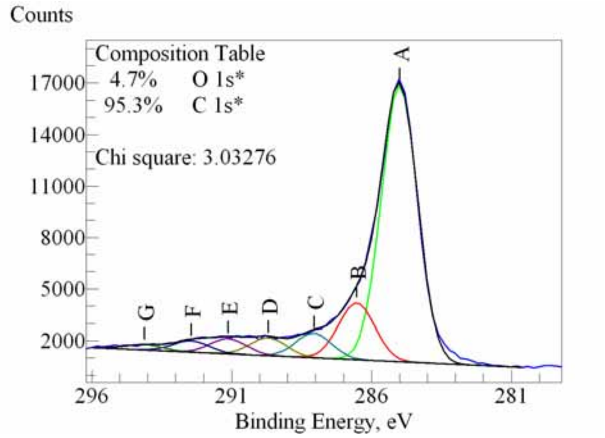

Figure 1. High resolution XPS spectrum of C 1s for a clean glassy carbon specimen.

For the plasma polymerization I am using the monomers maleic anhydride (MAH) and 1, 2-methylenedioxy benzene (MDOB) in gas phase. The concentration, distribution and reactivity of the chemically functional groups are systematically altered by varying the modification conditions (e.g. power). After polymerization the modified surfaces are characterized using the methods which are listed above, i.e. XPS, AFM and ATR-FTIR. The modified substrates are also placed in water (at room temperature) to hydrolyse the anhydride groups on the surface to carboxylic acid groups.

An example of a surface modified with maleic anhydride (10 mA current and 10 minutes treatment, 050616b) is shown in Fig. 2. From the XPS measurements there is clearly a significant difference between a clean glassy carbon spectrum and the modified one. Changes are observed in both the atom composition as well as in the shape of the C 1s signal. In the case of the modified glassy carbon specimen, the peaks C and D are due to C=O and C(O)O bonds, respectively. These components derive from the structure of monomer.

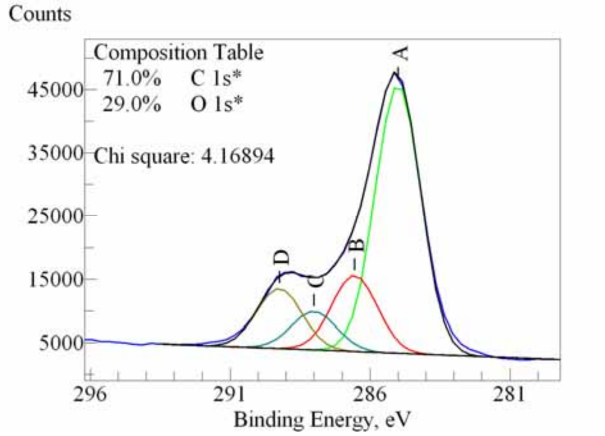

Figure 2. High resolution XPS spectrum of C 1s for a glassy carbon specimen plasma polymerized with maleic anhydride.

Fig. 3 shows the thickness of the films when varying the power of the polymerization for the two different monomers (MAH, MDOB) as well as for a mixture. The thicknesses are measured using AFM.

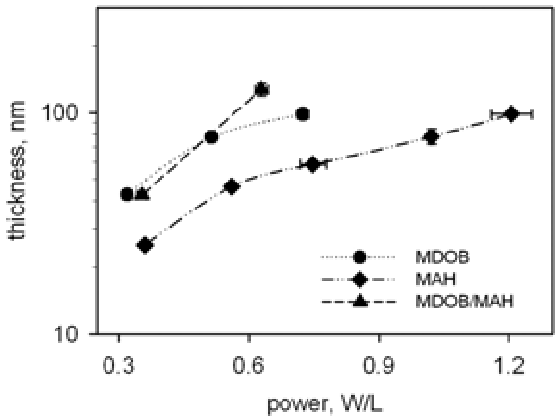

Figure 3. The thickness of the films as a function of the power of the plasma polymerization.

Conclusions

By using different (higher) power of the plasma polymerization, i.e. introducing different power into the system, it is possible to control (increase) the thickness of the modified layer. Likewise, it is possible to change the amount of anhydride groups on the surface [5] – increasing the plasma power decreases the number of anhydride groups (results not shown; as measured using the Toluidine blue staining method).

The adhesion strength has been measured for specimens polymerized with varying power. The preliminary results show that for MAH the adhesion increases with higher plasma power, until it reaches an optimum at ~20 mA (0.748 W/L) and then falls off. The reason for this behavior is not yet known, however, there are at least two possible explanations, which we need to investigate in more detail:

- The modified surfaces with different power have different thicknesses; the thickness increases with increasing power for all monomers. The thickness of the built-up film may therefore play an important role for adhesion.
- There is a correlation between the number of active carboxylic acid groups in the volume of a film and the fracture energy.

The matrix and how it is interacting with the polymer surface may also play a significant role. In this case the functional groups are more significant than the thickness of the modified surface.

Acknowledgements

The Graduate School of Polymer Science and The Technical University of Denmark, and the STVF are thanked for financial assistance.

I would like to thank Senior Scientist Bent Sørensen and postdoc Stergios Goutianos from the Materials Research Department, Risø National Laboratory for discussions and for measuring the fracture toughness of the modified surfaces; my supervisors Professor Søren Hvilsted and Peter Kingshott; and finally the staff of the Polymer Centers at DTU and Risø National Laboratory.

References

1. T.R. Gengenbach, R.C. Chatelier, H.J. Griesser, Surface and Interface Analysis 24 (1996) 611-619.
2. P.G. Hartley, H. Thissen, T. Vaithianathan, H.J. Griesser, Plasmas and Polymers 5 (1) (2000) 47-60.
3. S. Sano, K. Kato, Y. Ikada, Biomaterials 14 (11) (1993) 817-822.
4. P.S. Guldager, S.F. Christensen, B. Winther-Jensen, US2004086660 (2004) NKT Research A/S.
5. M.E. Ryan, A.M. Hynes, J.P.S. Badyal, Chem.Mater. 8 (1996) 37-42.

Runi Ditlev Egholm
Adress: Building 423, Room 220
Phone: +45 4525 6800
Fax: +45 4588 2161
e-mail: rde@kt.dtu.dk
www: http://www.polymers.dk

Supervisor: Peter Szabo
Ph.D Study
Started: July 2004
To be completed: July 2007

Emulsion Design: Experimental Studies on Drop Deformation

Abstract

In order to investigate the mechanisms behind drop deformation and breakup in complicated flow fields model experiments on single drops are being carried out at the Institute of Food Science and Nutrition at ETH, Zü rich. The experiments are carried out using a so-called rotor-stator device, which is an apparatus with two concentric cylinders each cylinder having 6 teeth on the inner wall. The reason for this geometry is to model the flow inside an extruder screw. The position of the drop relative to the inner and outer cylinder is monitored using a digital camera while a second camera with longer focal length is used to monitor the deformation of the drop. Using this setup it is possible to obtain insight into the mechanisms behind emulsion dispersion in extruder devices.

Introduction

When producing products based on emulsified systems the emulsifying process is of major importance. This makes studies of the dispersion process one of the key interests to industries producing e.g. pharmaceuticals, cosmetics and foods. Typical experimental studies on emulsion behaviour when subjected to shear and elongational stresses have been carried out using flow cells with very well defined flow fields and monitoring the drop deformation and breakup using a still or video camera. Investigations of this type were first carried out in the pioneering work of Taylor in the 30's [1, 2]. Taylor carried out experimental studies on drop deformation in flow cells with either pure shear flow (parallel band apparatus) or pure elongational flow (four roll mill). Taylor was also able to predict the steady state deformation in a given flow field when the surface tension (constant) and the viscosity of the dispersed and continuous phases were known. However his analysis is only valid in the small deformation region. Since the work of Taylor improvements in imaging technology (e.g. digital cameras) and controller systems has led to great improvements in the experimental techniques as demonstrated in [3] where a fully computer controlled shear flow cell is described. Controlling the size distribution of the disperse phase (drops) is very important, e.g. in emulsion polymerization processes. Very close to monodisperse drops can be achieved using a double capillary setup as reported in [4]. For general treatments on experimental and theoretical work carried out on drop deformation and breakup in various flow fields excellent reviews are given e.g. by Rallison [5] and recently by Windhab et al. [6].

In order to investigate the deformation of single drops on a theoretical level at large deformations and beyond the point of breakup large scale numerical simulations are necessary. The numerical methods used to simulate the drop behaviour need to be able to handle flows with deforming interfaces and should also be able to handle merging and breakup of the interfaces. The most popular methods are the Boundary Integral Method (BIM) and Volume of Fluid (VOF) method. In the BIM method the flow field is calculated using some flow solver, e.g. a finite difference, finite volume or finite element solver and then the information from the solver is passed along to the BIM part of the code which handles the interface. This method has been used with success by several authors, e.g. [7, 8]. The VOF is an interface tracking method, where different phases are identified by a colour function. If a point in space is inside the disperse phase the value of the colour function is 1 otherwise it is zero. In 2D this is comparable to a black and white image. The deformation of the two phases relative to each other is carried out by advecting the colour function in the flow field. As was the case for the BIM method the flow field is calculated using a flow solver. However in this case the VOF algorithm is coupled to the flow solver through the interfacial tension and the densities and viscosities of the disperse and continuous phase respectively. This method is well suited for handling breakup and merging of drops and has been applied with success by several authors [9, 10, 11].

The main objective of this ph.d. project is to implement a micro-mechanical model in order to make it possible to simulate drop breakup and merging in complicated flow fields and geometries. For this purpose we have chosen to base the model on the VOF method coupled with a Finite Element method. However, since I am currently visiting the Institute of Food Science and Nutrition at ETH, Zü rich, and conducting experiments in their rotor-stator device the remainder of this paper will be concerned with the experimental aspects of the project.

Theory

In this section some theoretical considerations will be presented together with some definitions used in connection with drop deformations. When a dispersed system is subjected to a flow field the structure of the drops will change according to the stresses arising from the flow field. In order to characterize the strength of the forces working on deforming the drop relative to the forces working to retain the drop shape one defines the capillary number as

$$Ca = \frac{G\mu_c r_0}{\sigma} \tag{1}$$

In Eqn. 1, G is the sum of the magnitude of the shear and elongation rate ($G = |\dot{\gamma}| + |\dot{\epsilon}|$), μ_c is the viscosity of the continuous phase, r_0 is the initial drop radius and σ is the interfacial tension. The value of Ca is therefore closely related to the drop deformation. Another dimensionless number that is important when characterizing a disperse system is the viscosity ratio λ between the disperse phase and continuous phase, i.e.

$$\lambda = \frac{\mu_d}{\mu_c} \tag{2}$$

For small deformations Taylor [1, 2] deduced an analytical expression relating the steady state drop deformation as a function of the capillary number and the viscosity ratio given by the following relation:

$$D = Ca\frac{19\lambda + 16}{16(\lambda + 1)} \tag{3}$$

In Eqn. 3, D is the deformation defined as $D = (L - B)/(L + B)$ where L is the length of the drop along its longest axis and B is the width of the drop. Extensions of the Taylor theory have been provided by eg. Cox [12] and Barthè s-Biesel and Acrivos [13]. At medium and large deformations expression (3) is no longer valid. In general the steady state deformation as a function of the capillary number shows an initial linear part agreeing with the Taylor theory whereafter the deformation either levels out, levels out and starts to decrease or increases rapidly. In the first case the flow field is not able to break up the drop, in the second case the drop breaks up into a number of smaller drops and in the third case the drop is elongated into a thin thread that eventually breaks up into many tiny droplets. In the region where the drop breaks up one finds the critical capillary number, i.e. the capillary number where a given drop bursts. In a technical point of view this region is of major importance since the breakup mechanism determines the final drop size distribution.

Experimental Setup and Procedure

In this section the experimental setup with the rotor-stator device will be introduced. The setup can be seen on the photographs in Figure 1. Two concentric cylinders each having 6 teeth on the inner walls (cf. Figure 1 right image) can be rotated independently from each other using electric motors. The cylinder gap is filled with the continuous phase liquid such that a flow field is generated between the gap when the cylinders rotate. A single drop ($\sim 1mm$) is then placed in the continuous phase using a syringe. In the left image in Figure 1 two digital video cameras can be seen. From the camera situated farthest away from the cylinders the width of the teeth and channel can be monitored while the camera closest to the cylinders is used to monitor the drop itself, i.e. the deformation. The cameras are mounted on a vertical bar that can be rotated independently from the rotation of the two cylinders. This makes it possible to keep the drop inside the camera view angle by constant manual movement of the cameras. The video recordings from the two cameras are analyzed using the Image Processing Toolbox in Matlab to obtain the drop deformation and the position of the drop relative to the teeth walls at a given time.

The experiments can be carried out either by rotating one cylinder and keeping the other stationary or by rotating both cylinders. The inner cylinder is rotated counter clockwise and the outer cylinder is rotated clockwise. Further details regarding the setup can be found in reference [14].

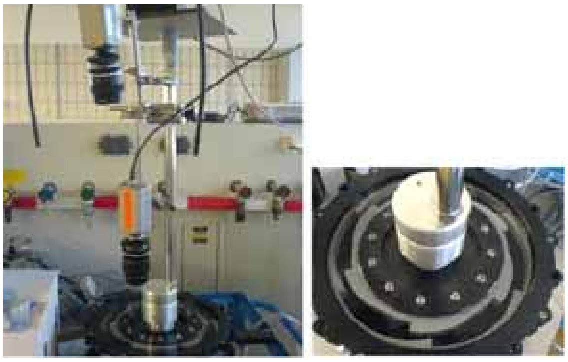

Figure 1: Images showing the rotor-stator device. Left image shows the two cameras attached to the apparatus. The right image shows a close up of the toothed channel between the cylinders.

The continuous phase consists of polyglycol and the disperse phase consists of a silicone oil. In table 1 the various data on the continuous phase liquid and the disperse phase liquid can be seen. In order to make the drop visible in the continuous phase TiO_2 is added to the silicone oil. TiO_2 is also used to adjust the density of the silicone oil to match the density of the continuous phase. The interfacial tension between the two phases has not been measured at the current time.

Table 1: Data on the system used in the experiments.

	Cont. phase	Disp. phase
Type	Polyglycol	Silicone oil
Producer	Hoechst AG	
Prod. Details	B11/700	
ρ, 25 °C [kg/m^3]	1.048	0.963
μ, 25 °C [$Pa \cdot s$]	1500	0.100

Results and Discussion

The experiments carried out at this point are of preliminary character in that they have been used for testing the setup of the two cameras and for testing and optimizing the Matlab code for the image analysis. However, the results are useful for visualizing how the drop geometry is influenced by the position of the teeth on the cylinder walls. Experiments have been carried out with two different angular velocities of the cylinders one where $\theta = 0.039 rad/s$ and one where $\theta = 0.059 rad/s$. In each experiment the angular velocities of the inner and outer cylinder are the same but with opposite sign. In Figure 2 the results from the experiment with $\theta = 0.039 rad/s$ can be seen.

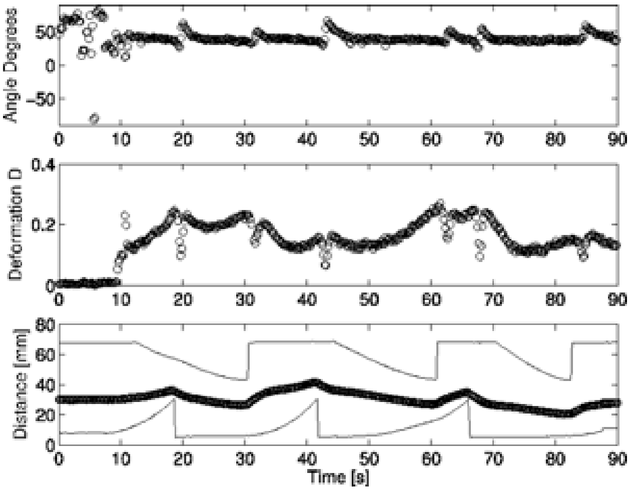

Figure 2: Top figure: Drop angle relative to the inner cylinder. Middle figure: Drop deformation. Bottom figure: The position of the center off mass of the drop (circles) and the position of the cylinder walls as a function of time. The lower wall corresponds to the outer cylinder. $\theta = 0.039 rad/s$.

The top figure shows the angle between the long axis of the drop and the inner cylinder. The middle figure shows the deformation D of the drop as defined in the theory section and the lower figure shows the position of the drop (center of mass) relative to the outer and inner cylinder. The outer cylinder corresponds to the lower wall in the bottom figure. In this experiment the strength of the flow field was not strong enough to break up the drop, however, Figure 2 clearly shows that the drop deformation increases with decreasing gap width. Furthermore Figure 2 shows that when the drop passes a tooth the deformation decreases rapidly (relaxation) and then increases rapidly again. It is also seen that the angle between the long axes of the drop and the inner cylinder fluctuates when the drop relaxes.

In Figure 3 the results from the experiment with $\theta = 0.059 rad/s$ can be seen. During this experiment one drop breakup occurs at approximately 120s and another breakup occurs at 135s as indicated in the figure. The figure shows that the breakup occurs just after the drop has passed the teeth when they have coincided (minimum gap width). it is also seen that as the teeth approach each other the angle decreases. This indicates that the elongation rate relative to the shear rate increases as the teeth approach each other.

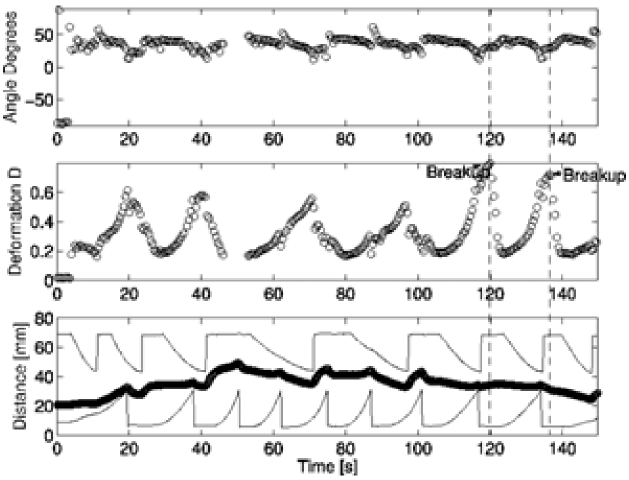

Figure 3: Experiment carried out with $\theta = 0.059 rad/s$.

Figure 4: Drop breakup for the experiment with $\theta = 0.059 rad/s$.

Images of the drop breakup from the experiment with $\theta = 0.059 rad/s$ at 120s can be seen in Figure 4. Here it is seen that as the drop passes the teeth (cf. also Figure 3) a number of small drops pinch off at the ends of the main drop. This process is repeated at 135s, however, fewer drops pinch off the main drop. This is in agreement with the fact that the radius of the main drop decreases every time end pinching occurs and at some point the critical Ca number of the main drop cannot be attained by the flow field.

Conclusion

Single drop experiments in a rotor-stator (or multi-tooth) device have been conducted. In order to monitor the position of the drop as well as its deformation during an experiment a two-camera system has been applied. One camera is used for recording the deformation and the other camera is used for recording the drop position. The image streams obtained are subsequently analyzed yielding information on deformation, angle and drop position as a function of time. Until now only preliminary experiments have been carried out, however, these indicate that the two-camera system can give insight into the mechanism of drop breakup in the rotor-stator device.

Future Work

In order to obtain information from the experimental setup described in this paper systematic experiments will be carried out. In these experiments parameters such as the viscosity ratio, the initial drop position, drop radius, interfacial tension etc. will be varied.

As regards the modelling part of the project a VOF algorithm and a Finite Element flow solver have been implemented and coupled, however, the incorporation of interfacial tension needs more work which will be carried out parallel to the experimental work and after the experimental work is completed.

Acknowledgments

This project is funded by the Danish Technical Research Counsil (grant no. 26-03-0282)

References

[1] Taylor, G. I., Proceedings of the Royal Society of London. Series A, Containing Papers of a Mathematical and Physical Character **138** (1932) 41.

[2] Taylor, G. I., Proceedings of the Royal Society of London. Series A, Containing Papers of a Mathematical and Physical Character **146** (1934) 501.

[3] Birkhofer, B. H., Eischen, J.-C., Megias-Alguacil, D., Fischer, P., and Windhab, E. J., Industrial and Engineering Chemistry Research **44** (2005) 6999.

[4] Walther, B. et al., Journal of Colloid and Interface Science **286** (2005) 378.

[5] Rallison, J. M., Annu. Rev. Fluid Mech. **16** (1984) 45.

[6] Windhab, E. J., Dressler, M., Feigl, K., Fischer, P., and Megias-Alguacil, D., Chemical Engineering Science **60** (2005) 2101.

[7] Loewenberg, M. and Hinch, E. J., Journal of Fluid Mechanics **321** (1996) 395.

[8] Pozrikidis, C., Journal of Engineering Mathematics **41** (2001) 237.

[9] Renardy, Y. and Renardy, M., Journal of Computational Physics **183** (2002) 400.

[10] Ginzburg, I. and Wittum, G., Journal of Computational Physics **166** (2001) 302.

[11] Scardovelli, R. and Zaleski, S., Annu. Rev. Fluid Mech. **31** (1999) 567.

[12] Cox, R. G., Journal of Fluid Mechanics **37** (1969) 601.

[13] Barthès-Biesel, D. and Acrivos, A., Journal of Fluid Mechanics **61** (1973) 1.

[14] Kaufmann, S. F. M., *Experimentelle und numerische Untersuchungen von Tropfendispergiervorgängen in komplexen laminaren Strömungsfeldern*, PhD thesis, ETH, Zürich, 2002.

Tobias Dokkedal Elmøe
Address: Building 201, Room 002
Phone: +45 4525 2936
Fax: +45 4593 2399
e-mail: tde@kt.dtu.dk
www: http://www.aerosol.kt.dtu.dk

Supervisors: Tue Johannessen
Hans Livbjerg

Ph.D Study
Started: March 2005
To be completed: February 2008

Production of Ceramic Catalytic Membranes by Deposition of Nano-Particles

Abstract

The deposition of nano-particles (catalytic or non-catalytic) on top of a porous substrate tube is a technique developed by the Aerosol Laboratory [1, 2] and offers a simple one-step method for preperation of membranes, compared to the more complex tradional sol-gel technique. During deposition (which is done at constant pressure) the flow through the membrane is measured and the accumulated flow is used in the calculation of the deposited mass. To enhance the stability and adherence of the membranes the particle deposition must occur at high temperatures, at which the particles will sinter together when deposited. As a new way of characterizing the generated membrane a permporometry apparatus is under construction. This will allow for the determination of the pore-size distrubtion. Modelling work is being applied to describe the various mechanisms during the nano-particle filtration.

Introduction

Porous ceramic membranes can be used for several purposes which includes particle filtration, liquid-gas/liquid separation or gas-separation. The ceramic material assures that the membranes are resistant to high temperatures whereas porous membranes based on polymeric materials are not. Futhermore, ceramic membranes also have higher chemical and mechanical stability than the polymeric membranes [3]. Apart from acting as a separating layer, where the difference in mass-transfer flux results in the separation of e.g. two gasses, the ceramic membranes can also be produced to include a supported catalyst. There are two types of such composite membranes: the porous catalytic membrane and the dense catalytic membrane. In the porous catalytic membrane, the membrane works as both a mass-transfer resistance and as a contacter between the reactant and the catalyst. This type of configuration can for instance be used to allow, what would otherwise be an explosive reaction to occur safely as the reactants are brought to the reaction-zone, due to the mass-transfer hindrance in the membrane. Another clear benifit is when the products have a higher permeation flux through the membrane, which can make equilibrium controlled reactions run at an even higher rate, due to Le Chatelier's principle. [4]. In the dense catalytic membrane a thin layer of usually metallic coating (e.g. Ag and Pd) is applied on top of a porous substrate, but also solid-oxide ionic conducting species such as modified zirconia or perovskites can be used. The dense layer is extremely selective in that it only allows for the permeation of a single species. The advantage of this is extremely selective membranes, but with a low permeation flux because solid-state diffusion is much lower than the Knudsen-type diffusion, which is usually the predominant type of mass-transfer in a the porous membrane [5].

Project goals

The scopes of this PhD project are mentioned here:

- Produce and characterize stabile (temperature, chemical and mechanically resistant) membranes with a well-defined thichkness and controllable pore-structure using the existing flame-pyrolysis equipment developed at the Aerosol Laboratory

- Generate porous and dense catalytically active membranes by using suitable methods (electroless deposition of Pd, co-combustion of precious metal-precursors and Mg/Al-precursors etc.)

- Test and compare these membranes against those mentioned in the litterature

Generation of nano-particles using flame-pyrolysis

Using the flame-pyrolysis equipment developed at the Aerosol Laboratory it has previously been shown that metal-oxide and precious metal-oxide particles, with a controllable size-distribution, can be produced [6]. Lately also composite oxides with an accurate stoichiometry such as $MgAl_2O_4$ spinel has been produced [2]. The equipment is shown schematically in figure 1.

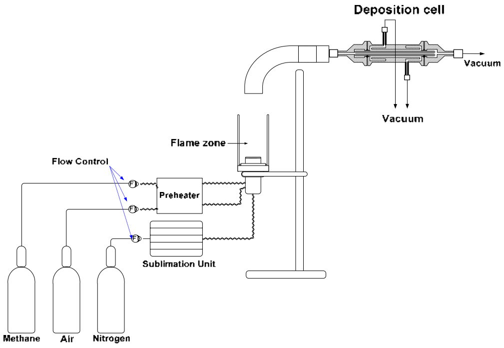

Figure 1: Nano-particle formation and deposition apparatus

A gas-stream of inert nitrogen is led through a heated saturator unit, where a metal-organic compound, in our case Metal-acetylacetonate (MeAcAc) is sublimated until the gas is saturated. The carrier gas is then led to a mixing chamber, where is it mixed with the fuel for the flame (air and methane/hydrogen). A flame arrestor accelerates the gas and assures that the flame-front is stable. In the flame the organic component (AcAc) is burned off and the metal part is oxided. The extreme super-saturation results in the nucleation metal-oxide moners and the formation particles. By adjusting the flame-temperature, saturator temperature and the carrier gas flow, one can control the particle size-distribution. The filtration experiments can now be carried out under constant pressure and the flow through the membrane is meassured on-line during the entire filtration, which allows for the calculation of the deposited mass (since the weight increase is too low to meassure directly).

Membrane formation

The Aerosol Laboratory has developed a simple method, where the particles generated in the flame are filtered off onto a porous substrate tube [1]. The particles form a "filter-cake" which constitutes a new membrane layer, with a much smaller pore size (nm) than the initial substrate pore-size (μm). One of the major concerns with this method is the adhesion of the deposited particles on the substrate tube. It is believed that a deposition at high-temperatures (+600°C) will give a good adhesion as well as a mechanically stable top-layer layer.

Membrane characterization

Because the deposited layer is very thin, the deposited pore-volume is very low. This means that traditional methods of characterization (Hg-porometry, BET meassurement etc.) can not be used. We have constructed an apparatus based on a method known as permporometry. The flux of oxygen is measured as a function of the open pore-size, which is controlled by a condensing a vapour such as cyclohexane. The relative pressure of cyclohexane (S) therefore determines the maximum size of the open pores. This size is directly expressed through the Kelvin-equation:

$$\ln S = -\frac{2\sigma}{r_k \rho_m RT} \tag{1}$$

where σ is the surface tension [N/m], ρ_m is the molar density [mole/m^3] and RT is the product of the temperature and the gas-constant [J/mole]. This apparatus is still under development. When the permporometry apparatus is fully functional the pore-size-distribution as well as the total pore-volume can be determined. The results combined with those of the filtration experiments will allow for the determination of a mean pore-diameter, top-layer porosity and top-layer thickness. All three are very important parameters as they determine the mass-transfer properties of this layer and the seperation properties of the new membrane.

Mathematical modelling

Apart from the goals mentioned in the project discription, the different mechanisms during the nano-particle filtration are also being looked into using mathematical modelling, as the knowledge of these mechanisms might increase the understanding of the final membrane properties.

References

[1] S.K. Andersen et al. *Journal of Nanoparticle research*, 4:405–416, 2002.

[2] M. Mosleh. *Preparation of Micro Porous Ceramic Membranes by Flame Generated Aerosol Nano-Particles.* PhD thesis, Technical University of Denmark, 2003.

[3] M. Mulder. *Basic Principles of Membrane Technology.* Kluwer Academic Publishers, second edition, 1996.

[4] J. Coronas et al. *Catalysis Today*, 51:377–389, 1999.

[5] J.G.S. Marcano and T.T. Tsotsis. *Catalytic Membranes and Membran Reactors.* Wiley-VCH, first edition, 2002.

[6] T. Johannessen. *Synthesis of Nano-particles in Flames.* PhD thesis, Technical University of Denmark, 1999.

Georgios K. Folas

Address: IVC-SEP Dept. of Chemical Engineering
Building 229
Technical University of Denmark
Phone: +45 4525 2869
Fax: +45 4588 2258
e-mail: gf@kt.dtu.dk
www: http://www.ivc-sep.kt.dtu.dk

Supervisors: Georgios M. Kontogeorgis
Michael L. Michelsen
Erling H. Stenby

Ph.D. Study
Started: November 2003
To be completed: October 2006

Modeling of Complex Mixtures Containing Hydrogen Bonding Molecules with the CPA EoS

Abstract

The Cubic-Plus-Association (CPA) equation of state has been successfully applied to different types of equilibria (vapor – liquid, liquid – liquid and solid – liquid) of industrially important binary mixtures of alcohol\glycol – water, alcohol – hydrocarbon and multicomponent mixtures of alcohol\glycol – water – hydrocarbon at various temperature and pressure conditions. The model can be successfully applied to binary mixtures of water-aromatic hydrocarbons, glycols – aromatic hydrocarbons and multicomponent mixtures of glycols – water – aromatic hydrocarbons, when adequately accounting for the solvation between water or glycols and the π electrons of the aromatic ring.

Introduction

The Cubic-Plus-Association (CPA) Equation of State (EoS) is a thermodynamic model which combines the well known Soave-Redlich-Kwong (SRK) EoS for describing the physical interactions with the Wertheim's first order perturbation theory, which can be applied to different types of hydrogen bonding compounds. The fact that the CPA model explicitly takes into account the interactions encountered in mixtures of associating compounds makes it applicable to multicomponent, multiphase equilibria for systems containing associating components. Mixtures of associating components, and in particular mixtures of water and alcohols or glycols with hydrocarbons, are of great interest to the oil and gas industry. Accurate description of such systems is a challenging problem of high technological importance for several petrochemical processes.

The model is recently extended to the solid-liquid equilibria of alcohol– hydrocarbon, alcohol/glycol–water systems including the modeling of the characteristic solid-complex phase which occurs at intermediate concentrations of MEG/methanol and to the multiphase equilibria of alcohol-water-alkane systems.

Another issue of great importance is the solubility of BTEX compounds (benzene, toluene, ethylbenzene, xylenes) in aqueous glycols due to the hydrocarbon emissions from glycol regeneration units, even if they are usually present at low concentrations in natural gas. However, reliable experimental data for glycols with aromatic hydrocarbons, and especially in the presence of water, are very scarce. Recently, experimental measurements were performed in collaboration with the R&D Centre of Statoil, regarding binary systems of MEG/TEG – BTEX compounds and ternary systems with water as the third compound, at various temperature conditions. The measured data in the R&D Centre of Statoil were correlated in the case of binary systems or predicted in the case of ternary systems with the CPA EoS in order to test the applicability of the model in systems with aromatic hydrocarbons.

Results

Figure 1 presents VLE/LLE/SLE correlation results of the binary system of methanol-cyclohexane using a common interaction parameter k_{12}= 0.04, while figure 2 demonstrates the ability of the model to satisfactorily calculate the VLE of ethanol-water system with a common interaction parameter k_{12}= -0.11 over an extended temperature and pressure range.

Figure 3 presents SLE of MEG-water system included the solid-complex phase. CPA with a single interaction parameter k_{12}= -0.115 provides a correlation of both freezing curves over a temperature range of more than 50K. The characteristic solid-complex phase which is formed at intermediate concentrations of MEG mole fraction is modeled using a simple chemical reaction model.

Figure 4 presents VLLE of water-ethylbenzene system over an extended temperature and pressure range with the CPA EoS and temperature independent interaction parameters. An extra parameter *BETCR* is used (in addition to the binary interaction parameter k_{12}) in order to account for the solvation between water and the aromatic hydrocarbon.

Figure 5 presents LLE of MEG-toluene system over an extended temperature and pressure range with the CPA EoS. A comparison to the LLE of MEG-heptane shows the increased solubilities due to the hydrogen bonding between MEG and the aromaric hydrocarbon compared to the aliphatic one with the same number of carbon atoms.

Finally figure 6 presents prediction results for the multicomponent DEG – water – benzene system based solely on binary interaction parameters.

Conclusions

Work in the project so far has demonstrated that the CPA equation of state is able to handle many systems of interest to the oil and gas processing industry. These systems contain a wide-ranging array of different fluid types, including highly associating fluids such as acetic acid, over a range of temperatures and pressures and including phase equilibrium between vapour, liquid and solid phases depending on the conditions of interest.

Acknowledgements

The author gratefully acknowledges Statoil for the financial support of this work and especially the R&D Centre in Trondheim, Norway, where the experimental work of the project was performed, for providing all the necessary facilities.

List of Abbreviations

DEG	diethylene glycol
EoS	equation of state
LLE	liquid-liquid equilibria
MEG	(mono)ethylene glycol
SLE	solid-liquid equilibria
TEG	triethylene glycol
VLE	vapour – liquid equilibria
VLLE	vapor-liquid-liquid equilibria

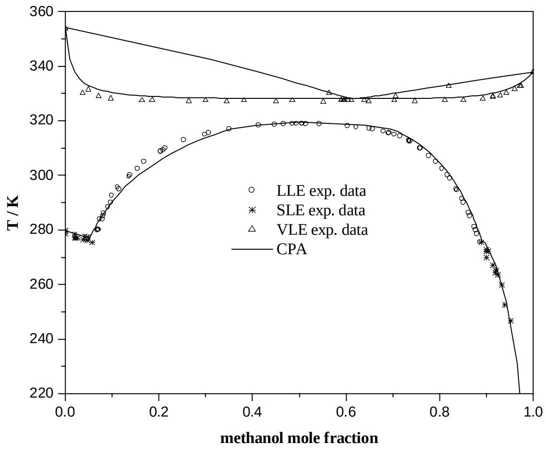

Figure 1. VLE, LLE and SLE in the system methanol-cyclohexane using a single binary interaction parameter over the whole range.

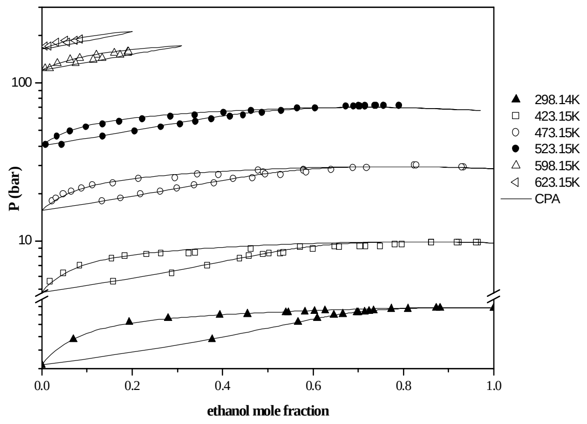

Figure 2. VLE in the system ethanol – water.

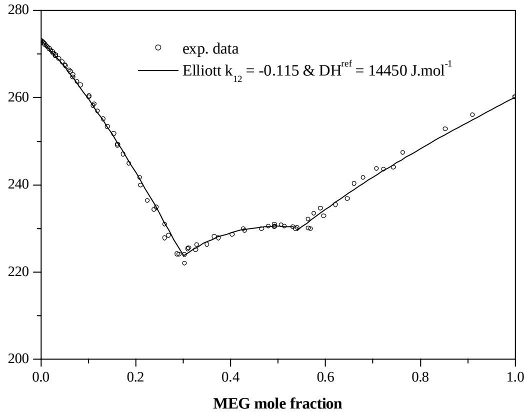

Figure 3. SLE in the system (MEG)-water, including the hydrate region. The two branches of the SLE are captured by the model. The hydrate phase that forms in the range 0.3 to 0.6 mole fraction MEG is modeled using a simple chemical reaction model.

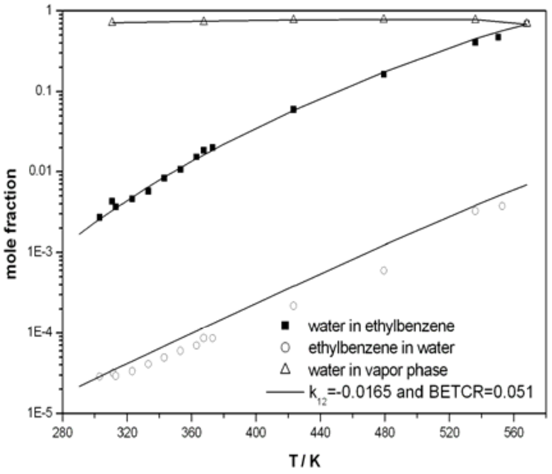

Figure 4. VLLE of water – ethylbenzene system with the CPA EoS.

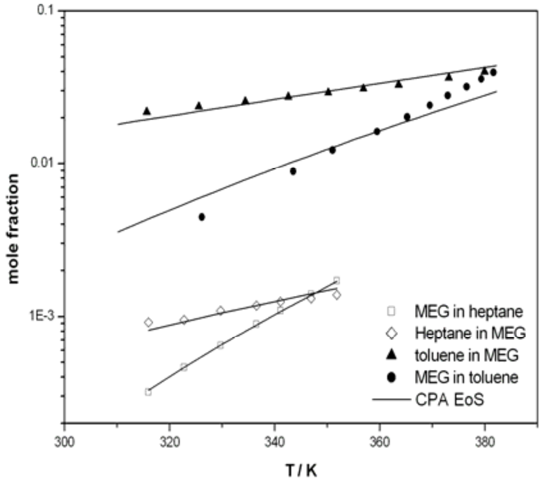

Figure 5. LLE correlation of MEG – toluene (k_{12}=0.055, BETCR=0.045) and MEG-heptane (k_{12}=0.031) systems.

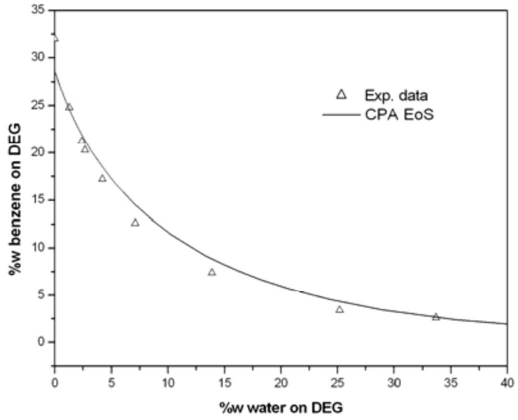

Figure 6. Prediction of %wt of benzene as a function of %wt of water on DEG.

List of Publications

1. Folas, G.K.; Derawi, S.O.; Michelsen, M.L.; Stenby, E.H.; Kontogeorgis, G.M. Recent applications of the Cubic – Plus – Association (CPA) equation of state to industrially important systems. *Fluid Phase Equilib.* **2005,** *228-229,* 121.
2. Folas, G.K.; Gabrielsen, J.; Michelsen, M.L.; Stenby, E.H.; Kontogeorgis, G.M. Application of cubic - plus – association (CPA) Equation of State to cross – associating systems. *Ind. Eng. Chem. Res.* **2005,** *44,* 3823.
3. Folas G.K.; Michelsen M.L.; Stenby E.H.; Kontogeorgis G.M. Application of cubic – plus – association (CPA) Equation of State to complex mixtures with aromatic hydrocarbons, submitted for publication to Ind. Eng. Chem. Res.
4. Folas G.K.; Michelsen M.L.; Stenby E.H.; Kontogeorgis G.M. Application of cubic – plus – association (CPA) Equation of State to mixtures with polar chemicals and high pressures, submitted for publication to Ind. Eng. Chem. Res.
5. Folas G.K.; Michelsen M.L.; Stenby E.H.; Kontogeorgis G.M.; Solbraa, E. Liquid-liquid equilibria for binary and ternary systems containing glycols, aromatic hydrocarbons and water. Experimental measurements and modeling with the CPA EoS, submitted for publication to J. Chem. Eng. Data.
6. Kontogeorgis G.M.; Michelsen M.L.; Folas G.K.; Derawi, S.O.; von Solms, N.; Stenby E.H. Ten years with the CPA (Cubic-Plus-Association) equation of state. Part I. Pure compounds and Self-associating systems, submitted for publication to Ind. Eng. Chem. Res.
7. Kontogeorgis G.M.; Michelsen M.L.; Folas G.K.; Derawi, S.O.; von Solms, N.; Stenby E.H. Ten years with the CPA (Cubic-Plus-Association) equation of state. Part II. Cross-associating and multicomponent systems, submitted for publication to Ind. Eng. Chem. Res.

Philip Loldrup Fosbøl

Address: IVC-SEP, Dept. of Chemical Engineering
Building 229, office 206
Technical University of Denmark
Phone: +45 4525 2868
Fax: +45 4588 2258
e-mail: plf@kt.dtu.dk
www: http://www.ivc-sep.kt.dtu.dk/staff/PLF/

Supervisors: Kaj Thomsen
Professor Erling H. Stenby
Kim Rasmussen, Mærsk Oil and Gas A/S

Ph.D. Study
Started: February 2004
To be completed: January 2007

Corrosion in Wet Gas Pipelines - Mixed Solvent Electrolytes

Abstract

Natural gas contains small amounts of CO_2. Produced natural gas is saturated with water (wet gas) and it condenses at the cold pipe wall during transportation. NaOH and glycol or methanol is injected to prevent gas hydrates and corrosion. CO_2 dissolves in the water-Glycol (MEG)-NaOH liquid phase mixture at the bottom of the pipeline. The electrolytic environment will corrode the lower peripheral part of the pipeline. Various protective corrosion products are produced, depending on the chemical environment. An equilibrium model of the corrosion products is being built using the extended UNIQUAC model. The model will be expanded to include diffusion and reaction at the surface of the pipe-wall to get an understanding of the mechanism behind CO_2 corrosion.

Introduction

Maintenance and repair cost from corrosion of process equipment is unbelievably immense. CoorrosionCost.com estimate that $276 billion dollars/year is lost and spend in relation to corrosion just in the US. 12 $billion dollars/year of those are related directly to the transportation line of the oil and gas industry [1]. The pipelines which are in focus of this study transport on average 4million m^3 natural gas/day it is very clear that a potential breakdown may ruin any economy relatively fast.

Corrosion problems are observed both on rigs and sub-sea. Unfortunately the companies most often deal with the problems as they arise, instead of using know-how to understand and prevent potential problems.

The literature has dealt with CO_2 corrosion since before the start of oil production. Through the recent years some significant advances has been made on a correct description of the CO_2 corrosion mechanism, [2-4].

Two types of corrosion is typically seen: Pitting and general corrosion. Pitting are small holes created by iron dissolution caused by flow phenomena and local acidification. Pitting is very stochastic and depends on many more parameters than just chemical effects.

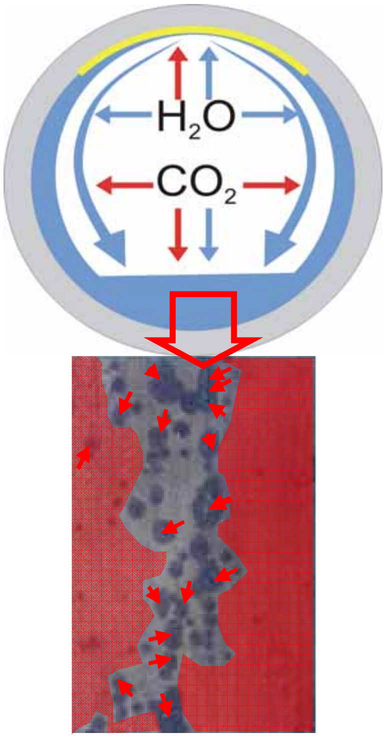

Figure 1: The figure shows an inner part of a pipeline. The dots marked by arrows are corrosion due to pitting. The remaining marked area has general corrosion.

General corrosion is caused by a mechanism similar to pitting but distributed on the whole area of the lower part of the pipelines. Figure 1 illustrates the two types of corrosion. Pitting is generally seen as a track of spots in the pipe bottom. General corrosion is typically seen on the wet surfaces where water may transport iron away.

Specific objectives

The aim of this study is to extend the present understanding of CO_2 corrosion by using the extended UNIQUAC model to describe phase equilibria of the CO_2-NaOH-H_2O-Inhibitor system. The activity coefficient model will be used for modeling corrosion.

CO_2 corrosion is the main part of this study. The first phase of this study was used for making an extended literature study on existing knowledge of CO_2 corrosion. The study has, besides other things, shown that scale formation of corrosion products is one of the important factors in determining corrosion. $FeCO_3(s)$ scale and its solubility is linked to the corrosion rate. At the moment UNIQUAC parameters are being regressed to 6 types of data for the system Na^+-MEG-H_2O-CO_2:

- Binary and ternary Solubility data
- PTx data
- Freezing point depression
- Heat of solution
- Heat excess
- Heat capacity

It will be shown which chemical factors control the dissolution of $FeCO_3(s)$ at equilibrium. The further goal will be to link the model into an extended model of electrochemistry and diffusion which takes care of diffusion of $CO_2(aq)$ to the steel surface and surface reaction at the steel.

Results and discussion

Mixed solvent electrolyte system

Figure 2 shows the important layers next to the pipe wall. The bulk phase contains the aqueous phase of NaOH and dissolved $CO_2(aq)$ plus inhibitor of mono ethylene glycol (MEG).

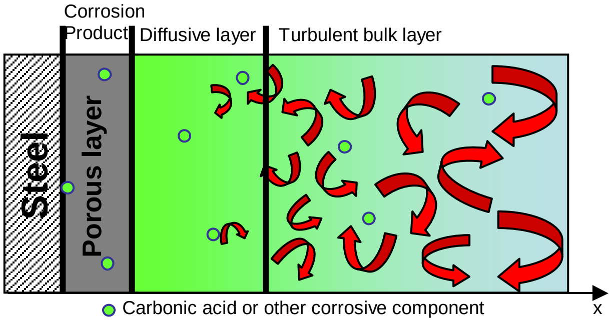

Figure 2: The figure shows the bulk phase containing corrosive species. They diffuse to the steel through a porous corrosion product layer, where they are reduced to corrosion products.

The bulk phase is very non-ideal. Often the ionic strength is above 1 and it is very important to apply a thermodynamic model to describe the activities in the liquid phase. The reaction scheme of the electrolytic phase is given by:

$$H_2O(g) \rightleftarrows H_2O(l) \tag{1}$$

$$CO_2(g) + H_2O(l) \rightleftarrows H_2CO_3(aq) \tag{2}$$

$$H_2CO_3(aq) \rightleftarrows H^+ + HCO_3^- \tag{3}$$

$$HCO_3^- \rightleftarrows H^+ + CO_3^{2-} \tag{4}$$

$$H_2O(l) \rightleftarrows H^+ + OH^- \tag{5}$$

$$Na_2CO_3(s) \rightleftarrows 2Na^+ + CO_3^{2-} \tag{6}$$

$$Na_2CO_3{\cdot}H_2O(s) \rightleftarrows 2Na^+ + CO_3^{2-} + H_2O \tag{7}$$

$$\begin{aligned}&Na_2CO_3{\cdot}NaHCO_3.2H_2O(s) \rightleftarrows \\ &3Na^+ + CO_3^{2-} + HCO_3^- + 2H_2O\end{aligned} \tag{8}$$

$$Na_2CO_3{\cdot}3NaHCO_3(s) \rightleftarrows 5Na^+ + CO_3^{2-} + 3HCO_3^- \tag{9}$$

The scheme is very complicated because HCO_3^- and CO_3^{2-} are linked through the equilibrium of carbonic acid. It includes both the heterogeneous equilibrium of VLE ((1)-(2)) and SLE ((6)-(9)) and homogeneous reactions in the liquid phase ((3)-(5)). In the system of $NaHCO_3$-Na_2CO_3-H_2O-MEG several different phases may possibly precipitate. The binary solubility of $NaHCO_3(s)$ in the mixed solvent of MEG-H_2O is shown in figure 3.

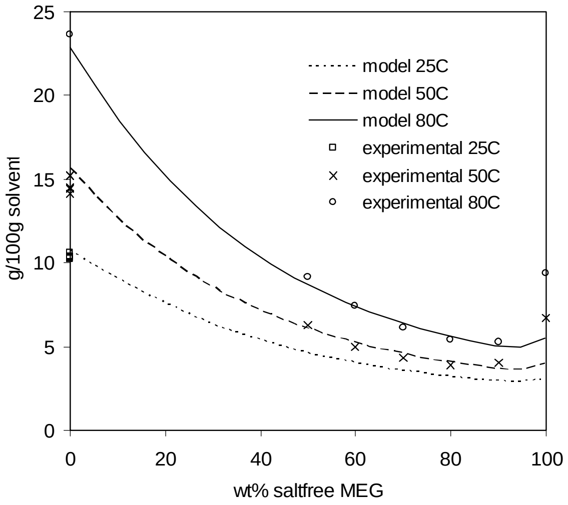

Figure 3: shows solubility in the system of $NaHCO_3$-H_2O-MEG. Lines are modeled using the extended UNIQUAC.

The data were taken from the work by Gärtner, [5]. Data of mixed solvent systems are generally very sparse and often inaccurate. Luckily the glycol system is related to a patent pending method and has therefore been studied. The lines are drawn by fitting the extended UNIQUAC model to heat data, VLE and SLE data. Model details may be found in [6]. The steep increase of the solubility of $NaHCO_3$ in pure MEG has not been included in the fitting process and may be erroneous. The figure shows a high solubility in pure water to the left and a salting out effect of $NaHCO_3$ the more MEG is added to the system.

A similar graph is shown in figure 4 for the solubility of Na_2CO_3 in the system with mixed solvent of MEG-H_2O. Data were taken from [5,7]. This system is much more complicated than the corresponding diagram for the solubility of $NaHCO_3$. The lines are drawn using the extended UNIQUAC model. The dotted lines near pure MEG signify that pure, anhydrous Na_2CO_3 precipitates. The full lines signify precipitation of the mono hydrate, $Na_2CO_3.H_2O$. A small offset is observed at pure water. This may be due to NIST standard thermodynamic data tables have been used as a basis. It may be corrected at a later point by fitting the Gibbs energy of the monohydrate.

A plot of freezing point depression not included here shows that the SLE at low temperatures can be modeled very accurately.

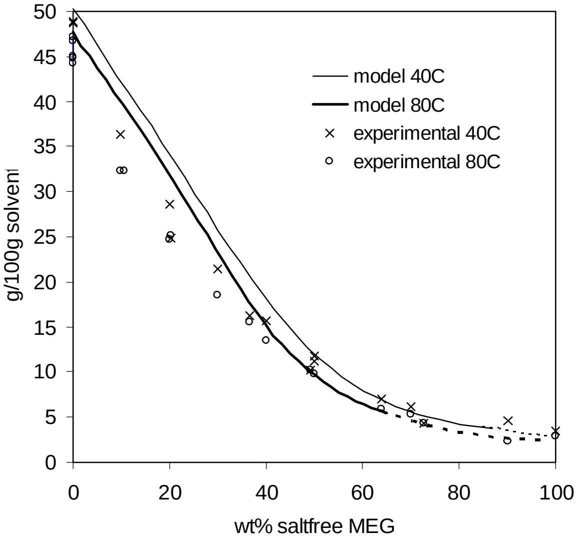

Figure 4: shows solubility in the system of Na_2CO_3-H_2O-MEG. Lines are modeled using the extended UNIQUAC and gives precipitation of $Na_2CO_3.H_2O$. Dotted lines signify precipitation of pure, anhydrous Na_2CO_3.

Figure 5 shows that the regressed parameters are consistent and that the model may also be used for describing the VLE. It is assumed that the vapor-phase consist only of water vapor. Data were taken from [8-11].

The more diverse thermodynamic data that are included in the model, the better basis the parameters have and the easier the fitting process is. Figure 6 shows that the model will even reproduce heat excess data to an acceptable degree at least within the extreme scatter of the data.

A diffusion model of CO_2 corrosion

The corrosive $H_2CO_3(aq)$ will diffuse from the bulk phase to the surface by transportation through a thin stagnant liquid film followed by diffusion through a porous corrosion product layer, see figure 2. A simple steady sate diffusion model may be set up for both diffusion schemes from Ficks law:

$$0 = D_{eff,i}\frac{d^2c_i}{dx^2} \tag{10}$$

$$0 = D_{eff,porous,i}\frac{d^2c_i}{dx^2} \tag{11}$$

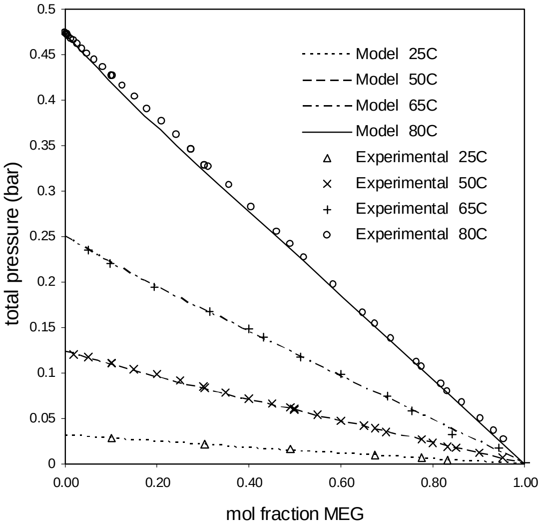

Figure 5: PTx phase diagram of the system MEG-H_2O modeled using the extended UNIQUAC model.

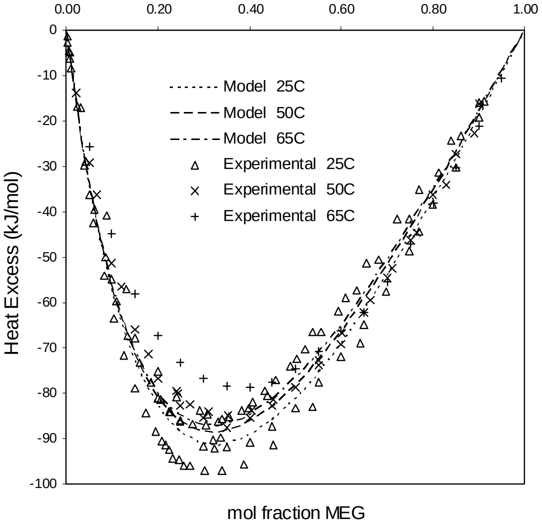

Figure 6: ΔH^E of the system MEG-H_2O modeled using the extended UNIQUAC model. Data taken from [12-17]

$D_{eff,porous,i}$ and $D_{eff,i}$ are linked through the porosity, ϕ, and the tortuosity, τ, by $D_{eff,porous,i} = D_{eff,i}\phi/\tau^2$. The effective diffusion coefficient are relation to the friction coefficient, D_i, by $D_{eff,i} = D_i\phi/\tau^2\left(1+d\gamma_i/dm_i\right)$ through an activity coefficient model like the extended UNIQUAC. It is important to stress that the diffusion coefficients are normally not dependent on the concentrations. But at ionic strengths of 1 and higher this becomes significant [18].

When H_2CO_3 reaches the surface it will react by the cathodic surface redox reaction:

$$H_2CO_3 + e^- \rightleftharpoons ½H_2 + HCO_3^- \tag{12}$$

The only way this reaction will run is if electrons are produced by another reaction. The dissolution of iron produces electrons and the cycle is complete:

$$Fe(s) \rightleftharpoons Fe^{2+}(aq) + 2e^- \tag{13}$$

A Volmer-Butler model [1,18] will be used for explicitly describing the amount of produced electrons. This model requires the surface concentration which is calculated from the diffusion model. The Volmer-Butler model becomes a natural boundary condition for the diffusion model together with the bulk composition. The model will show the dissolution rate of iron through reaction (13) and faradays law.

Getting real

Wet gas is moved from wells to platforms through 16” (40.6 cm) pipelines, at long distances (11km). There is a level difference from the inlet to the outlet of approximately 10 meters which causes problems with respect to general liquid holdup and local accumulation. Due to the small slope and high temperature of the pipe, high corrosion is seen in the first part of the pipeline just after the inlet.

Pipe	T(^{o}C)	P(barg)	L(m^3/day)
Inlet	45	Approx. 65	2.3
Outlet	23	Inlet P minus 5bar	6.5

The table shows how temperature, pressure and liquid phase flow varies from the inlet to the outlet. The temperature does not fall significantly in the pipeline. It means that liquid holdup is the controlling factor of corrosion. The column L in the table is the liquid phase flow. L is not zero in the inlet due to injection of a small liquid phase of Glycol and pH-stabilizer. The build up comes from condensation of water from the gas phase.

The amount of water in the inlet gas phase is very small, contributing with 0,1bar of the total pressure. Still it is one of the most significant factors controlling CO_2 corrosion. CO_2(g) is injected with a partial pressure of approximately 1bar and the CO_2(g) flow is much higher than liquid flow, up to volumetrically 130 times greater than the liquid flow. This way the gas phase acts as a storage of CO_2(g) to be dissolved in the liquid phase.

Conclusion

Corrosion can be avoided by planning and being alert at the production site. It is important always to have an understanding of the chemicals. This project will expand the understanding of CO_2 corrosion. The work shows the phase equilibria of the observed systems and the produced models will be used for making an extended CO_2 corrosion model.

Acknowledgement

I would like to thank Kaj Thomsen for his support in my studies and to Kim Rasmussen, Mærsk, for providing production data.

References

1. CorrosionCost.com: http://www.corrosioncost.com/infrastructure/gasliquid/index.htm
2. Nordsveen M, Nesic S, Nyborg R, et al., Corrosion 59 (5): 443-456, 2003
3. Nesic S, Nordsveen M, Nyborg R, et al., Corrosion 59 (6): 489-497, 2003
4. Nesic S, Lee KLJ, Corrosion 59 (7): 616-628, 2003
5. Gärtner RS, Seckler MM, Witkamp GJ, Journal Of Chemical And Engineering Data 49(1): 116-125, 2004
6. M.Iliuta, K.Thomsen, P.Rasmussen, Chemical Engineering Science 55: 2673-2686, 2000
7. Oosterhof H, Witkamp GJ, van Rosmalen GM. Fluid Phase Equilibria 155(2): 219-227, 1999
8. Gonzalez, C.; Van Ness, H. C. Journal Of Chemical And Engineering Data 28: 410, 1983
9. Horstmann, Sven; Gardeler, Hergen; et al., Journal of Chemical and Engineering Data 49(6): 1508-1511, 2004.
10. Nath A, Bender E., Journal Of Chemical And Engineering Data 28 (4): 370-375 1983.
11. Mokbel, I.; Porcedda, S.; Guetachew, T.; Marongiu, B.; Jose, J., The International Electronic Journal of Physico-Chemical Data, Eldata 5(2): 79-84. 1999
12. Miguel A. Villamanan, Carlos Gonzalez, Hendrick C. Van Ness, Journal of Chemical and Engineering Data 29(4): 427-429, 1984.
13. Kracht C, Ulbig P, Schulz S, Journal Of Chemical Thermodynamics 31 (9): 1113-1127, 1999
14. Matsumoto, Y.; Touhara, H.; Nakanishi, K.; Watanabe, N., Journal of Chemical Thermodynamics 9(8): 801-5, 1977
15. Dohnal, Vladimir; Roux, Alain H.; Hynek, Vladimir., Journal of Solution Chemistry 23(8): 889-900, 1994
16. Arroyo Gallego, A., Anales de Quimica, Serie A: Quimica Fisica e Ingenieria Quimica 84(2): 179-82, 1988.
17. Biros, Jan; Pouchly, Julius; Zivny, Antonin., Makromolekulare Chemie 188(2): 379-94, 1987
18. J. Newman: “Electrochemical systems”, John Wiley & Sons, 2004

Jostein Gabrielsen
Address: IVC-SEP Dept. of Chemical Engineering
Building 229
Technical University of Denmark
Phone: +45 4525 2869
Fax: +45 4588 2258
e-mail: jog@kt.dtu.dk
www: http://www.ivc-sep.dtu.dk

Supervisors: Georgios M. Kontogeorgis
Michael L. Michelsen
Erling H. Stenby

Ph.D. Study
Started: November 2003
To be completed: October 2006

CO_2 Capture from Coal Fired Power Plants

Abstract

Carbon dioxide (CO_2) solubility in aqueous solutions of monoethanolamine (MEA) has been correlated using a simple approach where only one chemical equilibrium reaction is taken into account, and assuming ideal gas and ideal liquid properties. The approach combines the Henry's law constant and the chemical reaction equilibrium constant for the formation of carbamate for primary alkanolamines, resulting in an explicit expression for calculating the partial pressure of CO_2 over an aqueous MEA solution. Accurate values for the solubility of CO_2 are obtained for a limited loading-, temperature-, and pressure range which is useful in modelling CO_2 capture from coal fired power plants. A rate-based steady-state model for CO_2 absorption into an MEA solution has been proposed, utilizing both the proposed expression for the CO_2 solubility and the calculated values of the heat of absorption along with an expression for the enhancement factor and physicochemical data from the literature. The proposed model has successfully been applied to absorption of CO_2 into an MEA solution in a packed tower, validated against pilot plant data from the literature.

Introduction

Approximately one third of all CO_2 emissions from human activity come from generating electricity. Therefore CO_2 capture and storage from fossil fuel power plants present an opportunity to achieve large reductions in greenhouse gas emissions without having to change the energy supply infrastructure and without having to make large changes to the basic process of producing electricity.

CO_2 capture from process streams is an established concept which has achieved industrial practice. There are different process schemes for integrating CO_2 capture with combustion available including pre-, post-, and oxyfuel-combustion. The focus of our work is on post-combustion capture which means that CO_2 is removed from the flue gas; therefore the combustion process is not directly affected. However, energy for the CO_2 removal is taken from the power process, thus lowering the net efficiency of the power production.

There are several techniques for CO_2 capture from process gas streams, of which chemical absorption using alkanolamines in a packed absorption tower is the most commonly used. The technology is currently widely used, though for applications of a scale much smaller than power plant flue gas cleaning. A bottleneck in the process of capturing CO_2 from flue gases with aqueous alkanolamines is the large amount of energy needed to regenerate the absorption liquid which in turn decreases the efficiency of the power plant dramatically. Efficiency reduction for coal fired power plants lies in the range of 7 to 12 %, depending on the alkanolamine and the packing of the absorption tower, which gives a relative decrease in efficiency in the range from 15 to 22 % (Lyngfelt et al.) [1]. The largest contribution to the efficiency decrease originates in the energy needed in the desorption of CO_2.

The focus of our work is to contribute to the modeling and simulation of both the absorption and desorption of CO_2 in aqueous alkanolamines in order to develop reliable tools for the design and optimization of the process. The system is very complex due to the fact that it contains weak electrolytes. Among the key parameters in the design process are the thermodynamics associated with the phase equilibria of systems containing CO_2-water-alkanolamines, the kinetics of the chemical reactions involved and the mass transfer in the system.

A simple thermodynamic model for MEA

To be able to develop more efficient processes for the separation of acid gases from flue gases, thermodynamic modeling of the vapor-liquid phase equilibrium is the first step. Most thermodynamic models used to represent the vapor-liquid equilibria of CO_2 in an aqueous solution of alkanolamines are very complex and require a large amount of adjustable parameters. This is due to the fact that the alkanolamines are weak electrolytes and chemical reactions between alkanolamine and CO_2 occur in the liquid phase. Another problem concerning the representation of the vapor-liquid equilibria is that the experimental data existing are not always plentiful and reliable. There is a large scattering particularly at low partial pressures and loadings. In this work a very simple model has been developed for representing the VLE of aqueous alkanolamine solutions. The chemical equilibrium taking place in the liquid phase when CO_2 is absorbed in an aqueous solution of MEA (monoethanolamine) can be written with the following equilibrium equations:

$$2H_2O \rightleftharpoons H_3O^+ + OH^-$$

$$CO_2 + 2H_2O \rightleftharpoons H_3O^+ + HCO_3^-$$

$$HCO_3^- + H_2O \rightleftharpoons H_3O^+ + CO_3^{2-}$$

$$MEAH^+ + H_2O \rightleftharpoons H_3O^+ + MEA$$

$$MEACOO^- + H_2O \rightleftharpoons MEA + HCO_3^-$$

The reaction of CO_2 with aqueous MEA can, given that the loading (moles of dissolved CO_2/moles of alkanolamine) is in the region between 0.02 and 0.48, be approximated by a single chemical equilibrium reaction (1) Astarita [2].

$$MEAH^+ + MEACOO^- \rightleftharpoons 2MEA + CO_2(aq.) \quad (1)$$

Equation (1) neglects the presence of bicarbonate (HCO_3^+), hydroxide (OH^-), and carbonate (CO_3^{2-}) ions since the concentration of these ions will be very small in the region of loading which of interest to describe in CO_2 capture from power plants fired with fossil fuels. The concentration of the species involved in the chemical reaction can be written in the following manner:

$$[MEA] = (1-2\theta)a_0$$

$$\left[MEAH^+\right] = \left[MEACOO^-\right] = \theta a_0$$

$$\left[CO_3^{2-}\right] \cong \left[HCO_3^-\right] \cong 0$$

The expression for the partial pressure of CO_2 can now be written as shown in equation (2).

$$p^*_{CO_2} = K_{CO_2} X_{CO_2} \frac{a_0\theta}{\left(a_0(1-2\theta)\right)^2} \quad (2)$$

Where the combined equilibrium – and Henry's law constant is given by equation (3):

$$\ln K_{CO_2} = A + \frac{B}{T} + Ca_0\theta \quad (3)$$

A, B and C are all parameters that have to be regressed from experimental data. Some calculations are shown in figure 1.

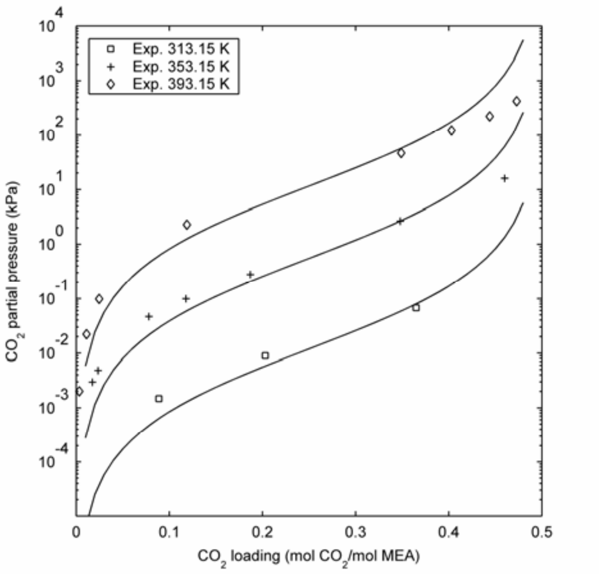

Figure 1 Comparison of model correlation results (solid lines) with experimental data for CO_2 equilibrium partial pressures over an aqueous 30 wt % MEA solution.

Furthermore by using the Gibbs-Helmholtz equation the heat of absorption of CO_2 in the MEA solution (ΔH_{CO_2}) is found to be -87990 J/mol CO_2.

Packed Column Model

Due to the nature of the process a rate based model is chosen, and since it is a packed column differential mass and energy balances are set up. The model in this work is based on the model developed by Pandya [3] where the process is described by the two film theory and utilization of the assumptions 1-7:

1. The reaction is fast enough to take place in the liquid film and the bulk of the liquid is in equilibrium.
2. Liquid side heat transfer resistance is small compared to the gas phase, thus the interface temperature is the same as the bulk temperature.
3. The liquid side mass transfer resistance for the volatile solvent is negligible.
4. The interfacial surface area is the same for heat and mass transfer.
5. Axial dispersion is not accounted for.
6. The absorption tower is considered to be adiabatic.
7. Both the liquid phase and the gas phase are assumed to be ideal.

The following system of differential equations can be set up for the packed column based on mole and energy balances on a differential section, solving for eight variables including mole flow, mole fraction of water and CO_2, and temperature in both phases.

$$\frac{dG}{dz} = -\left(N_{CO_2} + N_{H_2O}\right) aA_c$$

$$\frac{dy_{CO_2}}{dz} = \frac{N_{CO_2} aA_C \left(y_{CO_2} - 1\right) + N_{H_2O} y_{CO_2} aA_c}{G}$$

$$\frac{dy_{H_2O}}{dz} = \frac{N_{H_2O} aA_C \left(y_{H_2O} - 1\right) + N_{CO_2} y_{H_2O} aA_c}{G}$$

$$\frac{dL}{dz} = -N_{H_2O} aA_c$$

$$\frac{dX_{CO_2}}{dz} = \frac{\left(N_{H_2O} X_{CO_2} - N_{CO_2}\right) aA_C}{L}$$

$$\frac{dx_{H_2O}}{dz} = \frac{N_{H_2O}\left(x_{H_2O} - 1\right) aA_C}{L}$$

$$\frac{dT_G}{dz} = \frac{\left(N_{CO_2} + N_{H_2O}\right) aA_c T_G}{G} - \frac{\left(N_{CO_2} c_{p,CO_2} + N_{H_2O} c_{p,H_2O}\right) aA_c T_G}{Gc_{p,G}} - \frac{q}{Gc_{p,G}}$$

$$\frac{dT_L}{dz} = \frac{N_{H_2O} aA_c T_L}{L} - \frac{\left(N_{CO_2} c_{p,CO_2} + N_{H_2O} c_{p,H_2O}\right) aA_c T_G}{Lc_{p,L}} - \frac{q}{Lc_{p,l}} - \frac{\left(N_{CO_2} \Delta H_{CO_2} + N_{H_2O} \Delta H_{H_2O}\right)}{Lc_{p,l}}$$

The resulting boundary value problem is solved in Matlab 7.0 using a built in routine called *bvp4c* which implements a collocation method for the solution of boundary value problems. The boundary values needed are given by the conditions of the gas and liquid entering the column. All physicochemical data needed in the model is found in the literature. To verify the model it is compared with published pilot plant data. In figures 2 and 3 experimental data form Tontiwachwuthikul et al. [4]. are compared with the proposed model.

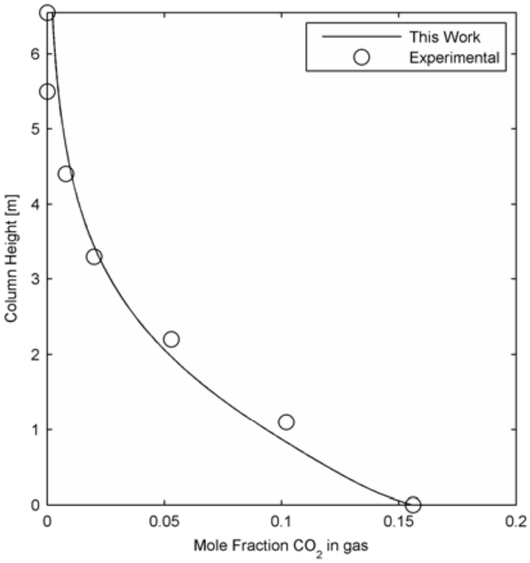

Figure 2 Concentration profiles for CO_2 in the gas phase in the MEA-CO_2 system. Modeled (line) results and experimental data (circles)

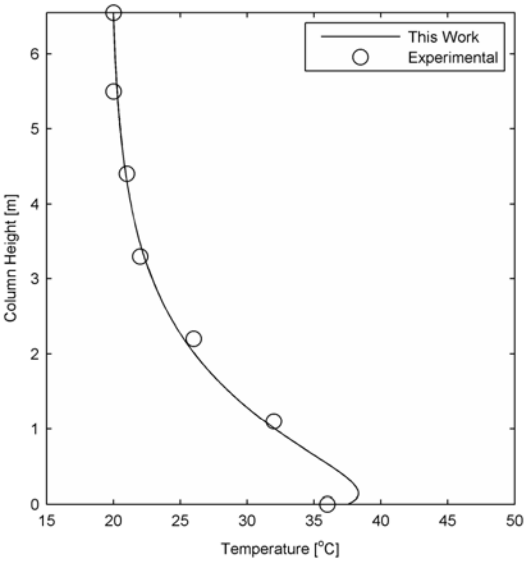

Figure 3 Temperature profiles for the liquid phase in the MEA-CO_2 system. Modeled (line) results and experimental data (circles)

As it can be seen the proposed model gives a better representation of both the CO_2 concentration in the gas phase and temperature in the liquid phase along the column.

Acknowledgements

The author gratefully acknowledges Nordic Energy Research for the financial support of this work.

List of symbols

a = specific wetted area for mass transfer, m^2 / m^3
$a_0 = \text{initial concentration of amine} = \frac{\text{amine}}{\text{amine+H}_2\text{O}}$
A_C = cross sectional area of the column, m^2
$c_{p,i}$ = molar heat capacity of component i in the gas phase, $J/mol \cdot K$
$c_{p,L}$ = molar heat capacity of the liquid, $J/mol \cdot K$
G = molar gas flow, mol/s
h = heat transfer coefficient in gas, $J/s \cdot K \cdot m^2$
H_{CO_2} = Henry's Law Constant for CO_2, $Pa \cdot m^3/mol$
ΔH_{H_2O} = heat of condensation of H_2O, J/mol
ΔH_{CO_2} = heat of absorption of CO_2, J/mol CO_2
K_{CO_2} = combined Henry's law and chemical equilibrium constant for CO_2 partial pressure, Pa
L = molar liquid flow, mol/s
N_i= Molar flux of component i, $mol/m^2 \cdot s$
p_i = partial pressure of component i in the bulk gas phase, Pa
p_i^* = partial pressure of component i gas phase if it were in equilibrium with the liquid phase, Pa
q= heat flux, $J/m^2 \cdot s$
T_L = liquid phase temperature, K
T_G = gas phase temperature, K
x_i = liquid phase mole fraction of component i, mol/mol
X_{CO_2} = liquid phase mole fraction of CO_2 in both reacted and unreacted form, mol/mol
y_i = gas phase mole fraction of component i, mol/mol
z = height of packing, m
$\theta = \text{loading} = \frac{\text{mole CO}_2}{\text{mole amine}}$

References

1. Lyngfelt, A., & Leckner, B. Technologies for CO_2 separation, Second Nordic Minisynopsium on Carbon Dioxide Capture and Storage. Göteborg, 2001
2. Astarita G., Mass transfer with chemical reactions, Elsevier Publishing Company, Amsterdam/London/New York, 1967

3. Pandya, JD. Adiabatic Gas Absorption and Stripping with Chemical Reaction in Packed Towers. Chem. Eng. Comm. 19 (1983) 343-361.
4. Tontiwachwuthikul P, Meisen A, Lim CJ. CO_2 Absorption by NaOH, Monoethanolamine and 2-Amino-2-Methyl-1-Propanol Solutions in a Packed Column. Chem Eng Sci. 47 (1992) 381-390.

List of Publications

1. J. Gabrielsen, M.L. Michelsen, E.H. Stenby, G.M. Kontogeorgis, A Model for Estimating CO_2 Solubility in Aqueous Alkanolamines Ind. Eng. Chem. Res. 44 (2005) 3348-3354.
2. G.K. Folas, J. Gabrielsen, M.L. Michelsen, E.H. Stenby, G.M. Kontogeorgis, Application of the Cubic-Plus-Association (CPA) Equation of State to Cross-Associating Systems Ind. Eng. Chem. Res. 44 (2005) 3823-3833.
3. J. Gabrielsen, M.L. Michelsen, E.H. Stenby, G.M. Kontogeorgis, Modelling of CO_2 Absorber Using a Sterically Hindered Alkanolamine Solution (submitted for publication)

Brian Brun Hansen
Address: CHEC
Department of Chemical Engineering
Building 227, Office 131
Technical University of Denmark
Phone: +45 4525 2829
Fax: +45 4588 2258
e-mail: bbh@kt.dtu.dk
www: http://www.chec.dtu.dk

Supervisors: Søren Zinck Kiil
Jan Erik Johnsson

Ph.D. Study
Started: March 2005
To be completed: April 2008

Gypsum Crystallisation and Foaming Prevention in Wet Flue Gas Desulphurisation (FGD) Plants

Abstract

An investigation of the crystallisation of gypsum and the unexpected occurrence of foaming in wet FGD plants will be performed. Experimental result from a pilot scale setup will be used to validate models describing the particle size distribution (PSD) of the gypsum crystals. Methods to control foaming in wet FGD plants will furthermore be assessed. The obtained knowledge will be used to point towards methods to optimize the operation of wet FGD plants

Introduction

A substantial part of the worlds present energy demand is based on the combustion of fossil fuels, such as coal, oil and gas. Despite increasing interest in alternative fuel sources, the combustion of fossil fuels is expected to continue to yield a significant part of the world's energy demand in the future (figure 1).

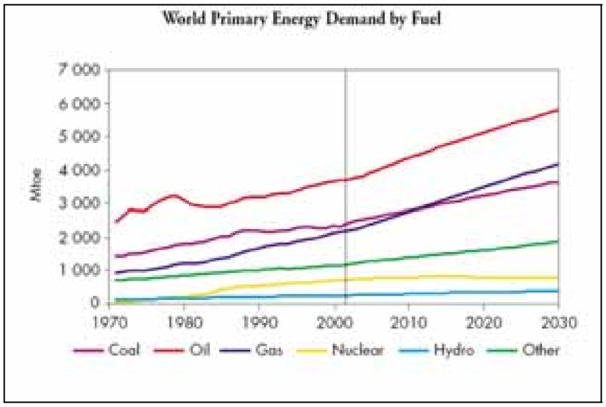

Figure 1: *Projected development of the world's primary energy demand (Mtoe = Million ton oil equivalents) [1].*

Due to the sulphur content of coals and oils, sulphur dioxide (SO_2), and to a lesser extent sulphur trioxide (SO_3), will be released by the combustion of these fuels. If the flue gas is released to the atmosphere untreated, sulphuric acid can be formed according to equation 1.

$$SO_2\,(g) + \tfrac{1}{2}O_2\,(g) + H_2O\,(l) \rightarrow H_2SO_4 \qquad (1)$$

The acidification of the environment caused by the formation of sulphuric acid in the atmosphere has been associated with a number of detrimental effects, such as

- A reduction of biodiversity.
- Reduced crop and forest growth.
- Damage to buildings and architectural heritage.

Emitted SO_2 can furthermore contribute to the formation of aerosols in the atmosphere, affecting human health (respiratory and cardiovascular diseases).

In order to reduce these detrimental effects a range of FGD plants have been installed at power plants all over the world. The vast majority of the installed FGD capacity consists of the wet scrubber FGD technology [2] that either produces $CaSO_3$ sludge (equation 2) or $CaSO_4{\cdot}2H_2O$ (gypsum, equation 3) depending on the operating conditions.

$$CaCO_3\,(aq) + SO_2\,(g) + \tfrac{1}{2}\,H_2O \rightarrow CaSO_3{\cdot}\tfrac{1}{2}H_2O\,(s) + CO_2\,(g) \qquad (2)$$

$$\begin{aligned} &CaCO_3\,(aq) + SO_2\,(g) + 2\,H_2O\,(l) + \tfrac{1}{2}O_2 \qquad (3) \\ &\rightarrow CaSO_4{\cdot}2H_2O\,(s) + CO_2\,(g) \end{aligned}$$

Most European power plants use the gypsum-producing process (forced oxidation), because of the sales potential of the gypsum for either wallboard or cement production. The gypsum must however fulfil certain quality requirements (moisture and impurity content) in order to be used for these applications.

A better understanding of the gypsum crystallisation kinetics could facilitate a more consistent gypsum quality and point to ways of manipulating the gypsum properties. The incorporation of crystallisation kinetics predicting the gypsum PSD into mathematical process models is one way to obtain an increased control and understanding of the FGD process.

Non-wanted and unexpected foaming in wet FGD plants has been observed at several Danish power plants. This has caused a range of problems like scaling at the demister and FGD unit shut down, due to excessive amounts of foam leaving the reactor. The origin of this phenomenon is unknown and will be investigated with the aim of controlling foaming in wet FGD plants.

Specific Objectives

The overall objectives of this PhD project are:

- Derivation of crystallisation and degradation kinetics for the prediction of gypsum PSD.
- Investigation of the origin of foaming and the development of methods to control it in FGD plants.
- The use of the obtained results to optimize the operation of wet FGD plants

Experimental work and modelling

A pilot plant version of the FGD unit from Avedøre power plant unit 1 (a falling film coloumn) has previously been constructed at the CHEC research centre. Figure 2 shows the basic outline of the pilot plant. The SO_2 containing flue gas is created by combustion of natural gas and subsequent SO_2 addition. The flue gas is then brought into contact with the slurry in the absorber (a 7 m pipe with multiple sampling sites). The slurry leaving the absorber is collected in a hold-up tank where air injection and reactant addition take place.

The initial investigations will focus on the extent of the mechanical degradation of the gypsum crystal in the pilot plant. Subsequently the effect of parameters such as the presence of additives and slurry saturation on the rate of crystal creation (nucleation) and crystal growth will be investigated.

Based on the experimental results population balance equations will be developed to predict the gypsum PSD based on operating conditions.

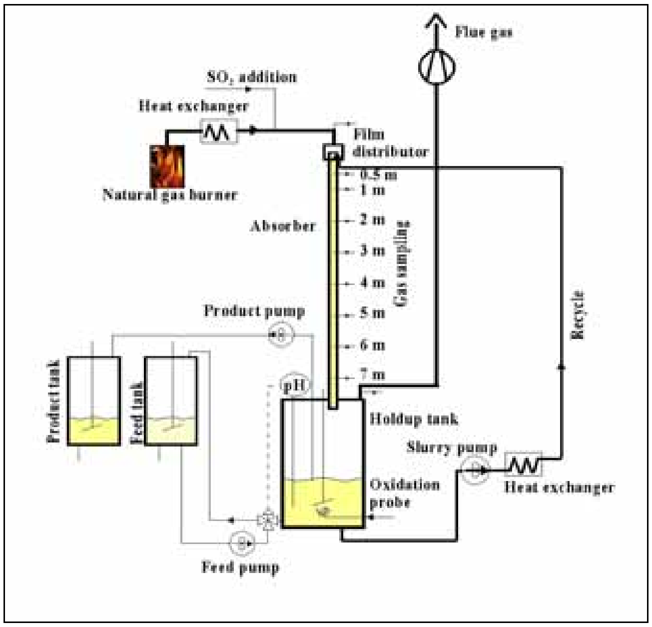

Figure 2: *Principal diagram of the pilot plant [p].*

Acknowledgements

The project is funded by the MP_2T Graduate School.

References

1. International Energy Agency (IEA)
   World energy outlook 2004 – Executive summary.
   http://www.igu.org/database/2004/WEOEnglishExecSum.pdf
2. Soud, H.N.
   Developments in FGD
   IEA Coal Research, London, 2000.
3. Wolfe, T.
   Chemical technician at the CHEC research group.

Natanya Majbritt Louie Hansen
Address: Building 423, room 206
Phone: +45 4525 6819
Fax: +45 4588 2161
e-mail: nha@polymers.dk
www: http://www.polymers.dk

Supervisors: Søren Hvilsted
Michael Gerstenberg, Novo Nordisk A/S

Ph.D. Study
Started: January 2004
To be completed: December 2006

Synthesis of Amphiphilic Block Copolymers by Atom Transfer Radical Polymerization

Abstract

Membranes are a crucial part of drug delivery devices for in-vivo use and the demands on the material properties are numerous. These requirements can be met by careful selection of chemical characteristics of two polymers joined into block copolymers. In the current project, synthesis of amphiphilic copolymers are proposed utilizing atom transfer radical polymerization (ATRP); a controlled radical polymerization method. Preliminary studies have shown that polymers with narrow polydispersity indexes can be obtained by this method. Studies of the kinetics of the homopolymerization of the fluorinated monomer by ATRP indicate controlled reaction mechanisms.

Introduction

It is expected that Diabetes Mellitus will reach epidemic dimensions in the next decades. Type 2 diabetes, which often is related to insulin deficiency in the body, is rapidly growing among the world population as the Western way of life is adapted. Especially among the Asian population a disproportional large number of new type 2 diabetes have been observed as the life style has changed. From being considered as a maturity onset condition, the age is rapidly declining for the onset of type 2 diabetes. Furthermore, only approximately half of all people with diabetes have been diagnosed. Poorly administered diabetes treatment can lead to difficult late complications such as cardiovascular diseases, kidney damage, and blindness. Thus, there exists a large and resource demanding task to treat people with diabetes. However, studies have shown that late complications can be reduced significantly by tight control of the glucose level in the body. For the immediate insulin demanding type 1 diabetes, glucose monitoring is an important part in maintaining a normal way of life. The right mix of insulin types can be found and low sugar levels (hypoglycemia), which can lead to unconsciousness and loss of life, can be avoided [1].

Objective

Membranes are integrated in many different types of drug delivery systems, e.g., for treatment of diabetes. Block copolymers have been an often sought route as membrane material, since they can be tailored to have the desired multifunctionality. In the current project amphiphilic copolymers i.e. copolymers containing both a hydrophilic and a hydrophobic functionality are designed.

Synthesis method

The strategy for the synthesis of the copolymers is atom transfer radical polymerization (ATRP), a technique of controlled/”living” radical polymerization developed by Matyjaszewski [2]. The method involves the use of a transition metal catalyst (Mt), a multidentate ligand (L) and a halogenated initiator, which all interact with the active polymer chain (see Fig. 1). There exists equilibrium between an activated (P·) and a dormant (P-X) polymer species with the deactivation reaction being kinetically favoured. Ideally, this eliminates the possibility of two activated polymer chain ends encountering to give termination, while in practice termination does occur to a small extent.

Using the ATRP method polymer products with well-defined structures and narrow molecular weight distributions can be obtained and the potential polymer structures are numerous. The product of an ATRP reaction is a potential initiator for yet another reaction, as it still has the halogen moiety in the growing chain end. This allows reactivation of the chain end and makes ATRP especially suited for synthesizing tailored block copolymers.

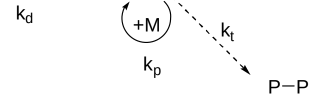

Figure 1. Mechanism of ATRP. Mt=metal catalyst, P=polymer chain, X=halogen, M=monomer, L=ligand. k_a, k_d, k_p and k_t are the rates of activation, deactivation, propagation and termination, respectively.

Fluorinated polymers are highly hydrophobic and polymers containing fluorine atoms have gained interest due to a number of properties that are unique including biocompatibility and low surface activity, as well as high chemical and thermal resistance. In the literature a number of fluorinated or perfluorinated methacrylic and acrylic monomers have been studied in the polymerization of block copolymers by ATRP. One aim of my thesis is to synthesize amphiphilic block copolymers utilizing fluorinated methacrylates.

ATRP of fluorinated methacrylates

As early as 1997 DeSimone and co-workers reported the polymerization of 1H,1H-perfluorooctyl methacrylate (DHFOMA) by ATRP [3] (fig. 2). For the polymerization of this monomer macroinitiators of poly(2-hydroxyethyl methacrylate) (PHEMA), poly(2-hydroxylethyl acrylate) (PHEA), poly(methyl methacrylate) (PMMA) and poly(*tert*-butyl acrylate) (P*t*BA) were synthesized also by ATRP. Reactions of the fluorinated monomers were run at 110 °C in trifluorotoluene using Cu(I)Br and bipyridine as catalyst and ligand. Polydispersities of 1.3, 1.5 and 1.6 were obtained for the synthesis by PMMA, PHEMA and P*t*BA, respectively. The PHEA macroinitiator was employed at 100 °C yielding copolymers with polydispersities of 1.1 for a large range of molecular weights (35 - 100 kg/mol).

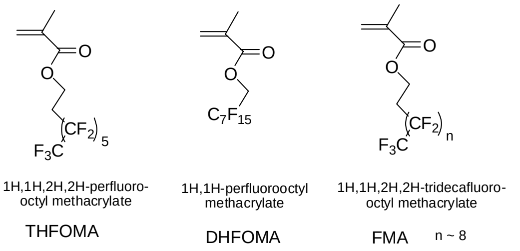

Figure 2. Fluorinated methacrylates polymerized by ATRP in the literature [3,4,5].

Amphiphilic triblock copolymers have been synthesized by Lim et al. [4] utilizing a poly(ethylene oxide) macroinitiator (M_n = 2000 & 5000 g/mol) for the polymerization of the fluormethacrylates DHFOMA and 1H,1H,2H,2H-perfluorooctyl methacrylate (THFOMA) (fig. 2). Reactions took place in a mixture of trifluorotoluene and benzene at 120 °C using Cu(I)Cl/bipyridine giving high conversions (85 - 95 %) with very high initiator efficiencies (> 90 %). It was, however, impossible to analyze the products by size exclusion chromatography (SEC), as the amphiphilic polymers aggregated in THF even at low concentrations therefore the polydispersities were not found. Measurements of interfacial activity of the block copolymers using a high pressure pendant drop apparatus showed that the polymers lowered the surface tension to a degree that allowed emulsion formation.

Poly(ethylene oxide) macroinitiators have also been utilized by Hussain et al. [5] to synthesize di- and triblock copolymers with perfluorohexylethyl methacrylate FMA. Poly(ethylene oxide) was converted to a macroinitiator with 2-bromopropionyl bromide and used for polymerization of FMA at 80 °C in butyl acetate using Cu(I)Br as catalyst with bipyridine or PMDETA (fig. 3) as ligand. The authors do not give information on yields or initiator efficiency, but polydispersities as low as 1.1 were found by SEC and monomodal curves were generated in all cases. A certain degree of aggregation of the copolymers during analysis was observed, as a lower molecular weight than for the initial macroinitiator was found in some cases. Four different molecular weights of poly(ethylene oxide) were used in this study: 2, 6, 10 and 20 kg/mol.

Preliminary experiments

A number of preliminary syntheses have been run with methyl methacrylate (MMA) to test the polymerization method with the used setup. The polymerizations have been carried out in xylene using Cu(I)Br as catalyst and varying the ligand. Altogether five different ligands used in the literature [6,7,8] have been studied (fig. 3) : 2,2’-bipyridine (Bipy), 1,1,4,7,7-pentamethyldiethylene triamine (PMDETA), N-(n-propyl) 2-pyridyl methamine (n-Pr-1), 1,1,4,7,10,10 hexamethyl triethylene tetramine (HMTETA) and tris[2-(dimethylamino)ethyl] amine (Me_6TREN). The results of the syntheses of MMA have been satisfactory with low polydispersity index (PDI) and number average molecular weights (M_n) close to the target of 20,000 g/mol (table 1). All reactions were run at 80 °C.

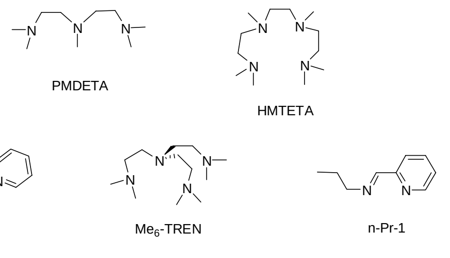

Figure 3. Ligands used for ATRP.

Table 1. Results of preliminary ATRP of MMA

Sample	*Ligand*	*PDI*^{a}	*$M_n{}^a$ (g/mol)*	*Yield (%)*
1	PMDETA	1.07	15,400	38
2	HMTETA	1.21	22,500	89
3	Bipy	1.20	22,600	40

^{a}*Determined by size exclusion chromatography*

The ligand Me_6-TREN was synthesized (yield 89 %) and used for ATRP of methyl acrylate (MA), but despite reports in the literature, the results for this ligand were not satisfactory. The yields with both ligands were very low, the polydispersities however were also low in all cases.

Table 2. Preliminary ATRP of MA

Sample	*Ligand*	*PDI*[a]	*M_n*[a] *(g/mol)*	*Yield (%)*
1[b]	PMDETA	1.07	19,600	26
2	PMDETA	1.13	10,200	19
3	Me_6TREN	1.1	9,690	38

[a] Determined by size exclusion chromatography

[b] PMMA "1" (table 1) used as macroinitiator

Results

Homopolymers of the perfluorinated methyl methacrylate 3FM were synthesized under the same conditions as MMA. The structure of the polymer is shown in figure 4, while results are given in table 3. In all cases the target molecular weight was 20,000 g/mol. Obviously the best results are obtained (with regard to both yield and molecular weight distribution), when using the ligand n-Pr-1 all else being equal, but PMDETA also gave a satisfactory outcome.

Table 3. Results of homopolymerization of 3FM

Sample	*Ligand*	*PDI*[a]	*M_n*[a] *(g/mol)*	*Yield (%)*
1	Bipy	-	270	-
2	HMTETA	1.8	12,900	21
3	n-Pr-1	1.41	29,100	88
4	PMDETA	1.58	14,400	68
5	PMDETA	1.67	11,000	54
6	PMDETA	1.64	27,500	75

[a] Determined by size exclusion chromatography

Polymerization of 3FM using poly(ethylene glycol)-macroinitiators (PEG) for the formation of amphiphilic block copolymers was also undertaken (fig. 5) and the results are shown in table 4. PEG with molecular weights of 2000 and 4600 g/mol were used.

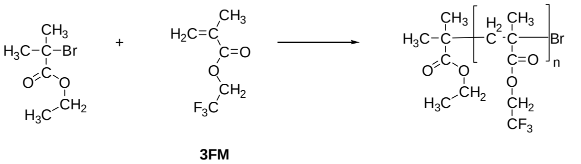

Figure 4. Homopolymerization of 3FM using ethyl 2-bromoisobutyrate as initiator.

In all cases yields were very good and molecular weights close to the target were obtained, but the distributions were quite broad. This was partly due to low efficiency of the macroinitiator, as unreacted macroinitiator was observed in all SEC-traces.

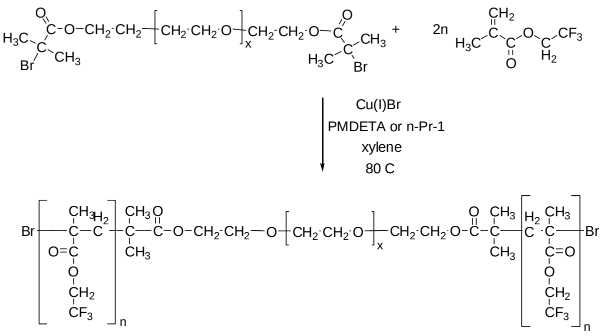

x = 45 or 105

Figure 5. ATRP of triblock copolymers using functionalized PEG as macroinitiator

The molecular weights of the triblock copolymers could be estimated by two different methods; size exclusion chromatography, which was used for the homopolymers, and nuclear magnetic resonance spectroscopy (^{1}H-NMR), which was only used for the block copolymers. In the latter method the signals from CH_2-CF_3 in the fluorinated blocks (4.15 ppm) was compared to the CH_2-O signals from the macroinitiator (3.6 ppm). Figure 6 shows a ^{1}H-NMR-spectrum of a triblock copolymer synthesized with a PEG with a molecular weight of 2000 g/mol, and a total molecular weight of 16,800 g/mol. There was good correspondence between the results achieved by the two methods.

Table 4. Results of ATRP of 3FM with PEG-macroinitiators

Sample	*Ligand*	*Macroinitiator*	*PDI*[a]	*M_n*[a] *(g/mol)*	*M_n*[b] *(g/mol)*	*Target M_n*	*Yield (%)*
1	PMDETA	PEG2000	1.97	18,300	20,300	22,000	79
2	PMDETA	PEG2000	1.86	14,700	16,800	22,000	79
3	n-Pr-1	PEG2000	1.80	22,100	26,900	22,000	>99
4	n-Pr-1	PEG2000	1.62	25,300	26,300	22,000	>99
5	n-Pr-1	PEG2000	1.51	6,240	5,260	4,600	>99
6	PMDETA	PEG4600	1.88	28,500	30,000	25,000	>99
7	n-Pr-1	PEG4600	1.47	26,200	27,600	25,000	97
8	n-Pr-1	PEG4600	1.23	12,000	10,000	9800	>99

[a] Determined by size exclusion chromatography

[b] Determined by ^{1}H-NMR-analysis

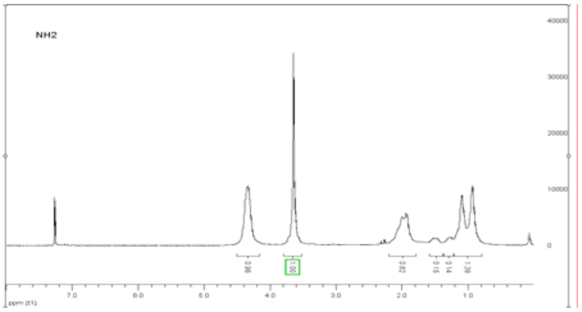

Figure 6. ^{1}H-NMR-spectrum of triblock copolymer of 3FM and PEG.

Kinetic study

The key to controlling the reaction is determining the kinetics of the reaction. Often the disappearance of monomer is monitored by H-NMR-spectroscopy, but this approach is only possible when running reaction in bulk, as a solvent would obliterate the signals from both monomer and polymer. Most polymerizations are conducted in solution due to the heat generated during reaction, and therefore the analysis of kinetics in bulk will only give insufficient information. An analysis on the reaction in solution gives a more exact indication of the reaction mechanisms.

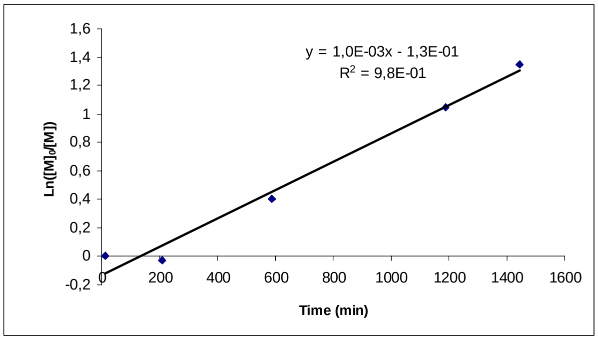

Figure 7. Kinetic study of homopolymerization of 3FM with internal standard. T = 80 °C, 40 % solution in xylene & trifluorotoluene (2:1).

As the polydispersities of the triblock copolymers were larger than normally observed in ATRP, a kinetic study was undertaken to ensure that the reaction was controlled. Samples were taken from the reaction tube during synthesis and analyzed by gas chromatography (GC/MS). The concentrations were determined by using an internal standard. The resulting curve was linear when plotting ln($[M]_0/[M]$) vs. time in accordance with kinetics theory, which states a pseudo first order reaction. At a constant concentration of radicals, the rate of propagation R_p is defined by equation (1).

$$R_p = \frac{-d[M]}{dt} = k_p[M]\sqrt{\frac{fk_{disp}}{k_t}} \quad (1)$$

Where k_{disp}, k_p and k_t are the rates of disproportionation, propagation and termination, respectively, [M] is monomer concentration, t is time and f is initiator efficiency. After rearrangement and integration (1) reduces to equation (2).

$$\ln\frac{[M]_0}{[M]} = k_{app}t \quad (2)$$

Where $[M]_0$ is the monomer concentration at t=0 and k_{app} is the apparent rate constant.

Conclusion

It is possible to synthesize fluorinated block copolymers by the chosen method and the reactions seem to be controlled as is required for ATRP reactions. Some optimization is however needed in order to obtain better control over the product i.e. the molecular weight distributions.

Future work

The future work will include characterisation of the synthesized block copolymers with regard to properties such as degradation temperature (thermogravimetric analysis), glass transition temperature (differential scanning calorimetry) and surface activity (contact angle). Further kinetic studies of the reactions will be undertaken.

The combination of the fluorinated monomers with other hydrophilic monomers might be a solution to solving the problem of low macroinitiator efficiency.

Once fabricated in thin films, the relation between bulk structure and chemical and physical properties (such as the permeability and tensile strength) will be evaluated in addition to the surface ordering and chemistry.

Acknowledgements

I would like to thank Novo Nordisk A/S for supporting this project.

References

1. For a more detailed description of Diabetes, see e.g. www.diabetes.org.
2. J.-S. Wang, K. Matyjaszewski, J. Am. Chem. Soc., 117 (1995) 5614 – 5615
3. D. E. Betts, T. Johnson, D. LeRoux, J. M. DeSimone, ACS Symposium Series 685 (1998) 418 – 432
4. K. T. Lim, M. Y. Lee, M. J. Moon, G. D. Lee, S.-S. Hong, J. L. Dickson, K. P. Johnston, Polymer Communication, 43 (2002) 7043-7049
5. H. Hussain, H. Budde, S. Höring, K. Busse, J. Kressler, Macromol. Chem. Phys 203 (14) (2002) 2103-2112
6. J. Xia, K. Matyjaszewski, Macromolecules 30 (1997) 7697 – 7700
7. J. Xia, S. G. Gaynor, K. Matyjaszewski, Macromolecules, 31 (1998) 5958 – 5959
8. D. M. Haddleton, M. C. Crossman, B. H. Dana, D. J. Duncalf, A. M. Heming, D. Kukulj, A. J. Shooter, Macromolecules, 32 (1999) 2110 - 2119

Thomas Steen Hansen
Address: Building 423 room 112
Phone: +45 4525 6807
Fax: +45 4588 2161
e-mail: tsh@polymers.dk
www: http://www.polymers.dk

Supervisors: Ole Hassager

Ph.D. Study: All polymer micropump
Started: October 2004
To be completed: September 2007

Testing and Fabrication of All Polymer Micropump

Abstract

The main objective of the project is to examine and test microfluidic pumps produced with polymers. Currently the main field of research is the AC electroosmotic micropump, which has the advantage of a simple structure, no movable parts and low requirements to the applied potential. The AC electroosmotic micropump has been constructed using conductive polymers, therefore making it possible to construct an all polymer micropump. Characterisation of the polymer pump and comparison with pumps made with metals is the next goal of the Ph.D. project.

Introduction

The ability to control chemical processes on the micrometer scale has many interesting perspectives and is a field in fast expansion. One of the main issues when dealing with microsystems is the pumping of fluid. Several techniques have been used for this purpose and one of the most interesting is the electroosmotic pump. A special case of this pump is the asymmetric AC electroosmotic pump (ACEO) first suggested by Ajdari[1]. The pump consists of an array of asymmetric electrodes in a channel with an AC potential between the electrodes. This is presented in figure 1. The advantages of the pump are the simple construction, no moveable parts and low potential (1-5 V) requirements. The ACEO pump has been described both experimentally[2-7] and theoretically[1,2,8,9], but no numerical simulations of the system have been performed. As a mean to optimise the geometry numerical simulations of the ECEO pump were therefore conducted.

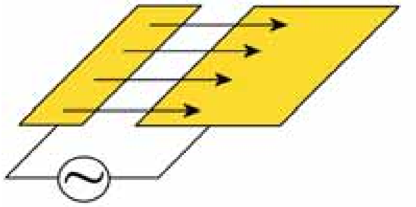

Fig. 1 The principle of an ACEO pump. The asymmetric shape of the electrodes creates an asymmetric electric field, which induces a non-zero horizontal force to the ions in the fluid. The friction between the ions and the fluid creates a pumping effect from the small to the large electrode.

Theory

The three governing equations when simulating the ACEO pump are Poisson's equation (1), the mass transfer equation (2) and the incompressible Navier-Stokes equation (3).

The electric regime is described by Poisson's equation, and simplifying the system to a monovalent salt yields equation (1) where ϕ is the potential, ρ is the space charge density and ε is the dielectric constant of the fluid, F is Faradays constant, c^+ and c^- are the concentration of the positive and negative ions.

$$\nabla\phi = -\frac{\rho}{\varepsilon} = -\frac{F\left(c^+ - c^-\right)}{\varepsilon} \qquad (1)$$

The flux of the charged ions is found by using the mass transfer equation[10] (2), where D is the diffusion coefficient, $\mathbf{v}$ is the flowfield with the components v_x and v_y, z is the charge of the ion and u is mobility.

$$\frac{\partial c_i}{\partial t} + \mathbf{v} \cdot \nabla c_i = D_i \nabla^2 c_i + z_i u_i \nabla \cdot \left(c_i \nabla\phi\right) \qquad (2)$$

The fluid mechanical part of the system is determined by the incompressible Navier-Stokes equation (3a) and (3b), where ρ_{dens} is the density of the fluid, μ is the viscosity and p is the pressure. The last term in eq. (3a) is the force caused by the moving ions.

$$\rho_{dens}\left(\frac{\partial \mathbf{v}}{\partial t} + \mathbf{v}\cdot\nabla\mathbf{v}\right) = -\nabla p + \eta\nabla^2 c_i + \sum z_i F c_i \nabla\phi \qquad (3a)$$

$$\nabla\cdot\mathbf{v} = 0 \qquad (3b)$$

Using equation (1), (2), and (3) it has been possible to perform numerical simulations of ACEO pump and optimise the geometry to its maximum performance.

Results and Discussion

The numerical simulations revealed that especially the height of the channel is important for the pumping properties. The propulsion of the fluid occurs at the walls near the surface of the electrodes and in contrary to normal systems the pump is most efficient at low diameters. The maximum pressure the pump is capable of delivering is approximately inversely proportional to the squared height of the channel. Another interesting perspective revealed by the numerical simulations was the pumps ability to pump in both directions. The pumping direction can be reversed by lowering the frequency of the AC potential, which enhances the positive prospects of the ACEO pump. The result of a simulation series is presented in figure 2. In the linear regime below 0.025 volts it has been possible to confirm analytical analysis made in the literature.

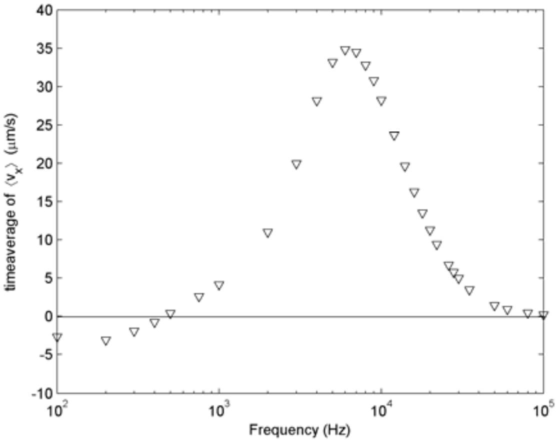

Fig. 2 A simulated frequency sweep of the micropump. The pump is capable of pumping in the reverse direction at low frequencies.

These have however not been conducted on the nonlinear regime above 0.025 volts and the numerical simulations in the ‘high’ potential is therefore used to examine the properties of this system. The studies shown complicated correlations between the maximum velocity in both directions and the potential applied, which have not been shown earlier. The reason for the reverse pumping effect is to be found in the phase shift between the potential and the charge at the surface. At the optimal frequency the charge is shifted 45º from the potential. At low potential the large and small electrode have the same phase shift, but at higher potentials the phase shifts begin to differ. This means that the small electrode has the optimal phase shift at low frequencies, and the large electrode has the optimal phase shift at higher frequencies. At low frequencies the small electrode is therefore governing causing the flow to be reversed, whereas at higher frequencies the large electrode takes over and changes the flow direction.

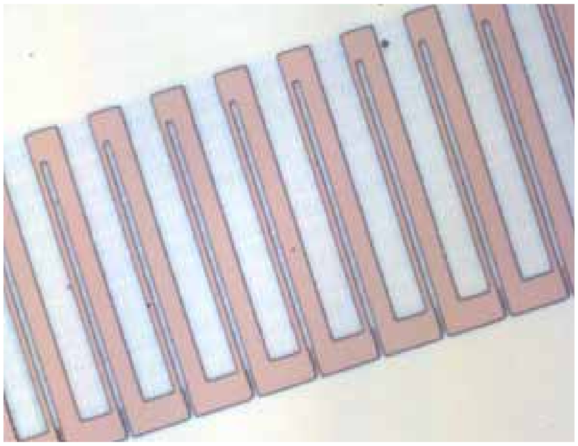

Fig. 3 A picture of the micropump seen from above. The pump consists of gold (bright) on glass (dark). The small electrodes have a size of 4 µm and the large electrodes have a size of 20 µm.

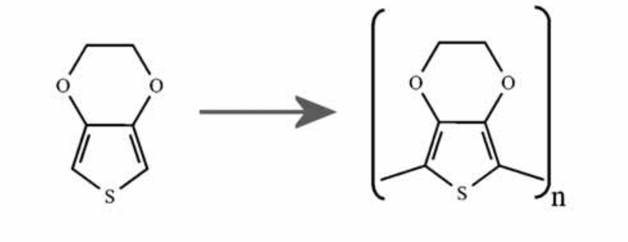

Fig. 4 The polymerization of 3,4-ethylenedioxythiophene yields the PEDT polymer.

The numerical simulations were followed up with experimental work and pumps were produced using classical lithographic methods for microsystems. A picture of a pump is presented in figure 3. The electrodes are gold layers on glass. The produced pumps have been tested and showed a pumping effect and the expected ability to pump in both directions. One of the problems with the current design and fabrication method is that the electrode array is damaged at high potentials (above 2-3 V). This problem could be solved by choosing another material than gold for the electrodes, because gold does not have good adhesive properties with glass.

Recent research has shown that the conductive polymer poly-3,4-ethylenedioxythiophene (PEDT) (figure 4) can be produced with a relatively simple method and have conductivity[13] up to 1000 S/cm. PEDT has the advantage of stability in aqueous solutions, but it required some work to be able to find a suitable method for micro patterning of the PEDT.

A micro pump produced in conductive polymers is shown in figure 6. This pump is produced with PEDT on PMMA, but because the PMMA is an organic material it is also etched in the RIE used for microstructuring. This is the reason for the uneven surface between the electrodes. It can however be avoided by optimizing the etching time, so only the PEDT is etched away and not the PMMA. This is one of the parameters, which will be examined in future work. The PEDT pump has been tested and was capable of pumping. It could actually withstand a potential up to 12

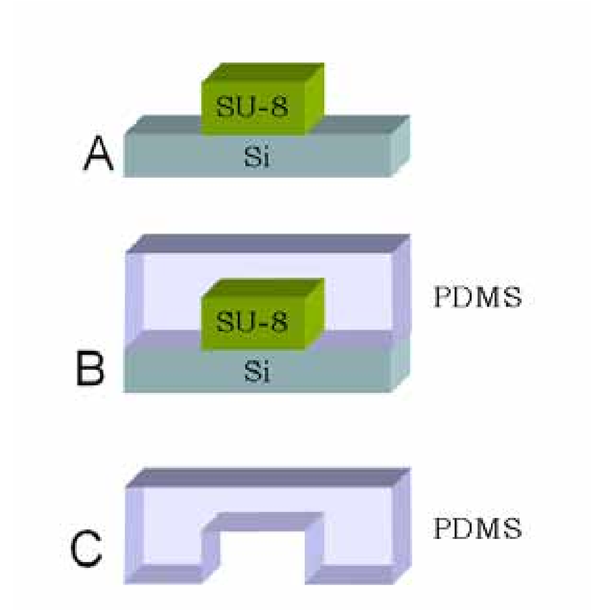

Fig. 6 The production of a PDMS structure. An SU-8 pattern is made using classical lithography (A), and the PDMS is cast on to the pattern (B) and finally removed (C).

Volts, where gold is damaged at much lower potentials. Several possible problems do however arise from the use of PEDT as electrode material, which have to be examined. One of the problems is the possible release of ions to the fluid. When the PEDT is polymerized, some of the tosylate ions from the oxidant are trapped in the polymer. This is essential for the conductivity of the polymer, because the negative charge of the tosylate makes the existents of positive charges at the backbone of the PEDT possible. The conductivity arises from the movement of these positive charges (electron vacancies) along the chain of conjugated π-orbitals in the backbone. Without the tosylate ions there would be no positive charges and therefore no conductivity. The tosylate ions is known to slowly migrate out of the polymer if it is exposed to a positive potential over a period of time, but how the ions will react to a high frequency AC potential is unknown and needs to be examined. This problem can solved by coating the surface with a thin layer of nonpermeable polymer, but this changes the properties of the pump, and might cause problems with heating.

A further comparison between gold and PEDT pumps is to be conducted in future research.

In order to test, control and measure the pumping effect a channel system is required. This is produced in Polydimethylsiloxane (PDMS). PDMS has several advantages; it is easy to mold, it is elastic and therefore tightening and it is transparent. The micro channels in PDMS are made from classical SU-8 lithographic methods. The SU-8 is an epoxy photoresist with good height to width aspect ratio. It is produced in the same manner as the microposit photoresist, but with the difference that the thickness can be up to several 100 µm and the edges still being close to vertical. The production method for a PDMS channel is shown in figure 7 A-C. Initially a silicon wafer is cleaned and prepared. Using UV-light and a mask a SU-pattern is produced on the wafer (A). The SU-8 and wafer is coated with a monolayer of 1,1,1,3,3,3 hexamethylsilazane, which prevents adhesion between the PMDS and the substrate. The PDMS is then poured on top of the pattern, heated and cured (B). The PDMS channel system can then be removed from the substrate (C), and the SU-8 pattern can be reused.

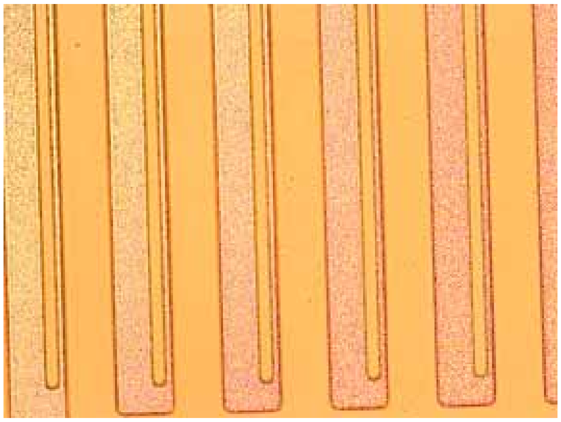

Fig. 5 An all polymer micro pump, consisting of a PEDT array on PMMA. The uneven surface is the PMMA that have been partially etched in the RIE. The thickness of the PEDT layer is 160 nm and the width of the electrodes is 8 µm and 40 µm.

PDMS is normally very hydrophobic, which normally would prevent water to enter the microchannels due to forces bound in high surface tension. If the PDMS is treated in a plasma chamber with air it is however possible to make it hydrophilic. This is because the oxygen radicals from the air form hydrophilic species on the surface of the PDMS. Another good property of the PDMS is that if a plasma treated PDMS surface is brought to contact with a glass surface, the metastable species formed during the plasma treatment will react with the glass. The PDMS will irreversibly bond to the glass surface and completely seal the channel system. The PDMS has however the disadvantage that it is permeable to air and in some extent water vapor. The concentration of salt in the channel system is therefore difficult to control, because of water evaporating through the PDMS. Furthermore is PDMS difficult to mass produce, which makes it unfit for future applications.

The next step of the project is to create a PMMA channel system, which is impermeable to water vapor and easy to mass produce by injection molding. The production of a PMMA channel system is shown in figure 7. To create a PMMA structure a SU-8 or a Nickel mask can be used. The SU-8 mask is produced as mentioned above and covered with HMDS (A). A piece of PMMA is placed on top of the SU-8 pattern (B) and a pressure of 20 bar is applied at a temperature of 140 ºC (C) which is well above the glass transition temperature of PMMA (app. 101 ºC). The PMMA flows down around the pattern and is subsequently cooled and the PMMA channel system is removed. The SU-8 mask is however not suited for this kind of molding and does therefore only withstand 2-10 replications. Another method is to evaporate chrome/gold onto the SU-8 mask and then electrodeposit nickel on top of the gold. A 1-2 mm layer of nickel can be achieved and afterwards the Silicium and SU-8 can be removed by etching. You then have a very strong nickel mask, which also can be used for injection molding. The process is however rather difficult and time consuming thus you should be certain that the design is correct. So in the initial

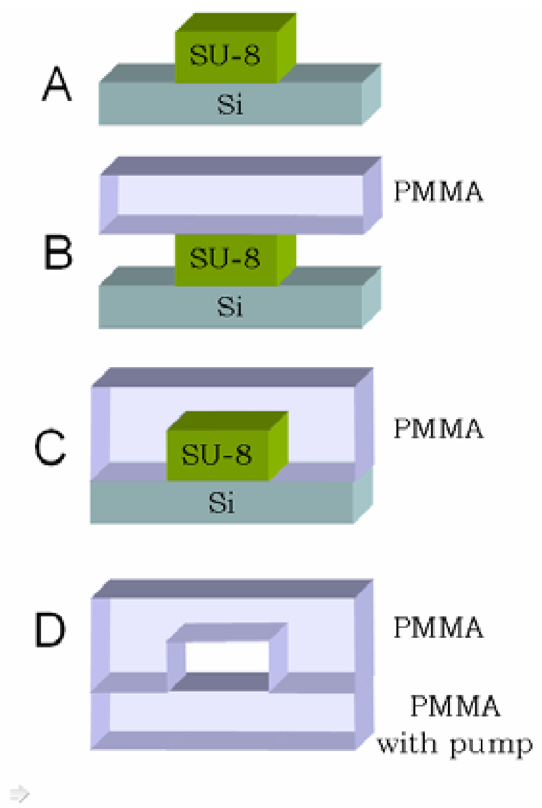

Fig. 7 The production of a PMMA structure. An SU-8 pattern is made using classical lithography (A) and covered with hexamethyldisilazane, a PMMA plate is placed on top of the SU-8 pattern (B) and by applying heat and pressure the pmma is cast (C). Finally the PMMA channel can be bonded to the PMMA substrate with the PEDT Micropump (D).

phase when different kinds of geometries are used the SU-8 mask is the best method for creating the channel structures.

After the molding the PMMA pattern is removed and it is bonded to the PMMA with the PEDT micropump. The bonding can either be done using ethanol or elevated pressure and temperature. Compared to the PDMS to glass bonding the PMMA to PMMA is more difficult, because the elevated temperature or solvent (ethanol) makes the PMMA deform. The exact size of the channel system is therefore difficult to establish with breaking apart the final PMMA system.

The testing of the micropump is conducted using fluorescent microspheres with a diameter of 0.25 – 1 µm. The microspheres are added to the pumping fluid and the pump is placed under a microscope with a fluorescent filter. By tracking the movement of the spheres it is possible to calculate the velocity of the fluid. The used microscope is a confocal microscope that makes it possible to view slices of the fluid down to a thickness of 2-3 µm. It is therefore possible to make 3D model of the flow in the microsystem.

References

1 A. Ajdari, *Physical Review E*, 2000, **61**, 45;
2 A. B. D. Brown, C. G. Smith and A. R. Rennie, *Physical Review E*, 2000, **63**, 16305
3 N.G. Green, A. Ramos, A. González, H. Morgan, A. Castellanos, *Physical Review E*, 2000, **61**, 4011
4 N.G. Green, A. Ramos, A. González, H. Morgan, A. Castellanos, *Physical Review E*, 2002, **66**, 26305
5 M. Mpholo, C. G. Smith and A. B. D. Brown, *Sensors and actuators B*, 2003, **93**, 262
6 V. Studer, A. Pépin, T. Chen, A. Ajdari, *The Analyst*, 2004, **129**, 944;
7 S. Debesset, C.J Hayden, C. Dalton, J.C.T Eijkel, A. Manz, *Lab on a Chip*, 2004, **4**, 396;
8 N.G. Green, A. Ramos, A. González, H. Morgan, A. Castellanos, *Physical Review E*, 2000, **61**, 4019
9 N. A. Mortensen, L. Belmon, L. H. Olesen. And H. Bruus, *Not published yet*;
10 E. yeager, J.O. Bockris. B. E. Conway And S. Sarangapani, *Comprehensive treatise of electrochemistry 6*, 1983, 1st ed., Plenum Press;
11 E. Gileadi, *Electrode kinetics*, 1993, 1st ed., VCH;
12 R. Byron, W. E. Stewart And E. N. Lightfoot, *Transport phenomena*, 2001, 2nd ed., Wiley;
13 B. Winther-Jensen And K. West, *Macromolecules* 2004**,** **37**, 4538-4543;

Peter Dybdahl Hede

Address:	CHEC, Dept. of Chemical Engineering Building 229, Room 127
Phone:	+45 4525 2853
Fax	+45 4525 2258
e-mail:	PtHd@novozymes.com
www:	http://www.kt.dtu.dk
Supervisors:	Anker Degn Jensen Poul Bach, Novozymes A/S
Ph.D. Study	
Started:	September 2005
To be completed:	August 2008

Fluid Bed Agglomeration and Coating

Abstract

Fluid bed granulation is a vital operation in the pharmaceutical, enzyme and food/feed industry and fluid beds are used extensively to form liquid formulations into solid products. Although widely used, fluid bed operations are still not fully understood or described. This means that modern industrial fluid bed operations and optimisation are still highly dependent on empirical approaches. This Ph.D. project aims at the fundamental understanding of the fluid bed granulation process in an industrial context. Trying first to model and describe the two particle agglomeration situation it is the goal to try to include this understanding into advanced population balance models capable of optimising as well as scaling fluid bed granulation systems.

Introduction

Particle processing in fluidised beds is a key operation to many types of industries including the food and pharmaceutical industries. In the production of solid enzyme products, fluid beds are used to produce enzyme granules with the proper product properties by spraying the enzyme concentrate through nozzles onto the agitated fluidised bed often consisting of inactive filler cores. In that sense agglomeration is an unwanted phenomenon but in other applications, agglomeration is indeed desired. In either case, control of agglomeration is essential.

Proper product quality is highly dependent on the precise control and optimisation of the process. As there is more than forty parameters involved in the fluid bed coating process and as many of these parameters interact, fluid bed optimisation is an extremely difficult exercise. The situation is further complicated by the fact that during fluid bed processing many different processes occur simultaneously including wetting, drying, chance of agglomeration, attrition and more. As, in addition, particle trajectories inside fluid beds are chaotic, modelling and simulation of the coating process with commercial products is not an easy task. Thus, the present situation with fluid bed processes and products is still highly dependent on experimental results although this is tedious, time consuming and thereby expensive. This is not a satisfactory situation - neither from an academic nor from an industrial point of view.

Specific Objectives

It is the objectives of the Ph.D. project to achieve a fundamental quantitative understanding at particle level of what is going on inside the fluid bed during processing. Further, it is the objective to be able to build this particle level knowledge into population balance models thereby being capable of describing the whole system quantitatively. The aim of such models is to be able to improve fluid bed process optimisation as well as scaling fluid bed processes from pilot plant scale into full scale production.

Results and Discussion

The Ph.D. project is a continuation of a Master Thesis with the title “Fluid bed coating and granulation” by the same author and much of the work in the first stages of the Ph.D. project will be a continuation of threads laid out by the results gained from the Master project.

Results from coating experiments in a small-scale GEA Aeromatic Strea-1 top-spray fluid bed gained from the Master Thesis indicated that the agglomeration tendencies is highly affected by the level of droplet penetration into the carrier particles. Colour coating studies of white Na_2SO_4 cores (200 – 300 μm) indicated a high level of droplet penetration.

The coating solutions consisted besides colour of crushed Na_2SO_4 using water as solvent and Dextrin as binder. Typical cut-through examples of coloured granules can be seen in Figure 1A and Figure 1B.

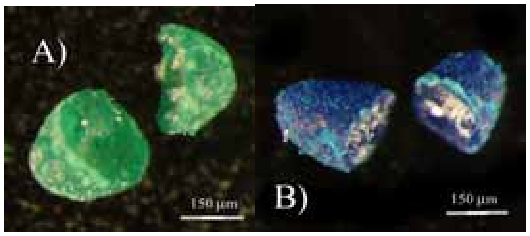

Figure 1: Examples of microscope pictures of: A) Cut through profile of a coated granule using Colanyl green (Water-insoluble) colour. B) Cut through profile of a coated granule using Patent Blue colour (Water-soluble).

It was verified in addition that the level of droplet penetration could be well predicted by calculations of the droplet drying time, τ_{drying} in seconds using Eq. 1 [1]:

$$\tau_{drying} = 0.001s \cdot \left(\frac{d_d}{1\mu m}\right)^2 \qquad (1)$$

in which d_d is the droplet diameter in µm, versus the time of droplet depletion τ_d in seconds using Eq. 2 [2,3].

$$\tau_d = \frac{2V_d^2}{\pi^2 \varepsilon_{pmsp}^2 r_d^4 R_{pore}} \frac{\eta_{liq}}{\gamma_{lv} \cdot \cos\Theta} \qquad (2)$$

in which where V_d is the total droplet volume, r_d the radius of the droplet, ε_{pmsp} is the porous media surface porosity (void fraction), γ_{lv} is the liquid surface tension, η_{liq} is the liquid viscosity, θ is the solid-liquid contact angle and R_{pore} is the effective pore radius based on the assumption of cylindrical parallel capillary pores in the porous structure given by the Kozeny approach according to Eq. 3 [2,3].

$$R_{pore} = \frac{2 \cdot \varepsilon_{pmsp}}{\left(1 - \varepsilon_{pmsp}\right) \cdot s_0 \rho_p} \qquad (3)$$

where s_0 is the particle specific surface area expressed in m^2/kg and ρ_p is the particle density.

The calculations showed that during normal coating operation using commercial Na_2SO_4 cores in the size range of 200 – 300 µm the time of droplet penetration is around a thousand times faster than the time of droplet drying. This explains the observed high degree of droplet penetration.

Initial approaches towards the modelling of the agglomeration situation involved the viscous Stokes theory in which the situation of coalescence in a fluid bed is analysed by considering the impact of two solid non-deformable spheres each of which is surrounded by a thin viscous binder layer of thickness h. A schematic of the collision situation can be seen in Figure 2.

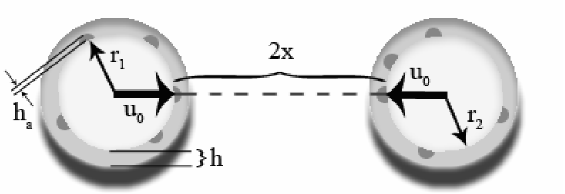

Figure 2: Schematic of two colliding granules each of which is covered by a viscous binder layer of thickness h.

The model assumes successful coalescence to occur if the kinetic energy of impact is entirely dissipated by viscous dissipation in the binder liquid layer and only elastic losses in the solid phase. The model predicts that collisions will result in coalescence when the viscous Stokes number (St_v) is less than a critical viscous Stokes number (St_v^*). The two numbers are given as [4]:

$$St_v = \frac{8 \cdot \rho_g \cdot r_{harm} \cdot u_0}{9 \cdot \eta_{liq}} \qquad (4)$$

and

$$St_v^* = \left(1 + \frac{1}{e}\right) \cdot \ln\left(\frac{h}{h_a}\right) \qquad (5)$$

where η_{liq} is the liquid binder viscosity, e is the coefficient of restitution, ρ_g is the granule density, h is the thickness of the liquid surface, h_a is the characteristic height of the surface asperities and r_{harm} is the harmonic mean granule radius of the two spheres given as [5]:

$$r_{harm} = \frac{r_1 r_2}{r_1 + r_2} \qquad (6)$$

u_0 is the initial collision velocity which is not easily obtainable due to the various phenomena influencing the granule motion in fluid beds. A rough estimate based on the bubble rise velocity U_{br} has been presented by [4]:

$$u_0 \approx \frac{12 U_{br} r_{harm}}{d_b \delta^2} \qquad (7)$$

where d_b is the gas bubble diameter and δ the dimensionless bubble space defined as the axial fluid bed bubble spacing divided by the fluid bed gas bubble radius. Whereas the gas bubble diameter and spacing can be found by experiments or estimated by the dimensions of the air distributor plate in the bottom of the fluid bed vessel, the bubble rise velocity is somewhat more difficult to determine. [6] have however proposed the following empirical relation for a fluid bed based on the bubble diameter d_b, gravity g, the minimum fluidisation velocity U_{mf} and the superficial velocity U_s measured on empty vessel basis:

$$U_{br} = U_s - U_{mf} + 0.711 \cdot (g \cdot d_b)^{1/2} \qquad (8)$$

The Stokes viscous number St_v can be seen as the ratio of kinetic energy to the viscous dissipation. During fluid bed batch granulation, St_v increases as the granules grow in size. This leads to three possible situations. The first so-called "non-inertial regime" occurs when $St_v << St_v^*$. All collisions result in successful coalescence regardless of the size of the colliding granules, granule kinetic energy or binder viscosity. As the granules grow larger the "inertial regime" occurs when $St_v \approx St_v^*$. The likelihood of coalescence now depends of the size of the colliding granules, and granule kinetic energy and binder viscosity begin to play a role [7]. Eventually the system enters the "coating regime" when $St_v >> St_v^*$. Here all collisions between granules are unsuccessful and any further increase in the St_v will maintain the size of the granules. The existence of the three regimes has been proved experimentally in different types of granulators elsewhere [4].

Granule growth is promoted by a low value of St_v and a high value of St_v^*. For instance, increasing the binder content will increase the binder layer thickness h which will increase St_v^* and hence increase the likelihood of successful coalescence. Increasing the nozzle feed rate could increase the binder content but this would most likely affect the droplet size distribution, which again would change the humidity conditions in the bed causing other problems. The effect of the binder viscosity is likewise not easily predictable in that e.g increasing the value η_{liq} (lowering St_v) alters the coefficient of restitution *e* decreasing St_v^* as well [5]. These examples illustrate that a-priory prediction of the agglomeration tendency based on well-known physical and adjustable parameters is not a simple task. Although the viscous Stokes theory model is limited by its assumptions (e.g that that there exists a uniform granule collision velocity) it gives a rough number for the indication of the limit between no-agglomeration and successful agglomeration and it is in fact the only theory that has proven valid for different fluid bed scales. The viscous Stokes theory is to be explored an expanded further in the Ph.D. thesis but results from the Master project allowed a first-hand comparison of the theory versus experimental data.

For eight coating experiments performed in the Strea-1 set-up (please refer to figure 3) the Stokes critical stokes number was calculated using equation 4 to 8. The values of the surface asperities h_a was estimated through visual microscopy of the uncoated granule cores and a value for h was estimated as 1/3 of the mean droplet diameter d_d determined according the Sauter mean diameter stated as [8]:

$$d_d = \frac{585 \cdot 10^3 \cdot \sqrt[3]{\gamma_{cl}}}{\nu_{rel} \sqrt{\rho_{cl}}} + 597 \cdot \left(\frac{\eta_{cl}}{\sqrt{\gamma_{cl} \cdot \rho_{cl}}} \right)^{0.45} \left(\frac{1000 \cdot q_{cl}}{q_{at}} \right)^{1.5} \qquad (9)$$

where η_{cl} is the coating liquid viscosity (in mPa s), ρ_{cl} is the coating liquid density (in kg/m^3), γ_{cl} is the coating liquid surface tension (in N/m), q_{cl} is the coating liquid volumetric flow rate through the nozzle (in m^3/s), q_{at} is the volumetric flow rate of atomising air through the nozzle (in m^3/s) and ν_{rel} is the difference between the nozzle atomising air velocity and the fluidisation air velocity in the vicinity of the nozzle muzzle (in m/s). The agglomeration percentage was found, based on initial microscopy analysis, as the fraction of the total coated bed load with particle diameters above 355 μm divided by the total coated bed load. The calculated St_v and St_v^* values as well as the experimentally determined agglomeration percentage values can be seen in table 1.

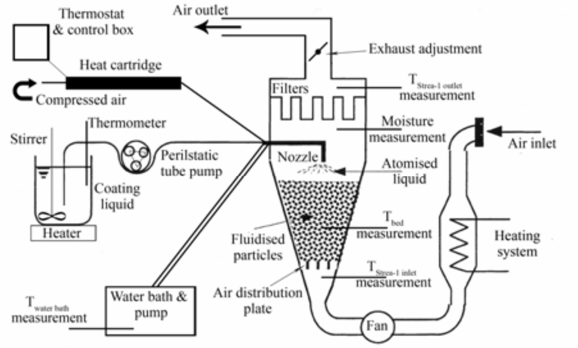

Figure 3: Sketch of the Strea-1 set-up.

Table 1: St_v^* and St_v numbers for the eight coating experiments performed in the Strea-1 set-up.

Experiment	St_v^*	St_v	Experimental Agglomeration percentage
1	3.6	6.0	99.6 %
2	2.7	6.0	81.0 %
3	2.5	6.0	32.2 %
4	2.4	6.0	5.4 %
5	1.4	6.0	0.9 %
6	0.2	6.0	22.2 %
7	3.1	6.0	92.9%
8	1.8	6.0	13.5 %

It may be seen first of all from table 1 that the St_v^* and St_v numbers are generally quite close to each other even though the St_v values are larger than the St_v^* values in all cases. As mentioned earlier, the coating system operates in the "coating regime" when $St_v >> St_v^*$ in which all granule collisions are unsuccessful. This condition is not fulfilled in any of the experiments in the present series as roughly the $St_v \approx St_v^*$ which means that the coating system has been run in the "inertial regime". In this regime the likelihood of permanent coalescence depends of the size of the colliding granules, and granule kinetic energy and binder viscosity plays a role in the success of agglomeration. Being a boundary regime between the "non-inertial regime" where excessive agglomeration occurs and the "coating regime" where no agglomeration occurs, the identification of the "inertial regime" may help to explain why agglomeration is often observed to be such a sensitive parameter during coating operations in general.

Interestingly, it can be seen form table 1 by comparing the sets of $\{St_v , St_v^*\}$ values with the agglomeration percentage values that there is a direct relationship between a high agglomeration tendency and a small distance between St_v and St_v^*. This can be further verified from figure 4 where the difference between St_v and St_v^* is depicted versus the corresponding agglomeration tendency for all eight experiments. Although some scattering in the data set is observed, the tendency with increasing agglomeration with decreasing distance between St_v and St_v^* can be identified. The chance of successful coalescence between two impacting granules increases as St_v^* approaches the St_v value reaching a situation where every collision results in permanent coalescence when $St_v << St_v^*$. Hence according to the viscous Stokes theory, the chance of agglomeration should increase as St_v^* increases in respect to St_v in full accordance with the tendencies seen in table 1 and figure 4.

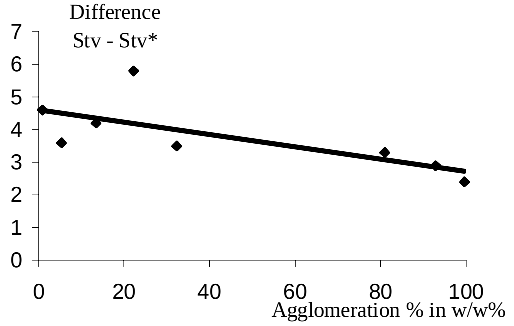

Figure 4: The distance between St_v and St_v^* depicted as a function of the agglomeration percentages for the eight coating experiments performed in the Strea-1 set-up.

Acknowledging that agglomeration is a sensitive parameter this initial approach towards a modelling of the agglomeration tendency quite clearly illustrates that it is in fact possible to approach the agglomeration tendency quantitatively. Further studies including a particle level modelling of the mechanical properties of the liquid binding mechanisms will hopefully improve the precision of the models as well as give the necessary background for further advanced population balance modelling.

Acknowledgements

This Ph.D. project is partly funded by Novozymes A/S who also financially supported the Master project.

The Author is a member of the Novozymes Bioprocess Academy as well as the MP_2T Graduate School in Chemical Engineering

References

1. Hinds, W.C.: Aerosol Technology. Properties, Behaviour and Measurement of Airborne Particles, John Wiley & Sons Inc., 2nd Edition, New York, 1999.
2. Denesuk, M., Zelinski, B.J.J., Kreidl, N.J., and Uhlmann, D.R.: Dynamics of Incomplete Wetting on Porous Materials, Journal of Colloid Interface Science, No. 168, pp. 141-151, 1994.
3. Denesuk, M., Smith, G.L., Zelinski, B.J.J., Kreidl, N.J., and Uhlmann, D.R.: Capillary Penetration of Liquid Droplets into Porous Materials, Journal of Colloid Interface Science, No. 158, pp. 114-120, 1993.
4. Ennis, B.J., Tardos, G. and Pfeffer, R.: A microlevel-based characterization of granulation phenomena, Powder Technology, No. 65, pp. 257-272, 1991.
5. Iveson, S.M., Litster, D.L., Hapgood, K. and Ennis, B.J.: Nucleation, growth and breakage phenomena in agitated wet granulation processes: a review, Powder Technology, No. 117, pp. 3-39, 2001.
6. Davidson, J.F. and Harrison, D.: Fluidized Particles, Cambridge University Press, NY York, 1963.
7. Abbott, A.: Boundary Between Coating and Granulation, Master Thesis, Department of Chemical Engineering, The University of Queensland, 2002.
8. Dewettinck, K.: Fluidized Bed Coating in Food Technology: Process and Product Quality, Ph.D. Thesis, University of Gent, 1997.

List of Publications

1. Hede, P.D., Bach, P. and Jensen, A.D.: "Small-scale top spray fluid bed coating: Influence of selected process and formulation variables on granule impact strength, agglomeration tendency and coating layer morphology", Powder Technology (In preparation).
2. Poster + Oral Presentation for the 5th World Congress on Particle Technology (WCPT5), Orlando, Florida, 2006 (In preparation).

Claus Hindsgaul

Address:	CHEC, Dept. of Chemical Engineering, Building 229, Office 112
Phone:	+45 4525 2838
e-mail:	chi@kt.dtu.dk
www:	http://www.chec.kt.dtu.dk http://bgg.mek.dtu.dk
Supervisors:	Anker Degn Jensen (KT), Bjørn Qvale and Ulrik Henriksen (MEK)
Ph.D. Study	
Started:	February 2003
To be completed:	February 2006

Disintegration of Char Particles during Thermal Conversion

Abstract

The disintegration of char during thermal conversion such as combustion and gasification can be an important factor in the conversion process as the particle size distribution changes and internal surfaces are exposed. In this project the strength and gas transport properties of wood char during combustion will be investigated in order to gain knowledge on the disintegration processes and aid detailed modelling of particle conversion and reactors.

Introduction

The increased utilisation of biomass as fuel for energy production has led to the need for detailed understanding of the behaviour of biomass during thermal conversion. In fixed bed co-current gasification and combustion, the gas permeability of the reaction zone depend heavily on the particle geometry, in particular the particle size distribution. If the char particles break into smaller particles these may cause undesired increases in pressure drop through the particle bed as well as dead zones and channelling, resulting in decreases in efficiency and stability of the reactor. Fluid bed reactors are sensitive to the particle size distribution in order to control fluidisation and the amount of particles escaping the reactor unconverted.

The strength properties and disintegration behaviour of biomass char is a topic, where knowledge is yet very sparse. Wood is known to retain much of its physical structure during charring, and is thus a highly anisotropic material. Detailed knowledge of the microstructure and physical properties of wood are available, but it has only to a very limited extend been utilised to evaluate the properties of wood char in the combustion science. For example, the limited data available on diffusion and heat transfer in char generally assume complete isotropy. This is unfortunate since the mechanical strength of a material is sensitive to inhomogeneities in the material, which can be caused by anisotropic gas and heat transfer.

The goal of this project is to investigate the strength development and breakage behaviour of wood char during conversion. Experimental determination of anisotropic diffusion properties and mechanical strength of wood char from different species will be made, and the results will be evaluated taking into account the wood char microstructure. By way of mathematical modelling, the processes and parameters determining char breakage will be investigated.

Char microstructure

The microstructure of the wood is retained very well in the wood char – despite the severe mass loss (75%) and shrinkage occurring during the conversion from wood to char (pyrolysis). Like wood is an orthotropic material i.e. it has different strength properties in three major orthogonal directions: (1) along the stem (*longitudinal*), (2) along the annual rings (*radial*) and (3) *tangential.*

Beech char have been selected as the basis material in this study. The pore size distributions in the beech char at different degrees of conversion by gasification was measured using mercury intrusion and adsorption isotherms. Light microscopy and scanning electron microscopy (SEM) was used to investigate the structural changes in the converted wood char. As an example, Figure 1 shows SEM pictures of the cell walls seen in the radial direction of char, which have been gasified 10% and 46%. The cell walls are perforated by holes (called “pits”), which are also present in the original wood. The widening of such pits, that these pictures indicate, may improve the gas transport in the radial direction. Such pits are also present in the tangential direction, but not in the same numbers.

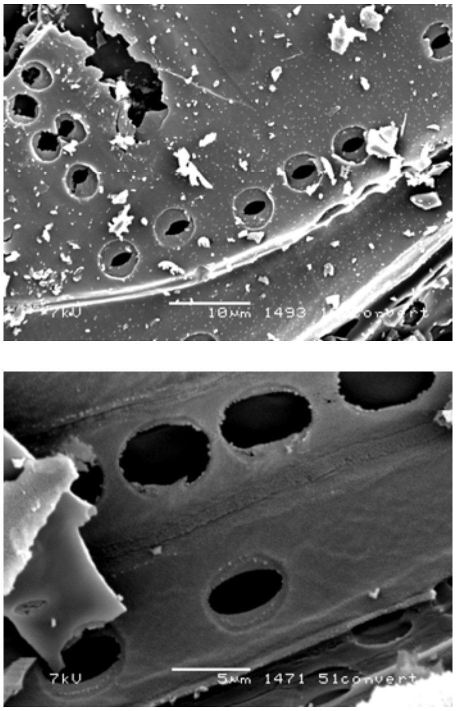

Figure 1: Pits in the beech char cell walls after 10% gasification (upper) and 46% gasification (lower).

Diffusion measurements

In order to study the gas diffusion flux through wood char a Wicke-Kallenbach diffusion cell designed to measure uniaxial diffusion and permeability of char at room temperature was built at The Department of Chemical Engineering. Figure 2 shows a diagram of a Wicke Kallenbach cell. The sample is placed between two chambers (A and B). A flow of two different pure gases (e.g. NO and CO) are blown onto the surface of each of the two chambers. “Gas A” in “chamber A” and “Gas B” in “chamber B”. The gas flow from chamber A will contain small amounts of gas B due to diffusion from chamber B through the sample. By analysing this concentration, the amount of gas B passing through the sample can be quantified. The same procedure is applied simultaneously to quantify the transfer of gas A through the sample. It is essential that there is a very low pressure difference between the sample surfaces in order to avoid forced convection through the sample. Grahams law can be used to verify this, when the gas transfer of both gases are quantified simultaneously as described above. Grahams law predicts that for ordinary and Knudsen diffusion (that is, with negligible forced flow and surface diffusion), the ratio of the opposing flow rates of the gases equals the square root of the ratio of their molar masses.

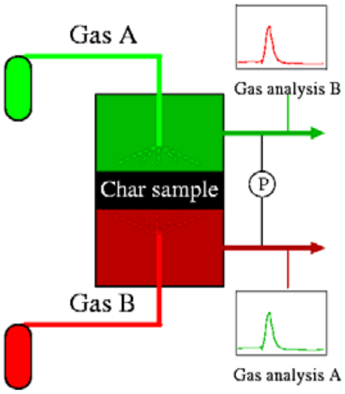

Figure 2: Schematic diagram of a Wicke-Kallenbach diffusion cell

The dusty gas model [1] of gas diffusion in porous media was used to derive the effective binary diffusion coefficient, $\mathcal{D}_{AB,eff}$ for ordinary diffusion of the used gas pair (gas A and B) through the char sample. For a given porous media, $\mathcal{D}_{AB,eff}$ is a certain fraction of the binary diffusion coefficient, $\mathcal{D}_{AB}$, for the same gases in an open space. Thus the *diffusion coefficient ratio* $\mathcal{D}_{AB,eff}/\mathcal{D}_{AB}$ is a constant, which is specific to the porous media. This fraction is often called the *porosity-tortuosity factor*, since in porous media with simple pore structures, it can be expressed as the ratio its porosity to its tortuosity (the length the gas has to travel relative to the direct distance):

$$\frac{D_{eff,AB}}{D_{AB}} = \frac{porosity}{tortuosity} \qquad (1)$$

This relation fails for media with very bimodal pore structures, constrictions or pore diameters <50Å. Since wood char have all of these properties, the ratio will be referred to as the *diffusion coefficient ratio.*

For orthotropic media such as wood char, the ratio can assume different values in the three principal directions. These were found by testing char samples cut in different orientations (longitudinal, radial and tangential). The development of diffusion properties during conversion was investigated by using samples subjected to different degrees of conversion by gasification. All samples were pyrolysed at 600C before gasification.

The char samples were cylindrical (thickness ~10 mm, diameter ~15 mm) and the sides were sealed with silicon paste. The pressure difference between the chambers was surveyed by a micromanometer. At all times it was below 0.3 Pa, which could only cause negligible forced flow.

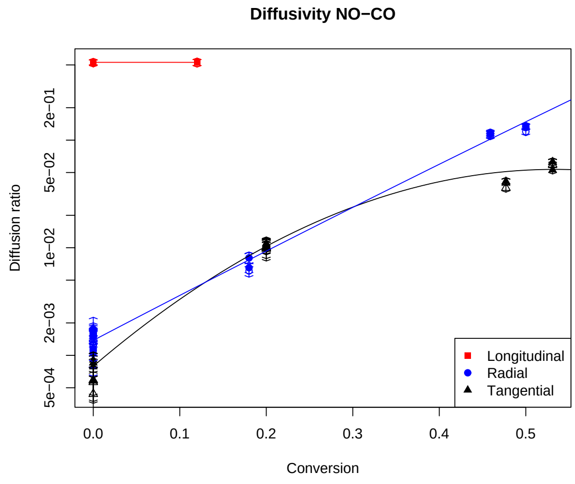

Figure 3: Uniaxial diffusion coefficient ratios ($\mathcal{D}_{AB,eff}$/ $\mathcal{D}_{AB}$) for beech char at different degrees of conversion.

The results are shown in Figure 3 for all three principal directions of the wood char. The *x*-axis shows the degree of conversion by gasification, while the *y*-axis is the measured diffusion coefficient ratio.

Large differences in the diffusion coefficient ratio in different directions were found; at zero conversion tangential diffusion was approximately 3 orders of magnitude smaller than the longitudinal diffusion.

The longitudinal diffusion coefficient ratio was 0.5, which was close to the sample porosity. In this direction, it can be safely assumed that transport mainly occur in a simple system of large pores. Thus equation 1 shows that the tortuosity is close to unity, which is consistent with the known pore structure of large straight pores in this direction.

Diffusion in the other directions was found to be severely limited, but increasing as the degree of conversion by gasification increased.

Gas permeability

The permeability, Φ, of a porous media is the proportionality factor between the pressure gradient and the molar gas flux:

$$J = -\Phi \frac{c}{\mu}\frac{\partial p}{\partial x}$$

where *J* is the gas molar flux, *c* and μ are the gas molar concentration and viscosity, and $\frac{\partial p}{\partial x}$ is the pressure gradient.

The uniaxial permeability was measured in the Wicke-Kallenbach setup forcing a flow of nitrogen through the sample and measure the resulting pressure difference. The results are shown in Figure 4. The permeability is given in milliDarcies (1 mD = 10^{-15}m^2).

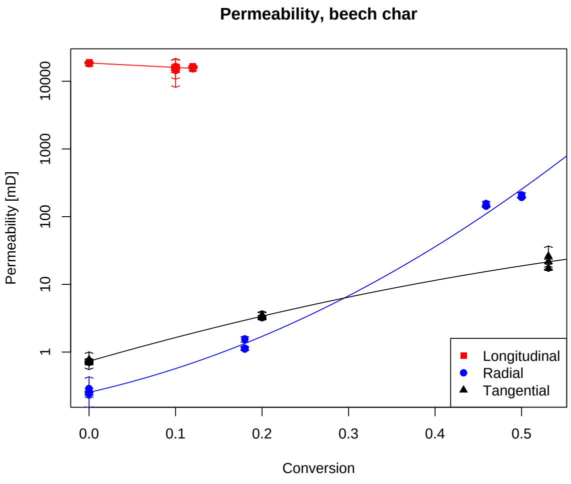

Figure 4: Uniaxial permeability for beech char at different degrees of conversion.

Generally the permeability follow the same trends as the diffusion coefficient ratio. The differences between different directions are even larger at zero conversion: The tangential permeability is more than four orders of magnitude smaller than the longitudinal permeability.

Modelling

A model is being developed to describe the influence of the large differences in gas transport properties in different directions found, and predict the resulting tensions and crack development.

Conclusion

Gas transport properties in the different directions in beech wood char have been measured. The structural changes in the char during gasification have been evaluated and will be used to quantitatively explain the changes in gas transport properties.

References

[1] E. A. Mason and A. P. Malinauskas, Gas Transport in Porous Media: The Dusty-Gas Model, Elsevier Scientific Press, vol. 17, 1983.

Acknowledgements

This project is kindly funded by the energy research programme (EFP) of the Danish Energy Agency. It is a cooperative effort between the CHEC group at the Department of Chemical Engineering and the Biomass Gasification Group at the Department of Mechanical Engineering at DTU.

Lusi Hindiyarti
Address: Building 229, room 122
Phone: +45 4525 2922
Fax: +45 4588 2258
e-mail: lh@kt.dtu.dk
www: http://www.chec.kt.dtu.dk

Supervisors: Peter Glarborg
Hans Livbjerg
Flemming Frandsen

Ph.D. Study
Started: September 2003
To be completed: August 2006

Gas Phase Sulfur, Chlorine, and Alkali Metal Chemistry in Biomass Combustion

Abstract

The high-temperature sulfur/chlorine/potassium chemistry has important implications for sulfur/chlorine emissions (SO_2, HCl), aerosol formation (KCl, K_2SO_4) and deposits formation in combustion. The S/Cl/K chemistry in combustion involves both gas phase and condensed phase reactions. An attempt to improve the gas phase chemistry model with addition of a simple aerosol formation mechanism to the model is being done. The model is validated using experimental results. A better understanding of the gas phase chemistry and successful modeling of these components may facilitate development of more efficient methods to minimize emission and operation problems in biomass or waste combustion also in boiler design.

Introduction

Combustion and gasification of renewable fuels (biomass, waste) involves a number of chemical reactions, which are important for emissions, aerosol formation and deposition/corrosion. The high-temperature sulfur/chlorine/potassium chemistry has important implications for sulfur/chlorine emissions (SO_2, HCl), aerosol formation (KCl, K_2SO_4) [1,2] and deposits formation in combustion [3].

Significant efforts in the past have focused on chlorine and sulfur chemistry, but little is known about alkali metal chemistry or the interaction between S, Cl and K. The S/Cl/K chemistry in combustion involves both gas phase and condensed phase reactions [4]. Despite the practical importance of Cl/S/K-interactions, few attempts have been made to understand the detailed kinetics of the system. Current modeling is largely limited to chemical equilibrium calculations. Such calculations do not account for kinetic limitations, which are known to be important for conversion of HCl to Cl_2 or SO_2 via SO_3 to H_2SO_4. Conversion of KCl to formation of K_2SO_4, a critical step in aerosol formation, is presumably also kinetically limited but little is known.

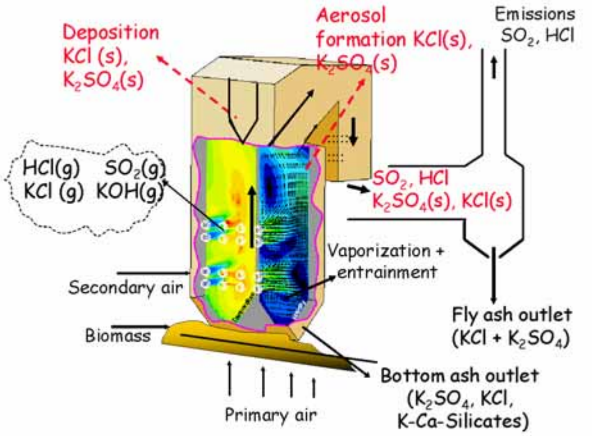

Figure 1: Illustration of the release and fate of K, Cl, and S in biomass combustion.

A better understanding of the gas phase chemistry of these components may facilitate development of more efficient methods to minimize emission and operation problems in biomass or waste combustion systems.

Objective

The objective of this project is to improve the fundamental knowledge of the gas phase chemistry which is important for emissions, aerosol or deposit formation in combustion of biomass and waste. The aim is to improve the available detailed chemical kinetic model for conversion of chlorine, sulfur and alkali-containing species and their interaction. Such a chemical description can be implemented in reactor models and used to simulate effect of fuel and process parameters on emissions and operation.

Modeling

Gas Phase Chemistry

Presently, existing kinetic models; provide a fairly good description of hydrocarbon oxidation and nitrogen chemistry in high temperature processes. Also a significant knowledge about sulfur and chlorine chemistry is available. Detailed mechanisms for alkali metal chemistry and S/Cl/K/Na interactions have been proposed recently [6]. Using the proposed mechanisms mentioned above as starting mechanisms, the model is expected to be extended and improved by conducting several experiments related to the system. The experimental and modeling work will be a step-by-step attempt to extend our knowledge of this chemistry. The Senkin code which runs in conjunction with Chemkin-II was used to model the flow reactor experiments, assuming plug flow. The reaction mechanism and thermodynamic properties used in this study were drawn mainly from the work of Glarborg and Marshall [6]

The reaction mechanism consists of subsets for CO/H_2, chlorine chemistry, sulfur chemistry and potassium chemistry.

Aerosol Formation

In biomass combustion as described in the figure 1 above, the gas phase chemistry of alkali metal, sulfur and chlorine is also accompanied by aerosol formation. Formation of aerosols is initiated by a nucleation process, which is a first order phase transition problem, where there is discontinuous change between two phases. In this work a simple model assuming all of the SO_3 formed in the gas phase will form aerosols is applied. The model prediction is validated with the experimental data available from the literature [8].

Experimental work

Potassium and Chlorine Chemistry

The experiments were done in an alumina tube reactor to simulate plug flow under well controlled reaction conditions. The inner diameter of the main tube was 24mm and it had a wall thickness of 3 mm. The length of the reactor and reaction zones was 750 mm and 300 mm, respectively. The alumina inner tube for KCl feeding was 12 mm in diameter and 150 mm in length, with a wall thickness of 2 mm.

The reactor inlet consisted of main and secondary inlet flows. Potassium was fed by saturating a nitrogen flow from the main inlet with potassium vapor in a packed bed of inert porous alumina pellets impregnated with potassium chloride. The packed bed of pellets was inserted in the inner tube close to the entrance section of the reactor. In order to avoid contact with the KCl in the pellets, the reactive gas was fed to the secondary flow. The two inlet flows were merged at the end of the inner tube.

Feed gases contained CO, H_2O, and N_2 of about 1 NL/min was used. The amount of KCl vapor was varied by setting the flow to the alumina packed bed. The gas outlet was analyzed for CO and CO_2 after gas conditioning. Pure CO oxidation experiments were done for reference.

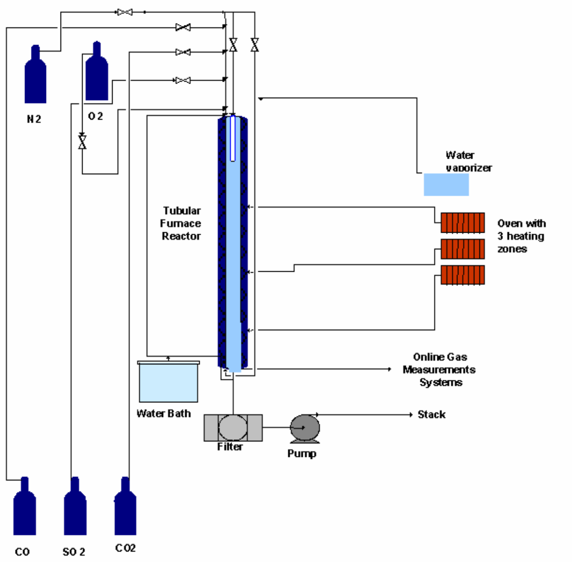

Figure 2: The schematic of experimental set-up for potassium and chlorine chemistry

Sulfur Chemistry

Experimental set-up used is one described in figure 3. The set-up consist two consequent reactors. In the first reactor, SO_2 was oxidized to SO_3 over the doped V_2O_5-WO_3-TiO_2 catalyst. The temperature in the catalytic reactor was set to 673 K. The product gas from this reactor was fed into the second reactor through a heated line in order to avoid condensation. The second reactor was homogeneous, operated at high temperatures (773 to 1373 K) to investigate the gas phase sulfur chemistry and its interaction with radical pools.

Sulfur dioxide, oxygen and nitrogen were fed to the catalytic reactor. The output of the catalytic reactor was fed to the quartz homogeneous reactor with adding some additional gas CO or N_2O. The concentration of SO_2 and CO or N_2O outlet from the homogeneous reactor was measured continuously by gas analyzers.

Result and Discussion

Potassium and Chlorine Chemistry

Experiments were performed by increasing the temperature in steps of 25 K. The initial mole fractions of CO were around 1900-2150 ppm or 7800 ppm. The concentration of the oxidizing agent, H_2O, was kept constant as 0.052, with N_2 as balance gas. The KCl vapor concentration was varied as 0, 157, 313, 470, or 626 ppm. Oxygen was present as an impurity, and the concentration was estimated to be approximately 75 ppm. The residence times used in the experiments are 0.95 - 1.70 seconds.

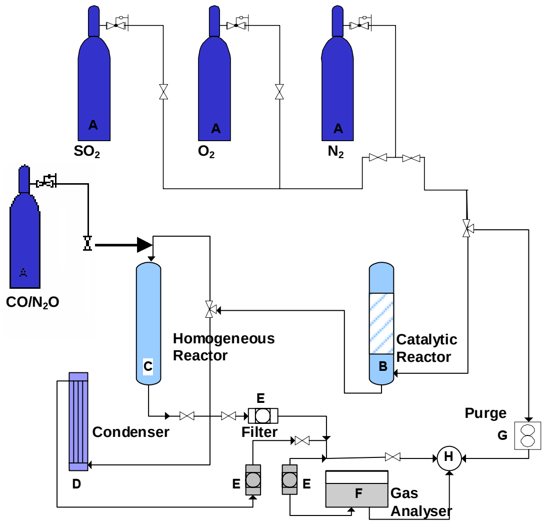

Figure 3: The schematic drawing of experimental set-up for sulfur chemistry

CO Oxidation without KCl Present

The oxidation of carbon monoxide (CO) under very reducing conditions was studied for a mixture of CO and H_2O with CO inlet concentrations around 1900 or 7800 ppm. The promoting effect of water vapor in larger amounts is opposite to what has been observed for CO oxidation under oxidizing condition; here an increase in the H_2O/CO inlet ratio will typically decelerate the CO oxidation.

From pathway analysis and sensitivity analysis the key reactions for CO/H_2 subset under the present conditions were identified. The CO conversion is dominated by $CO+OH \leftrightarrow CO_2+H$, which is also the most sensitive reaction in the system.

Since the OH radical is required for the reaction to occur, the availability of water will control the system. Most of the OH radicals are generated through the reaction $H_2O+H \leftrightarrow OH+H_2$ and only a small amount is formed by the reaction $H_2O+O \leftrightarrow OH+OH$.

In the interpretation of the flow reactor results, the potential impact of oxygen impurities and of reactions on the alumina reactor surface had to be taken into consideration. The presence of trace amounts of O_2 enhances the oxidation rate through $H+O_2 \leftrightarrow O+OH$, and $O+H_2O \leftrightarrow 2OH$. The amount of oxygen was estimated by kinetic modeling and assumed to be the same in all experiments.

The surface reaction was represented by a hydrogen atom loss at the reactor walls. The results of the model equipped with the hydrogen atom loss mechanism agree quite well with data for the clean reactor.

The presence of potassium chloride could be expected to alter the surface reactivity. Various potassium powders have been shown to enhance radical recombination on their surface.

These results suggest that the surface reactivity toward radicals has increased considerably due to the presence of potassium on the wall. Similar to the procedure used for the clean reactor, a hydrogen atom loss rate at the reactor wall was derived based on trial and error to achieve the closest agreement between modeling and experimental results. The resulting rate constant, k_{dirty}= 2.8 x 10^3 exp (-9800/RT) s^{-1} for the dirty reactor is more than two orders of magnitude higher than the value for the clean reactor.

This revised mechanism subset for the dirty reactor is used in the subsequent modeling with KCl addition.

CO Oxidation with KCl Present

A number of experiments with KCl addition to the $CO/H_2O/N_2$ system were conducted, varying the CO and KCl inlet concentrations. The presence of KCl clearly has an inhibiting effect on the CO oxidation; as the inlet KCl level increases, the CO conversion into CO_2 decreases, resulting in higher fraction of $CO/CO_{initial}$ (higher CO outlet). The inhibiting effect of KCl addition can be seen in the experimental data both with lower and higher CO inlet concentration. Similar to what has been observed in flames, the effect of potassium is non-linear, with increasing seeding levels resulting only in minor additional inhibition of the oxidation.

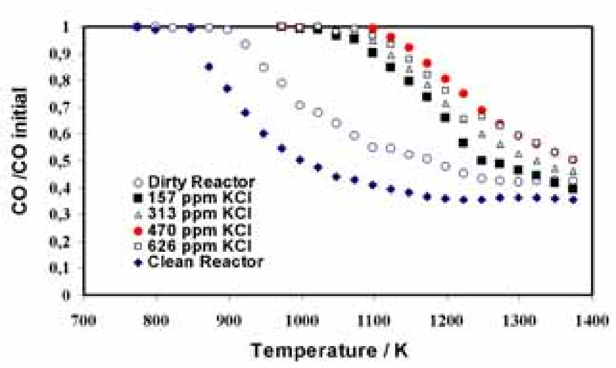

Figure 4: The fractions of $CO/CO_{initial}$ from the reactor from CO oxidation experiment with 0-626 ppm KCl addition, inlet composition CO: 7800 ppm; H_2O: 0.052; N_2: balance gas; and O_2 from kinetic modeling estimation (75 ppm).

Overall the results confirm that the potassium deposited on the alumina reactor surface reactivity is active and has some influence on the CO conversion in the reactor. However, the gas phase potassium chemistry dominates the CO oxidation rate and the experimental results are useful for characterizing the potassium/radical pool interaction.

Reaction-path analysis and sensitivity analysis were conducted to identify the key reactions under the present conditions. According to our kinetic model, the presence of KCl does not alter the key reactions for CO conversion.

After vaporization, part of the KCl is converted to KOH by reaction $KCl+H_2O \leftrightarrow KOH+HCl$. Potassium hydroxide is predicted to build up to a few ppm and then slowly decay. As the H atom concentration builds up, KCl is converted mainly to K atoms through reaction $KCl+H \leftrightarrow K+HCl$. The K atom reacts through several reactions, mainly $K+HO_2 \leftrightarrow KOH+O$ and $K+OH+M \leftrightarrow KOH+M$ with minor contributions through reaction $K+O_2(+M) \leftrightarrow KO_2(+M)$. Potassium dioxide will form KO by reacting with CO through reaction $KO_2+CO \leftrightarrow KO+CO_2$.

And potassium hydroxide will react further according to the reactions $KOH+HCl \leftrightarrow KCl+H_2O$ and $KOH+OH \leftrightarrow KO+H_2O$. According to the model, KO reacts almost solely through reaction with CO, $KO+CO \leftrightarrow K+CO_2$.

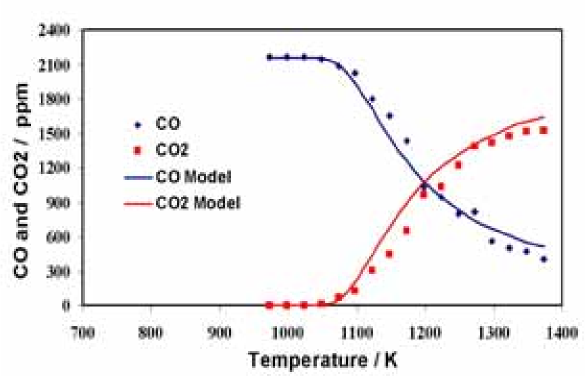

Figure 5: The outlet mole fractions of CO and CO_2 in CO oxidation experiments with CO: 2100 ppm, KCl: 626 ppm, H_2O: 0.052, N_2: balance gas, and O_2 from kinetic modeling estimation (75 ppm) . The solid lines denote modeling results and the symbols are experimental results.

To identify the rate limiting steps in the inhibition of CO oxidation by KCl, an A-factor sensitivity analysis was performed. The analysis indicates that the oxidation rate is mainly sensitive to the reactions that generate or consume free radicals in the system.

The sensitivity analysis indicates that the chain terminating reaction $K+OH+M \leftrightarrow KOH+M$ is the rate limiting step of the potassium inhibition to the CO oxidation system. For this reason the value of rate constant for this reaction has a considerable impact on the model predictions.

Glarborg and Marshall [6] adopted the rate constant proposed by Husain et al. [9], $k= 5.4 \times 10^{21} T^{-1.55}$. Using this value, experimental results and modeling prediction agree qualitatively, but the inhibiting effect of KCl is underpredicted. The expression by Husain et al. was based on a direct measurement at 530 K (with He as bath gas) and an extrapolation to high temperatures by RRKM theory. In the present work, we have chosen a rate constant of $k= 3.8 \times 10^{19} T^{-0.65}$. This value is in agreement with the measurement of Husain et al. at 530 K, assuming the collision efficiency of N2 to be twice that of He, and with the high temperature data of Jensen et al. [10], obtained from analysis of H2/O2/N2 flames doped with potassium.

The chosen rate constant (k) results in a significantly improved agreement between modeling predictions and experimental results as shown in figure 5. However, experimental uncertainties and uncertainties in the chemical kinetic model preclude a determination of rate constant for $K+OH+M \leftrightarrow KOH+M$ from the present work.

The experimental uncertainties include the amount of KCl fed to the gas phase, the oxygen concentration, and surface reactions at the reactor wall. The model uncertainties involve the heat of formation of KOH and the rate constants for potential key reactions.

Summary for Potassium and Chlorine Chemistry

Experimental results on the influence of gas phase potassium on CO oxidation under reducing conditions have been obtained. The addition of KCl results in a strong inhibition of the CO oxidation. The inhibition increases with the KCl level, but the effect levels off at high concentrations. The experimental data were interpreted in terms of a detailed chemical kinetic model. Analysis of the modeling results indicates that the reaction $K+OH+M \leftrightarrow KOH+M$ is rate controlling for the radical recombination. The experimental data support a high rate constant for this reaction, but an estimation of the value from the present work is difficult due to uncertainties in the potassium chemistry and in the experimental conditions. Experimental data in a wider range of conditions and alkali precursors is required for model improvement.

Aerosol Modeling

The result of simple modeling assuming all of the SO_3 formed in the gas phase to form potassium sulfate was compared to the experimental data by Jensen et al. [8] can be seen in table 1.

Table 1: Summary of the modeling prediction in aerosol formation compare to the experimental data by Jensen et al. using similar inlet composition and temperature profile.

No	T_{peak} °C	SO_2 ppm	KCl ppm	O_2 %	H_2O %	S/(S+Cl) Exp	S/(S+Cl) Model
1	950	200	200	4	4	6.8	0.77
2	950	100	200	4	4	5	0.48
3	950	200	200	19	4	15.9	1.74
4	1000	200	200	4	4	7.9	1.26
5	800	200	200	4	4	5.9	0.43
6	770	200	200	4	4	7.1	0.17

The results of modeling prediction clearly under predict the data from experimental work.

Role of Sulfur in Aerosol Formation

Conversion of sulfur from SO_2 to SO_3 in straw case is about 7%. In the modeling, the conversion of sulfur is more less the same in the case of normal combustion, around 16 %. In the case of comparison between model prediction and experimental data of Nielsen et al., the sulfur conversion is very low due to the slow kinetics of SO_2 oxidation below 800 °C. Christensen and co-workers assumed that SO_2 oxidation to SO_3 was a limiting step for K_2SO_4 aerosol formation.

Investigation of the influence of SO_2 and O_2 composition to the final particle composition results in the higher conversion of SO_2 to SO_3 in a high temperature but is lower in a lower temperature (around 1100 °C).

The HCl and SO_2 outlet from the model prediction, shows insignificant value while in field experiment done by Christensen et al. [7], it gave a significant amount of those species.

Effect of Operating Conditions

Aerosols from straw combustion field measurement were done by Christensen et al. shows no evident of correlation between temperature and submicron mass concentration estimated from SMPS data. They suggested that it may be a result of a very strong influence of random fluctuations in the straw composition.

For the laboratory scale experiments, data from straw combustion by Nielsen et al. shows that peak temperature in the oven and the concentration of O_2 and SO_2 influenced the aerosol formation. The results of the experiments show that the peak temperature has a small effect towards degree of sulfation and the size distribution of the aerosol particles. They suggested that it might be that the degree of sulfation depends on the temperature-time history of the gas at an intermediate temperature level, possibly in the 700 - 750 °C range, where the sulfation reaction rate is finite and not in the equilibrium controlled high temperature range [8]. This agrees with aerosol field measurements by Christensen and co workers. They also suggested that the theory they proposed above is supported by the fact that there is strong influence of the O_2 and SO_2 concentrations on the degree of sulfation.

The modeling results for straw combustion agree qualitatively with the experimental data, but the model prediction shows that the peak temperature gives a significant influence to the degree of sulfation.

Conversion of SO_2 to SO_3

The SO_2 and SO_3 concentrations in the gas phase is said to be determined by set of reactions $SO_2 + O (+M) \leftrightarrow SO_3 (+M)$ and $SO_3 + O \leftrightarrow SO_2 + O_2$.

The sensitivity analysis from model prediction shows that the reaction $SO_2+O(+M) \leftrightarrow SO_3 (+M)$ is one of the most sensitive reactions in the system, but reaction $SO_3+O \leftrightarrow SO_2+O_2$ is found not to be important in the current investigation, in another hand there are other reactions that are the bottle necks oxidation of SO_2 to SO_3 in the gas phase. These reactions are: $KO+SO_2 \leftrightarrow K+SO_3$, $SO_2+OH \leftrightarrow SO_3+H$, $SO_2+OH(+M \leftrightarrow HOSO_2 (+M)$.

Rate production analysis shows that, the reaction $KO + SO_2 \leftrightarrow K + SO_3$ is very dominant. Followed by $SO_2+O(+M) \leftrightarrow SO_3 (+M)$. And very minor contribution by reactions: $HOSO_2+O_2 \leftrightarrow HO_2+SO_3$ and $SO_2+OH \leftrightarrow SO_3+H$.

Summary for Aerosol Modeling

Comparison between model prediction and experimental data for aerosol formation in biomass combustion in case of straw has been done. The results of model prediction agree qualitatively with experimental data by Jensen et al. Both model and experiments shows the formation of sulfate aerosol is strongly influenced by the degree of conversion of SO_2 to SO_3 which also depends on O_2 inlet concentration and temperature history.

The quantitative agreement is not achieved since there is possibilities of some catalyzed reactions which enhance the conversion from SO_2 to SO_3 in the system. The catalytic effect might be induced by the particle (from the reactor refractory or deposit) onto the reactor wall.

Sulfur Chemistry

To investigate the kinetics of some important sulfur reactions mechanism, such as reactions $SO_3+O \leftrightarrow SO_2 + O_2$, $SO_3+ M \leftrightarrow SO_2+O+M$, $SO_2+OH \leftrightarrow SO_3+H$, several experiments were performed.

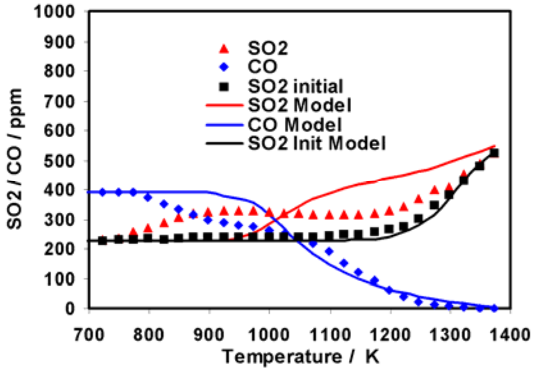

Figure 6: The outlet mole fractions of CO and SO_2 in sulfur chemistry experiments with inlet composition SO_2: 225 ppm , SO_3: 356 ppm, H_2 : 100 ppm, O_2: 4.7 %, CO: 393 ppm, N_2: balance gas. The solid lines denote modeling results and the symbols are experimental results.

The results of experiments show that the addition of CO or N_2O to the $SO_3/SO_2/O_2/N_2$ gas phase system clearly has a significant influence. The results of a detailed kinetic modeling of the $SO_3/SO_2/O_2/N_2$ systems from the experimental work are seen to be in good agreement with the theoretical rate coefficients. In the case of CO or N_2O addition to the system, there is a significant discrepancy between results of detailed kinetic modeling with the experimental data as can be seen in figs. 6 and 7. A rate constant was proposed. But due to unsatisfying agreement between experimental data and kinetic modeling, a determination of a value can not be done.

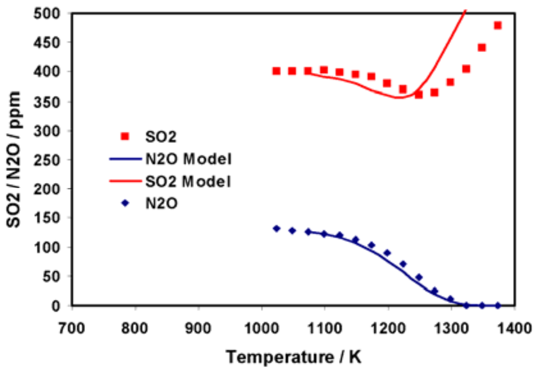

Figure 7: The outlet mole fractions of N_2O and SO_2 in sulfur chemistry experiments with inlet composition: SO_2: 401 ppm , SO_3: 202 ppm, H_2O: 100 ppm, O_2 : 1.01 %, N_2O: 131 ppm, N_2: balance gas. The solid lines denote modeling results and the symbols are experimental results.

An assessment of the kinetics in the reactions involved in the system is still on going work. Further study of these reactions would increase the confidence with which model predictions of SO_3 can be viewed.

Acknowledgements

Financial support for this project by PSO-Elkraft is gratefully acknowledged. Also author would like to acknowledge the technicians in the CHEC group for invaluable helps in the setting up of experimental work.

References

1. K.A. Christensen, H. Livbjerg, Aerosols science and Technology, (2000) 33, 470-489.
2. L.B. Nielsen, H. Livbjerg, J. Aerosol Sci. (1996), 27(I), S367-S368.
3. H.P. Michelsen, O.H. Larsen, F.J. Frandsen, K.D. Johansen, Fuel Process. Technol. (1998), 54, 95-108.
4. K. Iisa, Y. Lu, Energy & Fuels (1999), 13, 1184-1190.
5. I. Obernberger, T. Brunner and M. Joller, Characterization and Formation of Aerosols and Fly ashes from Biomass Combustion, Report EU Project ‘ Aerosols from Biomass Combustion’, 2001.
6. P. Glarborg, P. Marshall, Combust. Flame (2005)141, 22-39.
7. K.A. Christensen, PhD Thesis, Aerosol Laboratory, Chemical Engineering, DTU.
8. J.R. Jensen, L.B. Nielsen, C. Schults-Moller, S. Wedel, and H. Livbjerg, Aerosols science and Technology, (2000) 33, 490-509.
9. D. Husain, J Chem Soc Faraday Trans, (1989)85, 85-130.
10. D.E. Jensen, G.A. Jones, ACH Mace, J Chem Soc Faraday Trans I, (1979)75, 2377-85.

List of Publications

1. L. Hindiyarti, F. Frandsen, H. Livbjerg, P. Glarborg, “Influence of potassium chloride on moist CO oxidation under reducing condition” accepted in FUEL journal, article in press November 2005.
2. L. Hindiyarti, F. Frandsen, H. Livbjerg, P. Glarborg, 1st Baltic Combustion Meeting, Warsaw, 27-29 November 2005.
3. L. Hindiyarti, J. Kjällstrand and J. Frederick, “Chemical mechanisms of tar formation and destruction during gasification of biomass-derived fuels”, Colloquium on Black Liquor Combustion and Gasification, Park City, Utah, 13-16 May 2003.
4. A. Yilmaz, L. Hindiyarti, A.D. Jensen, P. Glarborg, P. Marshall, “Thermal dissociation of SO_3 at 1000-1400 K” submitted for Journal of Physical Chemistry A, October 2005.

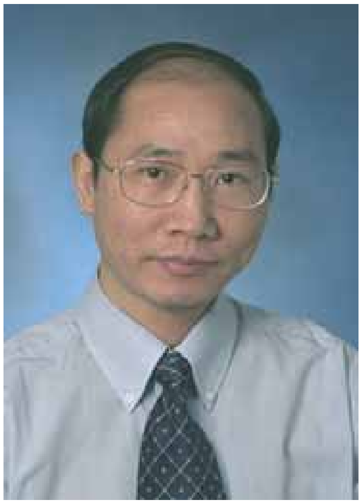

Guilin Hu
Address: Building 229, Søltofts Plads, DTU
Phone: +45 4525 2831
Fax: +45 4588 2258
e-mail: gh@kt.dtu.dk
www: http://www.chec.kt.dtu.dk

Supervisors: Prof. Kim Dam-Johansen
Assoc. Prof. Stig Wedel

Ph.D. Study
Started: February 2004
To be completed: January 2007

SO_2 Emission from Cement Production

Abstract

The emission of SO_2 from cement production is mainly due to the oxidation of pyrite contained in the raw materials. In the so-called “dry process”, the SO_2 emission problem is caused by the fast oxidation of the pyrite and the relatively slow sulfation reaction in the first two stage cyclones during preheating in the cyclone preheater.

The oxidation of the pyrite in the raw materials is significantly influenced by reaction conditions such as temperature, oxygen concentration, particle size and flow condition, and may take place by direct oxidation or by a two-step process (first thermal decomposition of the pyrite and then successive oxidation of the formed pyrrhotite) depending on the reaction conditions. In the cyclone preheater, the pyrite is directly oxidized in the first stage cyclone (the one on the top), but may be oxidized by the two-step process in the second stage cyclone.

The sulfation reaction of limestone in the cyclone preheater is the so-called “direct sulfation reaction” (limestone reacts with SO_2 in uncalcined state). This reaction can be significantly influenced by conditions such as gas composition, temperature and additives.

Introduction

Today, the so called “dry process” is the dominant process technology used for cement production due to its superior energy efficiency. In this process, raw materials are first milled to the required particle size and mixed to form raw meal (homogenised mixture of raw material powders). The raw meal is then preheated in a cyclone preheater through direct heat exchange with the hot flue gas from the rotary kiln and/or the calciner. After preheating, the raw meal passes first through the calciner, where limestone in the raw meal is calcined. The calcined raw meal goes then into the rotary kiln, where the raw meal is burned at high temperatures to form cement clinker. The formed clinker is then cooled down and milled to produce final cement products.

Figure 1 illustrates an in-line dry kiln system with a preheater consisting of 5 cyclones (the upper 4 cyclones are used for preheating).

In each stage of the cyclone preheater, the raw meal particles are suspended in the up-going and hot flue gas in the riser in cocurrent flow and heated up. The solid phase is then separated in the cyclone and enters the stage underneath. The flow in the preheater is cocurrent in each cyclone, but count current in general. The raw meal is typically heated up from app. 350K to app. 1073K before it enters the calciner. The flue gas is typically cooled down from app. 1173K to app. 573K.

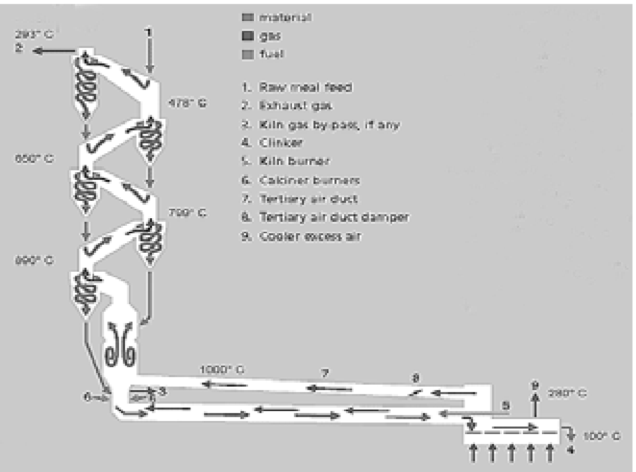

Figure 1 Illustration of a 5 stage cyclone preheater.

Cement production uses different types of limestone, clay and shale as raw materials. These raw materials are all minerals, and contain often a few percent of pyrite (FeS_2). During the preheating process in the cyclone preheater the sulfur contained in the pyrite is oxidized to SO_2 by the hot and oxygen-containing flue gas from the rotary kiln and/or the calciner. Part of the formed SO_2 is absorbed on the limestone particles in the raw meal. The rest is released into atmosphere with the flue gas, and is the main source of SO_2 emission from cement production. The emission level of SO_2 from different plants can vary from a few hundred ppm to several thousand ppm depending on the pyrite content in the used raw materials. It is desired that this emission is reduced as much as possible in the benefit of better environment.

Specific Objectives

In this project, the oxidation of pyrite and the sulfation reaction between limestone and SO_2 will be studied in laboratory scale reactors under the conditions similar to those in a cyclone preheater with the purpose of getting better understanding on the mechanisms and kinetics.

Oxidation of Pyrite

The oxidation of pyrite in an oxygen-containing atmosphere is complicated. Three different situations can occur depending on the reaction conditions [1, 2, 3, 4] as illustrated in Figure 2:

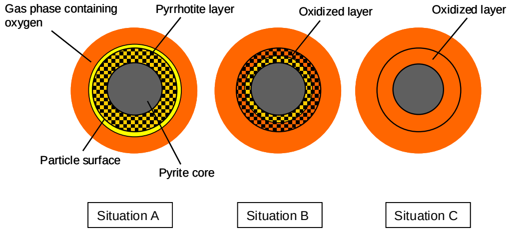

Figure 2 Illustration of pyrite transformation in an oxygen-containing atmosphere.

In situation A, the oxidation of pyrite takes place by a two-step process. The pyrite undergoes first thermal decomposition to form pyrrhotite and sulfur gas. The formed pyrrhotite is then oxidized successively after the decomposition process is completed. This situation can occur when the oxidation of the sulfur gas outside the particle is able to consume all oxygen during its diffusion to the particle surface. This is normally the case when the reaction temperature is high and/or the oxygen concentration is low. The whole process can be represented by the following overall reactions:

Pyrite decomposition:

$$FeS_2(s) = FeS_x(s) + (1-0.5x)S_2(g)$$

Oxidation of sulfur gas:

$$S_2(g) + 2O_2(g) \rightarrow 2SO_2(g)$$

Oxidation of pyrrhotite:

$$2FeS_x(s,l) + (1.5+2x)O_2(g) \rightarrow Fe_2O_3(s) + 2xSO_2(g)$$

$$3FeS_x(s,l) + (2+3x)O_2(g) \rightarrow Fe_3O_4(s,l) + 3xSO_2(g)$$

In situation B, the pyrite is also oxidized by the two-step process as in situation A. The oxidation of the formed pyrrhotite takes place now alongside the gas phase oxidation of sulfur gas before the completion of the decomposition of the pyrite. This situation can occur when the reaction temperature is not very high and the oxygen concentration is relatively high. The overall reactions are the same as in situation A.

In situation C, oxygen is in direct contact with the pyrite core. The pyrite is now oxidized directly. This situation can occur when the reaction temperature is low (often lower than about 800K) and the oxygen concentration is high. During the direct oxidation, small amounts of iron sulfates may be formed. This will result in a denser product layer since the molar volumes of iron sulfates are much higher than those of iron oxides. This dense layer will restrict the inward diffusion of the oxygen and the outward diffusion of the sulfur gas, and then influence the overall oxidation process. The whole process can be represented by the following overall reactions:

Oxidation of pyrite:

$$2FeS_2(s) + 5.5O_2(g) \rightarrow Fe_2O_3(s) + 4SO_2(g)$$

Formation of sulfates:

$$Fe_2O_3(s) + 3SO_2(g) + 1.5O_2(g) \rightleftarrows Fe_2(SO_4)_3(s)$$

$$FeS_2 + 3O_2 = FeSO_4 + SO_2$$

Which kind of situation occurs in practice will depend on the relative rates of the transport of oxygen to and into the particle and the thermal decomposition of pyrite under given conditions (the oxidation of sulfur gas can be assumed to be infinitively fast). The two-step process will take place if the rate of the oxygen transport through the gas film and the product layer toward the interface of the unreacted pyrite core is slower than what is needed for the oxidation of the sulfur gas generated by the decomposition of the pyrite. In this case, the oxygen will be consumed before it reaches the interface of the unreacted pyrite core. Direct oxidation of pyrite will take place if the rate of oxygen transport through the gas film and the product layer is faster than that needed for the oxidation of the released sulfur gas. In this case, the oxygen is able to reach the interface of the unreacted pyrite core.

Recent investigation [5] shows that in a cyclone preheater-like environment, the oxidation of pyrite contained in shale is strongly influenced by temperature, oxygen concentration and flow condition, and becomes significant at a temperature that is higher than around 623K. The formation of SO_2 is observed to be reduced significantly with the increase of the oxygen concentrations at temperatures lower than about 673K, probably due to the formation of sulfates. The pyrite is most likely directly oxidized (as in situation C) in the first stage cyclone as the temperature in this stage is normally much lower than 800K. In the second stage, the oxidation of the pyrite may take place by the two-step process as the temperature in this stage is often higher than 800K. Oxidation by the two-step process is more likely to occur with smaller particles in the raw meal due to the faster heating-up with small particles than with large particles.

Absorption of SO_2 on Limestone

Limestone ($CaCO_3$) is one of the most important and basic ingredients for Portland cement production. Limestone is fortunately also a sorbent of SO_2. In the cyclone preheater, calcination of the limestone does not take place because of the relatively higher CO_2 partial pressure in the flue gas. The sulfation reaction is therefore the so-called "direct sulfation reaction", which can be represented by the following overall reaction:

$$SO_2(g)+\frac{1}{2}O_2(g)+CaCO_3(s)\rightarrow CaSO_4(s)+CO_2(g)$$

Preliminary investigations show that this reaction can be significantly influenced by the concentrations of SO_2, O_2 and CO_2 and the presence of H_2O and diverse additives. At 823K and in a typical gas composition as in the cyclone preheater (SO_2: up to 1800 ppm; O_2: 3%; CO_2: 30%; H_2O: 7.5%), following phenomena are observed:

- The apparent reaction order of SO_2 is significantly lower than unity and has the tendency to decrease with the increase of its concentration at lower concentration area and to increase with the increase of its concentration at higher SO_2 concentrations.
- The apparent reaction order of O_2 decreases from about 0.4 at low O_2 concentrations (< about 10 vol.%) to zero at high O_2 concentrations (>15 vol.%).
- The sulfation is depressed by higher CO_2 partial pressure with an apparent reaction order of about –0.5.
- Addition of 7.5 vol.% water in the gas depresses the sulfation reaction by about 30%.
- The reaction is significantly enhanced by diverse additives such as alkali metal (Li, Na and K) salts and $CaCl_2$.

Examinations of the reacted particles by SEM (Scanning Electron Microscope) indicate that the "direct sulfation reaction" proceeds with a mechanism that is illustrated in Figure 3.

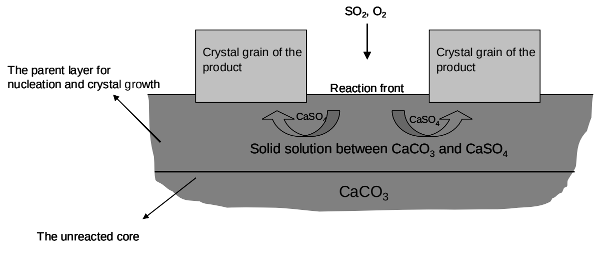

Figure 3 Illustration of the "direct sulfation reaction".

The sulfation reaction takes place at the gas-solid interface. Initially, a solid solution is formed between $CaSO_4$ and $CaCO_3$ at the surface of the limestone. Nucleation of the formed $CaSO_4$ takes place when the concentration of $CaSO_4$ reaches the minimum level for the nucleation process to proceed. The nuclei then grow to form crystal grains. The growth of the crystal grains is fed by the $CaSO_4$ formed by the sulfation reaction at the interface between the gas phase and the unreacted core. The $CaSO_4$ is transported from the interface to the roots of the crystal grains by ionic diffusion in solid state. With the progress of the sulfation reaction, a product layer consisting of crystal grains of $CaSO_4$ is formed. This product layer is usually porous due to the existence of pores between the crystal grains. The sulfation reaction thus proceeds with the following steps: gas film diffusion → pore diffusion → chemical reaction at the interface of the unreacted core → solid-state diffusion → growth of the crystal grains of $CaSO_4$.

Most of the observed phenomena can be explained by the resistance of the solid-state diffusion at the interface of the unreacted core. The decrease of the apparent reaction order of SO_2 with the increase of the SO_2 concentration can, for example, be explained by the decrease of the carbonate concentration at the interface of the unreacted core at higher reaction rates caused by the restriction of the solid-state diffusion. The depressing effect of higher CO_2 partial pressures on the sulfation reaction is due to its influence on the solid-state diffusion [6, 7, 8]. The enhancement by the additives is mainly due to their improvement on the solid-state diffusion by the mechanism of point defect formation [9].

SO_2 Emission from the Cyclone Preheater

In a cyclone preheater-like environment, the sulfation reaction is very slow at a temperature lower than about 823K. This means that the absorption of the SO_2 formed by the oxidation of pyrite is ineffective in the first two stage cyclones, particularly in the first stage cyclone. The emission of SO_2 from the cyclone preheater is thus a result of the combination of the fast oxidation of the pyrite contained in the raw meal and the relatively slow absorption of the formed SO_2 on the limestone particles in the raw meal in the first two stage cyclones.

Conclusion

The emission of SO_2 from cement production is mainly caused by the fast oxidation of the pyrite contained in the raw materials and the relatively slow sulfation reaction in the first two stage cyclones of the cyclone preheater.

In the cyclone preheater, the pyrite contained in the raw materials is probably direct oxidized in the first stage cyclones, but may be partly oxidized by the two-step process in the second stage cyclone.

The sulfation reaction at low temperatures is limited by solid-state diffusion, which is the main reason for the variation of the apparent reaction order of SO_2, the depressing effect of higher CO_2 pressures and the enhancement by additives such as alkali metal salts and calcium chloride.

Acknowledgements

This work was carried out as a part of the Combustion and Harmful Emission Control (CHEC) research program at the Department of Chemical Engineering, Technical University of Denmark, and financially supported by Technical University of Denmark and FL Smidth A/S.

References

[1] Jorgensen, F. R. A. and Moyle, F. J.; Journal of Thermal Analysis, 25 (1982) 473-485.

[2] Dunn, J. G. and De, G. C. and O'Connor, B. H.; Thermochimica Acta, 145 (1989) 115-130.

[3] Dunn J. G. and De, G. C.; Thermochimica Acta, 155 (1989) 135-149.

[4] Hong, Y. and Fegley, B.; Ber. Bunsenges. Phys. Chem. Vol. 101, No.12, 1997, pp1870-1881.

[5] Hansen, Jens-Peter.; Ph. D. thesis in the Department of Chemical Engineering, Technical University of Denmark, August 2003.

[6] Beruto, D.; Giordani, M. and Botter, R.; Journal de Physique, Colloque C1, Supplement au n°2, Vol. 47, 1986, ppC1-527-531.

[7] Tetard, F.; Bernache-Assollant, D.; Champion, E. and Lortholary P.; Solid State Ionics, Vol. 101-103, 1997, pp517-525.

[8] Tetard, F.; Bernache-Assollant, D. and Champion, E.; Journal of Thermal Analysis and Calorimetry, Vol. 56, 1999, pp1461-1473.

[9] West, Anthony R. Basic Solid State Chemistry, John Wiley & Sons, Ltd., 1999.

Ling Hua
Address: Dept. of Chemical Engineering
Søltofts Plads, DTU-Building 227
Technical University of Denmark
Phone: +45 4525 2861
Fax: +45 4588 2258
e-mail: lih@kt.dtu.dk
www: http://www.kt.dtu.dk
http://www.novozymes.com

Supervisors: John Villadsen
Mogens Wümpelmann, Novozymes A/S

Ph.D. Study
Started: September 2005
To be completed: August 2008

Recovery and Enzymatic Modification of Lipoteichoic Acid

Abstract

Lipoteichoic acid (LTA), a cell wall component of most gram-positive bacteria, has been reported to induce various inflammatory mediators and to play a key role in gram-positive-microbe-mediated septic shock. The purpose of this project is to explore an up-scalable purification process for the recovery of LTA from industrial biomass waste. In the meanwhile, it is necessary to establish relevant analytical methods to characterize LTA structure and biological properties. Further work may be required to modify LTA properties by using specific enzymes.

Introduction

The inflammatory responses to gram-negative and gram-positive bacteria can hardly be distinguished. However, although most of the immune stimulation caused by gram-negative bacteria could be attributed to lipopolysaccharide (LPS) as a general principle, no consensus as to its gram-positive counterpart has yet been reached. LPS has been available in a pure, biologically active form since 1952 [1] and its active principle, the lipid anchor lipid A, was finally proven by chemical synthesis in 1985 [2].

LTA is found in most gram-positive bacteria. It is an important component of the cell walls of gram-positive bacteria. Like LPS of gram-negative bacteria, it is an amphiphilic, negatively charged glycolipid. LTA has become increasingly considered to be an important pathogen-associated molecular pattern capable of stimulating innate immunity and responsible for gram-positive bacterial sepsis [3]. However, the biological properties of LTA are still under debate because the LTA used in previous studies may have contained biologically active contaminants [4] or may have been altered in structure [5].

Although LTA was discovered 35 years ago [6], there is yet no standard procedure for the preparation of this biopolymer. Traditional methods adopted from LPS purification are based on extraction of bacteria with hot or cold aqueous phenol [7]. When adequately purified, phenol-extracted LTA turned out to be essentially inactive in inducing cytokine release as a measure of immunostimulatory activity. It was found that LTA was degraded and the residues, especially D-alanine substituents, were lost after the phenol extraction [5]. Recently Morath *et al.* isolated LTA from *Staphylococcus aureus* by butanol extraction, in which the D-alanine substitutions of the polyglycerophosphate (Gro-P) backbone were preserved [5]. The highly purified LTA could efficiently stimulate moncytes via TLR2 to produce TNF-α [8].

Novozymes has a significant interest in investigating structure-function relationships with regard to immune modulating properties of LTA eventually in conjunction with other cell constituents.

Specific Objectives

The first objective of this project is to design an up-scalable, industry-friendly down stream process for the recovery and purification of LTA from *Bacillus Licheniformis*.

The second objective is to determine the chemical structure of recovered LTA, and to characterize its properties on immuno-modulation by applying relevant analytical methods.

The third objective is to modify LTA structure by applying pre-selected enzymes, and to investigate its structure-function relationship.

LTA Structure

Many LTAs are macroamphiphiles with their glycolipid anchored in the membrane and their poly(Gro-P) chain extending into the wall [3]. The glycolipid is Glc(β1-6)Glc(β1-3)(gentiobiosyl)diacyl-Gro in staphylococci, bacilli, and streptococci (Figure 1A). The chain length of poly(Gro-P) varies in LTA isolated from different bacteria (Figure 1B). Figure 1C shows the side chain substituents of LTA. Therefore, the microheterogeneity of LTAs is the result of several variables: (1) fatty acid composition, (2) kind and extent of glycosyl substitution, (3) length of hydrophilic chain, and (4) degree of D-alanylation [3].

Methodology

The approach for this study can be briefly described as the following:

1) Search literature sources for the existing purification procedures and the analytical methods;
2) Recover LTA from *B. Licheniformis* by adjusting the existing process;
3) Build up the analytical methods, and analyze the obtained LTA qualitatively and quantitatively;
4) Modify the existing process so that it can be up-scaled at some later stage;
5) Optimize the purification process in order to achieve high purity and high efficiency;
6) Introduce pre-screened enzymes to modify the LTA structure;
7) Analyze the properties of the enzymatically modified LTA.

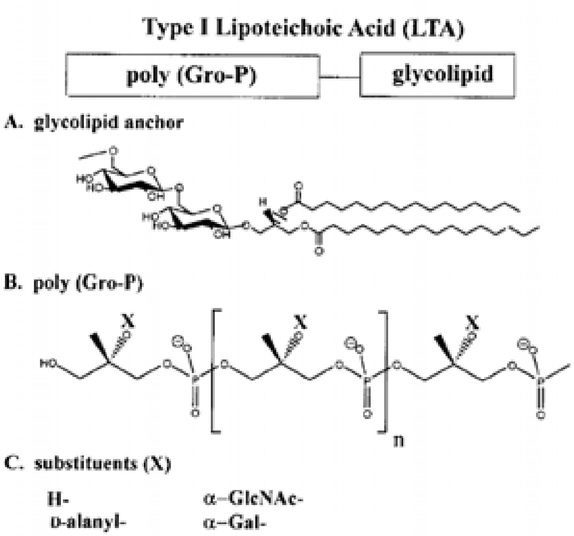

Figure 1. Type I LTA. (A) Glycolipid anchor, (B) poly(Gro-P), and (C) substituents (X) [3].

Acknowledgments

The PhD project is financed by Novozymes Bioprocess Academy, the Graduate School MP_2T in Chemical Engineering, and the Technical University of Denmark.

References

1. O. Westphal, O. Lüderitz, F. Bister, Z. Naturforsch. 7 (1952) 148–155.
2. C. Galanos, O. Luederitz, E.T. Rietschel, O. Westphal, H. Brade, L. Brade, M. Freudenberg, U. Schade, M. Imoto, H. Yoshimura, Eur. J. Biochem. 148 (1985) 1–5.
3. F.C. Neuhaus, J. Baddiley, Microbiol. Mol. Biol. Rev. 67 (4) (2003) 686-723.
4. J.J. Gao, Q. Xue, E.G. Zuvanich, K.R. Haghi, D.C. Morrison, Infect. Immun. 69 (2) (2001) 751–757.
5. S. Morath, A. Geyer, T. Hartung, J. Exp. Med. 193 (3) (2001) 393–397.
6. A.J. Wicken, K.W. Knox, J. Gen. Microbiol. 60 (1970) 293–301.
7. W. Fischer, H. U. Koch, R. Haas, Eur. J. Biochem. 133 (1983) 523–530.
8. E. Ellingsen, S. Morath, T. Flo, A. Schromm, T. Hartung, C. Thiemermann, T. Espevik, D. Golenbock, D. Foster, R. Solberg, A. Aasen, J. Wang, Med. Sci. Monit. 8 (5) (2002) BR149-BR156.

Jakob K. Huusom

Address: CAPEC Department of Chemical Engineering
Building 227, room 210
Phone: +45 4525 2801
Fax: +45 4593 2906
e-mail: jkh@kt.dtu.dk
www http://www.capec.kt.dtu.dk
Supervisors: Sten Bay Jørgensen & Niels Kjølstad Poulsen

Ph.D Study
Started: February 2005
To be completed: January 2008

Model Identification for Control - under Control

Abstract

Optimizing process operation through model based control strategies requires ideally a control oriented identification of the plant model. Identification for control should be performed under the conditions the process are operated at i.e. under closed loop control. Identification in closed loop implies an iterative procedure where the closed loop performance is optimized. Estimation of a process model from closed loop data needs to take the correlation between the process input and the external noise signal into account.

Introduction

The increasing competition on the global market has rendered optimizing process operation a necessity for new as well as existing production in the chemical industry. Advanced control strategies based on models for a specific process plays an important role in this respect. In particular implementation of model predictive controllers (MPC) in recent years, have contributed to increase competition capabilities. Control oriented process modelling is part of the frame work on application oriented modelling. System identification is an area that has received much attention but within identification for control there is still a need for development of systematic methods. Identification for control implies experiments where the collected data for identification are retrieved from a process operated under control i.e. in closed loop.

The benefits and challenges in closed loop identification has been motivated several times in the literature e.g. by [2], [5] and [3] where a key point is, that it is the performance of the closed loop that is object for the optimization. Since then several research groups have worked on development of suitable systematic methods for handling an iterative procedure of closed loop experiments, model parameter estimation, and enhanced control design. An iterative procedure is necessary due to the interaction between the implemented controller and the data collected from the experiment.

The need for optimizing control is particularly pronounced for nonlinear processes where the optimal operation is not necessarily on the process constraints. Optimization of time varying processes may require an adaptive control strategy due to the transient behaviors that occur in e.g. batch and continuous processes regarding changes in feed composition or other process conditions. There is a large challenge in optimization of nonlinear and time varying processes. Most existing theory is derived for linear time invariant system and its extension is not straight forward. This project is devoted to further developments of optimization methods for processes through control oriented system identification.

Closed loop identification

A stable feedback connection $\mathcal{T}(\boldsymbol{P},\boldsymbol{C})$, consisting of the possible unstable system $\boldsymbol{P}$ and the controller $\boldsymbol{C}$, will due to the controller reject disturbances and track set points. The performance of the loop can be evaluated through some norm of a performance cost function $\mathcal{J}(\boldsymbol{P},\boldsymbol{C})$. In order to excite the system to reveal the dynamics, two external perturbations signals can be introduced to the system. The closed loop system with external probing signals are shown on the figure.

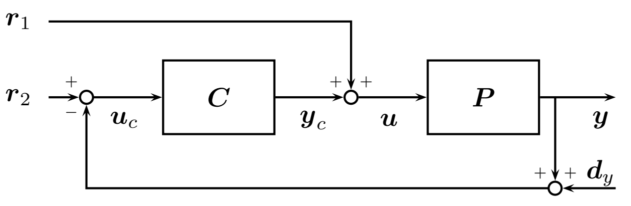

The signal $\boldsymbol{r}_1$ introduces a deviation from the optimal control input to the system which will act as a known disturbance on the plant input. The second signal $\boldsymbol{r}_2$ acts as a known perturbation in the reference signal and can therefore be used to move the process around to span a desired region of the output space.

Methodology

Closed loop identification is an iterative procedure due to the influence of the control. The identified plant model is used to design a new controller in order to enhance the performance of the loop. If the performance specifications are not met repeated iterations will have to be performed according to the following scheme until the performance is satisfactory.

- Closed loop experiment
- Estimation of a plant model, $\boldsymbol{P}_i$
- Implement controller $\boldsymbol{C}_{i+1}$ based on $\boldsymbol{P}_i$
- Evaluation of closed loop performance, γ_{i+1}

Identification in closed loop through the iterative scheme involves some inherent problems and design challenges that needs to be addressed in order to prevent divergence of the procedure [1]. It must be required that the performance of the control loop is equal or better that the performance of the loop for the previous iteration.

Estimation

Three main approaches to model estimation from closed loop data exit, each with a number of advantages and disadvantages [6, 4].

- Direct identification
- Indirect identification
- Joint input/output identification

In direct identification $\{\boldsymbol{u}, \boldsymbol{y}\}$ are used to estimated the process model as in open loop identification. The basic principle of not having inputs that are correlated with noise are violated by this method. A consistent estimate is only produced by this method if the data are informative and the estimate contains the true model structure. That is rearly the case in practice. This can imply that a very high model order have to be chosen in order to avoid bias. The advantages of the direct estimation is that it is simple and applicable regardless whether the controller are know and its complexity.

In the indirect identification a model is estimated using $\{\boldsymbol{r}_i, \boldsymbol{y}\}$ which prevent the problem with correlations. Given this estimate of the closed loop an estimate for the process is deduced using knowledge of the controller. This method will work if the controller is known. It also requires a linear control without input saturation and anti wind up, otherwise these effects can be transferred to the estimate of $\hat{\boldsymbol{P}}$.

The joint input/output identification estimates the transfer from the exitation signals $\boldsymbol{r}_i$ to both $\boldsymbol{u}$ and $\boldsymbol{y}$. The system model is then equal the ratio between the two transfer functions. The joint input/output method can be utilized even for a system containing an unknown nonlinear controller.

Conclusion

A method for optimizing closed loop performance requires a iterative scheme of repeated closed loop experiments, parameter estimation and enhanced control design. Estimation of a plant model from closed loop data have to take the correlation between the process input and the external noise signal into account.

References

[1] Raymond Arnoud de Callafon. *Feedback Oriented identification for Enhanced and Robust Control - a fractional approach applied to a wafer stage.* PhD thesis, Technical University of Delft, The Netherlands, Oktober 1998.

[2] Michel Gevers and Lennard Ljung. Optimal experiment design with respect to the intended model application. *Automatica*, 22(5):543–554, 1986.

[3] Håkan Hjalmarsson, Michel Gevers, Franky De Bruyne, and Juliette Leblond. Identification for control: Closing the loop gives more accurate controllers. *IEEE Proceedings of the 33rd Conference on Decision and Control*, pages 4150–4455, 1994.

[4] Lennart Ljung. *System identification - Theory for the user.* Prentice hall, 2 edition, 1999.

[5] Ruud J. P. Schrama. Accurate identification for control: The necessity of an iterative scheme. *IEEE Transactions on automatic control*, 37(7):991–994, 1992.

[6] Torsten Söderström and Petre Stoica. *System identification.* Prentice Hall, 1989.

Johnny Johansen

Address: Building 201, room 002
Phone: +45 4525 2963
Fax:
e-mail: joj@kt.dtu.dk
www: http://www.kt.dtu.dk

Supervisors: Tue Johannsessen
Hans Livbjerg

Ph.D. Study
Started: February 2003
To be completed: January 2006

Synthesis of Ceramic Membranes by Controlled Deposition of Flame-Produced Nanoparticles

Abstract

Asymmetric ceramic membranes are formed using a porous substrate tube (or surface) as a filter for flame produced, airborne nanoparticles (Andersen et al., 2002). The general principle behind flame synthesis of materials is the decomposition and/or oxidation of evaporated metal-precursors in a flame thereby forming stable metal-oxide monomers followed by nucleation, aggregation and - to some extent - coalescence of aggregated nano-particles. The product gas from a flame aerosol process is drawn through a macro-porous substrate by a vacuum pump thereby creating what in principle is a thin filter cake on the surface of the substrate.

The top-layer can is deposited directly on a coarse pore structure (>5 micrometer). Particles do not penetrate deep into the support structure due to the “lack” of fluid forces on the particles. This is an advantage compared with the preparation using a colloid suspension where several deposition steps are necessary in order to avoid penetration of the suspension due to the capillary forces.

We demonstrate a reduction in pore size from several micrometers of the macro-porous support to single digit nanometer mean pore size of the deposited micro-porous top-layer, i.e. a reduction of three orders of magnitude in pore size in one deposition step.

Introduction

Ceramic membranes are highly porous and are in general characterized by their high permeability but low selectivity. The use of highly porous ceramic membranes is favorable in high temperature applications where polymeric membranes can not been used. Inorganic membranes in general have higher chemical, thermal and mechanical stability than polymeric membranes. These properties make the use of ceramic membranes very attractive, even within areas where polymeric membranes are dominating today. This is mainly due to the higher resistance to mechanical and chemical degradation, which can result in a significant increase in membrane lifetime [1]

Porous membranes play an increasingly more important role in chemical reactor design, since chemical membrane reactors offer new and exciting possibilities for reactor design. Many heterogeneous catalytic reactions are endothermic, reversible and limited by chemical equilibrium and the conversion to the desired product may be favored at high temperature. In such cases, the use of inorganic membranes as both separator and reactor in a single unit operation may shift the equilibrium conversion if one of the products can be made to diffuse through the membrane at a rate much grater than the other products or reactants.

As will be shown in the present study, membrane top-layers prepared by deposition of flame-produced nanoparticles may result in a reduction of the pore size of the substrate by three orders of magnitude in a one-step-process. This can be done within the time-scale of an hour. This is in sharp contrast to the wet preparation techniques that needs several times of precipitation, filtration, drying and calcinations steps before nano-scale membranes can be produced.

Specific Objectives

The scope of this Ph.D. project is to develop porous membranes with pores in the nano (and sub-nano) meter range, synthesized by flame synthesis. These membranes can then be coated with a catalyst layer to enhance the formation of the desired reaction product.

Flame Synthesis

Membranes consisting of one or more metal oxides can be synthesized by flame pyrolysis [2,3]. The general principle behind flame pyrolysis is the decomposition and oxidation of evaporated organo-metallic precursors in a flame, thereby forming metal oxide monomers. The precursors (presently Al(acac)$_3$ and Mg(acac)$_2$; acac=acetyle acetonete) are sublimated into a stream of N_2 in a saturator unit as shown in figure 1. The precursor stream is then mixed with air and a fuel, which can be methane or hydrogen depending on the desired flame temperature.

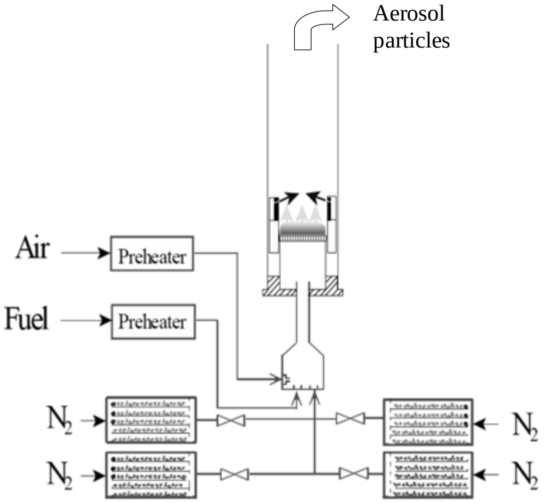

Figure 1: Schematic drawing of the flame synthesis setup.

In the flame the organic part of the precursor will decompose and combust, resulting in a metal oxide monomer, i.e. a molecule. Because of the extreme super-saturation created in the flame due to the low vapor pressure of metal oxides, the monomers will nucleate homogeneously and agglomerate to form aggregates of large ensembles of monomers. At high temperature, these aggregates will then sinter together to form single particles. If the flame temperature and the residence time are sufficiently high, the formed oxide particles will be spherical due to the fast coalescence at the high temperatures in the flame. This is desirable when synthesizing membranes, since the closest packing, and thereby the smallest pores, is achieved when the particles are spherical.

The primary product from the flame pyrolysis is an aerosol of metal oxide particles in the nano-size range. The aerosol gas from the flame can be utilized for several different purposes, depending on synthesis parameters and on the precursors fed to the flame. With the present technology it is possible to make supported catalysts composite metal oxides, catalytically active surfaces and porous ceramic membranes [2,3]. When producing catalysts the specific surface area normally has to be high in order to get very active catalysts. In flame synthesis, the high specific surface area can be achieved by quench cooling the aerosol gas with cold air after a short residence time in the flame zone [4]. The precursor will be transformed to metal oxide particles, but the residence time at the very high temperatures in the flame will be reduced, so that the extensive sintering can be avoided. This results in the formation of agglomerates that will only sinter very little, due to the rapid reduction in temperature. Mixed metal oxides can be synthesized by leading two precursors to the flame simultaneously, e.g. Al and Mg precursors, which will lead to the formation of the $AlMg_2O_4$ spinel structure.

Membrane Formation

Membrane layers can be formed by using a porous substrate tube (or surface) as a nano-particle filter. The aerosol gas from the flame is led past a porous substrate, where a part of the gas is sucked through the substrate, thereby creating a thin filter cake on the surface of the substrate [3]. This is illustrated in figure 2, where the porous substrate is a tube on which the deposition takes place on the inside, while suction is applied on the outer side of the tube.

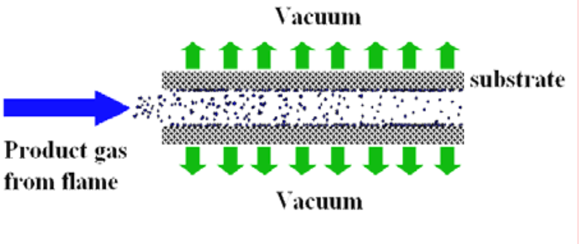

Figure 2: The aerosol phase from the flame is led through a porous substrate tube by applying vacuum on the outer side of the support tube and the particles form a layer on the inner side of the substrate.

The top-layer can be deposited directly on a coarse pore structure, which is in contrast to the use of wet colloidal suspensions, which require several deposition steps – each with a smaller particle size. In the flame aerosol process, the Brownian motion of the aerosol particles is fast compared to the fluid velocity through the substrate and the particles will not penetrate very deeply into the substrate. Particle deposition will initially take place inside the substrate pores, but because of the fast Brownian diffusion and the deposition of particles will rapidly decrease the pore diameter at the pore mouth, and hence lead to pore mouth blocking. After pore mouth blocking a top-layer will start to form. The top-layer deposition rate can be as low as 5-10 nm/min, which facilitates the production of very thin membranes needed for high fluxes [5]. A membrane consisting only of the substrate with the separating membrane layer located only in the upper part of the substrate pore mouths would be an interesting product, but because the pore mouth blocking happens within minutes or less. At the moment it has not been possible to produce such a product. Furthermore, there are several unresolved issues regarding stability of such a membrane.

The pore diameter of the deposited top-layer depends on the size of the aerosol particles, which can be controlled by changing the feed rate of metal precursor to the flame. Since the feed rate can be changed continuously - by changing the temperature of the sublimation unit or the flow of gas through the unit - also the particle size and thereby the pore diameter can be changed continuously, which greatly facilitates the one-step synthesis of a top-layer, where the pore diameter is decreased to less than 10 nm from a substrate pore size of several microns. Figure 3 shows the saturation temperature of the sublimation unit in such an experiment and the corresponding precursor concentration in the flame during deposition of an alumina top-layer. The precursor concentration is an exponential function of the temperature and since the particle diameter depends on the precursor concentration to the third power, a small decrease in saturator temperature leads to a dramatic reduction of the particle size.

The deposition is carried out in a deposition cell that is heated to 300°C in order to obtain a thermally accommodated membrane layer, which is more stable towards phase transformations during subsequent heating. There is, however, a problem when depositing alumina top-layers, since alumina nano-particles below roughly 10nm in size only are of the γ- orδ-phase, which is a meta-stable phase, i.e. not thermodynamically stable. The alumina membranes, furthermore, have poor chemical stability [1], but the synthesis method is easily transferred to other metal oxides, so in this context alumina serves as a model system. Other oxides such as MgO and $MgAl_2O_4$ have also been applied in the membrane formation process.

The pressure drop across the membrane is very uniform and the membrane will be without cracks, because any non-uniformity in the pressure drop will be leveled out by a temporary increase in the local deposition rate.

Characterization

For characterization of the porous α–Al_2O_3 substrate a permeation method is used, where hydrogen, helium and nitrogen are used as permeate gases. The model proposed by [3] for the gas permeation in porous ceramic membranes has been used for the evaluation of the structural parameters of the substrate, equation 1:

$$F = \frac{Q\,P_0\,l}{\overline{A}\,\Delta P} = \frac{d_p}{3}\sqrt{\frac{8\,R\,T}{\pi\,M}}\frac{\varepsilon}{\tau} + \frac{d_p}{32\,\mu}\frac{\varepsilon}{\tau}\overline{P} \qquad (1)$$

Here, F is the permeance, Q is the volumetric flow rate measured at atmospheric pressure P_0, l is tube thickness, $\overline{A}$ is the logarithmic mean area of the membrane, ΔP is the pressure drop across the substrate, M is the molecular weight of the permeation gas, and $\overline{P}$ is the mean gas pressure in the substrate. From permeation data, the average pore diameter, d_p and the structure parameter ε/τ can be estimated for the substrate.

After deposition, the top-layer and the substrate are again characterized by permeability measurements. The measured permeation flow will be influenced both by the resistance in the top-layer and the resistance in the substrate. The permeability data for the membrane top-layer are therefore extracted using a resistance-in-series model [3], where the permeation data for the substrate is subtracted from the data from dual-layer system. The data from the three permeation gasses (He, H_2, and N_2) are normalized with their molecular weights and the viscosities of the gasses according to:

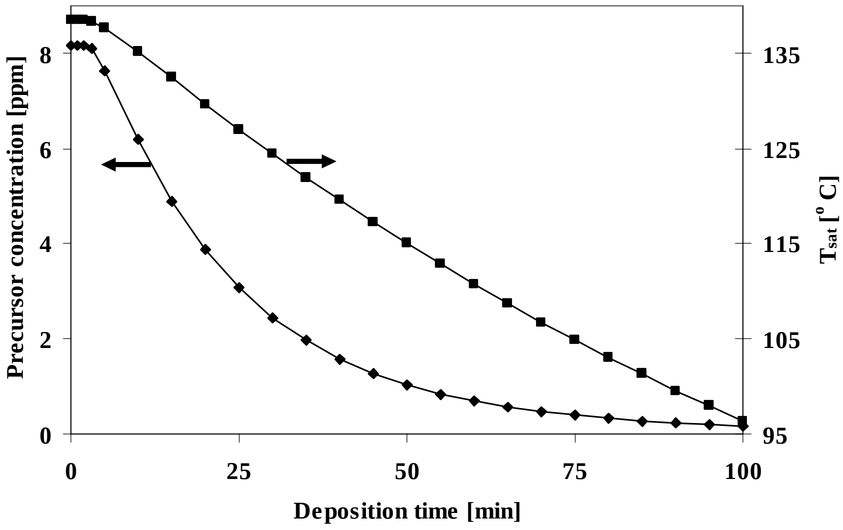

Figure 3: Saturation temperature of the sublimation unit and the corresponding precursor concentration in the flame during deposition. The drop in saturator temperature give a high drop in precursor concentration results in an even more significant reduction in particle size from the flame unit.

$$Y = F_i\sqrt{M_i} \text{ or } Y = F_i\sqrt{M_i}/\delta \text{ and } X = \frac{\overline{P}\sqrt{M_i}}{\mu_i}$$

Normalized permeation data for a substrate and the deposited alumina top-layer can be seen in figure 4. There is a strong linear dependence of the normalized permeation, *Y*, on the normalized pressure, *X*, for the substrate. For the top-layer, the pressure dependence is almost negligible, i.e. the slope is close to zero, which indicates that the dominant transport mechanism through the top-layer is Knudsen diffusion.

Membrane properties

The membranes have been synthesized using a macro-porous α-aluminum substrate tube, and the top-layers have primarily been made of Al_2O_3, MgO, and $MgAl_2O_4$ spinel. The lowest pore diameters, estimated to be as low as 2 nm, have been achieved by the dynamic deposition method. When depositing dynamically, the particle size from the flame exhaust is continuously decreased from an average particle size around 40 nm towards particles close to or smaller than one nanometer in size. Consequently, the membrane layer is “closed” with smaller and smaller particles and we have obtained membrane layers where Knudsen separation has been achieved in the time scale of an hour starting off with a macro porous support.

Currently, membrane layers consisting of MgO and $MgAl_2O_4$ spinel exhibits the best thermal stability, whereas alumina membranes made of ultra-fine particles have very poor thermal stability. Those alumina structures are also very sensitive to humid conditions. The poor stability of alumina is – as already mentioned – probably caused by the fact that the crystal phase formed by flame synthesis of alumina nano-particles is not the most stable α-alumina phase. As a consequence the alumina top-layer is degraded when it is exposed to high temperatures or water. Magnesia and $MgAl_2O_4$ spinel do not exhibit the same problem with phase transitions, and hence are more stable top-layers.

Figure 5 shows a SEM picture of a membrane cross section. The top-layer membrane is MgO on top of an α-Al_2O_3 substrate. The MgO layer has been produced using $Mg(acac)_2$ as the precursor. The formed top-layer has good thermal stability and the adhesion to the substrate is very good. In addition, the small inserts show the sharp interface between the top-layer and the substrate, which is remarkable keeping the difference of three orders of magnitude in pore size in mind. The top view shows the very homogeneous surface once a well-defined top-layer is formed after closing the pore mouths of the substrate.

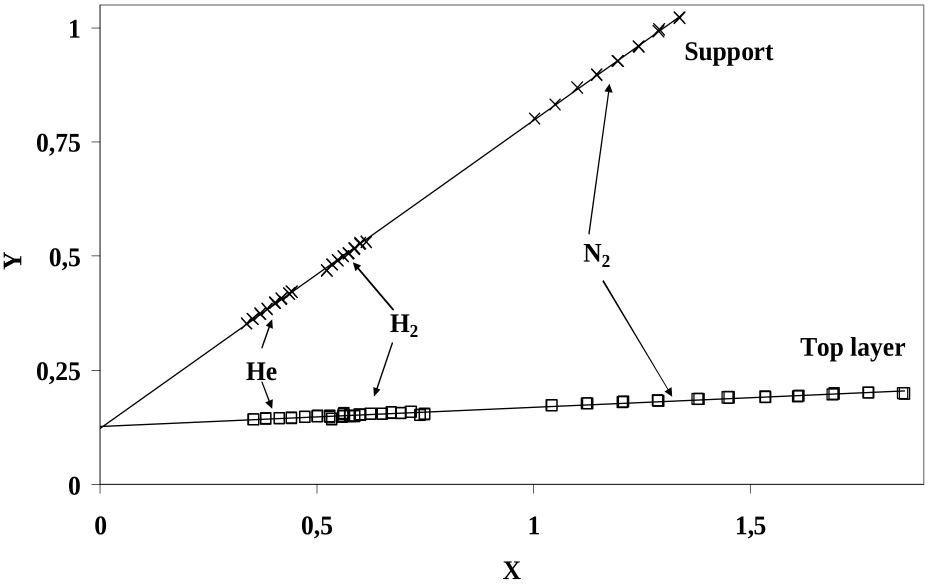

Figure 4: Dependence of $Y = F_i\sqrt{M_i}$ or $Y = F_i\sqrt{M_i}/\delta$ on the $X = \frac{\overline{P}\sqrt{M_i}}{\mu_i}$ for all gasses H_2, He and N_2 together in the support and top layer after 20 minutes of alumina deposition. T_{SAT} = 138°C

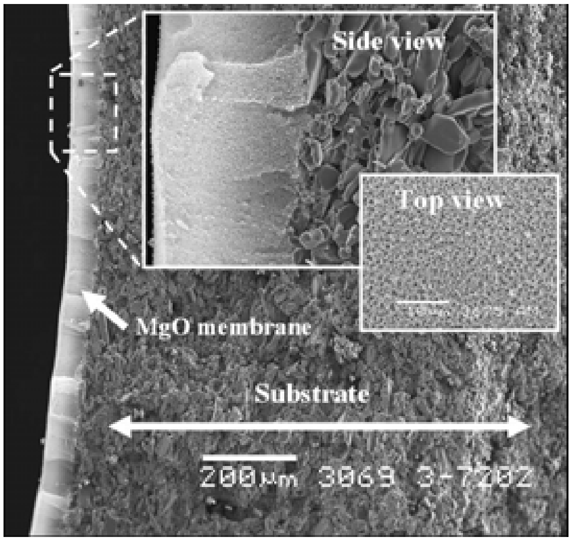

Figure 5: SEM picture of a membrane cross section. The membrane consist of a MgO top-layer and an Al_2O_3 substrate. The small inserts shows the insignificant penetration of the top-layer in to the support and also – from the top – a very homogeneous surface compared with the very rough alumina support.

Summary

The experiments have shown that it is possible to produce membranes with estimated pore sizes down to 2 nm by controlled deposition of flame synthesized nano particles. The MgO top-layer deposited on the macro porous substrate has good thermal stability and very good adhesion to the support.

The synthesized membranes are analyzed using a two-layer membrane permeation model. The model assumes a mixed Poiseuille flow and Knudsen flow in the substrate and pure Knudsen flow in the top-layer. The model connects the measured transport properties of the membranes to the membrane structure. The data used for the analysis are obtained from BET measurements, density measurements, and by permeability measurements with hydrogen, nitrogen, and helium as permeate gases. The data is then combined to give an estimate of the pore size.

Outlook

It has already been mentioned that one can produce both composite metal oxides and supported catalysts by flame pyrolysis, simply by feeding suited precursors to the flame. Examples of synthesized composite oxides are: $MgAl_2O_4$ [6] and $ZnAl_2O_4$ spinel [7]. Examples of produced catalysts are: Pt/TiO_2, Au/TiO_2 and $Cu/ZnO/Al_2O_3$. As a part of an ongoing research project, active catalyst material has been successfully deposited on various surface materials [8]. Since both membranes and catalysts can be prepared by flame synthesis, the potential for making catalytic membrane reactors seem inherent.

Acknowledgements

The α-alumina support tube used in this study were supplied by Haldor Topsøe A/S, Lyngby, Denmark.

References

1. A. J. Burgraaf & L. Cot, Fundamentals of Inorganic Membrane Science and Technology, Elsevier Science, Amsterdam, 1996.
2. Andersen et. al, *J. Nanoparticle Res.*, 4(5), (2002), 405.
3. M. Mosleh, Preparation of Micro Porous Ceramic Membranes by Flame Generated Aerosol Nano-Particles, PhD thesis, Department of Chemical Engineering, Technical University of Denmark, 2004
4. Hansen et. al, *AIChE J.*, 47, 2000, 2413
5. Johannessen et. al, *ChERD*, 82(11), 2004, 1444-1452
6. J.R. Jensen, Flame synthesis of composite oxides for catalytics applications, PhD thesis, Department of Chemical Engineering, Technical University of Denmark, 2001
7. Jensen et. al, J. Nanoparticle Res., 2, 363, 2000
8. Thybo et. al, J. Catal., 223 (2), 271, 200

Kent Johansen
Address: IVC-SEP Department of Chemical Engineering
Building 201, room 006
Phone: +45 4525 2876
Fax: +45 4588 2258
e-mail: kej@kt.dtu.dk
www: http://www.ivc-sep.kt.dtu.dk/STAFF/KEJ/kej.htm

Supervisors: Alexander A. Shapiro & Erling H. Stenby

Ph.D Study
Started: September 2004
To be completed: July 2007

Statistical Methods for History Matching

Abstract

A precise description of the physical properties of an oil reservoir can facilitate the operation of the oil field. Traditionally, the parameters determining the nature of the reservoir are determined by laboratory measurements and by history matching of the initial production data. In history matching measured production data is fitted by running full reservoir simulations. This process is very time consuming even when the simulations are carried out on powerful computers. Therefore, an alternative method to perform the history matching or parts of this is desired. This project deals with the application of statistical methods to carry out history matching and reservoir characterization.

Introduction

History matching is an important part of the characterization of an oil or gas reservoir. It is a process where production data from the initial stage of reservoir development is used to determine reservoir parameters and to predict the production in advance. The particular parameters measured at the production site are the injection rate, the oil production rate, the water cut, the gas-oil ratio, the bottom-hole pressures and others, as functions of time. History matching involves determination of permeability, porosity, relative permeabilities etc. Traditionally, full scale simulations on computers are carried out until the simulated production history matches the production history from the actual field sufficiently well. The method suffers from the fact that full scale simulations are computationally hard and time consuming. Also, the method demands an element of human intervention whenever parameters are adjusted which again makes the task of history matching a slow process. It is the aim of this project to develop a method which can facilitate the history matching of oil reservoirs.

Specific Objectives

The specific objectives of the project are the development of a viable method which can facilitate the process of history matching. The methods should honor the recorded production history from the field as well as honoring possible geological knowledge from e.g. test drillings or seismic surveys.

Results and Discussion

History matching may be regarded as an optimization problem where an error function measuring the misfit between simulated and observed production data is minimized. This is done by modifying the properties of the reservoir model on the grid block scale. The error function may take the form

$$E = \sum_{i=1}^{N_T} \left(\frac{p_i^{Sim} - p_i^{Obs}}{p_i^{max}} \right)^2 + (WCUT_i^{Sim} - WCUT_i^{Obs})^2 \qquad (1)$$

where p_i is pressure at time i and $WCUT_i$ is the corresponding watercut. The terms in equation (1) may be weighted by individual weights if specific parts of the history are expected to be more important than others.

In a general formulation the history matching problem may by formulated as the following optimization problem:

$$\boldsymbol{K}^* = \underset{\boldsymbol{K}}{\text{Argmin}}[E(\boldsymbol{K})] \tag{2}$$

where the matrix $\boldsymbol{K}$ represents the absolute permeability in every grid note of the reservoir model. Even for a small reservoir model the dimension of $\boldsymbol{K}$ is in the order of magnitude of $\mathbb{R}^{100} \times \mathbb{R}^{100}$. If additional properties such as porosity or water saturation are included in the history matching these must be included in the formulation. Solution of the problem in equation (2) is computationally hard and no unique solution exists since many different permeability fields may honor the measured production data.

Gradual Deformation

[3, 4] introduced the concept *gradual deformation* which is a simple way of forming a new realization of for instance a permeability field from a number of given ones. This is done by making a linear combination of the given permeability fields, i.e.

$$\boldsymbol{Z}_{new} = \sum_{i=1}^{N_{rel}} \alpha_i \boldsymbol{Z}_i$$

^{1}If the original $\boldsymbol{Z}_i$'s are normalized with mean 0, and ^{2}if $\sum_{i=1}^{N_{rel}} \alpha_i^2 = 1$

-then the global statistics of the original realizations is conserved in the new realization.

If two realizations are used then the linear combination may be formulated as

$$\boldsymbol{Z}_{new} = \cos\rho\pi \cdot \boldsymbol{Z}_1 + \sin\rho\pi \cdot \boldsymbol{Z}_2 \tag{3}$$

where ρ is referred to as the *deformation parameter.* Such a formulation conserves second order statistics such as variance and covariance. However, known permeabilities (hard data) is lost in the linear combination since this would require that $\sum_{i=1}^{N_{rel}} \alpha_i = 1$. To overcome this weakness three permeability fields have to be used in the linear combination with:

$$\alpha_1 = \frac{1}{3} + \frac{2}{3}\cos\rho\pi \tag{4a}$$

$$\alpha_2 = \frac{1}{3} + \frac{2}{3}\sin(\pi(-\frac{1}{6} + \rho)) \tag{4b}$$

$$\alpha_3 = \frac{1}{3} + \frac{2}{3}\sin(\pi(-\frac{1}{6} - \rho)) \tag{4c}$$

and the new realization is given as

$$\boldsymbol{Z}_{new} = \alpha_1\boldsymbol{Z}_1 + \alpha_2\boldsymbol{Z}_2 + \alpha_3\boldsymbol{Z}_3 \tag{5}$$

In both formulations the nature of the new field is controlled by only *one* parameter, namely ρ.

Geology

The permeability fields used to form the new gradually deformed permeability field in equation (5) must be constrained to hard data and any knowledge regarding the statistical properties of the permeability field. In this work such information is included in each realization of a permeability field by the use of sequential Gaussian simulation. The main feature of sequential Gaussian simulation are [1, 2]:

- Permeability is treated as a random variable
- Each unknown permeability is drawn individually from a *conditional cumulative distribution function*
- Simulated values are also used to condition new drawings
- The final result depends on the order of simulation - i.e. geologic artifacts may arise
- Simulation is performed in normal scores, i.e. a transformation of sampled values must be made!

The sequential Gaussian simulation follows the scheme:

1. Model the cumulative density function at the first location $\boldsymbol{u}_1$ conditional on the original n samples:

   $$F(\boldsymbol{u}_1; z|(n)) = \text{Prob}\{Z(\boldsymbol{u}_1) \leq z|(n)\}$$

2. Draw a realization from the ccdf
3. At position $\boldsymbol{u}_i$ model the ccdf conditional on the samples as well as previously simulated (drawn) values:

   $$F(\boldsymbol{u}_i; z|(n+i-1)) = \text{Prob}\{Z(\boldsymbol{u}_i) \leq z|(n+i-1)\}$$

4. Draw the ith realization, set $i = i + 1$

5. Repeat steps 3 and 4 until all grid notes have been visited

With sequential simulation techniques it is possible to generate a vast number of equiprobable realizations which all honor geostatistical data.

Optimization Scheme

Basically, the problem of history matching is the process of minimizing the objective function (1) as formulated in equation (2). By parameterizing the optimization by the use of the gradual deformation technique the problem is greatly simplified:

$$\boldsymbol{\rho}^* = \underset{\boldsymbol{\rho}}{\text{Argmin}}[E(\boldsymbol{\rho})] \quad \text{with} \quad \boldsymbol{\rho} \in \mathbb{R}^1 \tag{6}$$

In the parameterized optimization problem the only independent variable is now the deformation parameter, ρ. The problem (6) can therefore be solved using a univariate optimization method. In the present work the Dekker-Brent method, a hybrid golden-section search/polynomial interpolation method, has been utilized with success.

The prize of parameterizing the optimization problem is that the search space for the minimization is limited by the realizations used to form the gradually deformed realization. Consequently, the optimization has to be performed as a sequence where each sequence involves the generation of new realizations, i.e. search directions. Figure 1 illustrates the optimization algorithm used. The steps involved with optimization are summarized as follows:

1. Draw two initial realizations of permeability, $\boldsymbol{Z}_{new}$ and $\boldsymbol{Z}^*$

2. Find the optimal deformation parameter between $\boldsymbol{Z}_{new}$ and $\boldsymbol{Z}^*$

3. Set $\boldsymbol{Z}^*$ equal to the optimal deformation

4. Draw a new realization, $\boldsymbol{Z}_{new}$

5. Goto 2

If the gradual deformation scheme listed in equation (5) is used then *two* new realizations are drawn under points 1 and 4. Note that measured values and statistical data is conserved during the optimization as long as all realizations used are conditioned to the available data.

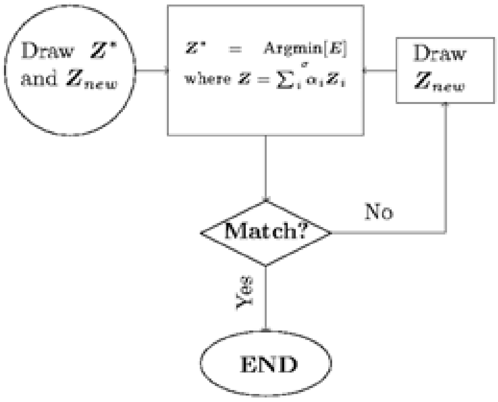

Figure 1: Optimization scheme used to history match the reservoir model.

Results

The method is tested using a synthetic oil field.

With the main simplifications being:

- 2D reservoir
- Oil and water phases present (immiscible)
- Only permeability varies with location
- Incompressible flow

Assumptions:

- Known permeability distribution
- Geostatistics known (anisotropi ratio, semivariogram)

A water injection process performed on the reservoir in a quarter-nine-spot pattern - leaving one producing well and 3 injection wells in the system. Figure 2 shows the reference field.

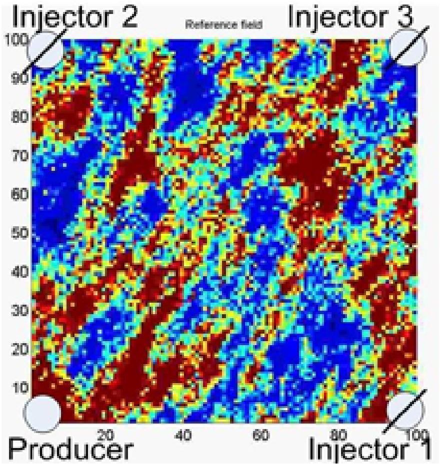

Figure 2: Sketch of the synthetic reference reservoir.

The test case has been implemented in accordance with the following setup:

- Geology conditioned to 4 samples
- Matching of 350 days of production
- Prediction of production until 1600 days

Geology is conditioned to 4 samples corresponding to the locations of the 4 wells. The outcome of the optimization is shown in figure 3.

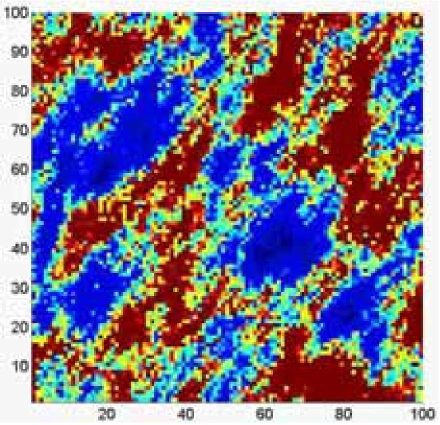

Figure 3: Result of the optimization.

Figures 4 and 5 show the matched production data which is pressure at the injectors and watercut at the producer. The watercut is matched well as well as the pressure at the injector placed diagonally to the producer. The other two injectors are not matched that well but the overall trend in pressure is refound. The matched field matches the correct water breakthrough time which is essential for a reservoir model since water production is economically unfeasible.

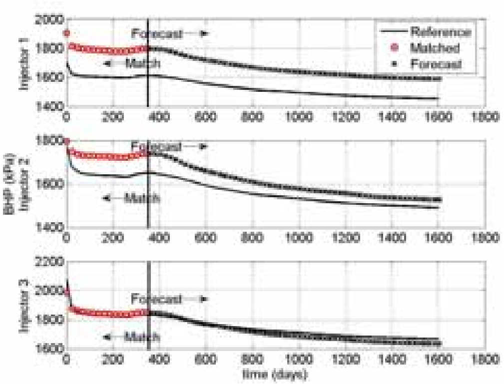

Figure 4: Matched and forecasted pressure evolution.

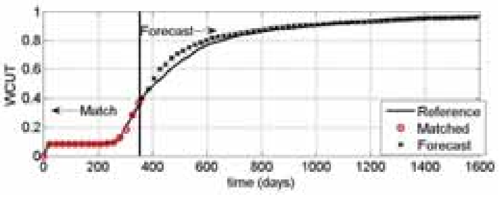

Figure 5: Matched and forecasted watercut evolution.

Conclusion

The gradual deformation is an effective parameterization of the history matching problem. The main advantage of the method is the simplification of the optimization problem which is reduced to a one-dimensional minimization problem. Integration of geological knowledge is done automatically if the used realizations of permeability are conditioned to samples and prior knowledge about the distribution. The method results in decent matches of the permeability and extension to matching of additional parameters such as porosity is easily done.

With respect to possible improvements of the method the main challenge is to make the optimization part more efficient. Combination with gradient methods is an obvious possibility, which however, requires some work to implement. Also, an efficient screening method to pick out "good" realizations could be a promising improvement. Such a screening method should not involve full reservoir simulations since these are computationally hard.

Acknowledgements

The project is part of the Molecular Products and Product Technology (MP_2T) in the graduate school in chemical engineering. The industrial cooperator is Dansk Olie og Naturgas A/S.

References

[1] Clayton V. Deutsch and André G. Journel. *GSLIB - Geostatistical Software Library and User's Guide.* Oxford University Press, 2 edition, 1998.

[2] Pierre Goovaerts. *Geostatistics for Natural Resources Evaluation.* Applied Geostatistics Series. Oxford University Press, 1997.

[3] Lin Y. Hu. Gradual deformation and iterative calibration of gaussian-related stochastic models. *Mathematical Geology*, 32(1):87–108, 2000.

[4] Lin Y. Hu. Combination of dependent realizations within the gradual deformation method. *Mathematical Geology*, 34(8):953–963, November 2002.

Carina Koch Kjellander

Address: Danish Polymer Centre, Risø National
Laboratory, Frederiksborgvej 399,
DK-4000 Roskilde, Denmark
Phone: +45 4677 4798
Fax: +45 4677 4791
e-mail: Carina.koch.kjellander@risoe.dk
www: http://www.risoe.dk/pol/

Supervisors: Søren Hvilsted, DTU
Kristoffer Almdal, Risø

Ph.D. Study
Started: December 2001
To be completed: Spring 2006

Chemical Degradation of Polymeric Materials

Abstract
Polymeric materials are used for a growing number of applications. This places high demands on the ability of predicting lifetimes and changes in the product properties when the polymeric material is used for different applications. Information about these things a very limited and often the information you can find are not useful for your application of a specific polymeric material. My PhD work is dealing with chemical degradation of specific polymeric materials. The objective is to get a fundamental understanding of what actually takes place at the molecular level. However, this is very complicated when dealing with commercial product and "model" materials are used in the study of chemical degradation of polyamides.

Introduction

The ever growing use of polymeric materials within almost all branches of industry, places very high demands on the producers' ability to predict lifetimes and changes in product properties when influenced from outside. Unexpected degradation of polymeric materials is often a very unpleasant experience and may result in catastrophic consequences e.g. with serious financial impacts. Examples of the use of polymeric materials are in pump housings, pipes, medical devices and electronic components.

At present predictions of how relevant chemicals influences the lifetime of a polymeric material require a study in various reference books. But the reference books often give information about the exposure of a polymeric material in a single chemical in high concentrations over a short period of time. This is normally not the condition for commercial use of a polymeric material and thereby not the information you are looking for. What you need is a quantitative estimate of the effect of mixed chemicals in small concentrations over a long period of time. Another problem is that the information often is presented with variable quality, and it is almost impossible to compare results from one reference book to another. Sometimes the information is not even to be found and you are forced to set up a standard test experiment, which is time and resource consuming. It is not possible to transfer the results of such standard tests from one environment to another and it is not possible to extrapolate to longer exposure times.

In order to predict the behaviour of polymeric materials (e.g. lifetimes) a fundamental understanding of what actually takes place at the molecular level when a polymer is exposed to a given environment is needed. Such knowledge hopefully makes it possible to transfer results from one test to another, from short to long time from one company to another etc. Today, such fundamental knowledge is very limited and even international research within this field is very sporadic.

This issue has lead to "Center for improved plastic products. Understanding the molecular decomposition mechanisms" (Monepol). Monepol is cooperation between The Danish Polymer Centre, FORCE Technology and 9 Industrial partners from the Danish Plastic Industry.

My PhD work is part of Monepol where I am working on different types of chemical degradation of the following three types of polymers: polyamide, poly(phenylene sulfide) and polycarbonate.

Since my PhD is part of collaboration with the industry the purpose of my work is to try to reflect the industrial use of the materials in order to look into some of the problems the industry have or might get. The results I will present in this yearbook are part of my work on chemical degradation of polyamide 66. Dealing with commercial polymeric materials reinforced with for instance glass fibers is very complicated. A “model” polyamide is therefore used. This material is selected as a commercial available unreinforced polyamide.

Results and Discussion

ISO standard testbars of unreinforced polyamide 66 (PA66) were exposed to 10% NaOH at 60 ^oC for 1, 2, 4, 6, 10, 14 and 18 weeks.

Visual inspection of the exposed samples shows that after two weeks the samples starts to get a weak yellow colour that becomes more and more intense as the exposure time is extended. After 10 weeks the polyamides starts to show crazes on the sample surface and after 14 weeks small pieces of the outer layer of the sample starts to “fall off” after drying the sample. However, by use of an optical microscope a few crazes were seen at the surface of the sample exposed for only one week. Figure 1 shows scanning electron microscopy (SEM) images of an unexposed PA66 sample (control), and samples exposed for 10 and 18 weeks to 10% NaOH at 60 ^oC.

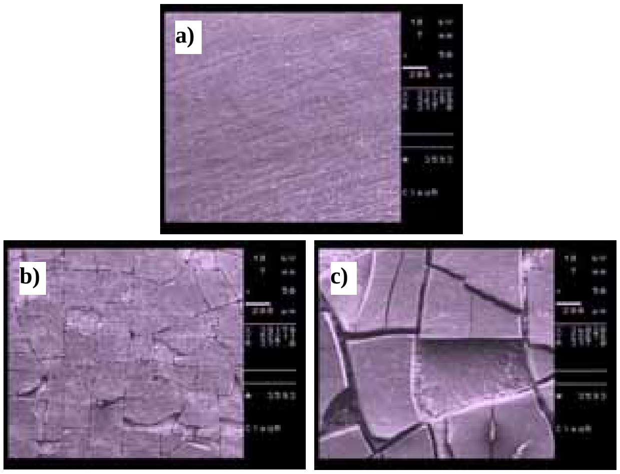

Figure 1. SEM images on a) control PA66, PA66 exposed for b) 10 weeks and c) 18 weeks to 10% NaOH at 60 ^oC.

The exposed samples show puzzle-like images with cracks in all directions. The cracks are more frequent and narrower in the sample exposed for 10 weeks, which gives a larger amount of smaller pieces compared to the 18 weeks sample. In the 10 weeks sample small pieces of the surface are missing, whereas in the 18 weeks sample it seem that the outer layer of the surface are quite loose and large pieces are missing.

The samples have been analysed with different analytical techniques. Figure 2 shows FTIR spectra of the control and exposed samples obtained using ATR-FTIR spectroscopy. In the IR spectra the most distinct changes are shown with arrows. The differences in the IR spectra are mainly seen in peaks arising from CH_3 and CH_2 deformation vibrations in the polyamide backbone for instance the four peaks in the 1500-1400 cm^{-1} region and the peak at 1370 cm^{-1}. These changes might be caused by changes in the environment around the polyamide backbone. Other peaks showing changes in the IR spectra are present at 1200, 1179 and 935 cm^{-1}. These peaks all arise from vibrations involving the C-O bonding of the amide groups. Previous work has shown that the peaks at 1223, 1200, 935 and 906 cm^{-1} in IR spectra of polyamides is characteristic for the crystalline phase of the polymer, whereas the peaks at 1179 cm^{-1} and 1140 cm^{-1} are characteristic for amorphous and partial amorphous phase, respectively [1-3]. Since it is possible to draw a common baseline for the peaks at 1200 and 1179 cm^{-1} the ratio between the areas of these two peaks can be calculated. The ratio between the peak at 1200 and the peak at 1179 increases from 0.9 in the control sample to 2.6 for the sample exposed for 18 weeks. This result indicates that the amount of crystallinity is increasing at the sample surface as the exposure time is extended.

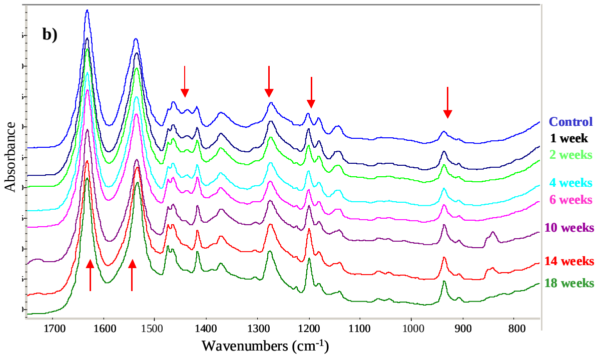

Figure 2. IR spectra on PA66 control and exposed to 10% NaOH at 60 ^oC.

The thermal stability of the polyamides have been analysed by thermogravimetric analysis (TGA) and differential scanning calorimetry (DSC). Figure 3 shows the TGA and DTG curves of control PA66 and PA66 exposed for 18 weeks.

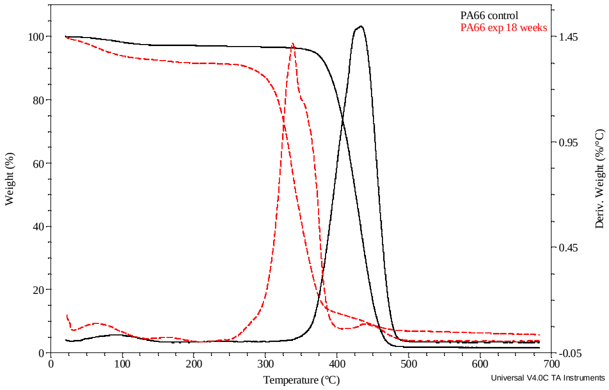

Figure 3. TGA on PA66 control and exposed to 10% NaOH at 60 ^oC for 18 weeks.

An initial loss in weight is seen in the exposed sample, this loss might arise from loss of water. The DTG trace of the control sample shows a uniform peak.

In the 18 weeks sample the main peak has been shifted to lower temperature and a “shoulder” had appeared at the high temperature side of the peak. Moreover, a small peak is seen at the same position as the peak from the control sample. The appearance of these extra peaks shows that the exposure of the polyamides to 10% NaOH had caused changes in the thermal stability of the samples.

DSC measurements on the polyamide samples shows that the melting curves are shifted towards lower temperature as the exposure time is increased (not shown). From the maximum point on the melting curve the melting temperature of the sample can be detected. However, in the polyamides the melting curve shows an additional peak with a lower intensity on the low temperature side of the melting curve. This peak might also gives information about an additional melting temperature of the sample. After 10 weeks this low temperature peak is decreasing in intensity and is almost only appear as a shoulder on the large peak in the DSC curve measured on the 18 weeks sample. The melting curves in a DSC experiment can also be used to calculate an apparent amount of crystallinity of the sample. Since it is difficult to separate the two melting peaks the crystallinity is calculated from the entire melting curve using the heat of fusion for a 100% crystalline PA66 found in literature as 190.0 J/g [4]. Figure 4 shows a plot of the two melting temperatures and the apparent amount of crystallinity of the PA66 control and exposed samples as function of exposure time.

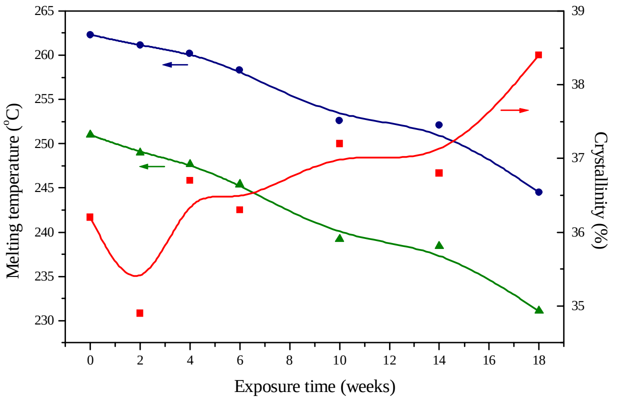

Figure 4. T_m (circle and triangle) and apparent amount of crystallinity (square) of PA66 control and exposed to 10% NaOH at 60 ^{o}C obtained from DSC.

The mechanical properties of the polyamide samples were also studied by measuring a stress/strain curve of the sample. Figure 5 gives the yield stress and the Young’s modulus of the samples calculated from the stress/strain curves. The values given are relative to the control sample (control = 100%). Both the yield stress and the Youngs’s modulus are found to decrease with increasing exposure time.

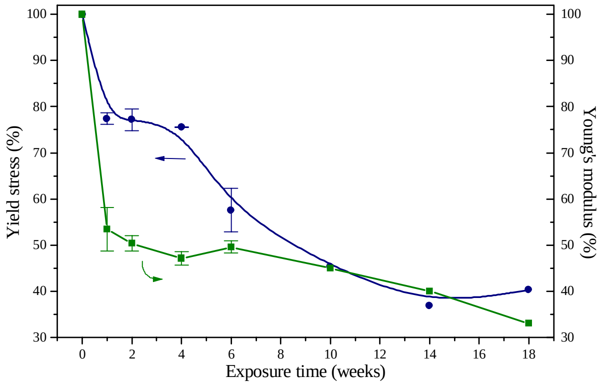

Figure 5. Yield stress (circle) and Young’s modulus (square) of PA66 control and exposed to 10% NaOH at 60 ^{o}C.

Changes of molar masses caused by the exposure to 10% NaOH at 60 ^{o}C have also been studied. The molar masses have been detected by size exclusion chromatography (SEC) and by use of a calibration curve based on poly(methyl methacrylate) samples with well-known molar masses. The detected molar masses of the polyamides are therefore not exact values, but changes in the molar masses caused by exposure to 10% NaOH at 60 ^{o}C can be analysed by comparing the molar masses of the exposed samples with the molar masses of the unexposed control sample. For the control sample and the samples exposed for one to ten weeks, the molar masses were measured on samples that were scratched from the surface. For the samples exposed for 14 and 18 weeks the molar masses were detected on the material that was falling off from the sample surfaces. The number-average molar mass (M_n) and weight-average molar mass (M_w) for PA66 control and exposed samples are given in Figure 6.

The molar masses decrease as function of exposure time and both M_n and M_w have dropped to around 16% of the value for the control sample.

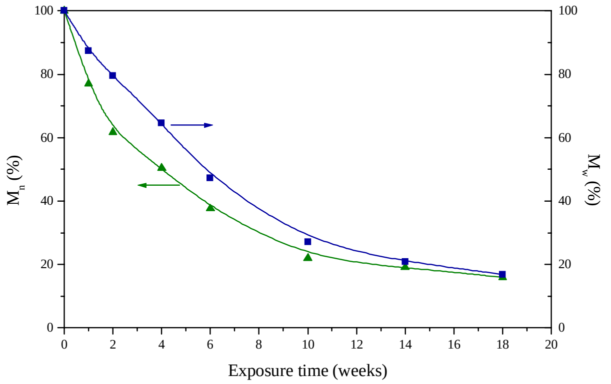

Figure 6. Number-average (triangle) and weight-average (square) molar masses detected on samples from the surfaces of PA66 control and exposed to 10% NaOH at 60 C^{o}.

Figure 7 shows the SEC traces on PA66 control and different samples obtained from PA66 exposed for 18 weeks. The surface layer was the layer that falls off from the sample surface. The second layer of the sample was scratched off the surface of the 18 weeks sample. The third layer was scratched off the surface after the second layer was removed. In SEC analysis the retention volume is closely related to the molar mass (higher retention volumes gives lower molar masses). Figure 7 shows that the surface layer of the 18 weeks sample gives rise to the SEC trace at the highest retention volume and thereby the lowest molar mass. The second layer shows a SEC trace that has moved to a little lower retention volume. The third layer gives a SEC trace present at an even lower retention volume and this trace starts to look more like the trace from the control sample. This result indicates that the degradation is most pronounced at the surface but also that the deeper layers of the sample have been affected by the exposure to 10% NaOH at 60 °C.

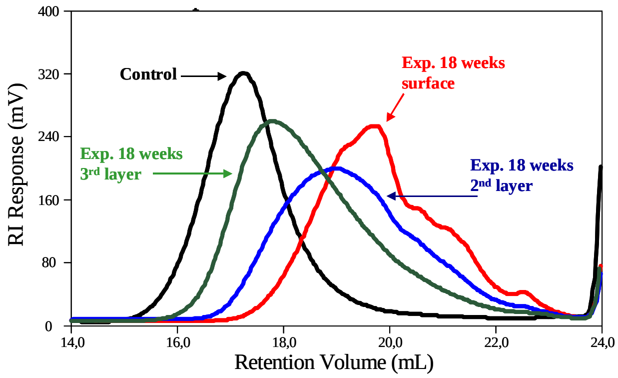

Figure 7. The SEC traces of PA66 control and exposed to 10% NaOH at 60 °C for 18 weeks.

The IR spectroscopy on the polyamides exposed to 10% NaOH at 60 °C showed that the surface of the exposed samples showed a tendency to get a more crystalline structure as the exposure time was increased. This was confirmed by the measured crystallinity from the DSC experiments. The DSC also showed that the melting temperatures were decreasing as function of the exposure time. The TGA showed a shift towards lower temperature for the process where most of the weight-loss was seen. This indicates a loss of thermal stability and additionally an initial weight-loss was seen probably arising from loss of water.

A loss of mechanical properties was also seen. The SEM images revealed that the samples exposed for more than 10 weeks shows a puzzle-like surface. The structure of the puzzle was different in the sample exposed for 10 weeks compared with the sample exposed for 18 weeks. Since the 18 weeks sample shows larger pieces, it might indicate that the surface layer of the sample exposed for 10 weeks has been completely degraded and a new surface layer attacked by the chemical environment in the 18 weeks sample.

The SEC results showed that the molar mass decreases as the exposure increases and that the different layers of the samples have been degraded to different extents. The surface layer of a sample is degraded and falls of - then the next layer is attacked and so on.

Acknowledgement

I wish to acknowledge the financial support from Monepol (“Center for improved plastic products. Understanding the molecular decomposition mechanisms”., a Danish Research Agency funded centre contract (J.nr. 2000-603/4001-51).

The following people are greatly acknowledged for helpful discussions of different parts of my work: Walther Batsberg Petersen, Afshin Ghanbari-Siahkali, Kristoffer Almdal and Søren Hvilsted. Lotte Nielsen is greatly acknowledged for her help in the experimental part of SEC and Keld West for helping with SEM.

References

1. D. Garcia, H.W. Jr. Starkweather, J. Polym. Sci., Polym. Phys. Ed. 23 (1985) 537-555.
2. N. Vasanthan, D.R. Salem, J. Polym. Sci., Part B, Polym. Phys. 38 (2000) 516-524.
3. J.L. Koenig, M.C. Agboatwalla, J. Macromol. Sci. – Phys. B2(3) (1968) 391-420.
4. H.W. Jr. Starkweather, P. Zoller, G.A. Jones, J. Polym. Sci., Polym. Phys. Ed. 22 (9) (1984) 1615.

Morten Rode Kristensen
Address: Building 201, Room 006
Phone: +45 4525 2876
Fax: +45 4588 2258
e-mail: mrk@kt.dtu.dk
www: http://www.ivc-sep.kt.dtu.dk/staff/MRK/more

Supervisors: Per G. Thomsen (IMM)
Michael L. Michelsen (KT)
Erling H. Stenby (KT)

Ph.D. Study
Started: August 2004
To be completed: August 2007

Numerical Simulation of In-Situ Combustion

Abstract

Numerical simulation of fluid flow in petroleum reservoirs has been an active area of research for several decades. Increasingly large models are being solved on powerful computers, but simulation capacity still limits the size and complexity of models needed to describe advanced recovery processes. This is especially true for simulation of the *in-situ combustion* enhanced oil recovery process, which rely on air injection into the reservoir. Simulating in-situ combustion is a challenging multi-scale problem. The purpose of this project is the development of accurate, efficient and reliable models and algorithms for performance prediction in in-situ combustion processes.

Introduction

The world continues to rely substantially on petroleum fossil fuels as a primary energy source. While the number of new discoveries of petroleum reservoirs decreases, the need to produce the known reservoirs more effectively increases. A large part of the remaining reserves are heavy oils, which require specialized recovery methods. Thermal recovery processes, which rely on a viscosity reduction of the oil through heat injected (steam or hot water) or in-situ generated, are well suited to unlock effectively these resources in an environmentally sound manner. The thermal recovery process known as *in-situ combustion* has been a source of interest and effort for several decades. In-situ combustion is the process of injecting air into oil reservoirs to oxidize a portion of the crude oil and enhance recovery through the heat and pressure produced. Contrary to other thermal recovery processes the main part of the energy required to displace the oil in in-situ combustion is generated inside the reservoir from the heat released by chemical reactions between oxygen and fractions of the crude oil.

In-situ combustion is technically and economically an attractive process, particularly since the portion of the crude burned is likely to be the heaviest and least valuable. Whereas it is generally classified as a technique that is applicable for heavy oils because of the dramatic reduction in oil viscosity with temperature, in-situ combustion also promotes production through thermal expansion and gas drive caused by combustion gases. The process has proven economically in recovering heavy oil from shallow reservoirs and lighter oil from deep reservoirs, where other processes, such as steam injection, are unattractive [4].

Process Description

The oil in the reservoir is ignited near the injection well either spontaneously after oxygen injection or by external means. The displacement is governed by several different mechanisms:

- The temperature increase caused by combustion increases the mobility of the oil.
- Vaporization of connate water forms a steam zone acting as a steam drive.
- Vaporization of a portion of the crude oil may form a miscible displacement.

- High-temperature combustion products may form an in-situ CO_2 flood.

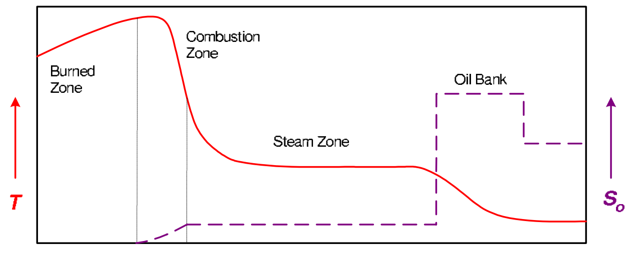

Figure 1: Characteristic zones in an in-situ combustion process. Qualitative temperature and oil saturation profiles are shown (adapted from Prats [3]).

As seen from Figure 1 a number of characteristic zones can be identified in an in-situ combustion process. The main area of activity is the combustion zone, in which the injected oxygen reacts with the oil. Ahead of the combustion zone is a zone containing combustion gases and vaporized formation water. The leading edge of this zone is the main area of oil mobilization.

A Complex Multiscale Process

In-situ combustion is one of the most physically complex enhanced oil recovery processes currently in use. Driven by complex chemical reactions the oil mobility is increased with the elevated temperatures and the fluids are displaced by a combination of steam, water and gas drive. The spatial as well as temporal scales in in-situ combustion vary over many orders of magnitude. The bulk of the chemical reactions take place in the narrow reaction zone that may be less than a meter in thickness compared to reservoir scales of hundreds or thousands of meters. Moreover, combustion reactions often occur in fractions of a second, whereas the temporal scales associated with convective transport may be running to days or years. Accurate prediction of field performance in such a multiscale process is an immense challenge requiring a hierarchical approach, in which both spatial and temporal resolution is adapted in order to capture the crucial input from all levels of activity.

The overall performance of an in-situ combustion process in governed in a complex way by reservoir heterogeneity, well configurations, injection rates and composition, initial oil saturation and distribution and both thermodynamic and chemical properties of the rock and fluids. Reliable prediction of field performance requires a fully integrated approach in which the important contributions from all levels are taken into account. In-situ combustion is indeed a multiphysics process bringing together multiphase porous media flow, chemical kinetics and phase equilibria. Current numerical simulators do not adequately resolve the important physics, but resort to non-physical adjustments, which seriously questions their predictive capabilities.

The spatial scales affecting in-situ combustion span from large geological features such as faults of the size of the reservoir to the very small scale at which chemical reactions happen in the combustion zone. Faults, fractures and the placement of wells determine global flow patterns, but local displacement efficiency is governed by small scale heterogeneity in porosity and permeability of the reservoir and by the chemical and thermodynamic behavior of the fluids. Permeability fields are often obtained from high-resolution geocellular models having gridblock sizes on the order of a meter. Reservoir simulations, however, are carried out using gridblocks that are 1–2 orders of magnitude larger due to computational constraints. Upscaling of the permeability or transmissibility field, in which local flow behavior is taken into account, is routinely done. As mentioned above, the bulk of the chemical reactions happen in a narrow combustion zone being less than a meter in thickness compared to standard gridblock sizes of, say, 50 meters. Thus, the spatial scale for chemical reactions is smaller than the smallest scale normally resolved in reservoir simulations. Consequently, the temperature profile on the simulation grid will be too smooth, and important phenomena such as ignition/extinction or quenching may not be predicted correctly.

Relating to temporal scale, a number of different processes may be identified in in-situ combustion, each having its own characteristic scale. Most of the existing in-situ combustion models include convective mass transfer, convective and conductive heat transfer, kinetically controlled chemical reactions and fluid phases in thermodynamic equilibrium [2, 1]. The phase equilibrium assumption implicitly states that the timescales for the interphase mass transfer processes occurring when phases come to an equilibrium state, are much faster than all other timescales. Of the remaining processes, the chemical reactions are likely to occur on timescales that are again much faster than the scales for mass and heat transport.

Although being multiscale in nature, the question remains whether all the processes in in-situ combustion represent essential physics that needs to be resolved in a simulation. The goal of in-situ combustion simulation is to provide reliable predictions of performance, typically in terms of production, for a given in-situ combustion project. The production certainly depends on large scale features such as well placement, but the small scale behavior, spatial as well as temporal, in the combustion zone may be equally important. In-situ combustion processes are driven by chemical reactions. Chemical kinetics depends strongly on temperature, thus failing to capture temperature peaks and, in general, smoothing out temperature profiles on too coarse a grid will lead to inaccurate prediction of reaction, which in turn will affect the amount of heat released and combustion gases evolved, ultimately resulting in wrong predictions of oil displacement. Ahead of the combustion front (see Figure 1) the oil is mobilized by a combination of steam, water and gas drive. Lighter oil components will vaporize easily and be transported downstream. The compositional behavior in this region will determine the amount and composition of the oil left behind as fuel for the combustion. Therefore, accurate prediction of phase behavior as well as flow is likely to impact overall performance. Errors at this small scale will feed into overall production calculations, thereby rendering the results unreliable. Hence, the important processes in in-situ combustion are indeed multiscale with strong nonlinear interactions between different scales and efficient computational methods must be developed that handle this multiscale nature.

Mathematical Formulation

The governing equations for in-situ combustion can be derived from the conservation of mass, momentum and energy. A generalized continuity equation for a fluid component i present in n_p different phases may be written as:

$$\frac{\partial}{\partial t}\left[\phi_f \sum_{j=1}^{n_p} x_{ij}\rho_j S_j\right] = q_i - \nabla\cdot\left[\sum_{j=1}^{n_p} x_{ij}\rho_j \mathbf{u}_j\right] + \sum_{k=1}^{n_r} A_{ik} r_k \tag{1}$$

in which S_j is the phase saturation, ρ_j the molar phase density and x_{ij} the mole fraction of component i in phase j. q_i represents sources and sinks due to wells. r_k is the kinetic expression for the kth chemical reaction and A_{ik} is the stoichiometric coefficient for component i in reaction k. The flow velocity in (1) may in principle be obtained by solving a set of balance equations for momentum. For porous media flow, however, this would be intractably complex. Instead, Darcy's law is often used, which states that the local flow velocity is proportional to the pressure gradient. For flow of multiple phases Darcy's law is given by:

$$\mathbf{u}_j = -\frac{\mathbf{k}k_{rj}}{\mu_j}\cdot\left(\nabla P_j - \rho_j g \nabla D\right) \tag{2}$$

in which P_j is the phase pressure, D the depth, μ_j the phase viscosity, $\mathbf{k}$ the Darcy permeability tensor and k_{rj} the relative permeability of phase j. The energy balance including effects of convection, conduction and chemical reaction may be written as:

$$\frac{\partial}{\partial t}\left[(1-\phi_v)\rho_r U_r + (\phi_v - \phi_f)\rho_s U_s + \phi_f \sum_{j=1}^{n_p} U_j \rho_j S_j\right] = \nabla\cdot\left[\mathbf{k}_t \nabla T\right] - \nabla\cdot\left[\sum_{j=1}^{n_p} h_j \rho_j \mathbf{u}_j\right] + \sum_{k=1}^{n_r}(-\Delta H_k) r_k \tag{3}$$

in which U_j is the molar internal energy of phase j, h_j is the enthalpy of phase j, ΔH_k is the reaction enthalpy of reaction k, $\mathbf{k}_t$ is the (volume averaged) effective heat conductivity for the solid and fluid phases and the rock. ρ_r and U_r are the density and internal energy of the reservoir rock, respectively.

Adaptive Framework for ISC Simulation

The multiscale challenge may be approached computationally by either attempting to resolve all relevant scales or by making use of appropriate subgrid scale models to represent the small scale processes. The approach taken in this project is to resolve the relevant scales by using adaptive numerical methods.

Adaptivity in space is achieved by using adaptive gridding techniques, in which the computational grid is adapted dynamically to the regions of interest. A dense grid can then by used to resolve the fine-scale changes in the combustion zone, whereas a much coarser grid is used in regions away from the combustion zone.

In order to capture the fast dynamics of chemical reactions in the combustion zone, the reaction kinetics must be integrated using timesteps that are much smaller than those necessary for capturing the effects of convection and conduction. An intuitive way of approaching this problem numerically is by splitting and fractional timestepping where convective and conductive terms in the equations are separated from reaction terms. Each global timestep then consists of a series of substeps, in which the individual terms are integrated separately, the advantage being that small timesteps can be applied only to those terms requiring high resolution. The separation of scales in the problem is thereby exploited numerically by adapting the time integration to the individual scales. The cost of using a fractional step approach is a numerical error introduced by the splitting, since in each substep only one process is taken into account and the interaction with the other processes neglected.

To give a simple example of operator splitting, the following semi-discretized PDE is considered:

$$\frac{\partial \mathbf{u}}{\partial t} = (\mathcal{A}+\mathcal{B})\,\mathbf{u}, \qquad \mathbf{u}(t_0) = \mathbf{u}_0 \tag{4}$$

in which $\mathcal{A}$ and $\mathcal{B}$ are, in general, nonlinear operators. For example, $\mathcal{A}$ could be reaction and $\mathcal{B}$ could be discretized convection. An often used splitting scheme for solving this two-operator PDE is the *Strang* splitting scheme, which is outlined below and illustrated in Figure 2. It consists of three substeps: (i) half a step on operator $\mathcal{A}$, (ii) a full step on operator $\mathcal{B}$, and (iii), finally, half a step on operator $\mathcal{A}$:

$$\mathbf{u}^{(1)} = \mathbf{u}_n + \frac{\Delta t}{2}\mathcal{A}\mathbf{u}_n \tag{5a}$$

$$\mathbf{u}^{(2)} = \mathbf{u}^{(1)} + \Delta t\mathcal{B}\mathbf{u}^{(1)} \tag{5b}$$

$$\mathbf{u}_{n+1} = \mathbf{u}^{(2)} + \frac{\Delta t}{2}\mathcal{A}\mathbf{u}^{(2)} \tag{5c}$$

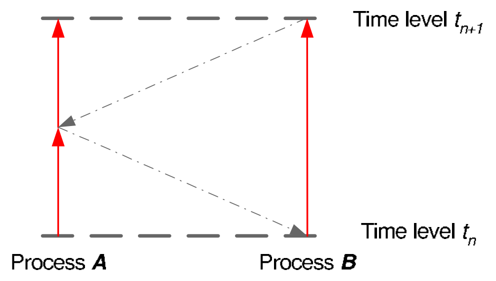

Figure 2: Illustration of Strang splitting for two operators.

In each substep only one operator is considered. In the reaction substep, for example, the convective term is ignored and the semi-discretized PDE reduces to a number uncoupled ODE problems. Effectively, this means that, in the reaction substep, each gridblock in the domain is treated as a small chemical reactor as illustrated in Figure 3. For the in-situ combustion problem a splitting scheme similar in structure to the one above will be applied.

Conclusion

In-situ combustion is a challenging multi-scale problem. Both spatial and temporal scales vary over many orders of magnitude. The key idea when building simulation tools for this process is to localize computational effort by using adaptive numerical methods that are tailored to the underlying physics of the problem. Current research is focusing on temporal discretization using splitting methods and developing efficient solvers for reaction and phase equilibrium in in-situ combustion.

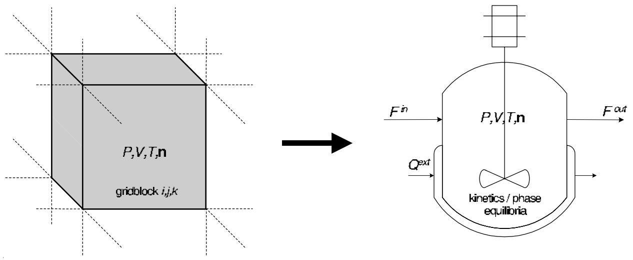

Figure 3: Using numerical splitting techniques for reaction each gridblock in the domain is effectively treated as a small chemical reactor, the advantage being that efficient solvers can be applied that are tailored for integrating stiff reaction kinetics.

Acknowledgements

The project is carried out in collaboration with Department of Petroleum Engineering, Stanford University.

References

[1] K. H. Coats. In-situ combustion model. *Society of Petroleum Engineers Journal*, 269:533–554, 1980.

[2] R. B. Crookston, W. E. Culham, and W. H. Chen. A numerical simulation model for thermal recovery processes. *Society of Petroleum Engineers Journal*, pages 37–58, 1979.

[3] Michael Prats. *Thermal Recovery*, volume 7 of *SPE Monograph Series*. Society of Petroleum Engineers, 1986.

[4] Partha S. Sarathi. In-situ combustion handbook – principles and practices. Technical report, U.S. Department of Energy, 1999. DOE/PC/91008-0374.

Morten Boberg Larsen

Address:	Institut for Kemiteknik Bygning 229 DK-2800 Kgs. Lyngby
Phone:	+45 4525 2842
Fax:	+45 4588 2258
e-mail:	mbl@kt.dtu.dk
www:	http://www.chec.kt.dtu.dk
Supervisors:	Kim Dam-Johansen, DTU Lars Skaarup Jensen, FLSmidth & CO Peter Glarborg, DTU Flemming Frandsen, DTU
Ph.D. Study	Industrial Ph.D.
Started:	October 2003
To be completed:	September 2006

Combustion Mechanisms Using Secondary Fuels in Cement Production

Abstract

The aim of this PhD-project is to investigate combustion mechanisms of secondary fuels used in the cement production. In particular the study is focused on combustion mechanisms of lumpy fuels fired in the Hotdisc-unit developed by FLSmidth & CO. The study is composed of four main components: Literature study, mathematical modeling, pilot scale/laboratory scale experiments and full scale measurements on industrial scale. Macro-TGA experiments to investigate pyrolysis mass loss behaviour of large tyre rubber particles is described and interpreted using a detailed mathematical model herein.

Introduction

The production of cement clinker is an energy intensive process that traditionally has been depended on coal, oil and other fossil fuel resources. The use of secondary fuels in the kiln-systems for cement production is an economically and environmentally feasible way to get rid of waste and replace non-renewable fossil fuel.

In the recent years, the use of secondary fuels in cement production has increased. Approximately 12% of the total fuel-usage in the production of cement is covered by use of secondary fuels in the EU. In Germany this figure has increased from 4% in 1987 to 30% in 2001. At some cement-plants more than 90% of the fuel-usage comes from waste. The different kind of secondary fuels employed at this moment in kiln-systems for cement production, are used tires, meat and bone meal, plastics, biomass and other [1]. It is expected, that the ability utilize secondary fuels in the in the cement-industry will become even more important in the future.

The advantages of using secondary fuels in the cement production are:

- The residual ash formed during combustion is incorporated into cement. This is classified as reuse by EU, whereas ash formed in traditional waste incineration plants is classified as disposal [2].
- The price of the secondary fuel is lower than conventional fossil fuels and sometimes the price is negative, i.e. the cement manufacturer is paid to receive the fuel.
- The utilization of secondary fuels in the cement industry creates further research in the areas of environmentally and economically utilization of waste.

The Hotdisc-technology, which is developed by FLSmidth & CO, is used for combustion of large fuel particles in the cement-industry. Figure 1 shows a schematic drawing of the Hotdisc-unit, which consists of a rotating plate in a combustion chamber, at which the combustion of the secondary fuels takes place. The waste is admitted to a rotating disc together with preheated atmospheric air (Tertiary air, 850-1000°C) followed by subsequent ignition and combustion releasing the energy for calcination of the limestone, which is a major component in the cement manufacturing process:

$$CaCO_3(s) \rightarrow CaO(s)+CO_2\ (g)$$
$$\Delta H=1782\ kJ/kg\ CaCO_3$$

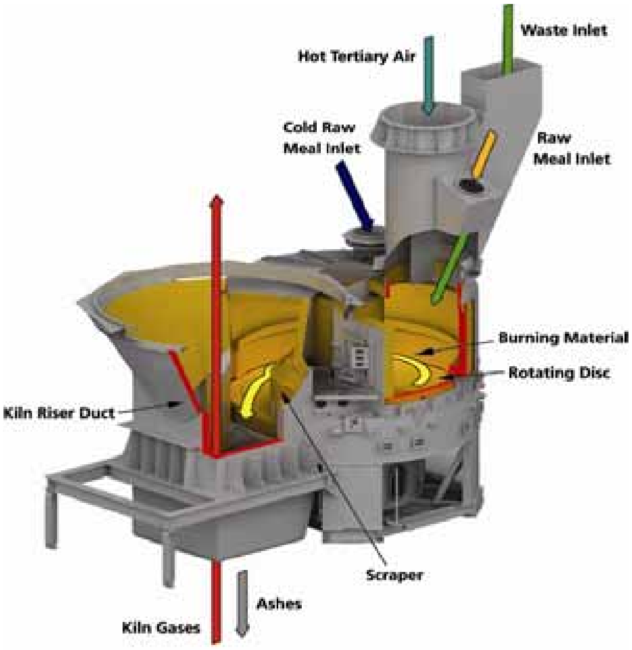

***Figure 1** – Schematic drawing of the Hotdisc.*

This endothermic reaction is the most energy consuming process in cement kilns, which uses approximately 65% of the fired energy input [3]. Waste and ashes, which is not burned completely at the Hotdisc enters the conventional system for calcination. The elements Fe, Al and Si in the secondary fuels are oxidized to Fe_2O_3, Al_2O_3, SiO_2 and incorporated into the cement clinker and thereby saving raw material.

At the end of the disc the remaining solids are transported to the conventional part of the kiln system. An important feature of processing secondary fuels in a cement kiln is the high residence time at high temperature, which ensures a complete conversion of polluting organic species. In order to comply with the EU regulation 2000/76/EC, the flue gas from combustion of non halogenated wastes should be treated at temperatures above 850°C for at least 2 seconds. This criterion is fulfilled in modern pre-calciner systems of the cement production as well as in the rotary kiln.

Specific Objectives

The aim of the ongoing industrial Ph-D study is to systematically create knowledge for further developments of the Hotdisc and other applications for use of secondary fuels in cement production. The knowledge should base on scientific methods. In particular the project is focused on the combustion mechanisms of waste, which include a detailed scientific description of the different stages in the combustion of the solid fuel and furthermore a scientific approach should be applied in order to understand the formation of inorganic pollutants, i.e. NO_x. The four main components of the PhD study are as follows:

- *Literature study*
- *Mathematical modeling*
- *Pilot scale / laboratory scale experiments*
- *Full scale measurements*

The PhD project should contribute to the earning of FLSmidth & CO in the future and help ensuring the position of FLSmidth & CO as the leading company supplying solutions to the cement industry.

Selected results

The first step in the combustion for a large piece of fuel is pyrolysis (or devolatilization), where the fuel releases its volatile components (e.g. gasses and tars). Pyrolysis has been widely studied in connection with pulverized coal combustion of small particles, where the chemical kinetics is the rate controlling step. However, a significant difference exists for large particles, because mass and heat transfer should be considered to interpret the pyrolysis of large particles. Since tyre rubber is used extensively as a fuel in the cement industry, a series of experiments are performed in a developed macro-TGA reactor in order to elucidate the fundamental aspects of pyrolysis of large tyre rubber particles.

Tyre rubber is cut into cylindrical particles with a diameter between 7.5 and 22mm and a height of approximately 35mm. Since tyre is an inhomogeneous material, containing tread and steel it is unsuitable for systematic experiments, due to the difficulties in producing identical samples. Consequently, new tyre rubber from the wearing face of a truck tyre without tread and steel wires were obtained from PointS, Denmark, and used for the experiments.

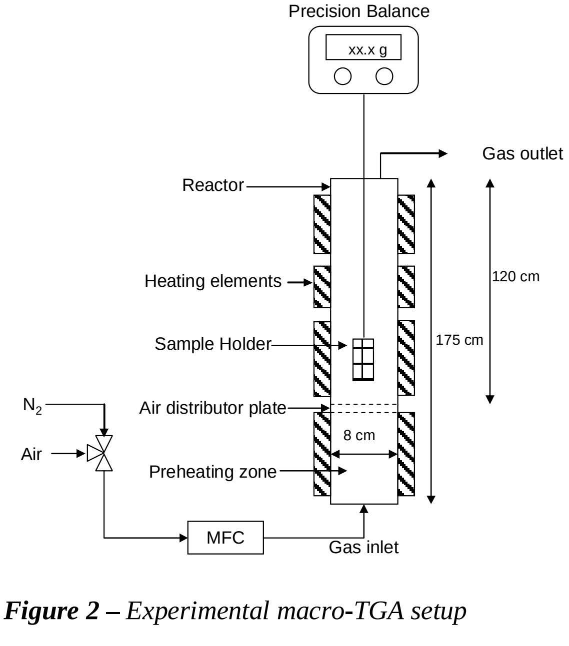

***Figure 2** – Experimental macro-TGA setup*

The Macro-TGA setup used for the experiments is depicted in figure 2. It consists of a vertical cylindrical reactor with four electrical heating elements. A valve and a Mass Flow Controller (MFC) are used for addition of a well defined flow of either pure N_2 or air (21 Vol.% O_2) to the bottom of the reactor. All experimental results herein are obtained with a gas flow of 17.5 Nl/min. Preheating of the gas takes place in the bottom of the reactor and experimental temperature measurements in the centre of the reactor for different set point temperatures of the heating elements gives the temperature that the sample experiences in the reactor. The cylindrical tyre rubber samples are placed in a holder prepared in the same diameter as the tyre sample. The holder is made of a stainless steel mesh where the wires have a diameter of approximately 0.5 mm and a quadratic clearance of approximately 0.5x0.5 mm. The purpose of the net is to retain the char layer during the pyrolysis process and thereby secure well defined conditions, i.e. swelling and removal of the char layer is inhibited. Each experiment is initiated by immersing the sample holder with tyre rubber into the preheated reactor under continuous gas flow, i.e. the tyre rubber particle experiences the same environment as a piece of tyre rubber under combustion conditions or continuous pyrolysis processes. A precision balance measures the weight of the sample, and a data acquisition program records the signal on a computer for later data interpretation.

Figure 3 shows the obtained experimental scaled mass-loss for four different particle sizes at different temperatures in inert atmosphere. The discontinuities observed in the experimental mass-loss curves are a consequence of the balance which has an accuracy of ±0.1 g. Since the weight of a rubber sample can be down to 2 g, a small variation in the scale readout may cause significant changes in the calculated scaled mass-loss. For the larger particles, the discontinuity diminishes as the particles have larger masses. The ultimate mass-loss observed in the macro-TGA experiments is observed to be approximately 0.65 independent of particle size, i.e. a volatile content of approximately 65 wt.% which is in agreement with the proximate analysis. For the 7.5 mm particle, the ultimate mass-loss is observed to vary in the range 0.50 - 0.70, with a temperature of 840°C yielding the highest amount of volatiles and these variations are attributed to experimental uncertainties for the small sample masses. If the pyrolysis time is defined as the time where the first derivative of the scaled mass-loss curve against time approaches zero, the effect of the surrounding temperature on pyrolysis time is seen to be very significant for all particle diameters. For a particle with a diameter of 22 mm, the pyrolysis time is observed to increase from approximately 300 seconds for a surrounding temperature of 840°C to approx. 400 seconds at 620°C and approx. 750 seconds at 490°C. The effect of particle size on the time of pyrolysis is also significant. At 840°C, the time of pyrolysis is observed to increase from approximately 75 to 300 seconds when increasing the particle diameter from 7.5 mm to 22mm. The shape of the mass-loss vs. time is observed to behave similarly. For the temperature of 840°C, the shape of the mass-loss curve is seen to be close to a straight line for all sizes, whereas the shape for the results at 490°C is seen to be more curved, and this behaviour is especially pronounced against the end of the pyrolysis process. Apparently each particle size seems to yield approximately the same slope of the mass loss against time independent of temperature.

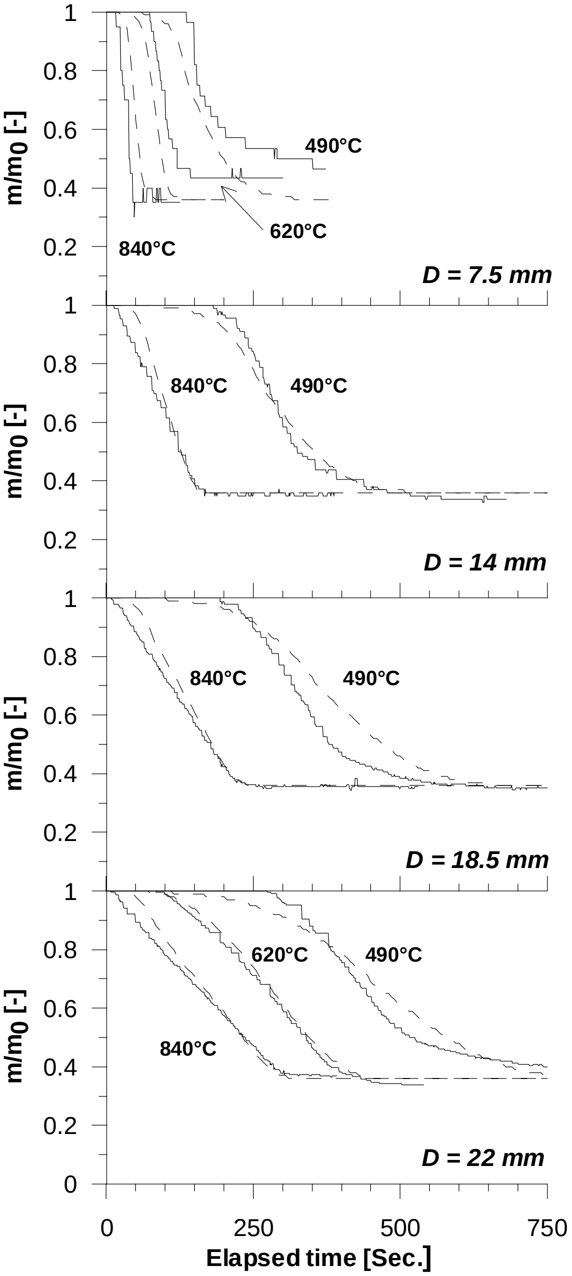

Figure 3 – *Measured and predicted scaled mass-losses for tyre rubber cylinders as a function of size and temperature in inert atmosphere. The dashed and solid lines represents the model calculation and measured values respectively.*

Mathematical model

The aim of the mathematical model is to predict pyrolysis mass-loss behaviour for large tyre rubber particles, under conditions pertinent to combustion.

The pyrolysis of a large tyre rubber particle may be subdivided into a number of physical and chemical processes. Figure 4 depicts a simplified drawing of a partially pyrolyzed solid fuel particle, where the pyrolysis is driven by external heating. The heat is transported into the material by conduction through the char-, reacting- and virgin fuel layers, where radiative heat transfer may have a role in the char- and reacting layers. In the reacting layer, the rubber polymers are depolymerised and evaporated, and as a consequence of the volatile-production, an outward mass transport through the particle is induced. Independent reactions may be endo- or exothermic and may also include secondary reactions. The outward mass-flow may also cool the hotter solid when the cooler gas flows from the interior. In an oxidizing atmosphere, the pyrolysis products may ignite in a flame front above the outer surface, enhancing the external heat transfer to the surface. Finally, the outflow of pyrolysis products may cause the solid to swell.

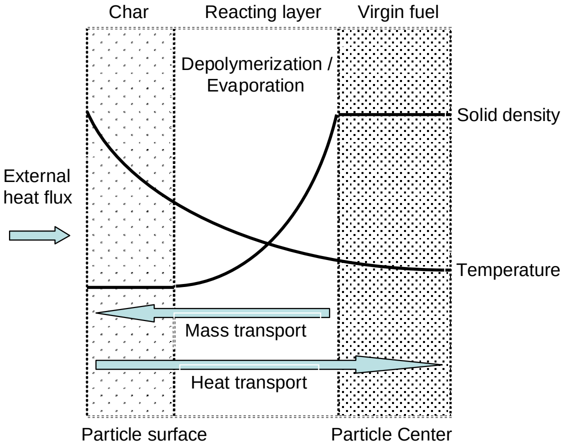

***Figure 4** – Schematic illustration of the pyrolysis of a large tyre particle.*

In the current model, the solid matrix is assumed to consist of constant char- and ash fractions as well as a varying volatile part made up of 3 sub fractions. The reaction scheme for the pyrolysis process is assumed to consist of 3 independent parallel reactions where the solid is depolymerised and evaporated forming gas in a single step according to (1), where the gas produced during the solid decomposition of the different fractions is assumed to behave identical and to have same specific heat capacity.

$$Solid_i \longrightarrow Gas \quad ,i=1,3 \tag{1}$$

where the solid is decomposed according to the following first order volumetric Arrhenius decomposition rate:

$$R_i=\frac{dx_i}{dt}=-A_i\exp\left(-\frac{E_i}{R_gT}\right)x_i \quad ,i=1,3 \tag{2}$$

here x_i is the mass fraction of the volatile component, *i*, based on initial mass (see nomenclature). Because the temperature may vary radially in the large tyre rubber particle, the rate of decomposition may be different in the particle centre from a position closer to the surface. Therefore an energy balance is needed to account for the temperature variation. If the outflow of volatile gasses is in thermal equilibrium with the surrounding solid, the complete energy balance for a cylinder with heat transport in the radial direction becomes:

$$\left(\rho_{solid}c_{p,solid}+\rho_{gas}c_{p,gas}\right)\frac{\partial T}{\partial t}+c_{p,v}m_v\frac{\partial T}{\partial r}-\frac{1}{r}\frac{\partial}{\partial r}\left(k\cdot r\frac{\partial T}{\partial r}\right)-\rho_{vf}\sum_{i=1}^{3}R_i\Delta H_i=0 \tag{3}$$

The first term represents accumulation of energy, the second term convective transport of energy, the third term conduction of energy and fourth term heat effects of reactions. A reduction of (3) may safely be performed acknowledging that $\rho_{solid}c_{p,solid} >> \rho_{gas}c_{p,gas}$ which yields:

$$\rho_{solid}c_{p,solid}\frac{\partial T}{\partial t}+c_{p,v}m_v\frac{\partial T}{\partial r}-\frac{1}{r}\frac{\partial}{\partial r}\left(k\cdot r\frac{\partial T}{\partial r}\right)-\rho_{vf}\sum_{i=1}^{N}R_i\Delta H_i=0 \tag{4}$$

The initial and boundary conditions for (4) are as follows, where (6) states that heat transferred to the outer particle surface is conducted into the material and (7) states that the particle is symmetric around the centre:

$$T(r,t=0)=T_0 \tag{5}$$

$$k\left.\frac{\partial T}{\partial r}\right|_{r=r_0,t>0}=h_{eff}\left(T_\infty-T_{r=r_0}\right) \tag{6}$$

$$\left.\frac{\partial T}{\partial r}\right|_{r=0}=0 \tag{7}$$

h_{eff} is the effective overall heat transfer coefficient including both convective and radiative heat transport. The outflow of volatiles accumulates towards the particle surface, since volatiles released closer to the particle centre flows towards the particle surface where decomposition reactions may further contribute to the volatile flux. A differential mass balance for cylinder geometry yields:

$$-\frac{d}{dr}\left(r\cdot m_v\right)=r\rho_{vf}\sum_{i=1}^{3}R_i \tag{8}$$

Upon integration the volatile flux at a given radial position, *r'*, is:

$$m_v(r')=-\frac{\rho_{vf}}{r'}\sum_{i=1}^{3}\int_0^{r'}r\cdot R_i\cdot dr \tag{9}$$

During the progress of the pyrolysis the physical structure of the solid changes, and therefore, the thermal conductivity and the specific heat capacity also changes.

In order to describe the change of physical parameters, a local pyrolysis conversion is introduced:

$$X_{local}(r) = 1 - \frac{\rho(r) - (1-V)\rho_{vf}}{V\rho_{vf}} \tag{10}$$

and from the local pyrolysis conversion, the effective thermal conductivity and effective heat capacity of solid is obtained:

$$k(r) = \left(1 - X_{local}\right) k_{vf} + X_{local} k_{char} \tag{11}$$

$$c_{p,solid}(r) = \left(1 - X_{local}\right) c_{p,vf} + X_{local} c_{p,char} \tag{12}$$

The total pyrolysis conversion, *X*, is determined by:

$$X(t) = 1 - \frac{mass\ of\ volatiles\ at\ t}{mass\ of\ volatiles\ at\ t=0} = 1 - \frac{2\int_0^{r_0} r\left(\rho(r) - (1-V)\rho_{vf}\right)dr}{r_0^2 V \rho_{vf}} \tag{13}$$

and from the pyrolysis conversion the normalized (or scaled) mass-loss, m/m_0, for comparison with the experimental results is derived:

$$\frac{m(t)}{m_0} = 1 - X(t)\cdot V \tag{14}$$

Equation is (4) discretized and solved together with the remaining equations using an implicit finite difference method. The obtained solution was tested and found to be independent of applied spatial discretization points and time step. The values of the employed physical parameters are not given here.

In figure 3 comparisons between the predicted and measured mass-loss is made for all particle sizes and surrounding temperatures. At a surrounding temperature of 840°C for the 14, 18.5 and 22 mm rubber particle, agreement between the experimental and predicted scaled mass losses are found. At 620°C and for a diameter of 22 mm excellent agreement between the model and experimental data are found. At 490°C and for particles with a diameter between 14-22 mm, the predicted mass loss is observed to initiate slightly faster than the experimental data. For prolonged times, the predicted mass loss curve is observed to cross the experimental curve. The predicted pyrolysis time is however observed to be in agreement with the experiments. For the particle with a diameter of 7.5 mm, discrepancies arises between the predicted and measured mass loss for longer times, and this is mainly caused by that the model uses a fixed volatile content whereas the experimental results yields varying ultimate mass loss (caused by uncertainties). However, the shape of the modeled mass loss curves for the 7.5 mm rubber particles is in agreement with the experimental findings.

Conclusion

The current industrial PhD project deals with combustion mechanisms of secondary fuels with regard to utilization in the cement industry. The project is composed of four main elements: Literature study, mathematical modeling, pilot/laboratory scale measurements and full scale measurements, which all should contribute to an overall understanding of the combustion mechanisms of waste when used as a fuel in cement production.

As a part of the pilot/laboratory scale experimental section, detailed experimental investigations are performed in a developed macro-TGA reactor in order to elucidate the pyrolysis mass loss behaviour of large tyre rubber particles. A detailed mathematical model was also developed and validated using the experimental data from the macro TGA. The developed and validated mathematical model may now be used to predict exactly the time of pyrolysis of tire rubber pieces of different sizes fired in the Hotdisc unit.

It is concluded that this is an example on how results from laboratory experiments may produced, analyzed and used as a development tool in the industry.

References

1. Smith, I.. Co-utilization of coal and other fuels in cement kilns. IEA Clean Coal Centre, August 2003.

2. Chandelle, J.M., Valorisation of waste in cement kilns, World Cement, 75, November 2003.

3. Andersen, P.S., Cementfabrikken (In danish). FLSmidth & CO, January 1981.

Thomas Ricco Ølholm Larsen
Address: DPC, Dept. of Chemical Engineering,
Building 423, Technical University of
Denmark
Phone: +45 4525 2974
Fax: +45 4588 2161
e-mail: tol@kt.dtu.dk
www: http://www.polymers.dk

Supervisors: Martin E. Vigild (DTU)
Tom L. Andersen (Risø)

Ph.D. Study
Started: January 2004
To be completed: January 2007

Tribological Properties of Polymer-Matrix Composites when Dry-Sliding Against Steel Counterfaces

Abstract

Polymer-matrix composites are a class of materials which is being used increasingly in applications where friction and wear are important parameters. Beside beneficial properties such as a high strength-to-density ratio and chemical resistance, polymers generally also have a relatively low coefficient of friction when dry-sliding against steel counterfaces. The friction and wear properties of an epoxy resin reinforced with a glass fiber weave (G/EP) and a carbon/aramid hybrid weave (CA/EP), respectively, are examined. Tribological data are collected using a custom made Pin-On-Disk apparatus capable of measuring wear rates, coefficients of friction (μ) and contact temperatures. It is found that μ in average are reduced by 35% by substituting the glass fiber weave with the carbon/aramid weave. Furthermore, the average level of wear rates for G/EP is found to be a factor of 12 higher than for CA/EP.

Introduction

Tribology is the science of friction, wear and lubrication of interacting surfaces in relative motion [1]. Polymer-matrix composites (PMC) are a class of materials, which is being increasingly used for purposes where friction and wear are important parameters [2]. Examples of this are gears, seals, rollers, tank track pads, bearings, brakes and artificial joints. PMC are often preferred to other materials because of their easy processability, high strength to density ratio, chemical resistance and generally low coefficient of friction [3-4]. Furthermore, some PMC have self-lubricating properties, which make them an excellent choice for systems where addition of lubricants such as oil or grease is inexpedient [5]. The dry-sliding ability of PMC decreases the need for maintenance and the risk of emergency sliding conditions, which are seen in the case of metals, when lubricating systems fail [6].

Despite of the increasing use of PMC, the knowledge on their tribological behaviour are largely empirical and have limited predictive capability. Thus, there is a need for a better understanding of how different designs and compositions of PMC affect their tribological properties [2].

The tribological behaviour of polymeric materials have frequently been optimized by reducing adhesion to the counterpart and improving the mechanical properties e.g. hardness, toughness and stiffness. This has traditionally been done by adding solid lubricants, e.g. PTFE (polytetrafluoroethylene) or graphite flakes, different strength giving fibers, e.g. carbon, glass and aramid fibers [7], or inorganic microscale particles e.g. CuO, Pb_3O_4 and TiO_2. [4].

Results regarding the ability of inorganic nanoscale particles to optimize tribological properties of PMC have been published recently [8-14]. The mechanism behind this optimization is not entirely understood, however, it seems to be the case that such particles in some cases promote adhesion of a transfer film to the counterface, which reduces wear and often also friction. Furthermore, a unique feature of nanoparticles is their ability to increase toughness and stiffness simultaneously [15], which is a desired property combination according to basic tribological models [16-17].

Objectives

The aim of this study is partly to produce a PMC with excellent tribological properties when performing in a well defined test system, and partly to examine new material combinations and thereby contributing with new knowledge in this area. In this study PMC based on an epoxy resin are tested. Epoxy resins do generally not exhibit good tribological properties due to the cross linked structure, which inhibits the formation of an efficient transfer film and results in a relatively high degree of brittleness. However, epoxy resins poses other favourable properties such as strong adhesion to many materials, good mechanical and electrical properties, relatively high chemical and thermal resistance [1], and a low price compared to state-of-the art polymers such as PEEK and Polyimide. From this perspective, it is an attractive goal to obtain an epoxy-based composite with excellent tribological properties by incorporating the right kind of components e.g. fibers and micro- or nanoscale particles. In this yearbook contribution, results regarding the friction and wear behavior of an epoxy resin reinforced with two types of fibrous reinforcement are presented. That is, a plain glass fiber weave (G/EP) and a carbon/aramid hybrid weave (CA/EP), respectively. Tribological tests are performed at nine different combinations of contact pressure (p) and sliding velocity (v) also refereed to as pv factors. The purpose is to systematically examine the relative performance level of these two materials while going from mild to severe sliding conditions.

Methods

The tribological properties of the produced composites are tested on a custom made Pin-On-Disk (POD) tribotester build at DTU as a part of this project, cf. figure 1. The principle of the Pin-On-Disk method is as follows: a test specimen in the form of a pin is fixated in a lever-arm and loaded perpendicular against a rotating steel disk. The normal load (W) is adjusted simply by placing different weights on top of the lever-arm. The latter, which can move freely both in the vertical and horizontal direction, will have a tendency to swing in the same direction as the disk revolves due to friction between the surfaces. However, it is not allowed to do so since it is kept in a fixed position by a force transducer which measures the frictional force (F_f). The coefficient of friction (μ) is obtained by using Amontons well-known first law of friction i.e. $\mu=F_f / W$, and is reported as a time-averaged value based on data points in the steady state regime. The wear rate is obtained simply by measuring the weight loss of the pin after being worn a certain amount of time under steady state conditions. Furthermore, a non-contact thermometer estimates the contact temperature by collecting infrared radiation from the side of the steel disk.

Information about the microstructure of composites, wear mechanisms and the appearance of transfer films on the counterface are examined by different microscopic methods such as optical, SEM, FE-SEM and TEM.

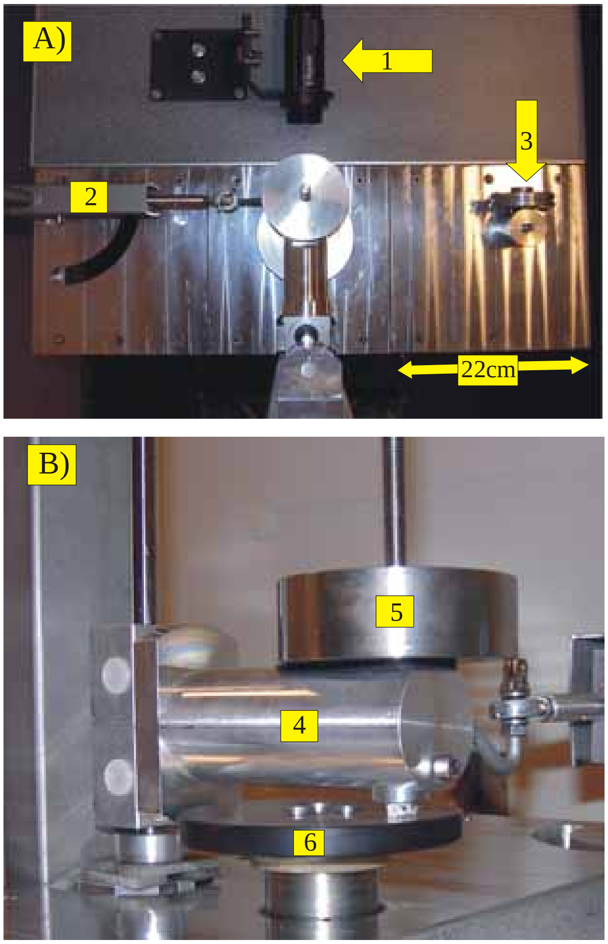

Figure 1. A) Top-view of the mechanical parts: 1. Infrared temperature sensor, 2. Force transducer and 3. Pulley for calibration of the force transducer. B) Side-view of a composite pin loaded against the rotating steel disk: 4. Lever-arm, 5. Weight and 6. Steel disk.

Theory

Wear can be defined as removal of material from interacting surfaces in relative motion. It has frequently been found experimentally that the volume, or mass, of lost material is proportional to W and the sliding distance (l) respectively. That this should be the case can also be shown theoretically, for instance, from simple models for abrasive and adhesive wear, respectively, or by assuming that the wear rate is proportional to the rate of energy dissipation in the interface. The specific rate of energy dissipation (Q_d) is given by equation 1, and is simply the rate of energy dissipation per unit apparent contact area.

$$Q_d = \mu \cdot pv \qquad (1)$$

Based on the relations mentioned above, a depth wear rate (w_t) can be derived, cf. equation 2.

$$w_t = \frac{\Delta h}{t} = k^* \cdot pv \tag{2}$$

Where Δh is height reduction of the worn component, t is time and k^* is the wear factor. Note, that w_t is directly proportional to the pv factor as long as k^* is a constant. The latter depends on both material properties and system properties. Thus, if the system properties are fixed, k^* can to some extent be regarded as a material property. The wear factor is often also refereed to as the specific wear rate (w_s), which conveniently can be calculated from measured quantities, cf. equation 3.

$$w_s = \frac{\Delta m}{l\rho W} \tag{3}$$

Where Δm is weight loss and ρ is density of the worn material. Equation 3 does not take temperature increases in the interfacial zone into consideration. However, in agreement with equation 1, the temperature in the interfacial zone will rise with increasing *pv* factors and does furthermore depend on the thermal conductivities of the sliding partners, the ambient temperature and on the real area of contact. Generally, equation 2 applies inside a certain range of moderate *pv* factors. However, if either *v* and/or *p* exceed a certain level, a change in wear mechanism might occur due to e.g. thermal softening, decomposition or yielding of the material. The *pv* factors where equation 2 breaks down and excessive wear can be observed is refereed to as the limiting *pv* factor (pv_{lim}) which can be regarded as a performance criterion for a given PMC. Thus, for performance improvement it is sought to decrease $k*$ and increase pv_{lim}.

Results and discussion

Figure 2 shows measured values of μ for the two composite materials. The average level of μ for CA/EP is 0.41 as opposed to 0.63 for G/EP, which means that a general decrease of approximately 35% is obtained by substituting the glass fiber weave with the given carbon/aramid weave.

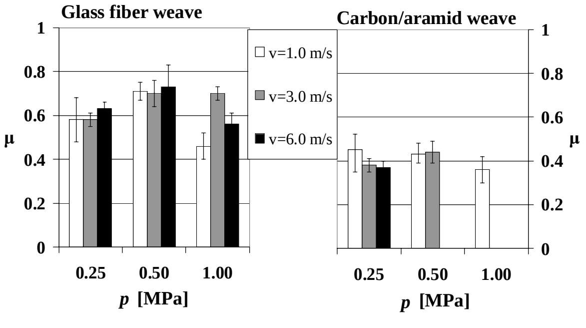

Figure 2. μ measured at different combinations of p and v for G/EP and CA/EP, respectively.

This difference in the level of μ might be attributed to the following factors. Due to the hardness of glass fibers these are observed to cause a significant roughening of the steel counterface. Furthermore, fragments of glass fibers located in the interfacial zone can act as abrasive particles. Both of these factors might increase the deformation, or plowing, contribution to μ. Carbon fibers, on the other hand, migth act as a solid lubricant decreasing the interfacial shear force due to the partial graphite structure of these fibers. With respect to abrasivness, carbon fibers are also found to roughen steel counterfaces under some circumstances but typically not to the same extent as glass fibers. According to Amontons laws of friction, μ should be independent of p and v. However, in the case of polymeric materials this have often been found not to be the case [17]. The data in figure 2 show some variation in μ at different combinations of p and v, however, no clear trends are observed. Thus, it might be concluded that despite of a few exceptions, μ is fairly constant considering the relatively large range of p, v and contact temperatures, cf. figure 3 and 4.

In figure 3 and 4 measured wear rates and contact temperatures for G/EP and CA/EP, respectively, are given. By comparing w_t at the same *pv* conditions for the two materials, it is found that the average wear rate is a factor of 12 higher in the case of G/EP compared to CA/EP. According to SEM images (not shown) this significant difference seems to be caused by the following main factors. The aramid fibers seem to inhibit micro-cracking of the resin, which in the case of glass and carbon fibers leads to exposed fiber ends. These exposed, and brittle, fiber ends seem to be fragmented and broken easily relative to the tough aramid fibers, which are worn by a fibrillation mechanism. Furthermore, third body abrasive wear caused by fragmented glass fibers probably also contributes to the high wear rate found for G/EP.

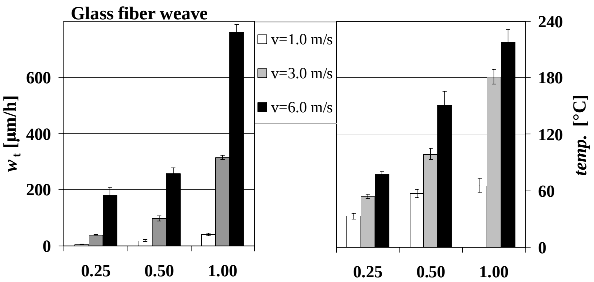

Figure 3. w_t and contact temperatures measured at different combinations of p and v for G/EP.

Furthermore, a gradual increase in both contact temperature and w_t are observed as a function of p and v, respectively, as expected from equation 1 and 2. More specifically, equation 2 predicts a linear relationship between w_t and the *pv* factor with a slope equal to w_s (or the wear factor). Actually, w_t increases more rapidly as a function of p and v than predicted by the linear model.

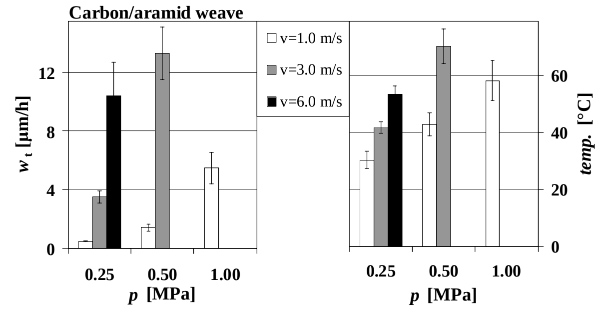

Figure 4. w_t and contact temperatures measured at different combinations of p and v for CA/EP.

As previously mentioned, the wear factor is a function of both material properties and system properties and these are both treated as constants. However, considering that the contact temperature varies from 33°C at the lowest *pv* factor to 218°C at the highest *pv* factor, it is obvious that the material properties will change in this relatively large temperature range. Certainly, the resin properties will change at the glass transition temperature and at the decomposition temperature. Thus, this excessive increase in w_t as a function of *pv* might be related to a gradual deterioration of the resin properties, and thereby also in the composite properties, with increasing contact temperatures.

Conclusion

An average decrease in μ of approximately 35% is found by substituting a glass fiber weave with a carbon/aramid hybrid weave. This decrease is considered to be due to the lubricating effect of carbon fibers as opposed to the abrasive nature of glass fibers. Besides from a few exceptions, μ are found to be roughly independent of *p* and *v*. The average level of wear rates for G/EP is a factor of 12 higher than for CA/EP. This significant difference is believed to be caused by the negative effect of the brittle and abrasive glass fibers compared to, partly the toughness of aramid fibers, inhibiting micro-scale cracking, and partly the lubricating effect of carbon fibers.

References

1. Serope Kalpakjian and Steven R. Schmid, Manufacturing Engineering and Technology, Prentice Hall, 2001.
2. Friedrich, K. & Reinicke, P, Mechanics of Composite Materials 34, 1998.
3. Harsha, A. P. & Tewai, U. S., Polymer Testing 21, p. 697–709, 2001
4. Schwarts, C. & Bahadur, S., Wear 251, 1532–1540, 2001.
5. Unal, H. & Mimaroglu, A. , Materials and Design 24, p. 182–187, 2003.
6. Häger, A. M. & Friedrich, K. , Wear 162, 1993.
7. Zhang, Z., Breidt, C., Chang, L. & Friedrich, K., Tribology International 37, p. 271–277,2004.
8. Li, F., Hu, K. a., Li, J. l. & Zhao, B. y., Wear 249, p. 877–882, 2002.
9. Sawyer, G. W., Freudenberg, K. D., Bhimaraj, P. & Schadler, L. S., Wear 254, 2003.
10. Shi, G., Zhang, M. Q., Rong, M. Z., Wetzel, B. & Friedrich, K., Wear 254, 2003.
11. Christian J. Schwarts and Shyam Bahadur, Wear 237, p. 261-273, 2000.
12. Jin Lu, Ming Qui Zhang, Min Zhi Rong, Shu Li Yu, Bernd Wetzel and Klaus Friedrich, Journal of Materials Science 39, p. 3817-3820, 2004.
13. Ming Qui Zhang, Ming Zhi Rong, Shu Li Yu, Bernd Wetzel and Klaus Friedrich, Wear 253, p. 1086-1093, 2002.
14. Min Zhi Rong, Ming Qiu Zhang, Liu Hong, Hanmin Zeng, Bernd Wetzel and Klaus Friedrich, Industrial Lubrication and Tribology 53, p. 72-77, 2001.
15. Bernd Wetzel, Frank Haupert, Klaus Friedrich, Ming Qiu Zhang, and Min Zhi Rong, Polymer Engineering and Science 42, 1988.
16. Klaus Friedrich, in: Klaus Friedrich (Eds.), Friction and Wear of Polymer Composites - Composite Materials Series volume 1, Elsevier, New York, 1986, p. 233-285.
17. I. M. Hutchings. Tribology: Friction and Wear of Engineering Materials, Edward Arnold, 1992.

Brian Lohse

Address: Risø National Laboratory
The Danish Polymer Centre, Risø
Building 111, POL 124
DK-4000 Roskilde
Phone: +45 4677 4743
Fax: +45 4677 4791
e-mail: brian.lohse@risoe.dk
www: http://www.brianlohse.dk

Supervisors: Søren Hvilsted
Rolf H. Berg
P.S. Ramanujam

Ph.D. Study
Started: September 2004
To be completed: October 2006

High Capacity Optical Data Storage in Polymers

Abstract
Photodimerization in pyrimidine-substituted di- and oligopeptides, was investigated with a view to their application as new materials for optical data storage. The effects of variations in the amino acid sequence, the spacer and substituent effects on the chromophores were investigated. Three of the synthesized compounds were identified as possible media for optical data storage.

Introduction

DNA is the ultimate data storage molecule, storing in four bases the information to make proteins and, essentially, life. The photodimerization of thymine, discovered long ago upon UV irradiation, is one of the most important reactions in photobiology. It is highly probable that dimerization in irradiated DNA constitutes one of the essential factors responsible for the sensitivity of nucleic acids and cells to the effects of UV-light. The dimerization takes place through the C5-C6 double bond of the pyrimidine and involves the formation of a cyclobutane ring, as shown in figure 1. Here we describe chromophores attached to a peptide backbone, where the storage of data can be achieved through the principle of photodimerization of neighboring chromophores undergoing (2π + 2π) cycloaddition, first in solution (H_2O), and then as a film applied onto a quartz plate, if good dimerization efficiency was observed.

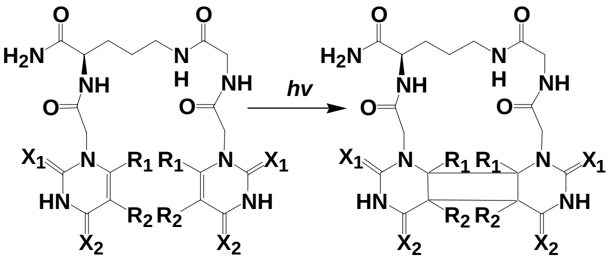

Figure 1: Photodimerization of neighbouring pyrimidine chromophores attached to an ornithine-glycine-based backbone X = O or S, $R_1/R_2 = CH_3$, F, Cl, Br, H.

Specific objectives

To develop a film of pyrimidine-substituted peptides, possessing five important criteria for digital optical storage:

1. Large contrast between irradiated and non irradiated areas of the medium (dimerization efficiency).
2. Fast response for recording
3. Stable during storage (-30^{o}C and 50^{o}C)
4. Good optical and mechanical properties
5. Cheap large scale production.

Results and discussion

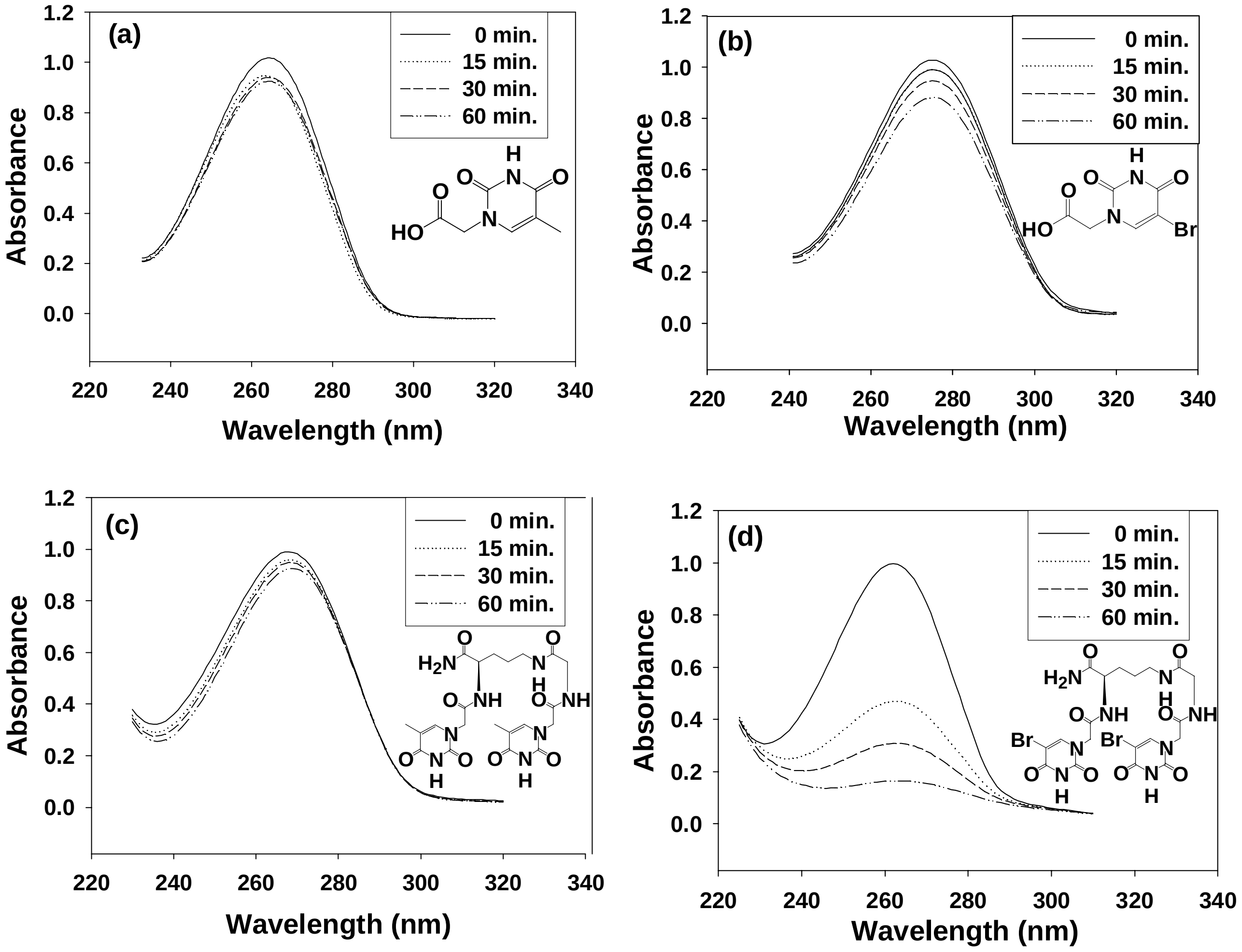

Figure 2: Absorption spectra of (a) thymine 1-acetic acid and (b) 5-bromouracil 1-acetic acid compared with the corresponding pyrimidine-substituted dipeptides (c) N^{α}, $N^{\alpha'}$-bis-(thymine-1-ylacetyl)-(N^{ε}-glycylornithine amide) and (d) N^{α}, $N^{\alpha'}$-bis-(bromouracil-1-ylacetyl)-(N^{ε}-glycyl-ornithine-amide), all in water, at different irradiation times.

The peptides were synthesized using the stepwise Merrifield SPPS method. The chromophores were synthesized using standard organic chemistry. The compounds were first tested in solution, and irradiated under a UV-lamp for 15, 30 and 60 min. see figure 2 and 3. If good dimerization efficiency was observed, the compound was prepared as a film and tested in our UV-laser setup (as shown in figure 4), in order to test how fast the compound could reach maximum transmission (figure 3c).

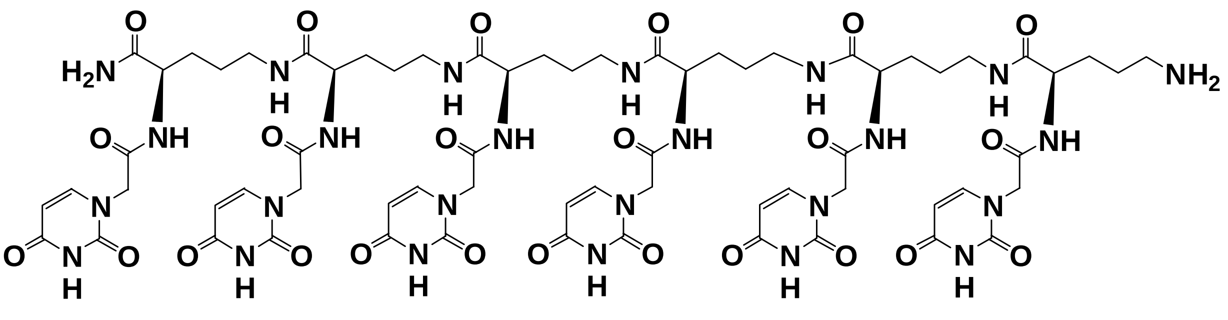

The chemical structure of the uracil ornithine hexamer

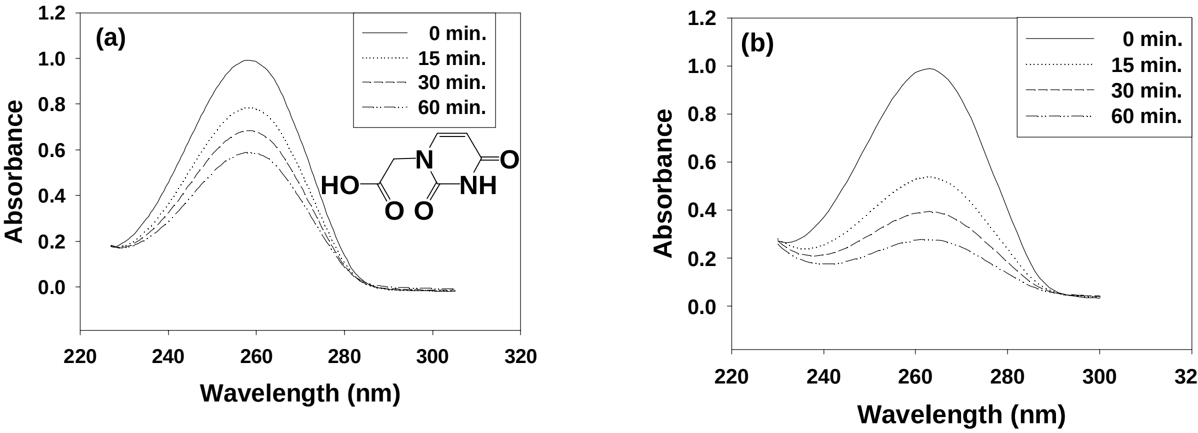

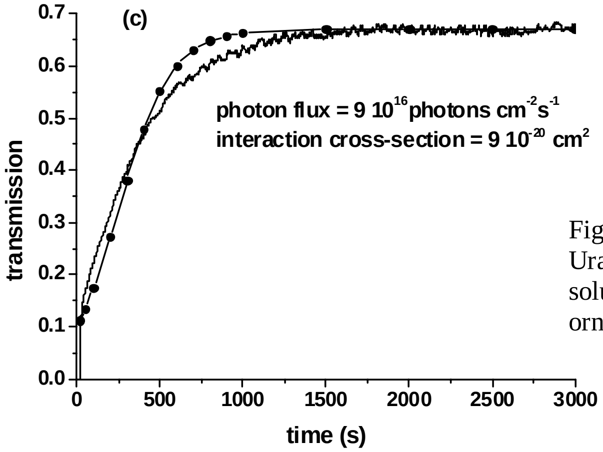

Figure 3: Experimentally measured absorption of (a) Uracil 1-acetic acid and (b) uracil ornithine hexamer in solution. Transmission through a thin film of uracil ornithine hexamer (c).

Figure 4a: The UV-laser setup, during an experiment on a uracil ornithine hexamer.

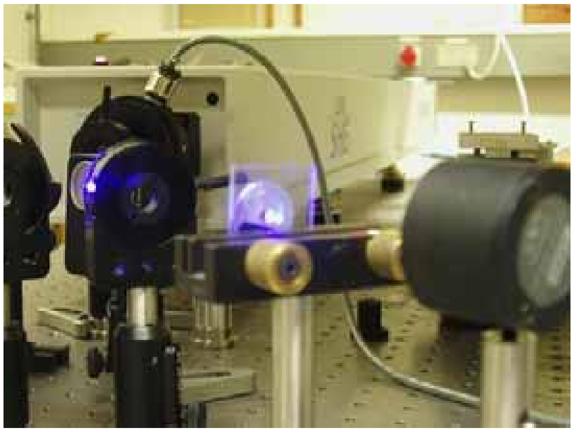

Figure 4b: The peptide film coated onto a quartz plate, and mounted in the holder. Here the UV-laser light hits the film.

Cunclusion

Overall we observed a significant increase in dimerization efficiency when going from a free chromophore in solution to a chromophore attached to a peptide. Furthermore the peptide films had good optical and mechanical properties, and were completely stable. Good correlation was found between solution and film, making solution testing an effective screening method. Finally, the peptides are environmentally safe and suitable for upgrade to large scale.

Perspectives

This new material for optical data storage using UV-laser, instead of red and Blu-ray, is a step towards the next generation. Bit storage at 257 nm can give a storage capacity of over 60 Gbytes compared to the latest Blu-Ray discs, and a further three fold increase in capacity can be achieved with multilevel storage. It is believed that a UV-diode laser will be on the market in ten years, and hopefully we will have been able to obtain a fully optimized material using peptides, which may store up to 1 terabyte on a conventional disc (12 cm).

A possible future technology, the Peptide Versatile Disc (PVD), as a conventional sized DVD.

Acknowledgements

We thank the Danish Technical Research Council (STVF) for financial support.

References

B. Lohse, P. S. Ramanujam, S. Hvilsted, R.H. Berg
J.Pep. Sci. 11 (2005) 499-505.
B. Lohse, P. S. Ramanujam, S. Hvilsted, R.H. Berg
J.Pep. Sci. xx (2006) (submitted).
B. Lohse, P. S. Ramanujam, S. Hvilsted, R.H. Berg
Jpn. J. Appl. Phys. 45 (1B) (2006) (in print).
P.S.Ramanujam, R.H. Berg
Appl.Phys.Lett. 85 (2004) 1665-1667.

List of Publications

Journals:

B. Lohse, P. S. Ramanujam, S. Hvilsted, R.H. Berg
J.Pep. Sci. 11 (2005) 499-505.
B. Lohse, P. S. Ramanujam, S. Hvilsted, R.H. Berg
J.Pep. Sci. xx (2006) (submitted).
B. Lohse, P. S. Ramanujam, S. Hvilsted, R.H. Berg
Jpn. J. Appl. Phys. 45 (1B) (2006) (in print).
B. Lohse, P. S. Ramanujam, S. Hvilsted, R.H. Berg
JACS xx (2006) (submitted).
B. Lohse, R. Vestberg, C. Hawker
Macromolecules xx (2006) (in prep.)

Conference Proceedings:

B. Lohse, P.S. Ramanujam, S. Hvilsted and R.H. Berg
in: Sylvie Blondelle, (Ed.)Proc. 19th APS.
Understanding peptides, Springer-Verlag, New York, 2005. Biopolymers 80 (4) (2005) p. 576.
B. Lohse, P.S. Ramanujam, S. Hvilsted and R.H. Berg
in: Sylvie Blondelle, (Ed.)Proc. 19th APS.
Understanding peptides, Springer-Verlag, New York, 2005.Biopolymers 80 (4) (2005) p. 504.
P.S. Ramanujam, B. Lohse and R.H. Berg in:
Proc. SPIE. 2005; (in print).
P.S. Ramanujam, B. Lohse and R.H. Berg in:
Proc. SPIE. Organic Photonic Materials and Devices VI; James G. Grote, Toshikuni Kaino (Eds.), 5351, 2004, p. 144.

Fellowships

Otto Mønsted Foundation fellowship (2005)
Augustinus Foundation fellowship (2005)
Department of Life Sciences and Chemistry fellowship (1999), by Roskilde University

Award

Third Place Winner in the Young Investigators' Poster Competition. Awarded by the American Peptide Society on the 19th American Peptide Symposium, June 2005, San Diego, California

Piotr Tomasz Mitkowski
Address: CAPEC, Dept. of Chemical Engineering,
Building 227, Office 213
Phone: +45 4525 2910
Fax: +45 4588 2906
e-mail: ptm@kt.dtu.dk
www: http://www.capec.kt.dtu

Supervisors: Rafiqul Gani
Gunnar Jonsson

Ph.D. Study
Started: February 2005
To be completed: February 2008

Generic Hybrid Models of Solvent-Based Reactive Systems Combined with Membrane Separation System

Abstract

Multi-step reactions are commonly found in pharmaceutical and biochemical processes where reactions progress in organic solvents or in aqueous-organic solutions. Usually desired products have to be separated from residual reactants and/or undesired products. Moreover, products may be heat-sensitive which renders the conventional thermal separation processes infeasible. In order to make the process economically feasible, one alternative is to increase the product yield by combining the reactor with a membrane separation unit or with better solvents, or both. Through model-based computer-aided techniques, it is possible to select better solvents and identify membrane-based separation operations which when combined with the reactor would increase process productivity. A systematic modelling framework for investigation of hybrid reactors-separator operations is presented and its application is highlighted through a case study.

Introduction

In pharmaceutical, fine chemicals and biochemical manufacturing, reactions are often carried out in batch or semi batch reactors followed by multiple separations and cleaning steps. Irrespective of whether these reactions are equilibrium or kinetically controlled, on-site removal of products usually enhance the yield and lead to reduced reaction times. Sometimes, the removal of products also reduces the undesired side reactions. In the cases where solvents are used, it can either be recycled or substituted with another more appropriate solvent. For all these reasons, it is beneficial to couple the reactor with a separation unit.

The products of the above mentioned reactions are usually heat sensitive, so in order to avoid thermal degradation the separation technique should operate at temperatures lower than the degradation temperature of the compounds. One option could be membrane-based separation processes where the separation proceeds because of the selectivity imparted by the membrane, based on either the difference in size or the chemical potential of the molecules. This could be a good choice in the cases [1] where the reactor effluent contains desired products having molecular weights (M_w) in the range of 300-1000, smaller by-products (M_w between 50-150) and much larger enzymes/catalyst. Also, membrane separation techniques enjoy advantages such as low operational costs, high selectivity, modular design and lower environmental impact.

Membrane separation techniques like pervaporation and nanofiltration have been extensively studied [1-3]. Pervaporation has been used in the production of MIBK (methylisobutylketone) [4] and MTBE (methyl tert-butyl ether) [5]. Nanofiltration is emerging as an option in separation of molecules with M_w ranging from 500 – 2000 from dilute solutions. Now the membranes which are resistant to degradation by organic solvents are also commercially available. These membranes are a fairly reasonable option when the separation is based on size.

Coupling of reactor and separation unit is called hybrid process since the two processes influence the performance of each other and the optimisation of the design must take into account this interdependency. Lipnizki et al. [6] highlighted two types (R1 and R2) of hybrid processes consisting of reactor and membrane-based separation based on the type of molecule to be separated. These hybrid processes are presented in Fig. 1a - b where the separation unit is physically set apart. However, it is also possible to integrate the membrane separation process with the reactor unit which is usually referred as the membrane reactor (see Fig. 1c). In type R1, the separation process removes the product from recycle loop around the reactor. Type R2 is an example of integration where by-product is removed from hybrid system.

The objective of this work is to present a model-based methodology for design/analyse of hybrid process systems.

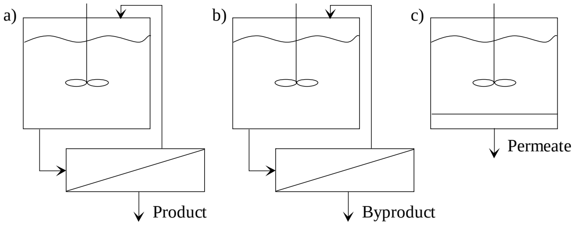

Fig. 1: Hybrid process layouts, a) type R1, b) type R2, c) internal membrane unit

Model-based design methodology of hybrid systems

Design of hybrid process systems consisting of reactor and membrane-based separation units are usually carried out through trial-and-error approaches involving experiments. Even through they are acceptable in terms of reliability, they are time consuming and expensive while the solution is ad-hoc by nature. Based on a model-based framework for systematic analysis, it is possible to design hybrid process systems to find improved process design alternatives in terms of process output parameters such as reaction yield, selectivity, processing time and environmentally friendly solvents.

A model-based framework for systematic investigation of hybrid process systems is presented in Fig. 2, where the workflow for each step is indicated by the grey-boxes, while the needed models and data are indicated through the white-boxes. Based on the knowledge of reactant properties like size of molecules, temperature of degradation, partial pressure etc, and reaction kinetics, conditions of reaction are defined (step 1). The process output depends on process parameters such as product purity, reaction yield and process time. The objective of step 2 is to specify these process parameters in order to determine the values of process variables such as temperature, permeability, membrane area etc. which will give the desired process output. In the next step (step 3), influence of solvent on reaction as well as on the process design is considered. A short list of chemicals which could be the potential solvents is generated based on the method of solvent selection given by Gani et. al. [7] and their performance evaluated in the hybrid process. This method includes use of computer-aided molecular design tool ICAS-ProCAMD [7]. The properties of solvent which play the biggest role in specific reaction are reactivity of solvent, miscibility with products, polarity, melting and boiling point, vapour pressure, selectivity and EHS (environmental, health and safety) properties. Influence of solvent on membrane-based separation method also needs to be considered due to membrane stability and fluxes. Step 4 combines all collected knowledge with membrane separation models to identify the feasible membrane-based separation techniques. The membrane parameters like diffusivity, solubility etc. used in membrane model should represent the available membranes. In the last step, hybrid process configuration has to be chosen and operational limits defined in terms of process yield, reaction time and membrane area. If these constraints are satisfied, a feasible design is obtained; otherwise, decisions from earlier steps will need to be reviewed. This methodology consists of an efficient and systematic generate and test approach, which is able to save time and resources by avoiding duplication of work and efficient decomposition of the problem into integrated sub-problems (as highlighted in Fig. 2).

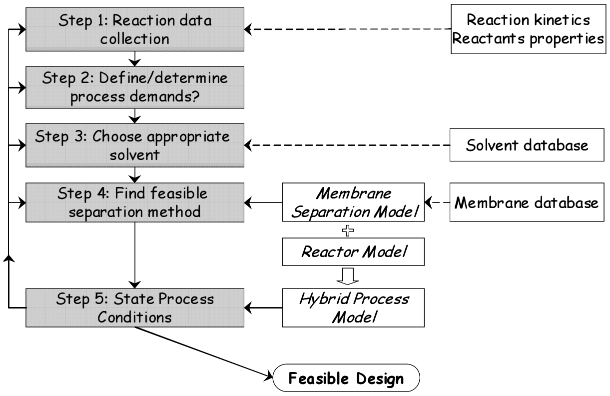

Fig. 2: Methodology of design/analyze hybrid process system

Generic model for the hybrid reactor-membrane process

The model-based framework needs a generic hybrid process model from which problem specific models can be generated. This generic hybrid process model contains process and property sub-models for both reactor and separation units. These equations are derived from mass, energy and momentum balances, which form a DAE system of equations. The differential equations could be the states of the system at discrete time points and algebraic equations are the constitutive and control equations. The generic form of different types of model equations used in the hybrid process model is given as:

$$\begin{aligned}\left[Accumulation\right] = \left[Flow\,in\right] - \left[Flow\,out\right] \pm \\ \pm\left[Reaction\right] + \left[Recycle\right]\end{aligned} \tag{1}$$

$$Recycle \equiv 0 = g_M\left(J_i, A_m\right) \tag{2}$$

$$Reaction \equiv 0 = g_r\left(K_i, K_{eq}, T_R, V, r, t\right) \tag{3}$$

$$Flow\ \ in \equiv 0 = g_{F,in}\left(\upsilon_{in}, C_{i,in}, T_{in}\right) \tag{4}$$

$$Flow\ \ out \equiv 0 = g_{F,out}\left(\upsilon_{out}, C_{i,out}, T_{out}\right) \tag{5}$$

Where A_m – membrane area, C_i – concentration, J_i –flux through the membrane, K_{eq}, – equilibrium constant, K_i – Michaelis-Menten constant, r – reaction rate, t –

reaction time, T – temperature, V – reactor volume, υ – volumetric flow, subscripts: i – components, *in* – inlet, *out* – outlet, R – reactor, r – reaction.

In addition to the above, constitutive models such as properties models, equilibrium relations, etc. are needed for the constitutive variables. Using this generic model and the specific details of any problem, the specific hybrid reactor-membrane process can be generated and tested.

Case study: Enzymatic esterification

Application of the model-based framework is illustrated through an enzymatic esterification reaction. Data used in this study is published by Egger et al. [8] and other data is being generated through in-house experiments.

Step 1: Reaction data collection

Enzymatic esterification reaction can be represented schematically as:

$$A+B+E \rightleftharpoons ABE \rightleftharpoons C+W+E$$

Where: A – lysophosphatidylcholine, B – oleic acid, C – phosphatydylcholine, E – enzyme phospholipaze-A$_2$, W – water.

Although, this kind of reaction has been studied at temperatures equal to or higher than 50°C, all data used in this work has been obtained in ambient conditions. Egger et. al. [8] reported equilibrium yields in various water activity conditions and substrate concentrations, which has been correlated and verified here to generate the kinetic model. All reactants except water are heat sensitive. Molecules A and C have M_w between 500 – 700 while M_w of B is 282.

Step 2: Process demands

Reaction, which is kinetically controlled, has a low product yield. The objective is to increase the process productivity by removing the water. Moreover, reaction requires an inert organic solvent.

Step 3: Solvent selection

Based on information obtained from literature [8] toluene was chosen as the solvent. Other likely solvents generated with ICAS-ProCAMD include ethylacetate, isopropylacetate, hexane and many more (note that only toluene has been considered in this study).

Step 4: Separation method selection

Pervaporation (PV) is chosen as the membrane-based separation technique because of possibility of introducing hydrophilic membranes that would allow only water to permeate.

Step 5: Process conditions and feasible design

The proposed hybrid process system is of type R2 (Fig.1b). This set-up is investigated under assumptions that: reactor is well mixed, reaction occurs only in the reactor volume, in the liquid phase, reaction medium density is constant, water flux in PV is constant and fluxes for all other components present in the system are neglected.

From the generic hybrid model (Eq. 1), the problem specific hybrid process model is generated (Eq. 6).

$$\frac{dC_i}{dt} = -\frac{C_i}{V}dV - \frac{1}{V}J_i \rho_{m.i} A_m - r \cdot \rho_e \qquad i = A,B,C,W \tag{6}$$

Where $\rho_{m,i}$ is molar density of component i and ρ_e enzyme density.

Note that in the above, only mass conservation is used because no heat effect was reported. The accumulation in the membrane process is neglected because change of state variables along the length and time (steady state) are assumed constant.

Reaction kinetics is described by reversible Michaelis-Menten kinetics:

$$r = r_{max}\frac{\dfrac{C_A C_B}{K_{mA}K_{mB}}\left(1-\dfrac{C_C C_W}{C_A C_B}\dfrac{1}{K_{eq}}\right)}{\left(1+\dfrac{C_A}{K_{mA}}+\dfrac{C_C}{K_{mC}}\right)\left(1+\dfrac{C_B}{K_{mB}}+\dfrac{C_W}{K_{mW}}\right)} \tag{7}$$

All other constitutive variables are assumed constant. Process yield is defined as ratio of moles of desired product (phosphatydicholine) to initial of limiting reactant (lysophospchatydycholine), (*Yield* = N_C/N_{A0}). The hybrid model is solved in the ICAS-MoT [9] modelling environment, which is a computer aided modelling tool with option of model translation, analysis and solution. With the generated problem specific hybrid process model, three scenarios have been investigated in terms of process yield and superiority of the hybrid process over batch reaction. Performance of the hybrid system is strongly dependent on the membrane area (A_m) and component fluxes (J_i). For reactor coupled with pervaporation unit (RCPV), two cases with different values of factor $J_W\, A_m$ (J_W – water flux) have been studied. Process yield is improved from 8% to 16.5% by removing water from the system using a reasonable design for a PV-unit. Values for the different design variables for the three scenarios are given in Table 1 while the yield-time behaviour is shown in Fig. 3.

Table 1: Process parameters and process yields

	Batch	RCPV 1	RCPV 2
V_0 [dm^3]	1	1	1
$J_W \cdot A_m$ [mmol/h]	-	0.005	0.01
C_{A0} [mmol/dm^3]	10	10	10
C_{E0} [mmol/dm^3]	400	400	400
C_{W0} [mmol/dm^3]	39,5	39,5	39,5
K_A=K_B=K_C=K_W [mmol/dm^3]	4,9	4,9	4,9
r_{max}[mmol·mg^{-1}·h^{-1}]	1,04E-04	1,04E-04	1,04E-04
t [h]	40	40	40
Yield [%]	7,8	11,2	16,5

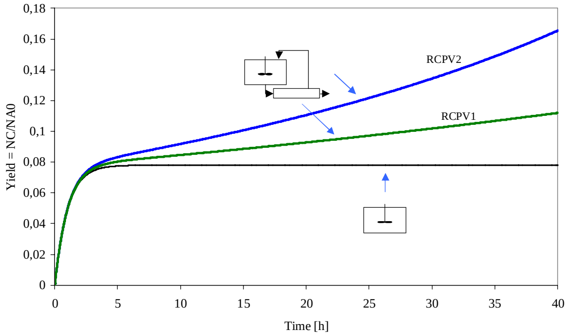

Fig. 3: Comparison of hybrid process systems with batch in terms of process yield

A membrane which should be able to match the design values of water flux is a cross-linked polyvinyl alcohol membrane. Set-up RCPV2 is recommended for further experimental studies together with experimental verification of membrane performance.

Conclusions

A model-based framework for systematic investigation of hybrid systems consisting of well mixed reactors and membrane separation units has been presented along with the application to a relevant case study. The work-flow and the corresponding data-flow for the methods and tools needed by the model-based framework have been developed. Problem specific hybrid process models are generated and used for specific reaction systems under investigation. From this work, it is clear that hybrid processes could show their advantages where difficulties exist to incorporate other separation methods. Reactor combined with membrane separation unit gives significant increase in process yield by overcoming limitations of kinetically controlled reactions and also by reducing the process time. Experimental trials needed to verify the hybrid process is reserved for the final step, thereby saving time and resources.

Acknowledgment

Funding for Piotr T. Mitkowski through the PRISM project under the Marie Curie Research Training Network, European Community's Sixth Framework Program, is gratefully acknowledged.

References

[1] J.A. Whu, B.C. Baltzis, K.K. Sirkar, Modelling of nanofiltration – assisted organic synthesis, Journal of Membrane Science, 163, (1999), 319-331

[2] F. C. Ferreira, S.Han, A.Boam, S.Zhang, A.G.Livingstone, Membrane aromatic recovery system (MARS): lab bench to industrail pilot scale, Desalination, 148, (2002), 267-273

[3] J.T.Scarpello, D.Nair, L.M. Freitas dos Santos, L.S.White, A.G. Livingstone, The seperation of homogeneous organometalic catalysts using solvent resistant nanofiltration, Journal of Membrane Science, 203, (2002), 71-85

[4] C. Staudt-Bickel, R.N.Lichtenthaler, Integration of pervaporation of the removal of water in production process of methylisobutylketone, Journal of Membrane Science, 111, (1996), 135-141

[5] M. Matouq, T. Tagawa, S. Gotp, Combined process for production of methyl tert-butyl ether from tert-butyl alcohol and methanol, Jurnal of Chemical Engineering of Japan, 27, (1994), 302-306

[6] F. Lipnizki, R.W. Field, P-K. Ten, Pervaporation-based hybrid process: a review of process design, applications and economics, Journal of Membrane Science, 155, (1999), 183-210

[7] R. Gani, C. Jim'ene-Gonz'alez, D.J.C. Constable, Method for selection of solvents for promotion of organic reactions, Computers and Chemical Engineering, 29, (2005), 1661-1676

[8] D. Egger, E. Wehtje, P. Adlercreutz, Characterization and optimisation of phospholipase A2 catalyzed synthesis of phosphatidylcholine, Biochimica et Biophysica Acta, 1343, (1997), 76-84

[9] M.Sales-Cruz, R. Gani, 2003, Computer-Aided Chemical Engineering, vol. 16: Dynamic Model Development, Eds. S.P. Asprey and S. Macchietto, Elsevier, Amsterdam

Matias Monsalvo

Address:	DTU-Building 229-2800 Lyngby
Phone:	+45 4525 2863
Fax:	+45 4588 2258
e-mail:	mmo@kt.dtu.dk
www:	http://www.kt.dtu.dk
Supervisors:	Alexander Shapiro Kaj Thomsen
Ph.D. Study	
Started:	November 2002
To be completed:	December 2005

Phase Behavior and Viscosity Modeling of Refrigerant-Lubricant Mixtures

Abstract
The understanding of thermophysical properties and phase behavior of refrigerant-lubricant oil mixtures is highly important for optimal design of refrigeration and air-conditioning systems. Refrigerant-lubricant mixtures, which are likely to have strong asymmetry, may develop complex type of phase behavior that must be considered when designing a cooling circuit. Such behavior may include, open miscibility gaps, closed miscibility gaps, liquid-liquid-vapor equilibrium and even barotropic phenomena showing mass density inversions. This will also have a profound effect in the mixtures transport properties. For that reason, the study (measurements and modeling) of phase behavior and thermophysical properties of such mixtures is essential. Thus, the main research objective of this project is the accurate numerical modeling of the phase, P-V-T and P-η-T behavior of refrigerant-lubricant mixtures under wide ranges of temperature and pressure using deferent models published in the literature.

Introduction

The ability to model the phase behavior and thermophysical properties of refrigerant-lubricant mixtures is of considerable industrial and academic interest. From an industrial point of view, the study (measurements and modeling) of the thermophysical properties of such mixtures is necessary for the successful transition into new environmentally alternative refrigerants. Information on solubility, density, and viscosity for this type of systems is extremely important for optimal design of refrigeration machines. Moreover, depending on the oil miscibility within the refrigerant-rich phase, even with an efficient oil separator installed, part of the lubricant oil may migrate from the compressor to other parts of the system such as the evaporator, condenser, expansion device and piping. Therefore, some related problems might also develop, for example, oil accumulation may take place inside the heat exchanger tubes reducing heat transfer capabilities and resulting in an overall decrement of the refrigeration cycle performance. These problems may become more serious in the presence of unforeseen barotropic behavior that may induce a refrigerant-rich phase denser than the lubricant-rich phase [1] Furthermore, good description of the thermophysical properties and phase equilibria is invaluable in choosing a proper lubricant for a particular compressor [1]. From an academic perspective, the ability to predict phase, P-V-T and P-η-T behavior of asymmetric mixtures (as in the case of refrigerant + lubricant systems) can serve as a rigorous test for the different models.

During the past few years new refrigerants, such as 1,1,1,2-tetrafluoroethane (HFC-134a, CF_3CH_2F), have been proposed as alternative refrigerants to chlorofluorocarbons (CFCs). This development has been based on a detail understanding of the refrigeration application and the chemistry of the refrigerants. However, this transition into new environmentally friendly alternative refrigerants requires the choice of suitable compatible lubricants. Polyalkylene glycol dimethyl ethers, polyol esters, and alkylbenzenes have been proposed as suitable lubricants for hydrofluorocarbons.

In spite of their importance, there are only a few studies available in the literature that present the study of thermophysical properties of refrigerant + lubricant mixtures. Thus, in this work the phase, P-V-T and P-η-T behavior of this kind of mixtures is studied using different models available in the literature.

Objectives

The main objective of this project is the ccurate numerical modeling of the phase, *P*-*V*-*T* and *P*-η-*T* behavior of refrigerant + lubricant mixtures under wide ranges of temperature and pressure. For that purpose two EoS have been evaluated: Peng–Robinson (PR) [2], and the perturbed-chain statistical associating fluid theory (PC-SAFT) [3]. The PR EoS is chosen because of its common use in industry and its simplicity. Even for complex systems, available literature shows that cubic equations are reasonably good. PC-SAFT was chosen because of its molecular basis, its extensive use among researchers, and its growing use by practicing engineers.

For the viscosity modeling of refrigerant + lubricant mixtures, two models recently developed have been used: the friction theory [4, 5] and the free-volume model [6, 7]. These two models have shown to deliver accurate viscosity estimations from very low to high pressures for pure hydrocarbons and their mixtures, among other fluids. In this work the extension of these models to refrigerant + lubricant mixtures is studied.

Results and Discussion

Phase and P-V-T behavior

The type of phase behavior that refrigerant-lubricant mixtures may develop, has been studied based on experimental information found in the literature. In addition to larger immiscibility regions, it has been shown [8] that asymmetric mixtures such as refrigerant-lubricant mixtures may develop density inversions, as observed by Hauk and Weiner [1]. For the understanding and study of the type of phase behavior that can be found in refrigerant + lubricant mixtures, one can take advantage of simple models such as the Peng Robinson EoS. This equation is commonly used in phase equilibria correlations at low and high pressures as well as in the design and simulation of a wide variety of industrial processes. Similarly to all of the van der Waals family EoS, the PR EoS is divided into a repulsive pressure term (p_r) and an attractive pressure term (p_a),

$$p = p_r + p_a \tag{1}$$

where

$$p_r = \frac{R\ T}{(v-b)} \tag{2}$$

and

$$p_a = \frac{a}{v(v+b)+b(v-b)} \tag{3}$$

For mixtures the PR EoS was employed in combination with the one-parameter van der Waals quadratic mixing rule for *a* and linear for *b*, given by:

$$a = \sum_i \sum_j x_i x_j \sqrt{a_i a_j}\,(1-k_{ij}) \tag{4}$$

and

$$b = \sum_i x_i b_i \tag{5}$$

where, k_{ij} is a binary interaction parameter.

An example of the phase diagram prediction for the HFC-134a + triethylene glycol (TRIG) mixture is shown in Figure 1 where it can be observed multiple phase equilibria and the presence of a high-pressure liquid-liquid immiscibility region. In Figure 2 a relevant feature is shown: barotropic phenomena showing density inversion. Both facts, immiscibility regions and barotropic phenomena, are associated with asymmetric mixtures [8].

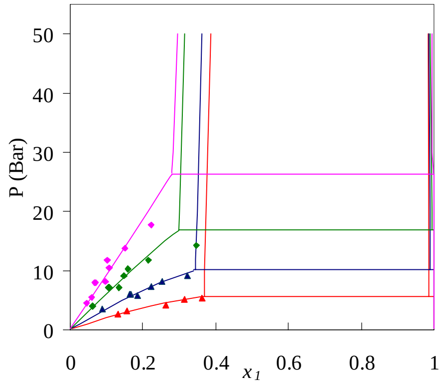

Figure 1. Example of solubility data correlation and VLLE prediction for HFC-134a (1) + TRIG, experimental data [9] at 293.15 K (▲), 313.15 K (▲), 333.15 K (◆), 353.15 K (◆). Solid lines denote the calculated data by the PR EoS. Horizontal lines represent the predicted VLLE region.

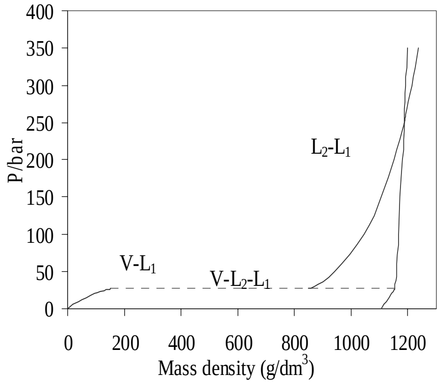

Figure 2. Pressure-density PR phase diagram of HFC-134a + TRIG at 353.15 K.

It is well known that simple cubic EoS can correlate *PTx* data with sufficient accuracy. However, it is also of relevance to mention that cubic EoS are known for not being too accurate in the prediction of the density of dense phases showing, in optimal circumstances, 2-5% overall absolute average deviations. For some applications a 5% density deviation may be considered quite tolerable. However, in other better-defined process this uncertainty may not be acceptable and alternative more accurate approaches are required. In cases when the process operates at subcritical conditions, within moderate pressure ranges, a widely used method for the improvement of the density accuracy given by cubic EoS is the Péneloux volume translation [10]. This approach consists of a simple translation of the frame of reference so that the volume (or density) representation may better be overlapped to the experimental data. Alternatively, other type of highly accurate reference EoS can be used, such as the PC-SAFT [3].

As an example of this, the densities values predicted by the PR and PC-SAFT EoS for a mixture of HFC-134a + triethylene glycol dimethyl ether (TriEGDME) at x_1 = 0.69 are shown in Figure 3 where it can be appreciated that PC-SAFT performs better than PR.

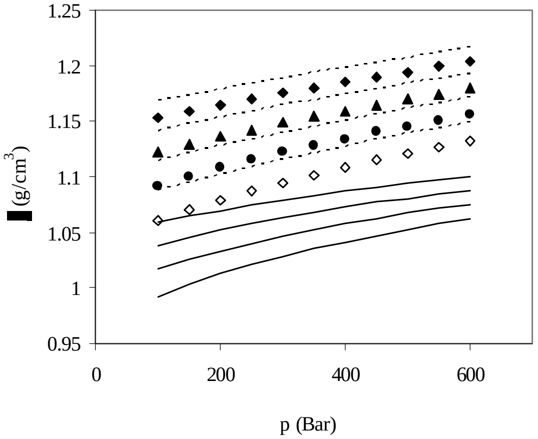

Figure 3. Density for HFC-134a (1) + TriEGDME using the PR (—) and PC-SAFT (---) EoS compared with experimental values [11] at *T* =293.15 K (♦), 313.15 K (▲), 333.15 K (●), 353.15 K (◊).

The performance of both models in predicting the density of these mixtures is further illustrated in Figure 4, where the density in plotted as function of molar fraction for different isochors at *T* = 373.15 K for the system HFC-134a + TEGDME. It is interesting to notice that both models can predict the maximum that it is experimentally found at molar fractions close to one. From this last figure it can also be observed that the PC-SAFT EoS delivers better results than PR EoS.

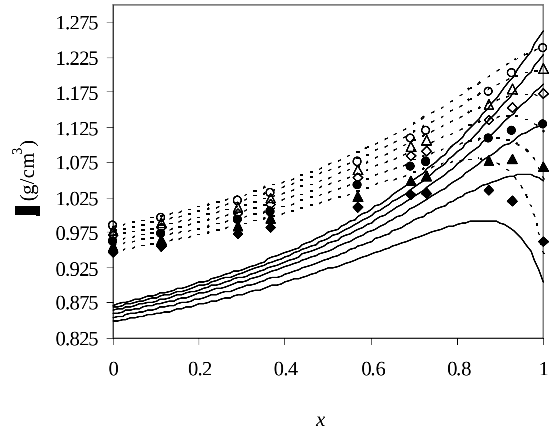

Figure 4. Density for HFC-134a (1) + TEGDME using the PR (—) and PC-SAFT (---) EoS compared with experimental values [12] at p = 100 bar (♦), 200 Bar (▲), 300 Bar (●), 400 Bar (◊), 500 (Δ) Bar, and 600 (○).

Viscosity behavior: free-volume model

Recently an approach in order to model the viscosity of Newtonian fluids (in the condensed phase) with small molecules has been proposed by Allal *et al.* [6]. This approach connects viscosity, η, to molecular structure via a representation of the free volume fraction. In its first version the model could be only applied to dense fluids but a version valid for low density states has also been developed [7]. For pure fluids, this model delivers accurate viscosity estimations from very low to high pressures with only three adjustable parameters for each compound. In this last version the viscosity has the following expression

$$\eta=\eta_0+\Delta\eta \qquad (6)$$

where η_0 represents the dilute gas term, and for many fluids it can be estimated with simple empirical models such as the one proposed by Chung [12]

$$\eta_0=40.785\,\frac{\sqrt{M\,T}}{v_c^{2/3}\,\Omega^*}F_c \qquad (7)$$

the residual term $\Delta\eta$ is calculated with

$$\Delta\eta=\frac{\rho l\left(\alpha\rho+\dfrac{pM}{\rho}\right)}{\left(3RTM\right)^{1/2}}Exp\left[B\left(\frac{\alpha\rho+\dfrac{pM}{\rho}}{RT}\right)^{3/2}\right] \qquad (8)$$

where M is the molar mass, ρ is the density, and *l*, α and *B* are adjustable parameters for each pure fluid. This model can be also applied for mixtures using the following mixing rules:

$$\alpha_{mix} = \sum_{j=1}^{n}\sum_{i=1}^{n} x_i\, x_j\, \alpha_{ij} \qquad (9)$$

$$\alpha_{ij} = \left(\alpha_i\, \alpha_j\right)^{1/2} \qquad (10)$$

$$l_{mix} = \sum_{i=1}^{n} x_i\, l_i \qquad (11)$$

$$\frac{1}{B_{mix}} = \sum_{i=1}^{n} \frac{x_i}{B_i} \qquad (12)$$

The three parameters (l, α and B) have been adjusted for pure refrigerants and pure lubricants their values are published in the literature [14, 15]. Taking into account the reported parameters and the mixing rules of Equations 9-12 the dynamic viscosity of the mixtures can be predicted.

An example of the performance of the free-volume model is shown in Figure 4 for mixture containing HFC-134a + TEGDME [14].

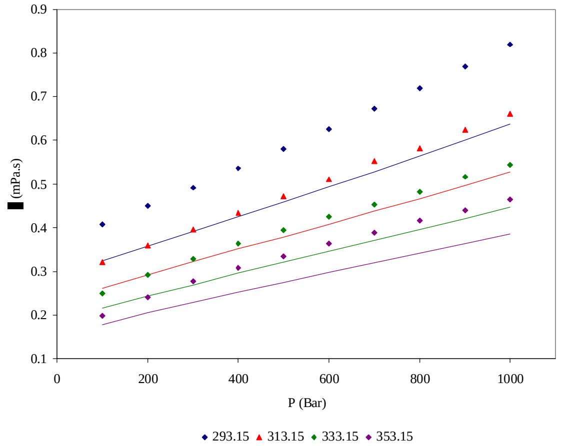

Figure 4. Viscosity for HFC-134a (1) + TEGDME using the free-volume model compared with experimental values [14] for a molar fraction x_1 = 0.92 at 293.15 K (▲), 313.15 K (▲), 333.15 K (◆), 353.15 K (◆).

From this Figure it can be observed that the free volume under estimates the viscosity in the whole range of pressure.

Viscosity behavior: the friction theory

The friction theory (*f-theory*) [4, 5] has also been applied to model the viscosity of refrigerant + lubricant systems. The *f-theory* in combination with simple cubic EoS has shown to deliver accurate viscosity estimation from low to high pressures, regardless of how accurate the density performance may be. This model has been successfully applied to the accurate modelling of several types of fluids including complex systems such as reservoir fluids among others. In the *f-theory* the total viscosity, η, is separated into a dilute gas viscosity term η_0 and a residual friction term η_f,

$$\eta = \eta_0 + \eta_f \qquad (13)$$

The dilute gas term applies at the zero pressure limit of the gas phase, and for many fluids it can be estimated with simple empirical models such as the one proposed by Chung [13]. The residual friction term can be written as follow:

$$\eta_f = \kappa_r\, p_r + \kappa_a\, p_a + \kappa_{rr}\, p_r^{\,2} \qquad (14)$$

where the kappas are temperature dependent friction coefficients given by

$$\kappa_r = \frac{a_0 + a_1\left\{\exp\left(T_r^{-1}-1\right)-1\right\} + a_2\left\{\exp\left(2T_r^{-1}-2\right)-1\right\}}{p_c}$$

$$\kappa_a = \frac{b_0 + b_1\left\{\exp\left(T_r^{-1}-1\right)-1\right\} + b_2\left\{\exp\left(2T_r^{-1}-2\right)-1\right\}}{p_c}$$

$$\kappa_{rr} = \frac{c_2\left\{\exp\left(2T_r^{-1}\right)-1\right\}}{p_c}$$

and p_r and p_a are given by the EoS.

The mixture viscosity has been estimated using the predictive mixing rules proposed in Ref. [4, 5]. That is, the mixture friction coefficients κ_r, κ_a, and κ_{rr} are obtained by the following mixing rules:

$$\kappa_r = \sum_{i=1}^{n} z_i \kappa_{r,i}$$
$$\kappa_a = \sum_{i=1}^{n} z_i \kappa_{a,i} \qquad (16)$$
$$\kappa_{rr} = \sum_{i=1}^{n} z_i \kappa_{rr,i}$$

Here, a mass weighted fraction of the form

$$z_i = \frac{x_i}{MW_i^{0.3}\, MM} \qquad (17)$$

with

$$MM = \sum_{i=1}^{n} \frac{x_i}{MW_i^{0.3}} \qquad (18)$$

is used in order to enhance the accuracy of the results; MW_i is the molecular weight of compound "*i*".

Figure 5 shows the *f-theory* PR model results for the mixture HFC-134a + triethylene glycol dimethyl ether (TriEGDME) for a molar fraction of x_1 = 0.63. It can be observed that the *f-theory* shows a good, consistent and stable performance from low to high pressures.

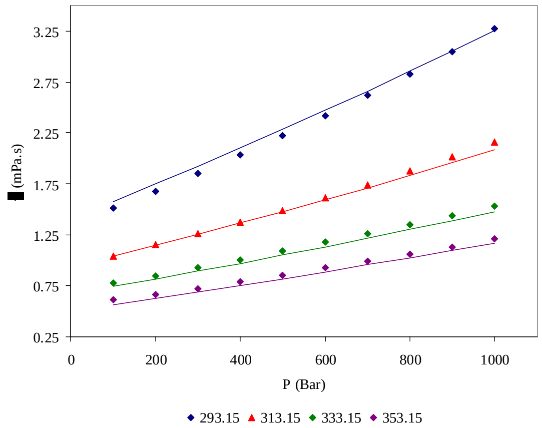

Figure 5. Viscosity for HFC-134a (1) + TriEGDME using the *f-theory* PR model compared with experimental values [15] at 293.15 K (▲), 313.15 K (▲), 333.15 K (◆), 353.15 K (◆).

Conclusions

In spite of their simplicity, it appears that simple cubic EoS such as the PR EoS with classical mixing rules may be appropriate for a description of the phase behavior of complex systems such as refrigerant + lubricant systems. Classical cubic EoS represent a powerful tool for the actual design of refrigeration cycles. This modeling approach can be used to prevent technical problems such as barotropic effects, decrease solubility-related compressor oil viscosity, among others. However, it should be pointed out that the accuracy of the density predictions is still limited by the algebraic structure of the cubic EoS. On the other hand, modern EoS such as PC-SAFT EoS has shown to describe the *p*-*v*-*T* behavior of these systems in a better way.

For the viscosity modeling two models were tested: the friction theory and the free volume model. It has been shown in the literature [14, 15] that these two models predict the viscosity of pure refrigerants and pure lubricants very accurately. However, in the case of mixtures, the friction theory seems to deliver better results than the free-volume model.

Acknowledgments

The present study is supported by the Danish Technical Research Council (Project No. 26-01-0217).

References

1. Hauk and E. Weidner, Thermodynamic and Fluid-Dynamic Properties of Carbon Dioxide with Different Lubricants in Cooling Circuits for Automobile Application, *Industrial and Engineering Chemistry Research*, 39, (2000) 4646.
2. D.-Y. Peng and D.B. Robinson, A New Two-Constant Equation of State, *Ind. Eng. Chem. Fundam.*, 15, (1976) 59-64.
3. Gross, J., Sadowski, G. Perturbed-Chain SAFT: An Equation of State Based on a Perturbation Theory for Chain Molecules. Ind. Eng. Chem. Res. 2001, 40, 1244-1260.
4. S.E. Quiñones-Cisneros, C.K. Zéberg-Mikkelsen and E.H. Stenby, The Friction Theory (*f*-theory) for Viscosity Modelling, *Fluid Phase Equilibr*. 169, (2000) 249-276.
5. Quiñones-Cisneros, S.E., Zéberg-Mikkelsen, C.K., Stenby, E.H. One Parameter Friction Theory Models for Viscosity. *Fluid Phase Equilib*. 2001, 178, 1-16.
6. Allal, A., Boned, C., Daugé, P. A New Free Volume Model for Dynamic Viscosity of Dense Fluids Versus Pressure and Temperature. Extension to a Predictive Model for Not Very Associative Mixtures. *Phys. Chem. Liq*. 2001a, 39, 607–624.
7. Allal, A., Boned, C., Baylaucq, A. Free-volume viscosity model for fluids in the dense and gaseous states. *Phys. R. E.* 2001b, 64, 011203/1 - 10.
8. S.E. Quiñones-Cisneros, Phase and critical behavior in type III phase diagrams, *Fluid Phase Equilib.*, 134, (1997) 103.
9. S. I. Tseregounis, M. J. Riley, AIChE J. 40 (1994) 726-737.
10. Péneloux A, Rauzy E, and Fréze R. A Consistent Correction for Redlich-Kwong-Soave Volumes. Fluid Phase Equilib. 1982; 8: 7-23.
11. M. J. P. Comuñas, J. Fernández, A. Baylaucq, X. Canet, C. Boned, Fluid Phase Equilib. 199 (2002) 185-195.
12. Comuñas, M.J.P., Baylaucq, A., Boned, C., Canet, X., Fernández, J. High-Pressure Volumetric Behavior of x 1,1,1,2-tetrafluoroethane+(1-x) 2,5,8,11,14-Pentaoxapentadecane (TEGDME) Mixtures. J. Chem. Eng. Data 2002c, 47, 233-238.
13. T.-H. Chung, M. Ajlan, L.L. Lee and K.E. Starling. *Ind. Eng. Chem. Res.* 27(1998), 671.
14. M.A. Monsalvo, A. Baylaucq, P. Reghem, S.E. Quiñones-Cisneros, C. Boned, Viscosity measurements and correlations of binary mixtures: HFC-134a + TEGDME, *Fluid Phase Equil.* **2005**, 133, 1-8.
15. M.A. Monsalvo, A. Baylaucq, S.E. Quiñones-Cisneros, C. Boned. High Pressure Viscosity Behavior of *x* 1,1,1,2-tetrafluoroethane (HFC-134a) + (1-*x*) triethylene glycol dimethylether (TriEGDME) Mixtures: Measurements and Modeling. *Submitted for publication.*

List of Publications

1. J. García, M. A. Monsalvo, S. E. Quiñones-Cisneros and J. Fernandez, Modelling Phase Equilibria and Viscosity for Refrigerant-Lubricant Oil Systems, *21st IIR International Congress of Refrigeration*, Washington D. C., 2003.
2. S. E. Quiñones-Cisneros, M. A. Monsalvo, J. García and J. Fernandez, Phase Behaviour of Refrigerant-Lubricant Mixtures, *20th European*

Symposium on Applied Thermodynamics, Germany, 2003.

3. S. E. Quiñones-Cisneros, J. Fernandez, J. García and M. A. Monsalvo Phase and Viscosity Behaviour of Refrigerant-Lubricant Mixtures. *Int. J. Ref.*, **2005**, 28, 714-724.
4. M.A. Monsalvo, A. Baylaucq, P. Reghem, S.E. Quiñones-Cisneros, C. Boned, Viscosity measurements and correlations of binary mixtures: HFC-134a + TEGDME, *Fluid Phase Equil.* **2005**, 133, 1-8.
5. M.A. Monsalvo, A. Baylaucq, S.E. Quiñones-Cisneros, C. Boned. High Pressure Viscosity Behavior of x 1,1,1,2-tetrafluoroethane (HFC-134a) + (1-x) triethylene glycol dimethylether (TriEGDME) Mixtures: Measurements and Modeling. *Submitted for publication.*

Martin Nordvig Mortensen

Address: I. C. Modewegsvej, 2800 Lyngby
Phone: +45 3347 3536
Fax: +45 3347 3327
e-mail: martin.mortensen@natmus.dk
www: http://www.polymers.dk

Supervisors: Søren Hvilsted (the Danish Technical University)
Jens Glastrup (the Danish National Museum)

Ph.D. Study
Started: June 2005
To be completed: May 2008

Stabilisation of Polyethylene Glycol in Archaeological Wood

Abstract
Polyethylene glycol (PEG) is a polymer that is widely used for impregnation of waterlogged archaeological wood. One example is the warship Vasa in Stockholm. There is concern that PEG may be degrading in the wood, one of the aims of this project is to establish if this is the case and if it can be stopped. Preliminary characterization of PEG in the Vasa showed that PEG 4000 was located at the surface only, PEG 1500 and PEG 600 was found at all depths. Accelerated ageing experiments showed that tetraethylene glycol readily oxidizes at 70 °C thereby shortening the polymer chain and producing formic acid as well as mono- and diformate esters of the polymer fragments.

Introduction

The warship Vasa sank close to Stockholm harbor only a few miles into its maiden voyage in 1628. In 1961 it was salvaged after 333 years on the seabed. The ship was then impregnated with polyethylene glycol (PEG) for 17 years to stabilize the dimensions of the timbers. PEG impregnation is widely used for waterlogged wood, the Vasa (SE), the Hjortspring boat (DK), the Mary Rose (UK), the Batavia (AU), the Skuldelev ships (DK) and the Bremen cog (D), are just a few examples. PEG degradation was observed during the latest treatment of the Hjortspring boat [1]. It is also a concern at the Vasa Museum that PEG may be degrading in the wood at room temperature. If this turns out to be the case, many artefacts are threatened.

It is a fact that PEG degrades under hot and oxidative conditions [2-5]. A few degradation studies has been conducted with modern techniques such as nuclear magnetic resonance (NMR) [6-8] however these studies were conducted at very high temperatures thus they have little in common with the climate in a museum. There is agreement though that degradation of PEG leads to shortening of the polymer chain. The ultimate consequence of PEG degradation in the ships would then be collapse of the wood since PEG turns into a liquid when the molecular weight gets to low.

Specific Objectives

It is the aim to characterize PEG and possible PEG degradation products in the Vasa and in other PEG treated artefacts using different analytical techniques such as for example mass spectrometry. Based on this information a method that can show if PEG degrades or not will be devised. If degradation is taking place then ways of inhibiting the process will be developed and tested.

Results and Discussion

Matrix Assisted Laser Desorption Ionisation-Time of Flight Mass Spectrometry (MALDI-TOF MS) is one of the techniques that was used in the characterisation of PEG in the Vasa. Such recordings are shown in figure 1 for extracts from three different depths below the wood surface of the Vasa. The spectra are dominated by ions due to cationised PEG molecules ($[(\mathrm{PEG})\mathrm{Na}]^+$).

The Vasa was treated with three different PEG types, PEG 600, PEG 1500 and PEG 4000. These PEG types are found in different parts of the wood as seen in the mass spectra (figure 1.). In the spectrum recorded on the extract of the outer 0 to 3 mm, three bell-shaped distributions of ions are seen.

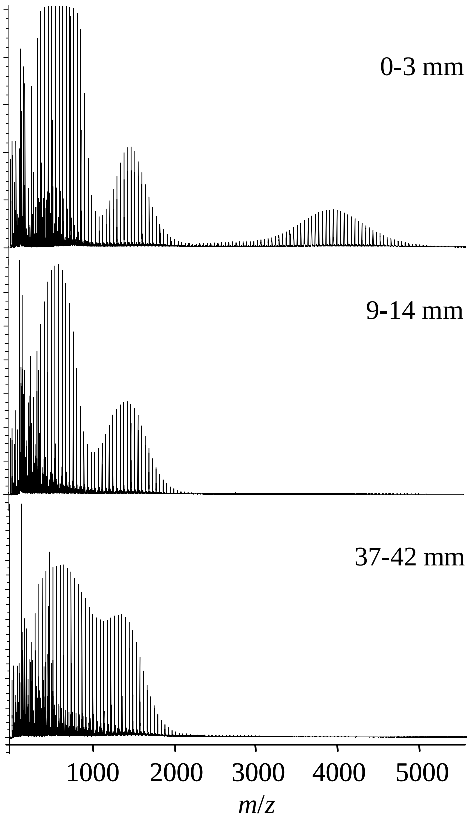

Figure 1. MALDI-TOF spectra recorded on extracts of wood from the Vasa (from top): the outermost 3 mm, 9-14 mm below the wood surface, 37-42 mm below the wood surface. The x-axis have the same scale on all three inserts, the y-axis have different scales. PEG 4000 is detected in the surface layers only, PEG 1500 and 600 are detected at all depths.

One is centred around *m/z* 4000, one around *m/z* 1500 and one around *m/z* 600 (the intensity of the latter is outside the range of the apparatus). Thus the extract contains PEG 600, 1500 and 4000 as one would expect. The spectra for the two other extracts (9-14 mm and 37-42 mm below the wood surface) have ions around *m/z* 600 and *m/z* 1500, but not around *m/z* 4000. These extracts only contain PEG 600 and PEG 1500. Thus PEG 600 and PEG 1500 are found at all depths whereas PEG 4000 is found almost exclusively in the outermost layers. This means that the PEG 4000 molecule is to large to enter the wood and therefore only works as a surface coating rather than occupying the vacant cavities in the wood as the PEG 1500 and PEG 600 seem to do.

An accelerated ageing experiment of the PEG model molecule tetraethylene glycol (TEG) has been conducted. Two glass vials contained equal amounts of pure TEG, one vial had a constant flow (10 cm^3/minute) of dry air passing through the liquid the other vial had dry nitrogen passing through at the same rate. The amount of TEG was measured by Gas Chromatography - Mass Spectrometry (GC-MS). Figure 2 shows the result.

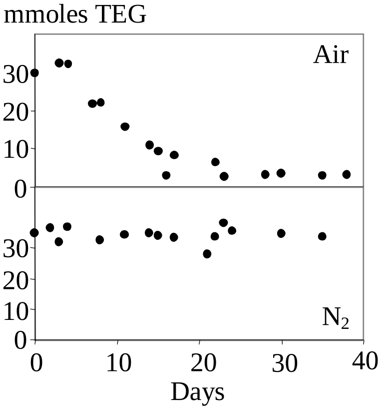

Figure 2. Total amount of TEG (mmoles) in a vial plotted versus days of ageing. The vials contain pure TEG, one was aged under a constant flow of dry air (top) the other under constant nitrogen flow (bottom). TEG is degraded in air in about 18 days under nitrogen it remains intact.

The number of moles TEG in the vials is plotted versus days of ageing. It is seen that the TEG is converted completely after about 18 days under air, under nitrogen it remains intact for more than 36 days. This shows that the degradation is an oxidation process. Results from the GC-MS analyses also showed that besides tetraethylene glycol, tri-, di- and monoethylene glycol was present along with formic acid and the mono- and diformate esters of these alcohols. Since formic acid is a product of the degradation, probably an end product, it might be possible to use it as a marker molecule for PEG degradation in the Vasa.

Conclusions

PEG 600 and PEG 1500 were found at all depths below the wood surface of the Vasa, PEG 4000 was found in the surface layers only.

Tetraethylene glycol is degraded oxidatively to form tri-, di- and monoethylene glycol along with formic acid and the mono- and diformate esters of tetra-, tri-, di- and monoethylene glycol.

Future work includes the evaluation of formic acid as a marker molecule for PEG degradation in wood and the development of PEG degradation inhibitors.

Acknowledgements

This project is funded by the National Maritime Museums of Sweden research project “Save the VASA” sponsored by The Bank of Sweden Tercentenary Foundation, The Swedish National Heritage Board, The Swedish Foundation for Strategic Research (SSF), The Swedish Research Council for Environment, Agricultural Sciences and Spatial Planning (FORMAS), and The Swedish Agency for Innovation Systems (Vinnova). The Danish Ministry of Culture and the Danish National Museum are also kindly acknowledged for funding.

References

1. T. Padfield, J. Winsløw, W. B. Pedersen, J. Glastrup, Decomposition of Polyethylene Glycol (PEG) on Heating, in: K. Grimstad (Ed.) 9th Triennial Meeting Dresden, German Democratic Republic 26-31 August 1990, ICOM Committee for Conservation, Los Angeles, 1990, 243-245.
2. J. Glastrup, Polym. Degrad. Stabil. 52 (1996) 217-222.
3. A. D. Dale, M. B. Evans, J. Chromatogr. 552 (1991) 161-167.
4. L. Costa, A. M. Gad, G. Camino, G. G. Cameron, M. Y. Qureshi, Macromolecules 25 (1992) 5512-5518.
5. S. Morlat, J.-L. Gardette, Polymer 42 (2001) 6071-6079.
6. L. Yang, F. Heatley, T. G. Blease, R. I. G. Thompson, Eur. Polym. J. 32 (1996) 535-547.
7. O. A. Mkhatresh, F. Heatley, Macromol. Chem. Phys. 203 (2002) 2273-2280.
8. O. A. Mkhatresh, F. Heatley, Polymer International 53 (2004) 1336-1342.

Jens Kromann Nielsen

Address: KT, DPC, Building 423, Room 112
Phone: +45 4525 6809
Fax: +45 4588 2161
e-mail: jkn@kt.dtu.dk
www: http://www.student.dtu.dk/~s973715/dpc/

Supervisors: Ole Hassager, DTU
Kristoffer Almdal, Risø
Kell Mortensen, Risø

Ph.D. Study
Started: February 2004
To be completed: January 2007

Rheology, Structural Studies and Synthesis

Abstract
The elongational flow dynamics of polymer melts reveals much about the structural information of the individual behavior chains in the melt. Current well established constitutive models for polymer flows are in good agreement with shear flow experiments, but recent experiments on linear and branched polymers [1-2], performed at DTU, cannot be explained by any of the available models. An essential part of the project is to measure the elongational rheology of polymers with well-known molecular structure and set up corrections to current models to get better agreement between theory and experiments.

Background: Measuring Extensional Viscosity for Polymer Melts

In many polymer-processing operations the polymer molecules experience a significant amount of orientation and chain stretching. These effects can sometimes be of benefit to the product, for example in a polymer fiber, when alignment of the molecules in the axial direction gives favorable characteristics for the finished product. On the other hand, the effect sometimes gives undesirable effects for the product, for example thermal form instability that may result in warpage of the product. Chain stretching and orientation also has a significant effect on the processing of the final product. Processing is often limited by sample breaks that are induced by the rheology of the polymer. Thus, knowledge of the chain orientation and stretch is of intrest for not only scientists who are interested in polymer dynamics, but also for product engineers.

The conventional way of measuring the rheology of a given material is by using a shear rheometer. This method is good at inducing chain orientation in the sample, and a large amount of data in this area has insured very reliable models of chain orientation and its effect on rheology. However, because of the rotational nature of the shear flow, the chains are given a chance to relax before a significant amount of chain stretching is observed. Hence, shear rheology is not usable for probing chain stretch. The consequence of this lack of data is poor modes available for estimating the effects of chain stretching on the rheology and as a result, poor model predictions of processes at high deformation rates.

Still, there have been attempts on creating measuring apparatuses for generating the necessary flow for chain stretching. The most common instrument is the Meissner rheometer where ideal extensional flow is achieved by stretching a sample between four conveyer belts and estimating rheological relevant properties by relevant forces and deformation rates. The problem with this approach is however, that only the overall deformation rate can be set. As the stretching of the filament becomes unstable very fast, local instabilities cannot be controlled and filament breakup usually occurs before the chains become fully extended. This problem is even more severe as the instabilities evolve very fast when the chains become extended. Another technique used for the measurement is the “Filament Stretching Rheometer” (FSR). In this approach, the sample is simply placed between two parallel discs, the discs are separated at a given rate, and the forces are measured on one of the discs.

As the flow in the beginning of the experiment defines where the instability takes place, the diameter of the filament at this place is measured during the entire experiment, using a laser micrometer, ensuring an exact measure of the deformation at all times. In addition, regulating the separation of the two discs can control this deformation. Until today, the FSR has only been used at room temperature. The reason is that high temperature gradients in the setup, measurement of the deformation is difficult in an oven and the polymer melts does not stick very well to the end plates.

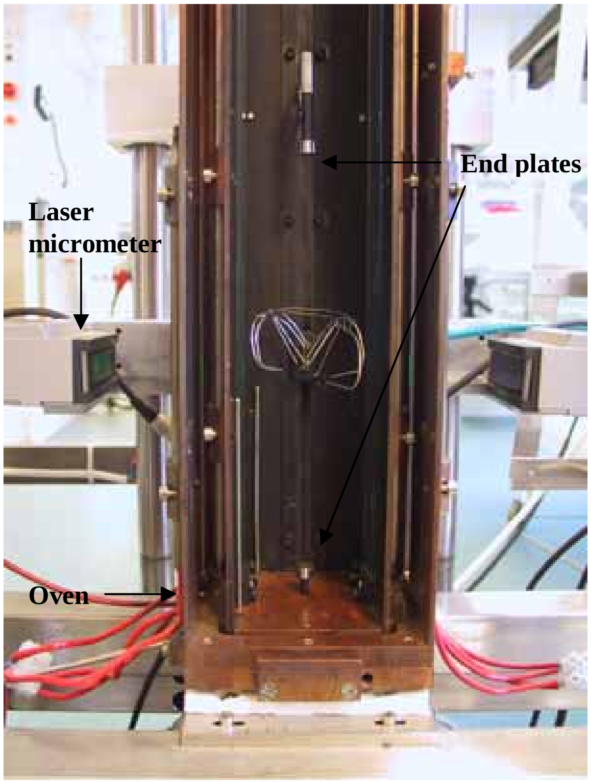

Figure 1: Close up of the Filament Stretching Rheometer

At the Danish Polymer Center Ph.d. Anders Bach constructed a filament stretching rheometer, in 2000-2003, which is capable of measuring extensional viscosity at high temperatures. Using several temperature controls solves the problem regarding temperature gradients. To further reduce temperature gradients inside the oven, the oven is build in copper, which is a good heat conductor, and all copper surfaces facing inside the oven are painted black to increase the radiant heat emission.

Another major problem in doing filament-stretching experiments is getting the filament to stick to the end plates. By choosing polymers melts, and take care in applying the end plates, we have overcome this limitation. However, we note that some polymer systems might not be measurable in the filament stretching rheometer without either gluing the sample to the end plates or use of some kind of mechanical grips.

“Master curve” approach

Another problem in doing experiments on polymer melts is controlling the deformation rate. To obtain usable data, the rate must be constant during the entire transient experiment.

We started using a “master curve” approach proposed by Orr and Sridhar (1999) [3], which relate the distance between the end plates and the radius of the filament.

We consider an axisymetrical filament between two parallel plates separated with distance L(t). The filament has a plane of symmetry parallel to the two end plates and the radius of the filament is here R(t). The desired mid radius, or set point of the system $R_{\text{ideal}}(t)$ is given by:

$$R_{ideal}(t) = R_0 \exp\left(-\frac{\dot{\varepsilon}t}{2}\right) \tag{1}$$

Where R_0 is the initial mid radius. The radius in the middle of the filament defines Hencky strain ε(t) at a given time in the experiment

$$\varepsilon(t) = -2\ln\left(\frac{R(t)}{R_0}\right) \tag{2}$$

We see that in an ideal experiment $\varepsilon = \dot{\varepsilon}t$. If the filament deforms as an ideal cylinder the extensional flow would demand the separation length between the end plates to be:

$$L(t) = L_0 \exp(\dot{\varepsilon}t) \tag{3}$$

L_0 is the separation between the endplates a t=0. To relate the connection between L and R, we define a function f such that

$$E = \ln\left(\frac{L(t)}{L_0}\right) = f\left(-2\ln\frac{R(t)}{R_0}\right) \tag{4}$$

The function *f* is a n’th order polynomial and is called the “Master curve”. *E* is a measure of the end separation.

In the Master curve-approach, successive stretching experiments are performed with different polynomial functions for *f*. After each experiment, $\ln(L(t)/L_0)$ is plotted against $-2\ln(R(t)/R_0)$ and a 10’the order polynomial is fitted to this. The plate separation in the next experiment is then performed according to the newly found function of *f*.

Using this approach the development in radius converges towards the desired profile, as defined in equation (1), and four experiments is usually required before a satisfactory development is obtained. In figure 2, we show how the radius converges towards the desired exponential decay.

Control approach

When working with stretching of melts one experiment usually takes 2-3 hours including temperature stabilization and sample preparation, so we have devolved a new technique to relate the plate separation with the diameter of the melt.

We approach the problem of plate separation as a closed loop-control problem, where the endplates must be adjusted during the experiment to ensure that the radius at the middle of the filament decreases in an exponential way, as defined in equation (2).

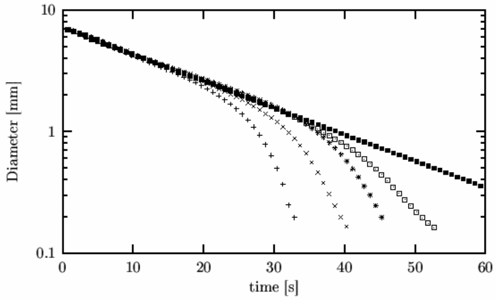

Figure 2: Measured radius as function of time in experiments with desired rate of 0.1 s^{-1}. Data (+), (x), (*) and (□) show convergence in the "master curve approach". (■) is obtained using the controller.

The controller was compared to the "master curve"-approach by performing stretching experiments on a duo disperse polystyrene melt.

The "master curve" approach was tested first, and the results are plotted in figure 2. The plot clearly shows poor convergence in the measured radius, and after 4 iterations, the radius only has an acceptable exponential decay until ε=3.5. In the plot we also show an experiment performed using the controller, which here includes proportional and integral terms, PI. This time the radius is exponentially decaying throughout the experiment and no further experiments are required. We further observe that the difference between desired and achieved radius is never more than ± 1%.

Measurements done on the rheometer have been compared with measurements done on a Meissner type rheometer (Rhemetrics polymer Melt Elongational rheometer RME [4]). In figure 3 we plot experiments done on a low-density polyethylene; experiments are performed at strain rates $1s^{-1}$ and $0.01s^{-1}$. The plot has been non-dimensionalized by plotting the transient Trouton ratio as function of Hencky strain. The Trouton ratio is the transient extensional viscosity normalized with the zero shear viscosity and

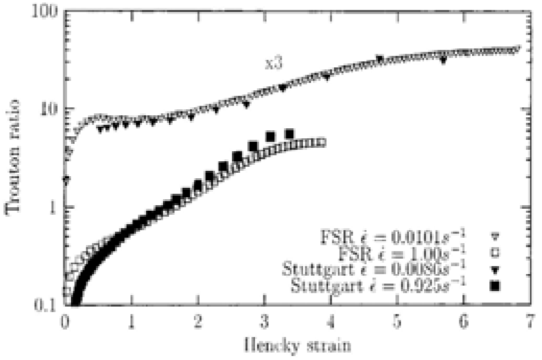

Figure 3: Comparison between DTU-FSR and Stuttgart measurements. Non-dimentional viscosity, Trouton ratio, vs. strain for LDPE.

Results

The control mechanism in filament stretching, combined with the design of the oven has made it possible to measure up to very high extensions. In other extensional rheometers without the control mechanism the melt usually ruptures at strains above 3, especially if the melts is not very strain hardening. Monodisperse polystyrene is an example of such a polymer, and this is why Anders Bach was the first to measure the extensional viscosity to such a high extension that the stress became constant. This steady state was known to exist for polymer solutions, but was until 2003 considered to be experimentally out of reach for melts.

Later, during my phd-study, the steady state viscosity was determined for a commercial polydisperse low density polyethylene, LDPE, which is a branched polymer. But the startup behavior of the linear PS and the branched LDPE was significantly different. Figure 4 shows the startup viscosity for the linear PS-melt, and figure 5 the startup stress for the LDPE, where $\sigma_{zz} - \sigma_{rr} = \eta^{+}\dot{\varepsilon}$

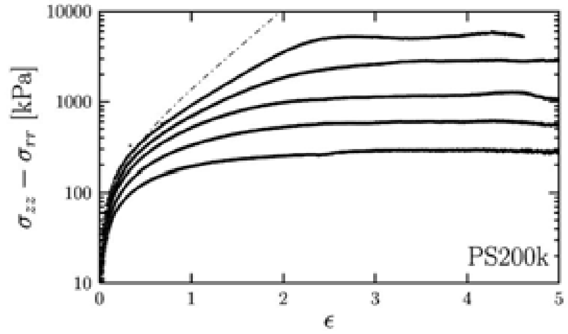

Figure 4: Startup stress of a monodisperse PS200K melt for four different elongational rates

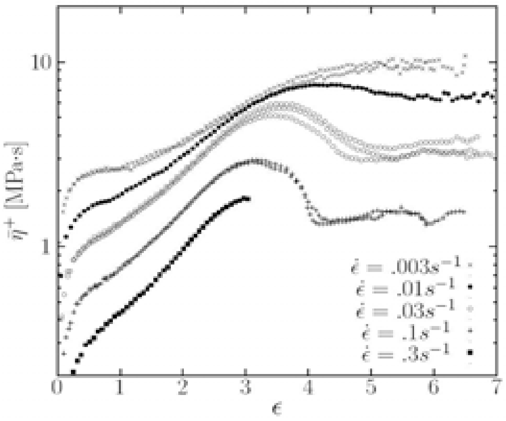

Figure 5: Startup viscosity of a polydisperse LDPE melt for five different elongational rates

We see that the startup viscosity for the monodisperse PS increases homogeniously vs. Hencky strain and finally reaches a steady state. The startup viscosity for the LDPE however increases with Hencky strain, and for high elongational rates, goes through a maximum and finally reaches steady state. We believe that this qualitatively different behavior is due to the fact that the side chains of the branched LDPE collaps into a tube along the axis of the backbone, as shown in figure 6.

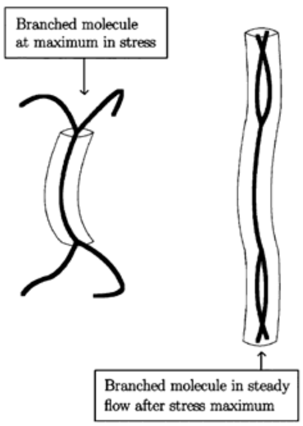

Figure 6: Interpretation of reduction in stress in terms of Pom-Pom picture. At the maximum in stress, the arms contribute to the tension in the backbone. At steady state, the molecule becomes effectively a linear polymer without arms

The specific structure of commercial LDPE is not known and the polymer is not suited for model working, because of its polydispersity and structural uncertainty. We have therefore synthesized a polystyrene with well-characterized branching using anionic polymerization [5]. The polystyrene we made is the simplest branched molecule, a triblock homopolymer, A_3-B-A_3, which has a backbone chain with a length of 100 kg/mole, and three arms in each end with individual molecular weights of 27 kg/mole, equivalent of two entanglements.

Elongational measurements on this so called “pom-pom” polymer will reveal if the proposed mechanism is correct.

1. Bach, A.; Almdal, K.; Rasmussen, H. K.; Hassager, O. *Macromolecules* (2003), **36**, 5174.
2. Rasmussen, H. R.; Nielsen, J. K., et. al. Viscosity overshoot in the start-up of uni-axial elongation of LDPE melts. *J. Rheology*, (2005), **49**, 369-381
3. Orr, N. V., and T. Sridhar, *J. Non-Newtonian Fluid Mech.* (1999), **82**, 203–232
4. Bastian, H., ‘‘Non-linear viscoelasticity of linear and long-chain-branched polymer melts in shear and extensional flows,’’ Ph.D. thesis, Institut für Kunststofftechnologie der Universität Stuttgart, (2001)
5. Knauss and Huang. *Macromolecules* (2002), **35**, 2055-2062

Anne Kathrine Kattenhøj Overgaard
Address: DPC, Dept. of Chemical Engineering
Building 423, Office 206
Technical University of Denmark
Phone: +45 4525 6817
Fax: +45 4588 2161
e-mail: ako@polymers.dk
www: http://www.polymers.dk

Supervisors: Søren Hvilsted
Jakob Vange, Coloplast Research
Hanne Everland, Coloplast Research

Ph.D. Study
Started: September 2004
To be completed: August 2007

Coupling of Active Components to Synthetic Polymers

Abstract

Materials for medical devices should provide more than just structure. Some synthetic polymers are ideal materials for healing of chronic wounds because of their high biocompatibility and the possibility of tailoring their properties. Active components can be coupled to the synthetic polymers to obtain wound healing materials that support cell ingrowth. This coupling could take place via the very mild and highly efficient "click" coupling of azides and alkynes.

Introduction

Future materials for medical devices should be more than just materials that provide structure. The materials should be intelligent and take an active part in the process, e.g. by absorbing smell or by initiating cell growth.

In the case of a chronic wound the normal biological wound healing process has been impaired and the application of a scaffold as a kind of artificial skin is necessary to help the healing process. The principle of a scaffold-assisted wound healing is demonstrated on a burn wound in Figure 1.

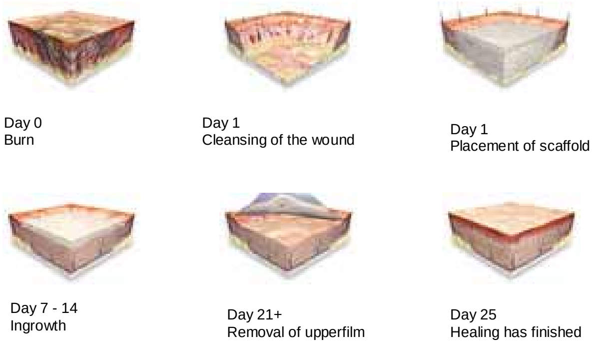

Day 0
Burn

Day 1
Cleansing of the wound

Day 1
Placement of scaffold

Day 7 - 14
Ingrowth

Day 21+
Removal of upperfilm

Day 25
Healing has finished

Figure 1 Principle of the wound healing process when a scaffold is applied[1]

The skin has been irrevocably destroyed by a burn wound. On day 1 the damaged tissue is removed and a scaffold is placed in the wound. The scaffold is porous and with interconnectivity, so during the first three weeks ingrowth of cells should take place. After this the upperfilm can be removed. The healing process should be finished after approximately one month and over the same period of time the scaffold material should be degraded and have disappeared so that only new skin remain.

For a material to be utilized in such a wound healing scaffold it has to comply with certain requirements. The ideal material for wound healing should be biocompatible, biodegradable and easy to process [1,2,3]. The material must mimic the extra cellular matrix (ECM), it has to uphold structure, i.e. maintain the mechanical properties to provide a suitable environment for the new tissue [4], it should promote cell adhesion and growth and degrade as new tissue forms.

The most important requirement for a wound healing material is the biocompatibility. The material should possess the right surface chemistry to promote cell attachment; it should support cell ingrowth and at the same time it should not provoke any unwanted tissue response [5].

Several different materials may be used in a scaffold for wound healing and among these natural as well as synthetic polymers could be considered.

---

[1] Courtesy of Hanne Everland, Coloplast Research

The advantage of using natural compounds for a wound healing scaffold is the excellent biocompatibility and the ability of the material to interact favorably with cells [6]. However, the differing batch compositions and the poor mechanical performance of the natural polymers might provide a problem, if these materials should be employed in a scaffold for wound healing [7].

As an alternative to the natural polymers, the synthetic polymers have certain advantages: They can, in principle, be tailored to give a wider range of properties and a more uniform composition than natural compounds. Furthermore, synthetic polymers are known for high processability, and porous materials with well-controlled micro-structure can be made available. The key advantages include the ability to tailor mechanical properties and degradation kinetics to suit various applications. Most synthetic polymers are degraded via chemical hydrolysis and insensitive to enzymatic progresses, so that their degradation will not vary from patient to patient. Moreover, it should be possible to design synthetic polymers with chemical functional groups that can induce tissue ingrowth [8].

Specific Objectives

The ideal material for a medical device would, however, presumably, consist of as well natural compounds as synthetic polymers. The material would exploit the excellent cell growth promoting properties of the natural compound in combination with the superior mechanical properties of the synthetic polymer.

The current project is mainly experimental. Focus is on obtaining an ideal material to be used in a wound healing scaffold or alternative medical devices. Mixes of natural compounds and synthetic polymers have previously been applied in medical scaffolds [9]. It is, however, believed that superior materials can be obtained if the compounds are chemically bonded to each other. The synthetic polymers will be able to uphold the structure of the scaffold as cell ingrowth and proliferation take place, and the natural compounds will promote these cell actions. By chemically bonding the materials the positive effects of both is ensured for a longer period of time.

The chemical bonding of the materials could be achieved through the well known 1,3-dipolar cycloaddition of an azide with an alkyne group to form a 1,4-triazole. This reaction has been known since the early 1960’s where Huisgen and coworkers carried out a monumental work in this area.

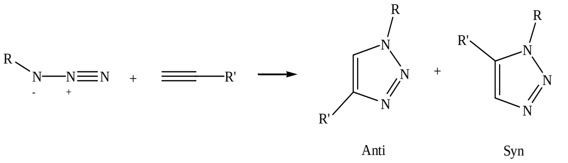

Figure 2 The general Huisgen reaction – 1,3-dipolar cycloaddition resulting in two products [10].

The reaction to form a triazole by the conventional Huisgen 1,3-dipolar cycloaddition at elevated temperature gives rise to two different products: an anti- and a syn-triazole. The formation of two products can be prevented by running the same reaction in the presence of a Cu(I) catalyst at room temperature. This reaction can take place in water; it gives rise to only one product: the anti product (1,4-triazole), and the reaction takes place with approximately 100 % conversion. Because of the very mild conditions, the high yield and the stereospecificity this reaction has been termed a “click” reaction by K.B. Sharpless *et al.* [11]. The advantage of this reaction is the formation of a stable bond under mild reaction conditions. The mechanism for the click reaction can be seen in Figure 3, which also explains why the reaction only takes place with terminal alkynes.

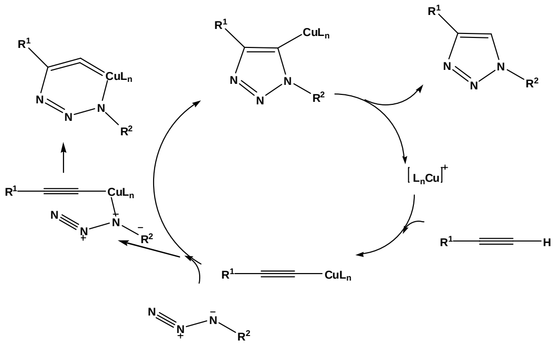

Figure 3 Reaction mechanism for the click reaction. The Cu(I)-catalyst can only coordinate to a terminal alkyne [12]

The aim of the project is to obtain materials consisting of natural components coupled to synthetic polymers via the 1,4-triazole. This is obtained by functionalizing the natural compound and the synthetic polymer with either an alkyne or an azide and then couple the materials by the click reaction.

Results and Discussion

The natural components, which are to be used in this project contain several hydroxy groups, which have similar chemical properties. Since it is desirable, if not crucial, that the functionalization with either azide or alkyne only takes place at one place in the molecule, it is very important to carry out stereoselective reactions. Therefore several attempts to functionalize a model compound, N-Acetyl-D-Glucosamine, have been carried out to find the optimal stereoselective reactions to carry out on the natural component.

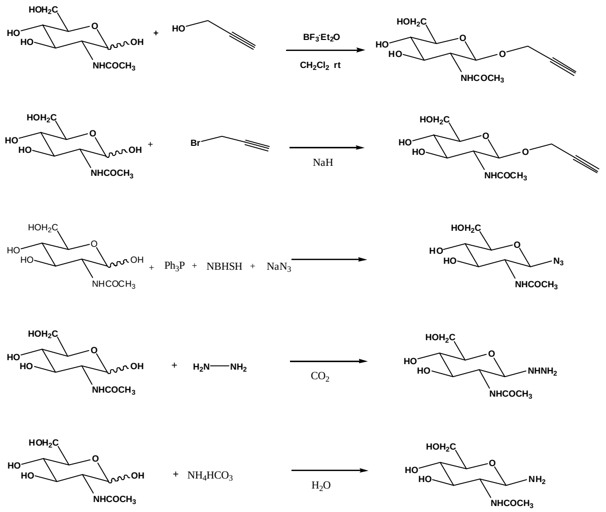

Figure 4 Reactions carried out on the model compound N-Acetyl-D-Glucosamine

The reaction products have been characterized by ^{1}H-NMR and the result from the amination reaction of N-Acetyl-D-Glucosamine can be seen in Figure 6. Comparison of this spectrum with the ^{1}H-NMR of the starting material in Figure 5 clearly shows, that a reaction has taken place.

In Figure 5 the proton from the anomeric center is to be found at δ 5.10 ppm and the coupling constant is small (~ 3 Hz) indicating that the proton is equatorial. Furthermore there are no peaks, from the compound[2], in the spectrum between δ 4.00 ppm and 5.00 ppm.

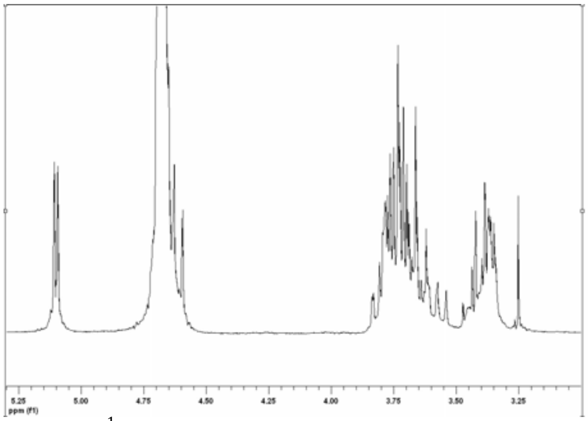

Figure 5 ^{1}H-NMR spectrum of the model compound N-Acetyl-D-Glucosamine

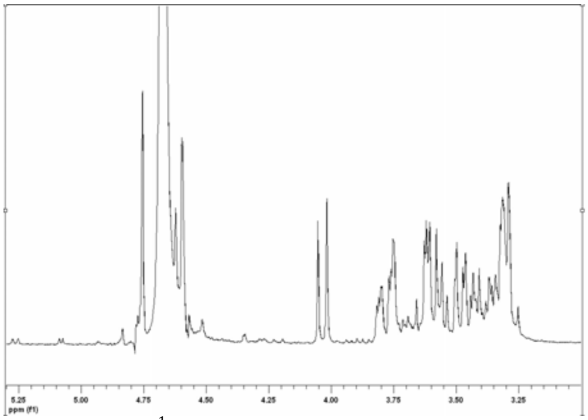

Figure 6 ^{1}H-NMR spectrum of N-Acetyl-D-Glucosamine after reaction with NH_4CO_3

In the spectrum of the reaction product (Figure 6) the proton from the anomeric center has moved to δ 4.05 ppm and the coupling constant is now ~ 8 Hz indicating that the anomeric proton now is in the axial position. Furthermore the coupling pattern of the glucosidic protons in the area between δ 3 and 4 ppm has changed, confirming that a reaction has taken place on the anomeric center.

In addition polymerizations employing different initiators have been and will be carried out to obtain synthetic polymers which can be coupled to the natural component.

The coupling of the natural component to the synthetic polymer should take place via the click reaction between an azide and a terminal alkyne. The product will be a 1,4-triazole with two substituents. It is not known whether it will have an effect on the material properties from which compound the azide and the alkyne stems. This will have to be investigated.

Characterization of the synthesized materials will take place by Size Exclusion Chromatography (SEC), Nuclear Magnetic Resonance (NMR) techniques, Differential Scanning Calorimetry (DSC) and Infrared Spectroscopy (IR).

Conclusions

Stereoselective reaction is a crucial point in the project. It has been possible to manipulate only the anomeric center of a model compound, and experiences from reactions on the model compound will be carried on to manipulation reactions on the anomeric center of the natural component. Polymerization reactions have been and will be carried out with different initiators. In addition an investigation of the material property dependence of the alkyne and azide origin will be carried out. Characterization of the synthesized materials is an essential point in the project and different methods (SEC; NMR; DSC and IR) will be employed to verify that the reactions have taken place.

Acknowledgements

The author greatly acknowledges Coloplast A/S, the Technical University of Denmark and The Danish Research Training Council for the financial support to

---

[2] The peak at ~ δ 4.70 ppm is from the NMR solvent D_2O

this project, which is part of The Graduate School of Polymer Science.

References

1. B.E. Chaignaud, R. Langer, J.P. Vacanti, in: A. Atala, D. Mooney, R. Langer, J.P. Vacanti, (Eds.), Synthetic Biodegradable Polymer Scaffolds, Birkhäuser, Boston, 1997, Chapter 1.
2. L.G. Cima, J.P. Vacanti, C. Vacanti, D. Ingber, D. Mooney, R. Langer, J. Biomech. Eng. 113 (1991), 143-151
3. C.M. Agrawal, R.B. Ray, J. Biomed. Mater. Res. 55 (2001) 141-150
4. M.A. Slivka, N.C. Leatherbury, K. Kieswetter, G.G. Niederauer, Tissue Engineering 7 (2001), 767-780
5. S. Yang, K.-F. Leong, Z. Du, C.-K. Chua, Tissue Engineering 7 (2001) 679-689
6. M.C. Peters, D.J. Mooney, Materials Science Forum 250 (1997) 15-42
7. V. Maquet, R. Jerome, Materials Science Forum (1997) 43-52
8. P.A. Gunatillake, R. Adhikari, European Cells and Materials 5 (2003) 1-16
9. F.A. Maspero, K. Ruffieux, WO2004056405, 2004
10. R. Huisgen, in: A. Padwa (Ed), 1,3-Dipolar Cycloaddition Chemistry, Wiley, New York, 1984, p 1
11. H.C. Kolb, M.G. Finn, K.B. Sharpless, Angew. Chem. Int. Ed. 40 (2001) 2004-2021
12. V.V. Rostovtsev, L.G. Green, V.V. Fokin, K.B. Sharpless, Angew. Chem. Int. Ed. 41 (2002) 2596

Kim Vestergaard Pedersen
Adress: Building 229, Room 122
Phone: +45 4525 2890
Fax: +45 4588 2258
e-mail: kvp@kt.dtu.dk
www: http://www.chec.kt.dtu.dk

Supervisors: Anker Degn Jensen
Kim Dam-Johansen

Ph.D Study
Started: September 2004
To be completed: August 2007

Application of Fly Ash from Solid Fuel Combustion in Concrete

Abstract

Fly ash, a by-product from pulverized coal combustion, is utilized in the concrete manufacture where it serves as partial replacement of Portland cement. The residual carbon in fly ash is known to interfere with the chemicals added to the concrete to enhance air entrainment. The degree of adsorption is not only related with the amount of residual carbon, but also the properties of this carbon. The main objective of this project is to obtain knowledge of how the combustion conditions of pulverized coal is related with the amount and properties of the residual carbon in fly ash with emphasis on its utilization in concrete. Part of the work will focus on improveming fly ash quality by post treatment methods.

Introduction

About 24 % of the electricity produced worldwide (2002) is generated in coal fired power plants. As a consequence, large amounts of fly ash are produced. The demand for environmentally clean and cost effective power generation has increased the motivation of fly ash recycling.

The pozzolanic property of fly ash, i.e. its capability to react with water and calcium hydroxide to form compounds with cementitous properties at ambient temperature, makes it useful in the concrete industry, where it serves as partial replacement of cement and thereby increases the strength of concrete [1]. However, the fly ash has been reported to interfere with air entrainment in concrete, which is important to obtain high resistance toward freezing and thawing conditions [2]. Special surfactants, called air-entraining admixtures (AEAs), control this air entrainment by stabilizing the air as small bubbles in the concrete paste. They adsorb strongly to the air-water interface, but fly ash present in the concrete paste are capable of adsorbing the AEAs as well. Hereby less AEAs are available to support the air bubbles and the entrained air is lowered. Increasing the dosage of the AEAs may compensate for the adsorption loss, but normal variations in ash properties leads to large and unacceptable variations in the entrained air [3].

Even though modern coal fired power plants have high burnout efficiencies, significant amounts of carbon still exist in the fly ash after combustion. This residual carbon and not the mineral matter of fly ash is responsible for the adsorption of AEAs [3]. A large part of the carbon surface is non-polar compared with the polar surface of the mineral matter. This provides active adsorption sites for the hydrophobic part of the surfactants, thus the carbon competes with the sites at the air/water interface [4] as illustrated in Figure 1.

The problem with air entrainment in fly ash concrete has worldwide lead to regulations for fly ash application in concrete taking the presence of carbon in fly ash into account. These regulations are based on a maximum limit of the amount of carbon in fly ash, e.g. according to the Danish Standard DS/EN 450 the carbon content in fly ash are not allowed to exceed 5 wt%. However, in recent years the carbon content of a fly ash has been found insufficient as a criterion for its application in concrete and problems with air entrainment has been observed with fly ashes having levels of carbon below the limits [3]. These observations have lead to further studies of the interactions between AEA adsorption and properties of carbon in fly ash; factors such as accessible surface area and surface chemistry of the residual carbon are believed to also affect the AEA adsorption [4].

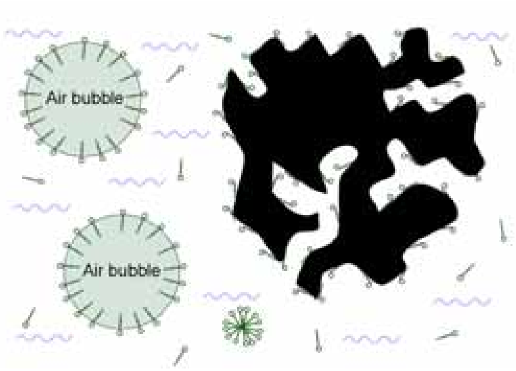

Figure 1: Adsorption sites for AEAs at air/water interface and at carbons inspired by Hachmann [4].

The combustion conditions under which the fly ash has been produced influences the properties of the residual carbon. The worldwide introduction of improved burner technologies in order to reduced NOx-emissions has lead to problems with achieving a correct amount of air entrainment in fly ash concrete [5]. These burner technologies work with hot fuel rich zones in order to combust under reducing conditions and these conditions are believed to create fly ash being poor in quality in terms of concrete utilization.

The degree of interference of fly ash with air entrainment in concrete is usually determined by the foam index test, which is a simple laboratory titration procedure involving the use of commercial air-entraining agents (AEAs) and visual observation of foam stability. These parameters reduces the comparability of the test, i.e. commercially available AEAs vary in chemical nature and criterion on foam stability is operator individual. Therefore, it is of interest to develop a reproducible method, which is able to determine the fly ash quality with respect to air entrainment in concrete [6].

Specific Objectives

The aim of this project is to obtain further knowledge of how the combustion conditions of pulverized coal influences the fly ash quality for concrete utilization with emphasis on the air entrainment in concrete. Part of the work will focus on improvement of fly ash quality by post treatment methods. Furthermore, steps will be taken toward the development of a reproducible test method to replace the foam index test.

Method Development

The new method developed to determine fly ash quality is based on surface tension measurements instead of foam stability observations. Moreover, a standard surfactant (sodium dodecyl benzene sulfonate, SDBS), which can be prepared in known concentrations, is used as a model for a commercial AEA. The surface tension is measured on a suspension of cement and fly ash particles and the procedure only slightly differs from the foam index test, i.e. in the foam index test the AEAs are added continuously until stable foam is obtained on top of the suspension, whereas in the new method the surfactants are added in one step. After 5-30 minutes of mixing, the aqueous phase is separated from the particles followed by surface tension measurements using the maximum bubble pressure method; a capillary is introduced into the solution and bubbles are grown on the tip. The pressure difference required in the bubble formation is proportional to the dynamic surface tension of the solution [7]. The lifetime of the bubbles have an impact on the measured surface tension, e.g. increasing bubble lifetime lowers the measured surface tension due to the surfactants will have more time to diffuse to the bubble surface.

First part of the method development included determination of initial SDBS concentration and applied bubble lifetime, and the optimal conditions are based on the experimental data presented in Figure 2 and 3.

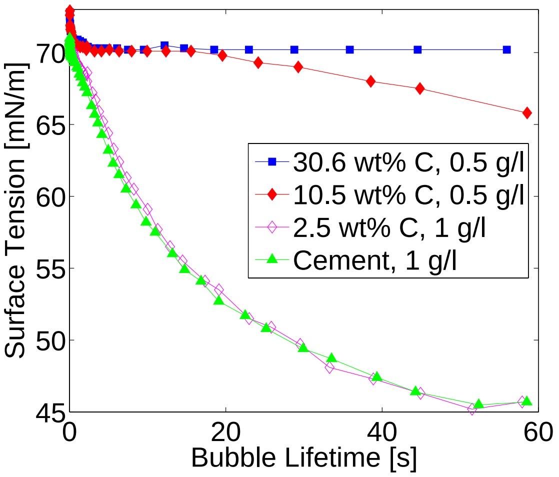

Figure 2: Dynamic Surface tension compared with bubble lifetime at starting concentrations 0.5 and 1 g/l SDBS.

The consequence of having a low initial concentration of SDBS is revealed in Figure 2, where only a minor difference in the measured dynamic surface tension can be detected in a wide span of bubble lifetime between two high carbon ashes. It appears as if both ashes have adsorbed most of the added surfactant, making it difficult to measure any difference in their adsorption capacity. On the other hand, a high initial concentration of SDBS leads to similar dynamic surface tension measurements of both cement and a low carbon ash, indicating that the amount of surfactant adsorbed by the fly ash is low compared to the remaining SDBS in the solution. The critical micelle concentration (CMC) of SDBS may explain this observation. Normal surfactant behavior are observed below CMC, i.e. surfactants are found as monomers and the concentration relates to the surface tension [8]. Above CMC the hydrophobic part of the surfactant interacts with other surfactants leading to micelle formation, where only the hydrophilic part is in contact with the aqueous phase. The micelles are not surface active and hence will not contribute to changes in surface tension.

Addition of a 0.6 g/l SDBS solution appears to give a detectable difference between both low and high carbon ashes as shown in Figure 3.

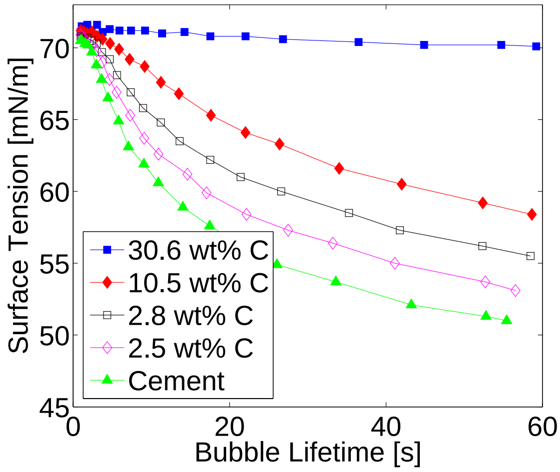

Figure 3: Dynamic surface tension compared with bubble lifetime at initial SDBS–concentration on 0.6 g/l.

It is evident, how utilization of a short bubble lifetime leads to similar surface tension results. Equilibrium between surfactants in the solution and at the surface are not obtained due to a short surface age and the surface tension of the pure solvent is measured, being water in this case (72.3 mN/m at 23°C). At high bubble lifetime, the surfactants move toward equilibrium and the surface tension is lowered. Hence, any variation in surface tension between the samples can be detected. On the other hand, the difference in surface tension between the samples appears not to increase more when a bubble lifetime above 20 seconds is applied, making it a reasonable choice in further measurements. Moreover, testing time will be significantly extended with higher bubble lifetime due to the results are based on the average of several measurements.

Other parameters that influences the test method have been investigated in the present study. Both the mixing time of the surfactant, cement and fly ash suspension and variation in temperatures were found to have a significant impact on the reported surface tension values. The transport of surfactants from the aqueous phase into the interior of the residual carbon particles is diffusion controlled [3] and thus, the surfactant concentration decreases with longer mixing time. No endpoint was found even after 30 minutes, and it was decided to proceed with 10 minutes in incubation time corresponding to the usually time expenditure of the foam index test. The surface tension of the filtrate was found to decrease with rising temperature, which lead to implementation of isothermal conditions.

Figure 4 presents surface tension measurements on filtrate from cement/fly ash samples compared with their respective foam index values. The results displays a good correlation between the two methods.

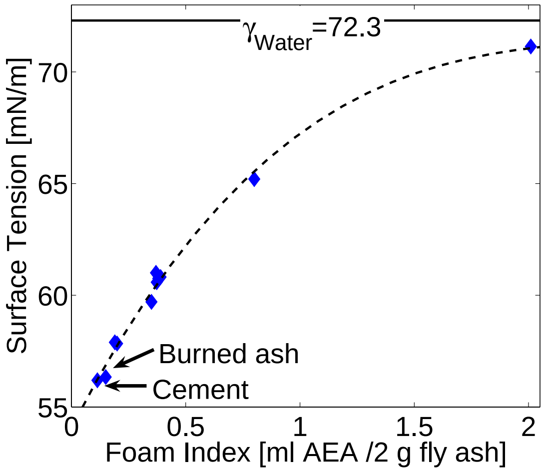

Figure 4: Surface tension of filtrate compared foam index. The temperature of the filtrate was between 22.7–22.9°C. 0.6 g/l SDBS in initial concentration and 10 minutes in incubation time.

Increasing foam index of a fly ash corresponds to higher absorptivity toward surfactants. In the surface tension method, the concentration of surfactants in the aqueous phase is reduced by the adsorption, leading to higher surface tensions. The correlation appears to be linear within lower adsorption capacities of fly ashes. At higher adsorption capacities, the test meets its limit under the applied conditions. Surface tension values can not exceed the surface tension of the pure liquid. Thus, ashes with high adsorption capacities will result in filtrates with low surfactant concentrations and show surface tensions close to pure water, making it difficult to detect any variance in their adsorption capacity. Measurements on activated carbon (FI>14 ml/2 g C) confirm this behavior. The surface tension was measured to 71.9 mN/m, indicating that the surfactant may have exhausted from the supernatant fluid completely. To include these high adsorption ashes in the detectable region involves higher initial concentration of SDBS. However, as Figure 2 shows, the difference between ashes with lower adsorption capacities will be more difficult to detect.

Conclusion and Future Work

The commonly employed foam index test, which determines fly ash quality for concrete utilization, has been compared with a new method based on surface tension measurements and there appears to be a good relationship between the two methods. The new method takes away the individual operator criterion on foam stability, making the test easier to standardize. Moreover, the test can be based on using a pure surfactant instead of an air-entraining agent, where commercial products show variation in chemical nature and concentrations.

Until now, the work has mainly focused on the development of an analytical method to determine fly ash quality. In the next part of the project, effort will be put into uncover how combustions conditions of pulverized coal affect the performance of fly ash in concrete. Moreover, post treatment methods to improve of fly ash quality will be investigated.

References

[1] K. Wesche (Ed.), Fly Ash in Concrete: Properties and Performance, 1st Edition, E & FN Spoon, London, 1991.

[2] Y.-M. Gao, H.-S. Shim, R. H. Hurt, E. M. Suuberg, N. Yang, Energy & Fuels 11 (1997) 467–462.

[3] E. Freeman, Y.-M. Gao, R. Hurt, E. Suuberg, Fuel 76(8) (1997) 761–765.

[4] L. Hachmann, A. Burnett, Y.-M. Gao, R. H. Hurt, E. M. Suuberg, Proceedings of the Combustion Institute 27 (1998) 2965–2971.

[5] Y.-M. Gao, I. Külaots, X. Chen, E. M. Suuberg, R. H. Hurt, J. M. Veranth, Proceedings of the Combustion Institute 29 (2002) 475–483.

[6] O. E. Manz, Fuel 78 (1999) 133–136.

[7] L. Schulze, K. Lohmann, Tenside Surfactants Detergents 36(6) (1999) 384–386.

[8] D. J. Shaw (Ed.), Introduction to Colloid and Surface Chemistry, 4th Edition, Butterworth-Heineman, Cornwall, 2000.

Trine Lütken Petersen
Address: Novozymes Bioprocess Academy
Department of Chemical Engineering
Currently sitting in:
Building 223, Room 211
Technical University of Denmark
Phone: +45 4525 2708
Fax: +45 4588 4148
e-mail: tlp@biocentrum.dtu.dk
www: http://www.biocentrum.dtu.dk

Supervisors: John Villadsen
Timothy Hobley
Jesper Brask, Novozymes

Ph.D. Study
Started: April 2004
To be completed: April 2007

PEGylation of Enzymes: Novel *in Vitro* Methods for Their Study and Scaleup

Abstract

The process of attaching polyethylene groups (PEG) to enzymes needs to be controlled in order to obtain PEG conjugates with the desired properties. Magnetic adsorbents with appropriate ligands can be used for binding enzymes in their active site, thus orientating the protein and protecting the catalytic pocket. It is proposed that the immobilised enzyme can then be added to activated PEG and the time of exposure controlled due to manipulation with a magnetic field. The enzyme chosen as model for proving the concept of controlling the PEGylation reaction is Savinase and magnetic supports having bacitracin as the ligand show high affinity for Savinase. Even after being reused 4 times, the supports show good binding characteristics. From batch PEGylation of Savinase, 3-4 PEG-conjugates are identified and experiments on PEGylating immobilized Savinase have been initialized.

Introduction

Covalent binding of polyethylene glycol groups to enzymes (PEGylation) may lead to improved physico-chemical and biological properties. The attachment of the correct amount of PEG groups in the right positions on an enzyme is fundamental to obtain the desired properties. Conventional batch PEGylation, however, often gives rise to a family of by-products with too few or too many PEG groups, leading to reduced product yield, and also requiring concentration and purification of the desired PEG-conjugate. Therefore a scaleable process with improved control over PEGylation is desirable.

Specific Objectives

The concept behind this project is that it is possible to bind an enzyme via its active site to a *magnetic* support by using an affinity ligand. Following binding the active site will be protected from the PEG groups. Also, the enzyme molecules should all be bound in the same orientation with respect to the support surface. When this is combined with a means of controlling the time of exposure of the immobilised enzyme to activated PEG due to manipulation with a magnetic field it is expected that the extent and location of attachment of PEG groups should be controllable. Furthermore, the use of an affinity ligand for binding the enzyme permits concentration and purification of the PEGylated product. Figure 1 shows the principle behind the process proposed.

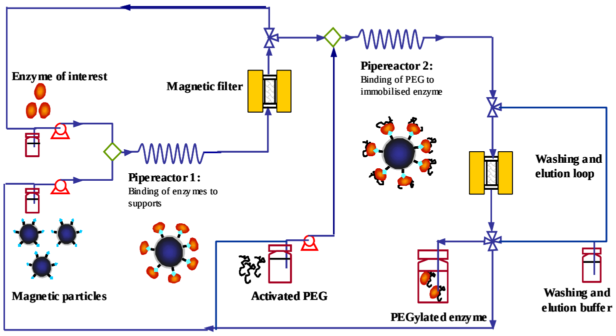

Figure 1: Schematic of the process proposed for magnetic support mediated control of enzyme PEGylation.

In the process described in Figure 1 the enzyme is rapidly bound to the adsorbent in pipe reactor 1 and the adsorbent-enzyme complex is rapidly captured in a magnetic filter while the protein in surplus pass through and is recycled. In pipe reactor 2 activated PEG is added, attached to the enzyme and the mixture is pumped into a magnetic filter where the adsorbent-PEGylated-enzyme complex is captured while the reactants pass through and can be reused. Washing is then conducted and the PEGylated enzyme is eluted from the supports. After elution the magnetic particles are recycled for reuse.

The process proposed above is novel and has never been examined before, thus the aim of this project is to examine how magnetic solid phases can be exploited for conducting *in vitro* PEGylation of proteins. Specifically to study: (i) how magnetic supports can be used to control the extent of PEGylation of enzymes, (ii) how the number and position of PEG groups affects enzyme activity as well as pH and temperature stability.

Results and Discussion

Different enzyme-ligand model systems have been identified with the most promising being the binding of the subtilisin Savinase, to the inhibitor bacitracin.

Magnetic supports derivatised with bacitracin have been constructed and the adsorption isotherm showed high specific binding of Savinase with a dissociation constant of $1.8 * 10^3$ U/L [0.79 μM] and a maximum capacity of $3.6 * 10^3$ U /g [158 mg/g].

Propylene glycol, a competitive inhibitor of Savinase, has been used for eluting Savinase from the magnetic supports, and the recovery of Savinase has been found to be approximately 60% when the recovery is based on measurements of Savinase activity. If the recovery is based on measurements of total protein concentration a value of approximately 100% is found. The reason for the observed loss in specific activity of the enzyme is still not known but may be related to the choice of eluent used (propylene glycol). Presently propylene glycol is used by Novozymes in the liquid formulation of savinase for stabilizing the enzyme. It is therefore very convenient to use the same propylene glycol solution for eluting savinase from the magnetic particles that is used in the formulation and at present it has been decided to continue using propylene glycol.

Magnetic particles that are reusable are highly desirable not only with respect to potential large-scale processes but also for laboratory use. Testing the reusability of the manufactured particles has been carried out by completing many binding/elution cycles. (Figure 2)

The result of this testing showed no loss in binding and elution characteristics after 4 cycles.

The first PEGylation trials have been carried out as batch reactions at pH 9.6 and 7.5. The PEG-conjugates were identified by SDS-page using Coomassie for protein staining and iodine for PEG staining (Figure 3).

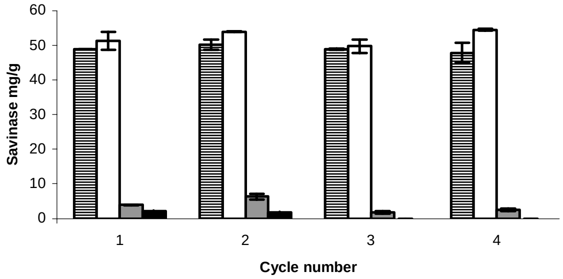

Figure 2: Plot of the reusability of magnetic particles. The striped bars show the amount of Savinase bound to the particles while the white, grey and black bar show three sequential elutions of Savinase for each binding cycle.

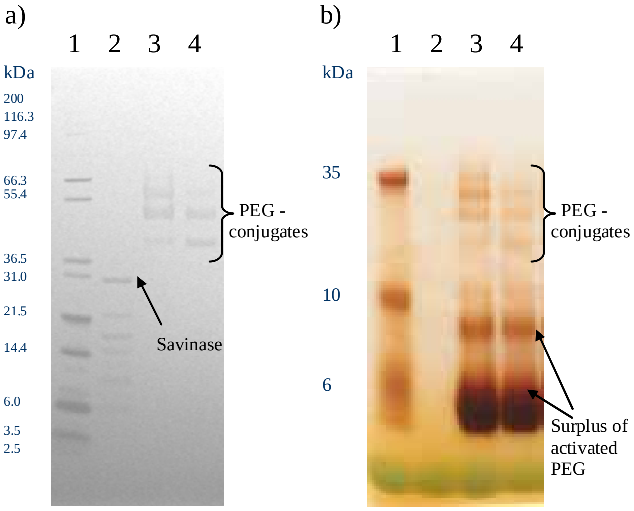

Figure 3: SDS-page gels stained with a) Coomassie and b) iodine. Lane 1: Protein marker and PEG marker respectively, lane 2: Savinase solution before PEGylation, lane 3: Batch PEGylated Savinase at pH 9.6, lane 4: Batch PEGylated Savinase at pH 7.5.

The Savinase solution in lane 2 is seen to contain impurities of different sizes. However, the main part is Savinase. Lane 3 and 4 of the batch PEGylated Savinase show 3-4 bands with molecular weights different from Savinase. This indicates the presence of 3-4 PEGylated products, with sizes corresponding to proteins of approximately 40, 50, 60 and 70 kDa.

The first trials of the PEGylation of Savinase immobilised on magnetic particles have been carried out. From the initial experiments it was found that the PEGylation must be carried out at a pH below 8 to have a stable ligand coupling to the magnetic supports when using divinylsulfone as the linker. Also it was found from the PEGylation of immobilised Savinase that under high concentrations of PEG, the Savinase was eluted from the magnetic particles due to PEG displacing the protein from the bacitracin. Thus in the next period it will be investigated how changing the PEG concentration for the PEGylation process can improve the conditions for PEGylating immobilised Savinase.

Christian Lund Rasmussen
Adress: Building 227, Room 132
Phone: +45 4525 2923
Fax: +45 4588 2258
e-mail: CLR@kt.dtu.dk
www: http://www.student.dtu.dk/~s973578

Supervisor: Peter Glarborg
CHEC Research Centre

Ph.D Study
Started: February 2004
To be completed: February 2007

Direct Partial Oxidation of Natural Gas to Liquid Chemicals

Abstract

Conversion of natural gas to methanol by homogeneous direct partial oxidation at high pressure and low temperature is an attractive industrial process to improve the utilization of the World's natural gas resources. Optimization of the process relies on a fundamental understanding of the interactions between the reaction conditions and the complex chemistry involved. Detailed chemical kinetic modeling enables such investigations of the governing chemistry on an elemental reaction level. Model predictions are verified by well–defined experiments performed on a newly constructed high pressure flow reactor setup.

Introduction

A significant fraction of the World's natural gas reserves is presently unavailable to the markets of utility duo to extraction and transport limitations. Large quantities are allocated under the tundra and beneath the sea near the continental shelves. Even if a fraction of these resources could be captured and converted to a readily transportable state, it would have a significant effect on the environmental impact of fuel and electrical power production as well as the production of chemical feedstock. In order to facilitate transportation, it is beneficial to convert the natural gas to a liquid chemical, known as the gas–to–liquid (GTL) process.

The direct partial oxidation of methane to methanol or mixtures of oxygenated hydrocarbons in a homogeneous process is a promising industrial GTL process. Direct conversion is an exothermic process, which is superior in terms of energy efficiency and simplicity to the conventional industrial production of methanol based on synthesis gas (CO/H_2) obtained from steam reforming of natural gas.

Economic assessments of the homogeneous process are generally outdated, but in–house calculations performed by Res. Ass. Hanne Hostrup Nielsen from CHEC indicate that a production facility that utilizes the direct homogeneous process with a capacity $<100\,\mathrm{m^3\ CH_3OH/day}$ is competitive with the conventional indirect process if about 5% of the methane is converted with 60% selectivity of methanol in a single pass of the reactor.

Kinetic Approach

The gas phase partial oxidation of methane is operated by a free radical mechanism, which is only partly understood and extremely difficult to control. The very stable methane molecule must be converted to methanol without promoting further oxidation to undesired carbon oxides. The rate limiting step is the initial breaking of the very stable C–H in methane. This typically requires high temperatures, which has an adverse effect on the selectivity towards the desired product. The selectivity is greatly improved by applying relatively low temperatures together with high pressure. Further improvement of the product yield is expected to be achieved by interactions with gas phase sensitizers. These include nitrogen– and sulphur oxides (NO_x and SO_2).

Product Objectives and Description

The main objective of this project is to identify a combination of process conditions and reactant composition that results in a competitive yield and selectivity of methanol or mixtures of methanol and other oxygenated hydrocarbons.

Due to the limited knowledge of the complex chemistry involved in the process, previous work has mainly been experimental. A more fundamental approach based on an understanding of the chemistry on an elemental reaction level is applied in this project. Detailed chemical kinetic modeling (DCKM) is emphasized in contrast to previous work, where an experimental optimization was attempted or a simplified kinetic model was used. A DCKM will be developed based on available knowledge of hydrocarbon oxidation chemistry and its interaction with various gas phase sensitizers, and the model performance will be validated in close interaction between theory and well–defined experimental measurements.

For this purpose, a pressurized laboratory scale flow reactor made of quartz has been designed and constructed to handle pressures up to 100 atm at 650 °C. Based on DCKM, an automated process optimization routine will eventually be developed in order to identify the optimal combination of reaction conditions and sensitizers that provides the best selectivity and yield of the desired products.

High Pressure – A Key Parameter

Pressure is the most important reaction parameter in order to compensate for the low temperature that is necessary to ensure thermal stability of the desired oxygenates. High pressure increases the collision frequency between reactants, which inevitably results in a larger reactant flux through the transition state to the products. Increasing the collision frequency further promotes stabilization of excited intermediate complexes since colliding molecules can absorb excess internal energy that would otherwise lead to decomposition of the complex. This process only involves energy transfer between the colliding molecules. Following Le Chatelier's Principle, high pressure also favors the overall conversion of methane and oxygen to oxygenated hydrocarbons ($CH_4 + 1/2\, O_2 \leftrightharpoons CH_3OH$) in order to decrease the total number of molecules.

From a practical point of view, it is unfortunate if exceptionally high pressures must be applied in order to obtain a competitive yield since gas compression is a very expensive unit operation. The well–head pressure that naturally occurs at the gas recovery sites is typically in the vicinity of 80–90 atm, and this pressure range should not be exceeded in order to limit the production costs. Reported studies of the pressure dependency predict a significant increase in the methanol yield when the pressure is increased up to 100 atm after which, this dependency declines until no apparent effect is observed after ~150 bar[1]. Hence, it is expected that an optimal pressure can be identified within the practical upper limit.

Reaction Mechanism

The conversion of methane at high pressure is governed by a complex network of radical reactions. The most important pathways are shown in Figure 1. The fractional formation of oxygenated hydrocarbons and deep oxidation products is very dependent on the reaction stoichiometry (ϕ).

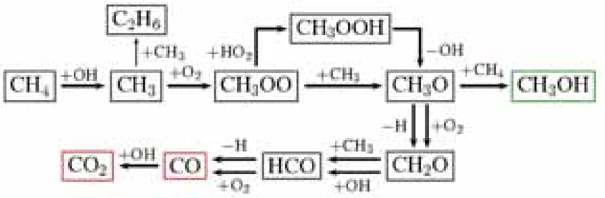

Figure 1: Oxidation of methane at high pressure. Overview of the reaction network. Framed species are methane (CH_4), methyl radical (CH_3), ethane (C_2H_6), methylperoxyl radical (CH_3OO), methylperoxide (CH_3OOH), methoxy radical (CH_3O), methanol (CH_3OH), formaldehyde (CH_2O), formyl radical (HCO), carbon monoxide (CO) and carbon dioxide (CO_2). Other species are important reactants (+) or products (-) from the individual reactions. The primary product is methanol, while CO and CO_2 constitute the unwanted deep oxidation products.

The reaction sequence is initiation by H–abstraction from CH_4, which is facilitated by a hydroxyl radical (OH):

$$CH_4 + OH \leftrightharpoons CH_3 + H_2O \qquad (1)$$

The methyl (CH_3) radical pool has three primary drains with their individual contributions being highly dependent on the reaction conditions:

$$CH_3 + O_2 + M \leftrightharpoons CH_3OO + M \qquad (2)$$

$$CH_3 + CH_3OO \leftrightharpoons CH_3O + CH_3O \qquad (3)$$

$$CH_3 + CH_3 + M \leftrightharpoons C_2H_6 + M \qquad (4)$$

Self–recombination of CH_3 to ethane (C_2H_6) only provides a significant contribution when $\phi >> 1$ and it is particularly favoured by high temperature and a low absolute concentration of O_2. Reaction (2) is the sole methylperoxyl (CH_3OO) formation channel, which means that the hydrocarbon flux through reaction (3) is restrained by the flux through reaction (2). The thermal stability of CH_3OO is poor, but the high pressure combined with the low temperature promotes it to become a key intermediate species.

A fraction of the CH_3OO radicals is intermediately stabilized as methyl peroxide (CH_3OOH) by H–addition from hydrogen peroxyl (HO_2) or hydrogen peroxide (H_2O_2) instead of being directly converted to methoxy (CH_3O) via reaction (3). As shown in Figure 1, the formation of CH_3OOH only constitutes a minor detour for the hydrocarbon flux since CH_3OOH subsequently decomposes to CH_3O. The reaction sequence is outlined in (5)–(7).

$$CH_3OO + HO_2 \leftrightharpoons CH_3OOH + OH \tag{5}$$

$$CH_3OO + H_2O_2 \leftrightharpoons CH_3OOH + HO_2 \tag{6}$$

$$CH_3OOH \leftrightharpoons CH_3O + OH \tag{7}$$

Since excess O_2 combined with low temperatures and high pressure favour peroxide and peroxyl formation, a significant flux is expected to pass through CH_3OOH under oxidizing conditions. Reducing conditions combined with a low absolute concentration of O_2 favour CH_3 as the primary reactant for CH_3OO, while by–passing CH_3OOH. The formation of CH_3OOH is largely determined by the ratio $^{r_3}/_{(r_5+r_6)}$, which makes this a key ratio. A decreasing ratio is equivalent to an increasing net production of the initiating and chain–carrying OH radical via intermediate formation and decomposition of CH_3OOH.

CH_3O decomposes or reacts with O_2 to yield formaldehyde (CH_2O); or it may be converted to methanol (CH_3OH) by H–addition from CH_4.

$$CH_3O + M \leftrightharpoons CH_2O + H + M \tag{8}$$

$$CH_3O + O_2 \leftrightharpoons CH_2O + HO_2 \tag{9}$$

$$CH_3O + CH_4 \leftrightharpoons CH_3OH + CH_3 \tag{10}$$

Reaction (9) and (10) require sufficient concentrations of O_2 and CH_4 respectively to make them frequent collision partners. If this is not the case, decomposition will predominate. Hence, a high $^{CH_4}/_{O_2}$–ratio favors methanol formation, while the opposite has an adverse effect and increases production of CO and CO_2. Based on experiences from the literature $10 < {}^{CH_4}/_{O_2} < 30$ is recommended in order to obtain high methanol yields.

Oxidation of CH_2O to formyl radicals (HCO) can be operated by a number of radical species depending on the reaction conditions. The most important reactions are shown in (11)–(14).

$$CH_2O + H \leftrightharpoons HCO + H_2 \tag{11}$$

$$CH_2O + CH_3 \leftrightharpoons HCO + CH_4 \tag{12}$$

$$CH_2O + HO_2 \leftrightharpoons HCO + H_2O_2 \tag{13}$$

$$CH_2O + OH \leftrightharpoons HCO + HO_2 \tag{14}$$

Reaction (11) and (12) are only important at reducing conditions, while (13), and especially reaction (14), predominate at oxidizing conditions.

HCO is converted to CO either by decomposition or by H–abstraction performed by O_2 in reaction (15) and (16) respectively. The ratio $^{r_{15}}/_{r_{16}}$ changes from > 1 to $<< 1$ as the reaction conditions change from reducing towards oxidizing conditions.

$$HCO \leftrightharpoons H + CO \tag{15}$$

$$HCO + O_2 \leftrightharpoons HO_2 + CO \tag{16}$$

CO_2 is obtained from reaction with HO_2 or OH. This conversion is limited under reducing conditions.

$$CO + HO_2 \leftrightharpoons CO_2 + OH \tag{17}$$

$$CO + OH \leftrightharpoons CO_2 + H \tag{18}$$

Detailed Chemical Kinetic Modeling

Detailed chemical kinetic models (DCKM) are comprehensive models that approach chemical mechanisms on an elemental reaction level. Hence, it represents the unsimplified conversion of the fuel and proportionate formation of the products as it actually takes place through a chain of elementary reaction steps. This is in contrast to empirical models. Ideally, DCKMs can be regarded as complex mechanistic models with an inherent understanding of the real chemical processes. As a consequence, model extrapolation to reaction conditions outside the range of experimental verification can be allowed with an expected accurate response. This makes DCKM an ideal tool to investigate the complexity of the homogeneous oxidation of methane to methanol and ultimately search for the optimal reaction conditions.

At the present time, a DCKM has been developed to provide accurate predictions of the oxidation chemistry of C_{1-2} fuels in the presence or absence of NO_x. The model is designed to comply with the CHEMKIN–software [2]. The designated operational range of the model includes pressures from 1 to ~100 atm and temperatures from roughly 300 to 800 °C. The current model includes 779 reversible elementary reactions of which, 511 are used to describe the pure hydrocarbon oxidation chemistry. The model will later be extended with a SO_x/HC subset. The model was originally adapted from Glarborg et al.[3], but all reaction subsets have been subjected to extensive review and the latest updates from the literature on rate constants and thermodynamic properties have been implemented with special notice on pressure dependent reactions.

High Pressure Flow Reactor

The experimental setup consists of a laboratory–scale high pressure flow reactor designed to simulate homogeneous gas phase chemistry at pressures from 10 to 100 atm and temperatures up to 650 °C. The detailed design was prepared during the Spring 2004 by Technician Jørn Hansen and Christian L. Rasmussen. Construction and preliminary tests were conducted during the Autumn 2004 by the author and M.Sc. student Anja E. Rasmussen. M.Sc. Anja E. Rasmussen continued to work with the setup during her subsequent employment as a research assistant until the end of August 2005. At this time, experimental results were achieved that were both reproducible and consistent with theoretical expectations.

The homogeneous reaction takes place in a tubular flow reactor made of quartz to minimize surface reactions (i.d. 8 mm, o.d. 10 mm). The reactor is enclosed in a stainless steel tube (i.d. 22 mm) that acts as a pressure shell. A pressure control system delivers N_2 to the shell–side of the reactor to obtain a pressure similar to that inside the reactor, thus avoiding devastating pressure gradients across the fragile glass. The steel tube is placed in an oven with three individually controlled electrical heating elements that produce an isothermal reaction zone (±5 °C) of approx. 0.5 m. The reactor temperature is monitored by thermo–couples positioned inside two steel thermo pockets placed in the void between the quartz reactor and the steel shell.

Reactant gases are premixed before entering the reactor. The flow rates are regulated by high pressure differential mass–flow controllers. All gases used in the experiments are high purity gases or mixtures with certificated concentrations. The reactor pressure is controlled by a pneumatic pressure valve positioned after the reactor. The pressure valve reduces the pressure to atmospheric level prior to product analysis that is conducted by on–line GC–TCD/FID and a NO_x chemilumescence gas analyzer. The downstream section of the system is gently heated to avoid condensation of potential condensible components before product analysis. The typical accuracy of the NO_x measurements is ±10 to 15 ppm. The GC has three operational columns (DB1, Porapak N and Molesieve) that allow detection of hydrogen (H_2), nitrogen (N_2), oxygen (O_2), carbon monoxide (CO), carbon dioxide (CO_2), most hydrocarbons and oxygenated hydrocarbons, nitromethane (CH_3NO_2), sulphur dioxide (SO_2) and hydrogen sulfide (H_2S). The relative uncertainty of the GC measurements is typically 2–5 % depending on the applied calibration gases.

Experimental data are obtained as mole fractions as a function of the reactor temperature measured at intervals of typically 25 °C. Each measurement represents the steady state concentration at a constant temperature, pressure and flow rate. This makes the residence time depend solely on the temperature.

Figure 2 shows examples of experimental results from the high pressure flow reactor and the comparison with predicted concentration profiles from the developed DCKM.

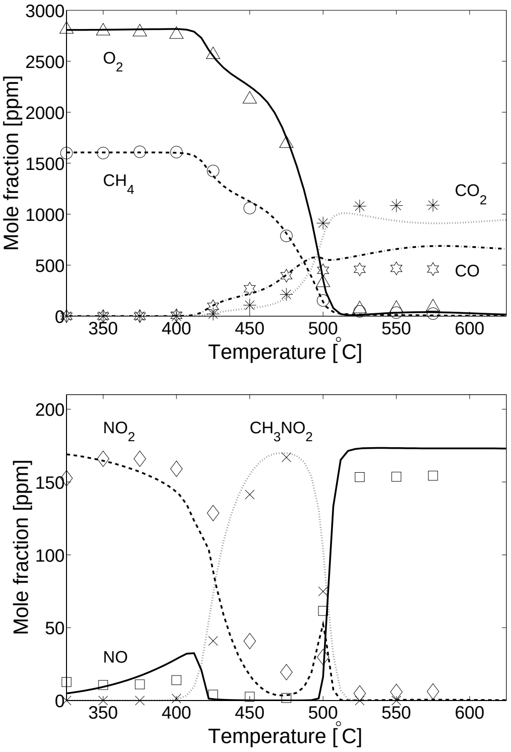

Figure 2: Concentration profiles as a function of the reactor temperature from N_2–diluted $CH_4/O_2/NO_X$ experiment at 100 atm, $\phi = 1.14$ and a constant flow rate of 3 NL/min. Comparison between experimental (points) and modeling (lines) results.

References

[1] Arutyunov, V. S.; Basevich, V. Y.; Vedeneev, V. I. *Ind. Eng. Chem. Res.* **1995,** *34,* 4238–4243.

[2] Kee, R. J.; Rupley, F. M.; Miller, J. A. "*Chemkin II: A Fortran Chemical Kinetics Package for the Analysis of Gas Phase Chemical Kinetics*", Sandia Report SAND89–8009B.UC–706, Sandia National Laboratories, Livermore, CA, USA, 1989.

[3] Glarborg, P.; Alzueta, M. U.; Dam-Johansen, K.; Miller, J. A. *Combust. Flame* **1998,** *115,* 1–27.

Jan Kamyno Rasmussen
Address: Building 227, Room 210
Phone: +45 4525 2801
Fax: +45 4593 2906
e-mail: jkr@kt.dtu.dk
www: http://www.kt.dtu.dk

Supervisors: Sten Bay Jørgensen, KT
Henrik Madsen, IMM
Henrik Steen Jørgensen, Novozymes A/S

Ph.D. Study
Started: March 2003
To be completed: August 2006

Datadriven and Mechanistic Model based Control and Optimization of Fed-Batch Fermentations

Abstract

Fed-batch processes are widely used in chemical and biochemical industry. Fermentations in biochemical industry are most often carried out as fed-batch processes. Operation of these processes is not possible using standard regulatory control schemes because of their non-linear nature and limitations in the production equipment. In this project a methodology for control and optimization of such processes will be developed based on the use of mathematical models.

Introduction

Fermentation processes are commonly used in biochemical industry for production of a wide variety of products. The true nature of these processes is rarely fully understood which makes the implementation of efficient control schemes very difficult. First principle engineering models are not used because the limited knowledge about the processes would make them very time consuming to develop.

Another promising strategy is to develop datadriven models entirely based on data from actual fermentations. When knowledge about the process is available a hybrid modelling approach to extract pertinent information from data can be applied.

The purpose of modelling these processes is to develop control structures that ensure uniform operation and optimize the productivity of the process.

This project is a part of the Novozymes Bioprocess Academy which is a newly established cooperation between Novozymes A/S, The department of Chemical Engineering and Biocentrum at DTU.

Process studied

The process studied is fermentation of the filamentous fungi *Aspergillus oryzae* for production of the enzyme amylase. The fermentation is initiated by transferring the contents of a seed tank to the main fermentation tank when a certain transfer criterion has been satisfied. The main fermentation tank contains an initial amount of substrate and the main fermentation process starts immediately after inoculation. The main fermentation is carried out in a batch and fedbatch phase. When the initial substrate has been consumed by the microorganisms the fedbatch phase is initiated. Feed dosing is started at a low level and increased to its final value within a certain time span. The fedbatch phase continues for the rest of the fermentation process.

The fermentors are equipped with sensors for online measurements of different variables but some values are only available as offline measurements which makes closed loop control more difficult and requires a more accurate model for predicting the variable values.

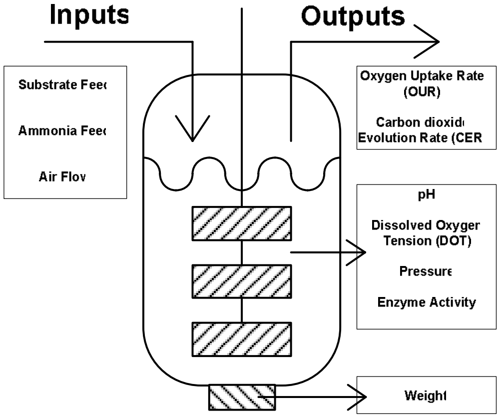

Figure 1. Sketch of fermentor used in the fermentation process

Specific Objectives

The objective of this project is to develop a methodology to identify mathematical models which can predict the behaviour of fed-batch fermentations in biochemical industry. Based on the identified models it is possible to control the fed-batch process. The models may also be developed for optimizing the process performance. The results of the models will be validated against experimental data obtained on the plant and a control structure based on the models will be implemented in a pilot plant for validation purposes.

Two different modelling strategies will be used for this purpose: Black-box modelling and grey-box modelling.

Black-box modelling

Black-box modelling is also referred to as datadriven modelling. The advantage of datadriven modelling is that only limited prior information about the process is required. The disadvantage is that the resulting models do not have an immediate physical interpretation and can not directly provide information about the biological state of the fermentation process.

A methodology for generation of such models has already been developed in earlier projects [1]. The framework is called “Grid of Linear Models” (GoLM) and it has been shown that this kind of datadriven models is able to account for disturbances that occur in the process. The methodology divides the duration of the entire batch into time steps, termed grid points. A linear time invariant model is fitted to each grid point and each model describes the behaviour of the process between two grid points. The combination of these linear models results in a model which covers the entire time span of the fermentation and approximates the highly non-linear behaviour of the process. The principle behind this methodology has been sketched in figure 2.

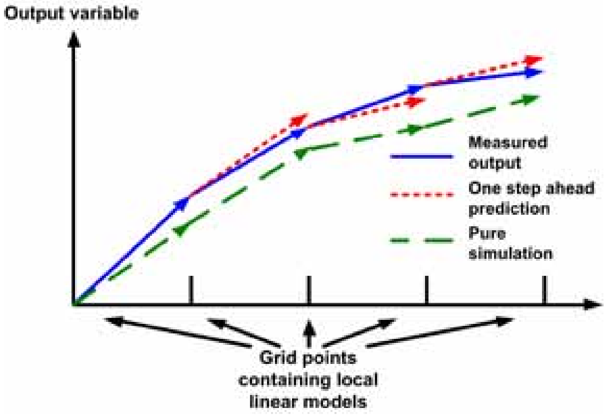

Figure 2. Illustration of the principle behind the GoLM modelling framework

Two types of simulation is shown in figure 2. One step ahead prediction is a prediction for the successive grid point based on the information available at the current grid point. Pure simulation is a prediction of the entire batch based only on the information available at the beginning of the batch (t=0). The GoLM modelling framework models deviations from a given reference trajectory. A reference batch therefore needs to be specified before a simulation can be carried out. Based on a given reference batch and a trajectory for the input signal/signals exerted on the system all the output variables included in the model can be simulated.

Successful application of data-driven models shows that the data contains sufficient information to predict the behaviour of future batches.

A GoLM model has been identified based data from 37 historical batches from a production plant. The duration of the entire batch has been divided into 112 grid points. One hour intervals have been used for the first 60 hours and 2.5 hour intervals have been used for the last 130 hours. The finer division in the beginning of the process is due to the dynamic batch phase. Here strongly varying behaviour is observed as opposed to the fed-batch phase where the process is less dynamic.

The model contains 7 outputs and 1 input. These are given in table 1.

Table 1. Output variables and their sampling rates used for the GoLM model identified.

Output variable	Sampling rate
Dissolved O_2 tension	10 minutes
Enzyme concentration	24 hours
Weight	10 minutes
O_2 uptake rate	10 minutes
CO_2 evolution rate	10 minutes
Ammonia flow	10 minutes
Air flow	10 minutes

Most of the variables are available as online measurements but the enzyme activity, which can be regarded as the quality variable, is only measured once a day.

Simulations based on this GoLM model are presented in the following.

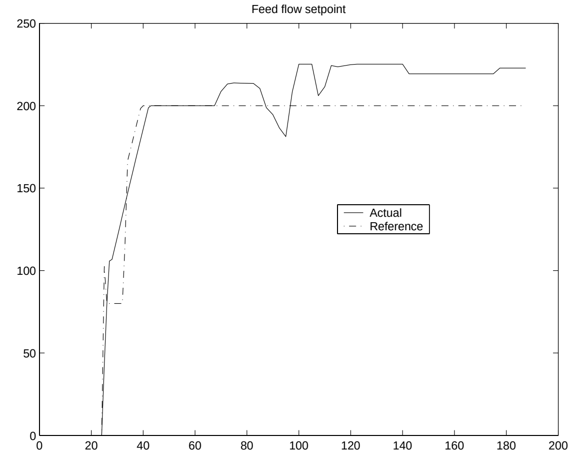

Figure 3. Feed flow set point (input variable) used for GoLM model. Actual: simulated trajectory. Reference: Trajectory used in the reference batch.

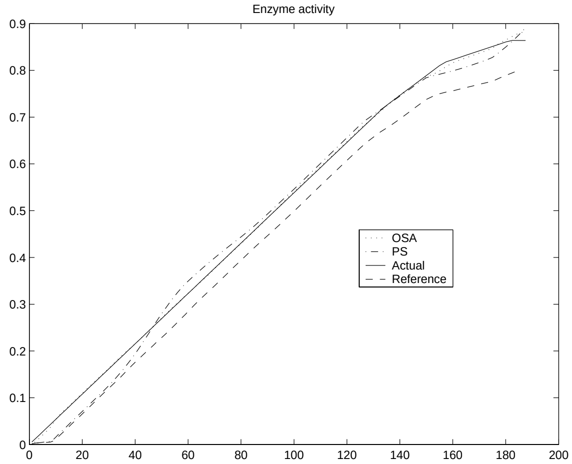

Figure 4. Enzyme activity predicted by GoLM model. OSA: One step ahead prediction. PS: Pure simulation. Actual: Simulated batch. Reference: Reference batch.

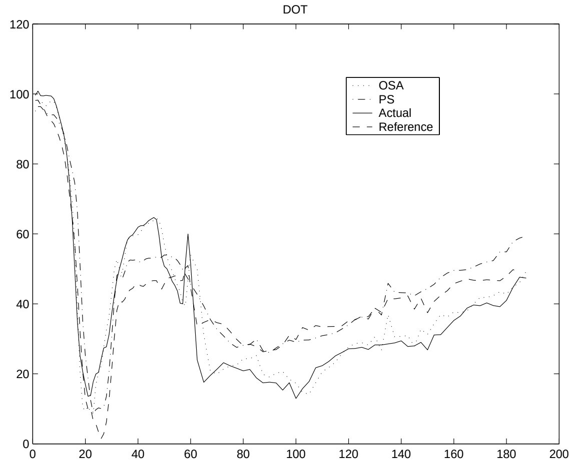

Figure 5. Dissolved oxygen tension predicted by GoLM model. OSA: One step ahead prediction. PS: Pure simulation. Actual: Simulated batch. Reference: Reference batch.

The model generally provides good predictions of the final enzyme concentration and it is able to catch much of the dynamics occurring in the process.

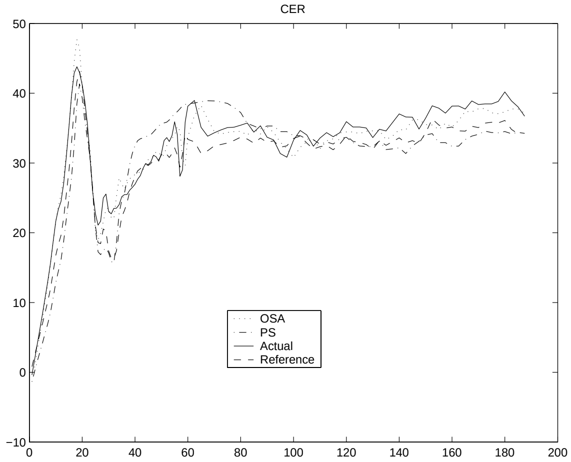

Figure 6. Carbon dioxide evolution rate predicted by GoLM model. OSA: One step ahead prediction. PS: Pure simulation. Actual: Simulated batch. Reference: Reference batch.

Grey-box modelling

In the grey-box modelling framework knowledge about the micro-organism and how the process is carried out is combined with operational data in order to develop knowledge based models. A methodology for development of such knowledge based grey-box models has already been developed [2]. It is based on the use of stochastic differential equations which are well suited for combining first principle engineering models with data because they account for random uncertainty and noise.

One of the key ideas behind the grey-box stochastic modelling framework is to use all prior information for formulation of an initial first principles engineering model. Unknown parameters of the initial model are then estimated from experimental data and a residual analysis is carried out to evaluate the quality of the resulting model. The next step in the modelling cycle is the model falsification or unfalsification which aims to determine if the model is sufficiently accurate to serve its intended purpose. If the model is unfalsified the model development is completed assmuming that data are representative for the intended applications. In case of falsification the modelling cycle must be repeated by reformulating the initial model. In this case statistical tests can be used to provide indications of which parts of the model that are deficient. Nonparametric modelling can be applied to estimate which functional relationships are needed to improve the model.

If the developed model is sufficiently accurate it can be used for online monitoring of the process or serve as a software sensor for otherwise unobservable states. Furthermore it can serve as the process model for development and tuning of advanced multivariable controllers.

Model formulation

Initially a very simple first principles based model for the fermentation is proposed. Measurements show that only a small amount of enzyme is formed in the batch phase (before the substrate feed begins) and the two phases are therefore modelled separately. Only the batch phase is considered in the model presented here and it is assumed that no enzyme is formed in this phase of the process. If necessary this assumption can be changed in later iteration of the model. In order to keep the model simple further assumptions have been made regarding product formation and yields. It is assumed that substrate is converted to only carbon dioxide and biomass and that the yield coefficients for conversion of substrate and uptake of oxygen are constant. The assumed yield coefficients can therefore easily be calculated from information about the initial amount of substrate, the total evolution of carbon dioxide and the total uptake of oxygen. It has been shown that the biomass consists of both active and inactive regions [3] and [4] but due to the early stage of the cultivation all the biomass is considered as active. The specific growth rate, μ, and the oxygen mass transfer coefficient, k_La, are furthermore assumed constant.

The initial model is given by 3 types of equations. Stochastic differential equations, algebraic equations and observation equations.

Stochastic differential equations:

$$dx = \left(\mu x + \frac{x}{V}F_{evap}\right)dt + \sigma_1 dw_1 \qquad (1)$$

$$ds = -\left(\frac{1}{Y_{sx}}\mu x - \frac{s}{V}F_{evap}\right)dt + \sigma_2 dw_2 \qquad (2)$$

$$dc_{O_2} = \left(-r_{O_2}x + k_La\left(c_{O_2}^{sat} - c_{O_2}\right) + \frac{c_{O_2}}{V}F_{evap}\right)dt + \sigma_3 dw_3 \qquad (3)$$

$$dV = -F_{evap}dt + \sigma_4 dw_4 \qquad (4)$$

The states considered in this system are: biomass (x), substrate concentration (s), oxygen concentration (cO_2) and volume (V).

w_i are four independent Wiener processes with incremental standard deviations given by σ_i. These terms account for the noise on the system states.

Algebraic equations:

$$r_{O_2} = Y_{xo}\mu \qquad (5)$$

$$r_{CO_2} = Y_{xc}\mu \qquad (6)$$

Here the specific rates of oxygen consumption (rO_2) and carbon dioxide evolution (rCO_2) are given. These are modelled as being proportional to the specific growth rate, the proportional factors being the yield coefficients.

Observation equations:

$$OUR = r_{O_2}xV + e_1 \quad ; \quad e_1 \in N(0, s_1^2) \qquad (7)$$

$$CER = r_{CO_2}xV + e_2 \quad ; \quad e_2 \in N(0, s_2^2) \qquad (8)$$

$$DOT = \frac{c_{O_2}}{c_{O_2}^{sat}} \cdot 100\% + e_3 \quad ; \quad e_3 \in N(0, s_3^2) \qquad (9)$$

$$Volume = V + e_4 \quad ; \quad e_4 \in N(0, s_4^2) \qquad (10)$$

For the above modelling 4 variables are used from the experimental data sets. OUR is the Oxygen Utilisation Rate, CER is the Carbon dioxide Evolution rate and DOT is the Dissolved Oxygen Tension (oxygen concentration measured in percent of saturation). The volume is included directly in the model. e_i are independent white noise processes taken from a normal distribution with a mean of zero and standard deviation of s_i.

Paramater estimation and results

Experimental data are taken from three batches run in pilot plant at Novozymes A/S. All batches have been run inder similar conditions and using the same fermentation recipe. Parameters and corresponding standard deviations are estimated using a maximum likelihood method implemented in a computer program called CTSM (Continous Time Stochastic Modelling). The program solves the stochastic differential equations in continuous time and estimates parameters using discrete time measurements.

The initial parameter estimation shows that the uncertainties on parameters μ and k_La are very large and additionally the standard deviations of the Wiener processes in the equations for biomass concentration and oxygen concentration are significant. This shows that the assumptions of constant μ and k_La do not hold. In order to reveal the time variation of the two phenomena they are introduced as states and two stochastic differential equations are therefore added to the previous four:

$$d\mu = 0 + \sigma_5 dw_5 \qquad (11)$$

$$dk_La = 0 + \sigma_6 dw_6 \qquad (12)$$

The phenomena are assumed to be constant over time which is clearly not true, but the CTSM approach allows for subsequent estimation of the timewise behaviour of the phenomena and furthermore of their functional dependence of other states.

Table 2. Estimation results for batch 1 using eq. (1-12) with corresponding standard deviations of initial states.

Parameter	Estimate	Std. dev.
x_0	5.71E-01	1.30E-01
$cO2_0$	4.16E-04	3.16E-06
V_0	1.17E+03	4.54E+00
μ_0	1.62E-01	3.21E-02
k_La_0	9.51E+02	1.06E+02

Table 3. Estimation results for batch 2 using eq. (1-12) with corresponding standard deviations of initial states.

Parameter	Estimate	Std. dev.
x_0	9.51E-02	8.35E-02
$cO2_0$	4.18E-04	5.61E-07
V_0	1.17E+03	7.97E-01
μ_0	1.56E-01	2.97E-02
k_La_0	5.22E+02	6.76E+01

Table 4. Estimation results for batch 3 using eq. (1-12) with corresponding standard deviations of initial states.

Parameter	Estimate	Std. dev.
x_0	4.19E-01	1.55E-01
$cO2_0$	4.13E-04	8.26E-07
V_0	1.16E+03	4.10E-01
μ_0	1.41E-01	3.70E-02
k_La_0	1.04E+03	8.56E+01

Table 2 to 4 give estimates of the initial states in the model as well as uncertainty information (standard deviation). The initial substrate concentration is a known parameter and is therefore not estimated. It is seen that the initial estimates of cO_2, V and μ are similar for the three batches. The initial estimate of biomass (x) varies a lot from batch to batch suggesting that different amounts of biomass have been transferred to the main fermentation tank. The estimate on k_La is similar for batch 1 and 3 but only aproximately half the value in batch 2.

The estimates of the state noise terms are important because they give information on whether or not the model equations are correct. When a state noise term is insignificant it indicates that the corresponding SDE gives a satisfactory description of the particular state variable. Any model deficiencies present will be contained in the noise term. As long as the noise term is significant the corresponding SDE does not match with the experimental observations and should be modified

The estimates of the standard deviations of the state noise terms in the three batches investigated here (not shown) show that the parameters σ_1, σ_3, σ_5 and σ_6 are significant. This suggests that functional relationships related to x, cO_2, μ and k_La should be improved.

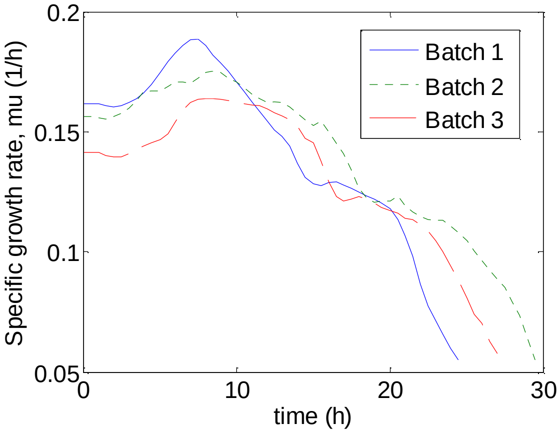

Figure 7. Estimate of specific growth rate, μ, as function of time.

The specific growth rate (Figure 7) is seen to exhibit a very similar behaviour in all three batches. In the beginning the growth rate increases to a maximum value around 7-10h, which can be explained by intracellular formation of proteins due to the new growth conditions in the batch phase. Thereafter a decrease appears and at a certain point (around 15-18h) the growth rate seems to level off for a few hours whereafter the decrease continues. This phenomenon is not simple to explain but is likely to be due to the cells producing biproducts. The evolution of μ as shown in the figure is only valid if the yield coefficients indeed can be assumed constant.

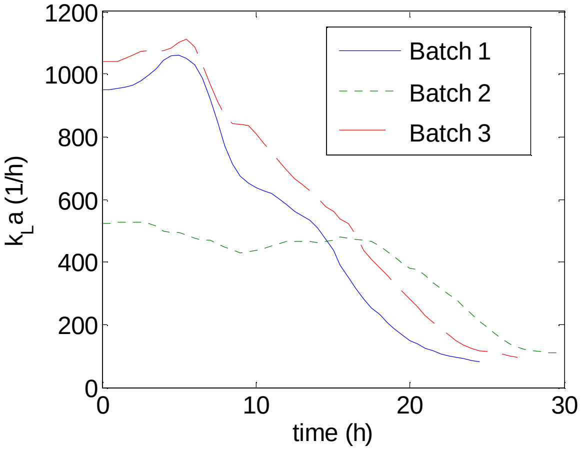

Figure 8. Estimate of oxygen mass transfer coefficient, k_La, as function of time.

The k_La (Figure 8) shows a very similar behaviour for two of the three batches. For batch 2 it is seen that the value is much lower in the beginning of the process than for the two other batches. This might be due to poor aeration or stirring conditions.

Conclusions

The limited knowledge about the nature of the fermentation processes used in industry makes it time consuming to develop first principle engineering models. An alternative is datadriven modelling based on process data. A framework for developing this kind of datadriven models has been applied on industrial data and it is seen that it can provide good predictions of the behaviour of the batch.

If some information about the process is available knowledge based grey-box models can be developed and efficiently used to uncover unknown functional relationships. A stochastic model has been combined with experimental data to obtain information on phenomelogical dependencies and uncertainties. Data from three batches run under similar conditions has been used and similar behaviour, in eg., the specific growh rates is observed. This indicates that this modelling methodology provides a sound basis for development of a model which can capture essential process dynamics.

The control structures used today are most often decentralized and lack the ability to account for limitations in the process equipment and micro-organisms. Furthermore industrial operation often relies on the operators experience and can not be guaranteed to be uniformly reproducible

In this project both types of modelling are being explored and the results will be validated against actual plant data.

References

1. D. Bonné, S. B. Jørgensen, Datadriven Modelling of Nonlinear and Time-Varying Processes, IFAC SYSID 2003, 2003.
2. N. R. Kristensen, H. Madsen and S. B. Jørgensen, 2004, A Method for Systematic Improvement of Stochastic Grey-Box Models, Comp. & Chem. Eng., 28/8, 1431-1449
3. T. Agger, A. B. Spohr, M. Carlsen and J. Nielsen, 1998, Growth and Product Formation of Aspergillus oryzae during Submerged Cultivations: Verification of a Morphologically Structured Model Using Fluorescent Probes, Biotechnol. Bioeng., 57, 321-329.
4. T. C.Zangirolami, 1998 Modeling of Growth and Products Formation in Submerged Cultures of Filamentous Fungi, Ph.D. thesis, Technical University of Denmark, Denmark.

Jakob Sloth
Adress: Building 227, Room 132
Phone: +45 4525 2923
Fax: +45 4588 2258
e-mail: jsl@kt.dtu.dk
www: http://www.chec.kt.dtu.dk

Supervisors: Søren Z. Kiil
Anker D. Jensen
Paul Bach, Novozymes A/S

Ph.D Study
Started: September 2004
To be completed: August 2007

Formation of Enzyme Containing Granules

Abstract

The droplet drying process which takes place inside a spray dryer is investigated using both a modelling based and an experimental approach. The modelling is carried out to quantify the phenomena controlling the drying kinetics and to achieve a fundamental understanding of morphology formation. Experiments are conducted to support the theoretical approach and validate developed models. The knowledge obtained by the investigations is used to meet product requirements such as mechanically stable particles and a narrow particle size distribution when spray drying enzyme containing slurries.

Introduction

Spray drying is of one several methods used in industry for conversion of a solution or slurry into a dried powder product. Spray drying is a flexible process which allows production of powders with many different properties such as a special particle size, particle morphology and residual solvent content. Enzymes for detergents are subject to spray drying because product handling is easier and enzyme stability is better than in liquid formulations.

In production of enzyme granules it is crucial that the formed particles have a low porosity to provide mechanical stability. Further, the particles must have a narrow size distribution to prevent segregation in the final detergent product. These particle properties must be obtained while avoiding thermal enzyme deactivation due to the high temperatures which exist in the spray dryer.

Though spray drying is used in numerous industrial applications fundamental understanding of drying kinetics and morphology formation remains limited.

Spray Drying and Single Droplet Drying

In spray drying a slurry or solution is fed to the drying chamber where it is atomized (figure 1). The formed droplets are mixed with a hot gas and the contact between the droplets and the gas causes the solvent of the droplets to evaporate, leaving dried particles. These particles may subsequently be separated from the gas stream, using a cyclone or a particle filter [1].

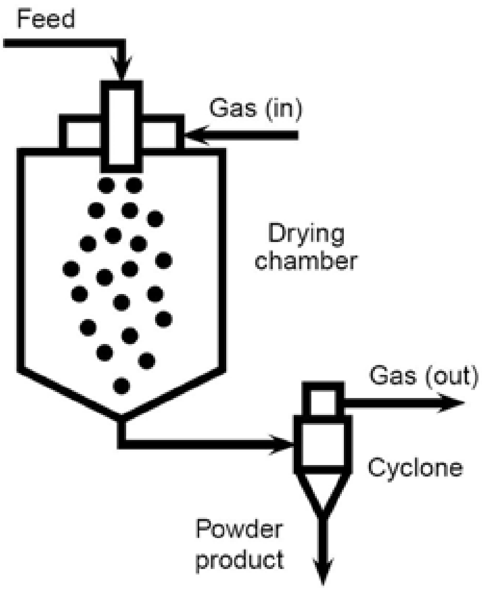

Figure 1: Spray Dryer

Droplets drying in a spray dryer undergo different periods with different rates of evaporation and droplet temperatures. Changes in droplet mass and temperature during the course of drying is shown on figure 2.

After atomization the droplet experiences initial heating followed by a period where the evaporation is fast because the solvent is readily available at the droplet surface. As drying progresses the droplet shrinks and the concentration of solute at the droplet surface increases. The concentration is a significant resistance to evaporation and the rate of mass change decreases. This gives rise to considerable droplet heating [2].

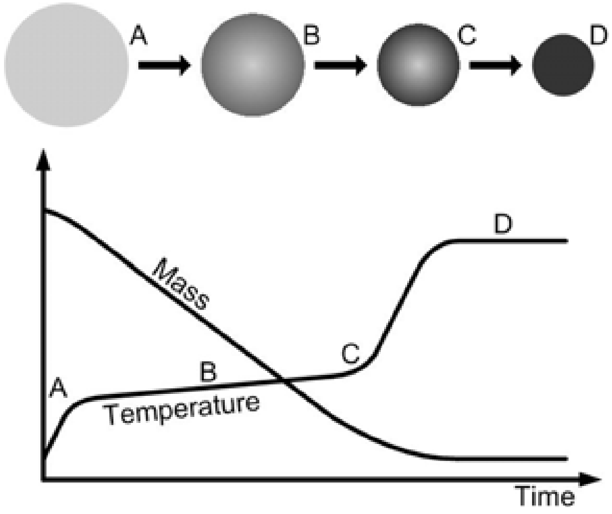

Figure 2: Mass and temperature change during the course of drying for a droplet in a spray dryer. The formation of a solid dense particle is shown - darker color indicates higher concentration.

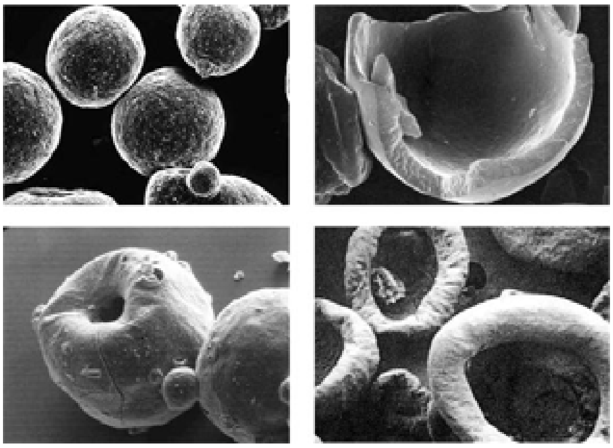

Figure 3: Examples of different morphologies of spray dried particles [3].

The droplet drying process is complex and several different morphologies may form depending on drying conditions and the nature of the droplet (figure 3).

Specific Objectives

In this PhD project the effect of formulation on the drying kinetics and morphology formation of enzyme-containing granules during spray drying is investigated and modelled. This knowledge is subsequently used in the design of improved granules (i.e. stable particles with uniform size distribution). The results must be applicable to industrial scale process equipment.

Methods

The project consists of two parts – an experimental and a theoretical part. In the experimental part the drying kinetics and morphology formation of drying droplets is investigated using a spray dryer pilot plant located at the Department of Chemical Engineering. The results are compared to experiments conducted with a commercial spray dryer at the Novozymes test facilities in Bagsværd, Copenhagen.

The experimental investigations are supplemented by theoretical modelling studies. A model for the droplet drying process is set up as the various phenomena controlling the process are quantified and the most important ones identified. Coupling the thermodynamic properties of the formulation mixture is important in order to achieve a fundamental understanding of drying kinetics and morphology formation. Further, computational fluid dynamic (CFD) simulations are conducted for the Novozymes spray dryer to map differences between this commercial unit and the pilot plant.

Below the different parts of the project are elaborated and current status of the work is given.

Experimental Work

The experimental apparatus (figure 4) named the Droplet Dryer used for drying kinetics and morphology investigations consists of two parts – a droplet generator and a drying tower. The droplet generator (called the JetCutter) is located at the top of the drying tower and generates droplets with a size of approximately 275 µm at about $0.4\,{}^{\mathrm{g}}/_{\mathrm{s}}$.

The droplets falls freely down the 6 m tall ($\varnothing$200 mm) drying tower in a cocurrent air stream. The temperature of the air stream may be set in the interval of $[25 - 250°\mathrm{C}]$ and the velocity in the interval $[0.1 - 1.0\,{}^{\mathrm{m}}/_{\mathrm{s}}]$. In the bottom of the tower the dry particles are collected in a steel bucket while the drying air is exhausted to the ventilation.

The drying tower is equipped with sampling ports at 12 different levels. Through these sampling ports the droplets may be collected in a small aluminum foil cup containing a small amount of paraffin oil. When the drying droplets hit the paraffin oil they immediately sink to the bottom of the oil because of a difference in density. This means that evaporation from the droplets is stopped. The samples collected are subsequently subject to Karl Fischer titration by which the droplet water content is found. Sampling at different levels in the tower allows for a drying profile to be determined because the droplet water fraction as a function distanced traveled in the tower is known.

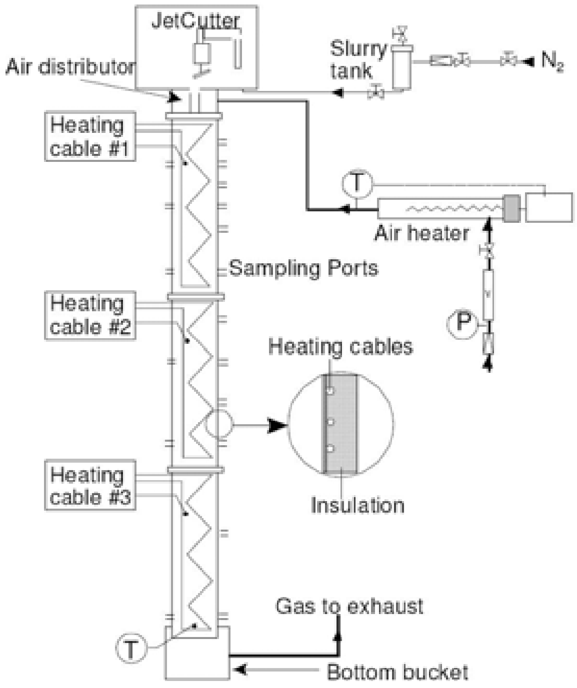

Figure 4: The Droplet Dryer – experimental apparatus for investigations of droplet drying kinetics and morphology formation

The slurry from which the droplets are formed consists of primary particles, solvent and usually a third component. The primary particles are insoluble particles (e.g. rice starch, Al_2O_3 or TiO_2) in the size range $[0.1 - 10\mu m]$. The solvent is always water while the third component may be inorganic salts, binders (dextrins) or viscosity enhancing compounds (e.g. carboxy methylcellulose).

Experimental Results

As described above the drying kinetics are determined as the percentage water evaporated as a function of the distance traveled by the droplets. An example for a result for the drying kinetics is given in figure 5. The slurry used contained water, $43.95\%_{wt}$ rice starch and $0.99\%_{wt}$ carboxy methylcellulose. The drying temperature was 150°C.

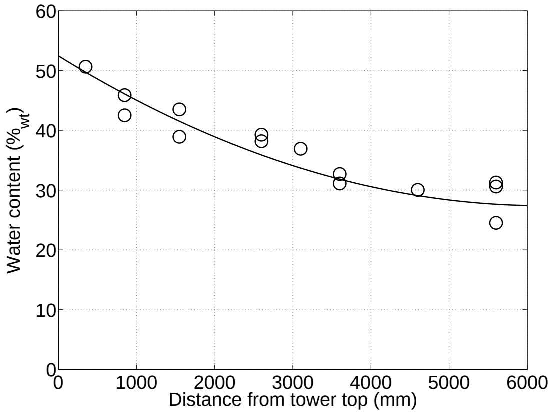

Figure 5: Kinetics for drying a slurry containing water, $43.95\%_{wt}$ rice starch and $0.99\%_{wt}$ carboxy methylcellulose. A trend line is inserted.

Also, the particles collected at the bottom of setup are investigated using scanning electron microscopy (SEM). Two examples of particles with different morphologies are shown in figure 6.

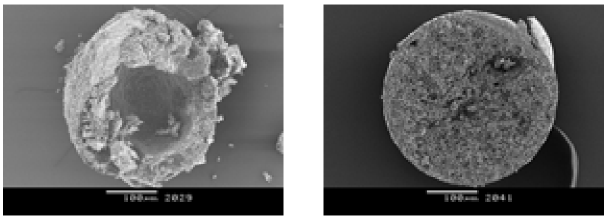

Figure 6: SEM pictures showing morphology of particles dried on the Droplet Dryer. Left: water, $40.21\%_{wt}$ rice starch and $9.24\%_{wt}$ Na_2SO_4. Right: water, $42.79\%_{wt}$ rice starch and $3.24\%_{wt}$ Na_2SO_4. In both cases the drying temperature is 150 °C.

Modelling results

The results from the Droplet Dryer are to be compared to experimental results from a commercial spray dryer located at the Novozymes test facilities in Bagsværd, Copenhagen. To achieve a fundamental understanding of the drying process inside the commercial spray dryer CFD-simulations are conducted using the FLUENT® software.

Figure 7 shows a simulation of the air flow field inside the spray dryer. The air enters the so called air distributor at the top of the dryer. It is then forced down the funnel part of the distributor into the drying chamber. Inside the drying chamber the air moves rather chaotically before exiting in the bottom of the dryer.

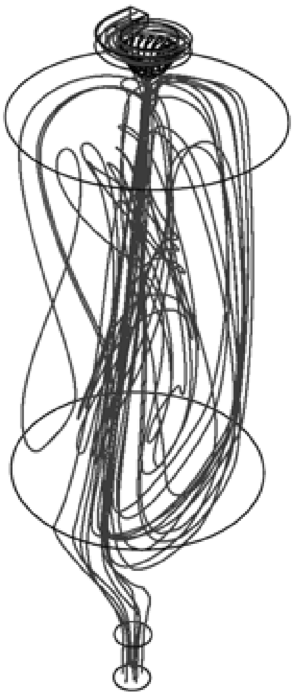

Figure 7: CFD-simulations of the air flow field inside the Novozymes spray dryer.

Further Work

Further work is to include theoretical modelling of the drying kinetics and morphology formation. The model will be compared to the experimental results from the Droplet Dryer. A theoretical model will give a better understanding of the phenomena involved in the drying process.

Also, further work is to include conduction of experiments using the Novozymes spray dryer. These experiments will clarify how well drying in the Droplet Dryer corresponds to drying in a commercial spray dryer. Also, these experimental data may be used for validation of the model.

Acknowledgments

The Novozymes Bioprocess Academy is acknowledged for financial support.

References

1. K. Masters, Spray Drying Handbook, 5th ed., Longman Scientific and Technical, 1991.
2. S. Nesic & J. Vodnik, Kinetics of Droplet Evaporation, Chem. Eng. Sci., 46, 1991, pp. 527-537.
3. D. E. Walton & C. J. Mumford, Spray Dried Products – Characterization of Particle Morphology, Trans IChemE, 77, 1999, pp. 21-38.

List of Publications

1. J. Sloth, A. Jensen & S. Kiil, Development and Validation of a Model for Drying Kinetics of Droplets in a Spray Dryer, Oral Presentation at the 2nd EFCE Congress on Product Technology, Groningen, Holland, November 22nd 2004.
2. J. Sloth, S. Kiil, A. Jensen, S. K. Andersen, K. Jørgensen, H. Schiffter & G. Lee, Model based analysis of the drying of a single solution droplet in an ultrasonic levitator, Chem. Eng. Sci., 2005, *Accepted for publication*
3. K. Jørgensen, A. Jensen, J. Sloth, K. Dam-Johansen & P. Bach, Comments to "Analysis of constant rate period of spray drying of slurry" by Liang et al., (2001), Shorter Communication, Chem. Eng. Sci., 2005, *Accepted for publication*

Vipasha Soni
Address: CAPEC, Dept. of Chemical Engineering
Building 227, Office 264
Phone: +45 4525 2910
Fax: +45 4593 2906
e-mail: vso@kt.dtu.dk
www: http://www.capec.kt.dtu

Supervisors: Rafiqul Gani
Gunnar Jonsson
Jens Abildskov

Ph.D. Study
Started: November 2004
To be completed: October 2007

Structural Design of Polymers for Membrane Based Separation Processes Using Reverse Simulation Approach

Abstract

In separation processes involving polymeric membranes one is interested in the design of new structured polymers that can match the desired degree of separation for the specified separation task. A reverse approach where the optimal polymeric membrane together with a list of candidate polymers all of which satisfy defined design (permeability) targets, is presented. The polymers are represented by their repeat units as well as their microscopic structure. The new method employs the permeability properties of a polymeric system, its relation to microscopic and/or chain conformation, as well as the separation task, to design the membrane based separation process as well as the polymeric membrane.

Introduction

The membrane separation technology is currently receiving increased attention and enjoys numerous industrial applications. It has the potential to replace conventional processes like distillation and other energy intensive processes to produce high quality products with greater flexibility in design or operation at partial capacity. The highlight of this work is simultaneous design of the membrane based separation process and of the polymeric membrane. This can be achieved by first defining the design targets through the properties of the polymer for the specified separation task (step 1), and then finding (designing) polymers that match the property targets (step 2).

Theoretical background

The basic design problem is to define the design parameters that affects any given membrane based separation and to identify which of these are important in order to design the separation process. Each design problem depends on variables such as the system properties ($\underline{S}$), mixture inlet variables ($\underline{I}$), outlet conditions ($\underline{O}$) and membrane properties ($\underline{P}$). Membrane properties in turn depend on the microscopic structural parameters ($\underline{S}^P$) of the polymer that is used as the membrane. The first step is to develop a process model of the membrane process in terms of these variables, where both $\underline{P}$ and $\underline{S}$ are to be determined. This kind of problem requires generation of alternatives in terms of $\underline{S}$ and $\underline{P}$ in order to achieve a desired degree of separation defined through ($\underline{O}$) for any given inlet concentration ($\underline{I}$) of the feed mixture. This means that the feasible alternatives for operational parameters like temperature, pressure, flowrates and polymer (which includes polymer repeat unit, number of repeat units and branching) must be found. We are trying to slove this problem using reverse design approach.

Reverse design approach

In membrane based separation processes, using polymers as the separation media it is important to find or design the polymers that can assure the desired separation standards for a specified mixture. The commonly used forward approach, is essentially a trial and error procedure. A polymer is chosen/designed and the properties for the polymer-mixture pair are calculated using an appropriate polymer property model. Inserting this polymer model in the membrane process model the product purity is predicted and this procedure is repeated until the desired purity is obtained. This is an iterative procedure where for each polymer, all the steps need to be repeated. In contrast to the forward approach, a reverse approach is employed in this work (shown in Fig. 1) according to which the membrane process model is used to calculate the polymer properties (design targets) that are needed to achieve the desired separation and product purity while any number of polymer property models (including databases) are used to find the polymer structural design that matches the calculated design targets. In this way, the membrane process model does not need a polymer property model, since the properties are the unknown variables. On the other hand, many polymers may be designed (found) without having repeatedly to solve the membrane process model coupled with the corresponding polymer property model.

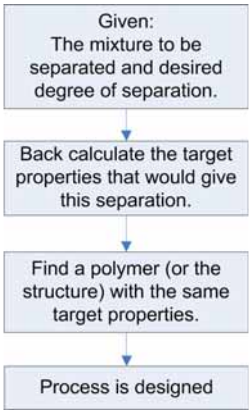

Fig. 1 Reverse approach

The procedure requires that in the first step the target properties are calculated and then polymers corresponding to these properties are found. This can be done mainly by three ways: I. Making an extensive literature search to find out polymers that matches the targets; II. Finding out monomer units using group contribution methods; III. Finding out microscopic structural parameters using property models. Advantages of this approach include a lot of saving of computational efforts as in the first step, where target values of the properties are calculated, there is no need to incorporate the property model, reducing thereby the problem complexity. Note that, permeability calculations in pervaporation process generally need diffusivity and solubility data. Diffusivity and solubility of a component through a polymer can be predicted using a group contribution method for example. Now these calculations depend on the composition, temperature and pressure at each spatially discrete point of the membrane module. So, incorporating them in the membrane model could be fairly complicated.

Membrane based gas separations

Process Description:

Membrane gas separators are separation units which split a given gas stream into two product gas streams, a high pressure retentate stream and a low pressure permeate stream. The membrane provides a selective mass transfer layer. Due to difference in chemical potential the species permeate through the membrane material at different rates [1]. Polymeric membranes are normally asymmetric in shape, i.e., a thin active membrane layer is laminated on a highly porous support layer giving mechanical support against the large pressure gradients applied in practice. Pressurized feed gas is normally fed to the shell side and the components permeate at different rates to the fibre bore. The retentate gas that is depleted in fast permeating components is withdrawn at essentially the feed pressure. In this work a non-porous membrane is being considered.

Mathematical models

Membrane gas separation model

Mass transfer in gas separation membrane: The mass transfer mechanism in the nonporous membranes is a combination of thermodynamically (solution) and kinetically (diffusion) controlling phenomena and the underlying model is called solution-diffusion model. According to this model, gas separation with membranes occurs via a pressure driven diffusion [2]. From thermodynamics, diffusion process occurs only if chemical potential (μ_k) of diffusing species *k*, along the diffusion path is negative. The change of chemical potential across the membrane from the feed to the permeate is therefore given by, where the difference in fugacities provide the driving force for the transport of gas molecules across the membrane.

$$\mu_{Pk} - \mu_{Rk} = R_g T \ln\left(\frac{f_{Pk}}{f_{Rk}}\right) \qquad (1)$$

Diffusion is a kinetic process and hence cannot be completely described by thermodynamics. The one-dimensional flux N_{Mk} of component *k* through a nonporous polymer membrane is given by Fick's first law (assuming constant diffusivity). Inserting the phase equilibrium relation describing the solution equilibrium, the equation becomes:

$$N_{Mk} = -D_k(c)\frac{dc_k}{dl} \Rightarrow N_{Mk} = \frac{D_k}{\delta}(c_{Rk} - c_{Pk})$$

$$= \left(\frac{D_k S_k}{\delta}\right)(x_k \phi_{Rk} P_R - y_k \phi_{Pk} P_P) \qquad (2)$$

The product of diffusivity D_k and solubility S_k is called *permeability*.

Material balance in membrane gas separators: Starting point of material balance is the continuity of component *k;* the balance is done over the membrane module (shown in Fig. 2). Inserting the expression for flux (Eq. 4) and writing the equation in dimensionless variables leads to,

$$\frac{du_k}{dX} - Q_k\left(\frac{z_k + s_k - u_k}{1 + S - U}\phi_{Rk} p_R - \frac{u_k}{U}\phi_{Pk} p_P\right) = 0 \qquad (3)$$

Where,

$$Q_k = \frac{P_k A_m P_F}{n_{FT}}, X = \frac{z}{L}, u_k = \frac{n_{PT}}{n_{FT}}, U = \frac{n_{PT}}{n_{FT}}, z_k = \frac{n_{Fk}}{n_{FT}}$$

$$p_P = \frac{P_P}{P_F}, p_R = \frac{P_R}{P_F}, U - \sum_{k=1}^{N_C} u_k = 0$$

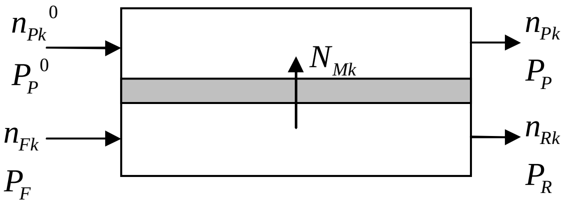

Fig. 2 Membrane module

The boundary condition in dimensionless form is $X = 0 : u_k = s_k$

Momentum balance in membrane gas separators: Applying symmetries of the system to the Navier-Stokes equation, and introducing dimensionless permeate pressure yields

$$p_P \frac{dp_P}{dX} + \frac{8\eta R_g T L n_{FT}}{\pi R^4 P_F^{\ 2} n_f} U = 0 \qquad (4)$$

Energy balance in membrane gas separators: Membrane gas separation is in general a non-isothermal process, which can be characterized by an isenthalpic expansion of the high pressure feed gas to the low pressure permeate conditions. A steady state integral energy balance around the entire membrane module assuming no work on the system yields

$$Q_{out} + H_f(T_f,P_f,n_f) - H_P(T_P,P_P,n_P) - H_R(T_R,P_R,n_R) \qquad (5)$$

In the case, where Joule-Thompson coefficient is very small, the separation can be considered isothermal. In that case $T_F = T_R = T_P$ and Q_{out} can be calculated from the heat balance.

Property models:

The property of the polymer that determines the extent of the membrane based gas separation is the permeability of the gas-polymer pair (q_K). Two types of property models have been considered in this work, one for each of the two methods given by II and III in section 2.

Correlation and prediction of gas permeability through a group contribution method: As stated above the permeability coefficient P_k, is comprised of both kinetic and thermodynamic factors which in principle depend on different aspects of the gas/polymer pair, i.e. $P_k = D_k S_k$

D_k is the diffusion coefficient of the gas through a polymer and it varies from polymer to polymer to a much larger extent as compared to the solubility coefficient S_k. The most important factor on which the diffusion coefficient and solubility coefficient depends is the free volume of the polymer. And so it is reasonable to correlate the permeability coefficient to the free volume. Extensive work has been done [3] to show the utility of the expression in the following form:

$$P_k = A_k \exp\left(-B_k / FFV_k\right) \qquad (6)$$

Where, A_k and B_k are constants for a particular gas k. The fractional free volume, FFV_k, has been defined as

$$\left(FFV\right)_k = \frac{\left[V - \left(V_0\right)_k\right]}{V} \qquad (7)$$

Here, V is the volume of the polymer which is obtained from experimental measurement of the polymer density at the temperature of interest. The term V_0 is the volume occupied by polymer chains. For any gas k:

$$\left(V_0\right)_k = \sum_{n=1}^{N} \gamma_{kn} \left(V_W\right)_n \text{ and } V = \sum_{n=1}^{N} \beta_n \left(V_W\right)_n \quad (8)$$

Where, γ_{kn} and β_n represents a set of empirical factors [4].

Correlating the gas permeability with structural parameters: Developing such property models requires information on how properties like density, diffusivity, solubility, etc., vary as a function of polymer structure and architecture (e.g., length and degree of branching). Acquiring this information through molecular modeling approaches is particularly appealing if accurate data can be obtained and since experimental measurements can be time consuming or expensive.

In general, a hierarchical modeling approach of three steps is followed: 1) Monte Carlo (MC) simulations to extract information about the density, radius of gyration and static structure factor (i.e. local packing of the polymer atoms) [5]; 2) Molecular Dynamics (MD) simulations to extract information about the diffusivity of the polymer chains and characteristic relaxation times; 3) Transition State Theory (TST) to extract information about the free volume, solubility, diffusivity and permeability of small gas molecules to a polymer matrix [6].

In this work, the structural, volumetric and dynamic properties of a rather simple polymer, those of polyethylene (PE), as a function of its molecular architecture, defined by branch length and branch frequency are used. Sufficient data about the equilibrium radius of gyration of linear and branched PE, the longest relaxation time, and the chain center-of-mass self-diffusion coefficient have been obtained in this case through a state-of-the-art Monte Carlo simulation algorithm. By analyzing these data using well established group contribution methods, closed-form analytical expressions have been developed capable of relating these properties to features of molecular structure and conformation of the polymer. For the case of PE considered here, the permeability of oxygen and nitrogen has been related to the molecular length (number of carbon atoms) of the main chain backbone. Enough data is available to generate property models for PE giving permeabilities as a function of N_{Carbon} in the straight chain:

$$\begin{aligned} P_{O_2} &= -\ln\left(\frac{N_{Carbon} - 67.42}{1.867e6}\right)7.66e-13 \text{ with } R^2 = 0.9989 \\ P_{N_2} &= -\ln\left(\frac{N_{Carbon} - 65.96}{1.212e7}\right)1.67e-12 \text{ with } R^2 = 0.9984 \end{aligned} \tag{9}$$

Illustrative example

The case study of air separation is illustrated in this work. Oxygen of more than 30% purity (for combustion) and more than 40% purity (for medical use) are required.

Problem definition: The reverse problem to be solved requires the following information: <u>Feed:</u> 200 mole/s air; $T_F = 298.15^0$C; P_F = 1 bar

<u>Permeate:</u> Desired Separation: X_{O2} = 50%; O_2 recovery = 0.0038;

Where, Recovery = moles of O_2 in permeate/moles of O_2 in feed

Based on this information, it was found that the polymer that would do the desired separation should have the following permeabilities:

$P_{O2} \geq 4$ barrer and selectivity ≥ 4.5

Results: 20 polymers from literature; 13 polymers from group contribution method and 9 polymers generated through molecular modeling were selected and plotted as shown in fig. 3 (selectivity vs. permeability). The horizontal and vertical lines show the property targets and all the polymers in the shaded region match the target properties. Hence, the validation step was performed only for these polymers (shown in Table 1). It can be seen that the separation tasks are achieved for the polymeric membranes.

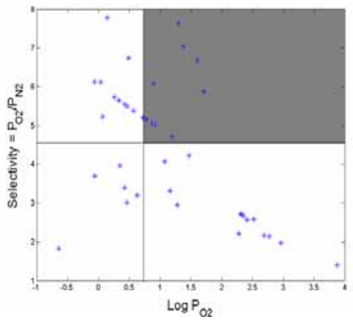

Fig. 3: All polymers on property target plots

No.	Polymer	% Purity	Recovery	Method
1	6FDA-6FpDA	54.24	1.40E-02	Literature
2	6FBPA/TERE	50.68	1.04E-02	Literature
3	HFPC	56.91	4.66E-03	GC
4	TMHFPC	55.95	7.10E-03	GC
5	TMHFPSF	56.86	4.81E-03	GC
6	TBHFPC	56.67	1.09E-03	GC
7	PE-78	59.02	5.19E-03	MM
8	PE-142	62.27	3.46E-02	MM
9	PE-500	63.77	2.09E-02	MM
10	PE-1000	65.69	1.73E-02	MM

Table 1: Validation for selected polymers

Conclusions

A general algorithm for design of polymeric membranes that includes the molecular modeling as an option has been highlighted through a case study that gave very promising results. From the calculations for the case study, it can be seen that it is comparatively easier to formulate and solve the models for the reverse approach. Furthermore, no trial and error procedure is involved while making it more efficient, robust and having a wider application range. Current and future work is extending the design methodology to other polymeric membranes-based separation processes as well as generating new data for other polymers for the microscopic-macroscopic polymer models.

References

1. R. Rautenbach and W. Dahm, 1986, J. Memb. Science, 28, 319-327
2. S. Tessendorf, R. Gani and M. Michelsen, 1999, Chem. Eng. Science, 54(7), 943-955
3. J. Park and D. Paul, 1997, J. Memb. Science, 123, 23-29
4. V. Krevelen, 1990, Properties of Polymers, Elsivier
5. N. Karayiannis, V. Mavrantzas and D. Theodorou, 2002, The American Physical Society, 88(10), 1-4
6. N. Karayiannis, V. Mavrantzas and D. Theodorou, 2004, Macromolecules, 37, 2978-2995

Piotr Szewczykowski

Address:	DPC, Dept. of Chemical Engineering, Building 423, Technological University of Denmark
Phone:	+45 4525 6814
Fax:	+45 4588 2161
e-mail:	pps@kt.dtu.dk
www:	http://www.polymers.dk
Supervisors:	Martin E. Vigild, KT Sokol Ndoni, Risø
Ph.D. Study	
Started:	February 2005
To be completed:	February 2008

Nano-Porous Materials from Self-Organizing Soft Matter

Abstract

Block copolymers are interesting materials from both scientifical and applicational points of view thanks to their self-assembly properties. Nano-porous materials are based on the selective removal of the minority component of self-organized block copolymer. The aim of this project is to design, create and find at least one application for such material.

Introduction

Self-organization in block copolymers is very interesting in relation to active nanostructuring. [1] The interplay between block immiscibility and connectivity generates a rich variety of nanophase-separated mesoscopic morphologies. Different morphologies can be obtained by controlling molecular weight and composition of block copolymers. "Living" anionic polymerization offers a readily feasible preparation of copolymers in a wide range of molar masses and chemical structures. [2,3]

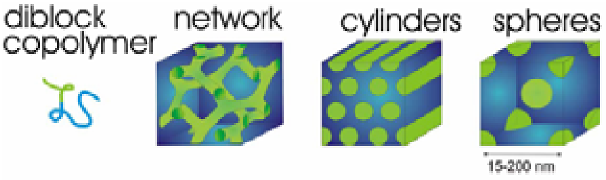

Fig. 1 Illustration of gyroid (network), cylindrical and spherical morphology of minority block (green) in AB diblock copolymer.

The main force which causes microphase separation is chemical incompatibility between different blocks. In the simplest case of diblock copolymers (Fig.1) there is only the issue of compatibility between A and B blocks. By multiplying Flory-Huggins interaction parameter x_{AB} (segment-segment interaction energy) and degree of polymerization N we obtain degree of segregation $x_{AB}N$. On the phase diagram for AB diblock copolymer we can observe changes of copolymer morphology depending on composition f for fixed $x_{AB}N$, where $f_A=N_A/N$ (Fig. 2). [4, 5]

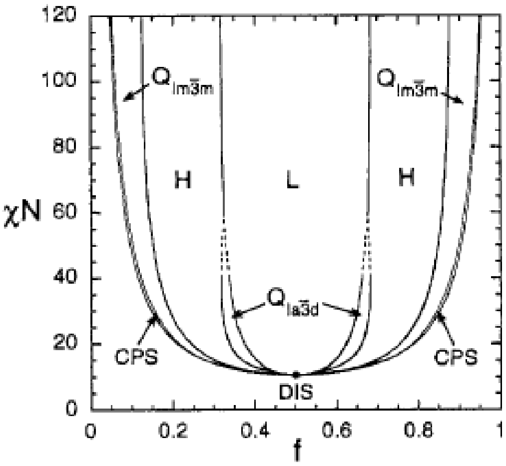

Fig.2 Phase diagram for linear AB diblock copolymers showing equilibrium morphologies: lamellar (L), hexagonal cylinders (H), gyroid *Ia3d* cubic (Q_{Ia3d}), bcc spheres (Q_{Im3m}), close packed spheres (CPS) and disordered (DIS). [6]

After removal of the minority block from the copolymer one can obtain nanoporous material with predictable morphology and narrow pore size distribution. Depending on morphology and possible alignment of internal structure the nanoporous materials can find very interesting applications like-high-surface area support for catalyst, templates for the synthesis of nanoobjects and for confined crystallization, membranes for selective transport. [7-11]

Method of producing nanoporous material

The processing steps for obtaining nanoporous material are presented:

Synthesis

Block copolymers, which are used in this project, are synthesised by anionic polymerisation. The studies started with polyisoprene – poly(dimethylsiloxane) (PI-PDMS). Also polybutadiene – poly(dimethylsiloxane) were synthesised and this material will also be investigated. Till now the composition of copolymer was designed to ensure the organization of minority block (PDMS) into cylinders.

Alignment

The minority block which form cylindric domains can be oriented in the parallel or perpendicular direction to the main sample surface. In the first case extrusion process is used.

Fig.3 Extrusion device for block copolymer alignment

It is not trivial to find the right way for loading the material into the extruder (to avoid air bubbles) and obtain uniform material after processing. Perpendicular orientation of the minority block is interesting for many possible applications. However, it is a challenge to find methods to obtain this. Electric field alignment and controlled solvent casting are promising methods for such processing

Crosslinking.

Dicumyl peroxide is used as a crosslinking agent. One of the aims of this study is to standardise the crosslinking process and be able to control the efficiency of the process and material's properties after crosslinking. It is important to finally obtain a copolymer with good elastomeric properties, but also crosslinked enough to "survive" the following etching process.

Etching

Two chemical compounds were used for etching process: HF (hydrofluoride) and TBAF (tetrabutylammonium fluoride). It is essential to find the most efficient (and safe) way for the etching process. Checking the loss of sample mass after etching is the first evidence for nanoporousity of the material.

Materials characterisation.

Size Exclusion Chromatography and Nuclear Magnetic Resonance is being used to characterise the synthesised polymers. Electron microscopy (Low Voltage Scanning Electron Microscopy), Small Angle X-ray Scattering and Small Angle Neutron Scattering are being used to characterise the finally etched (nanoporous) samples.

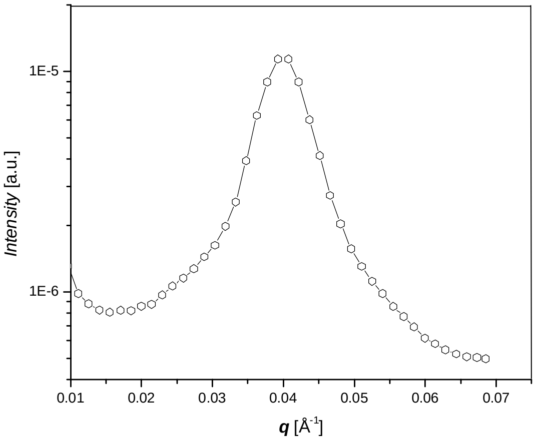

Fig.4 SANS experimental data. Plot shows intensity of scattering vs scattering vector q for a PI-PDMS based nano-porous material in d-Toluene. The peak is evidence for a nanoscale structure with a characteristic length scale of 15.7 nm.

References

1. M. S. Hansen, M. E. Vigild, R. H. Berg , S. Ndoni, Polymer Bulletin 51, (2004) 403-409
2. S. Ndoni, M. E. Vigild, R. H. Berg, J. Am. Chem. Soc. 125 (2003) 13366-13367
3. S Ndoni, C. M, Papadakis, F. S. Bates, K. Almdal , Rev. Sci. Instrum. 66 (1995) 1090-1095
4. F. S. Bates, G. H. Fredrickson, Physics Today 52 (2) (1999) 32-38
5. N. Hadjichristidis, S. Pispas, G.A. Floudas "Block Copolymers-Synthetic Strategies, Physical Properties, and Applications" A John Wiley & Sons, New York, USA, 2003
6. M.W. Matsen, F.S. Bates *Macromolecules* 29 (4) (1996) 1091-1098
7. K. A. Cavicchi, A. S. Zalusky, M. A. Hillmyer, T. P. Lodge *Macromolecular Rapid Communications* 25 (2004) 704-709
8. J. Rzayew, M. A. Hillmyer *Macromolecules* 38 (2005) 3-5
9. Huiming Mao, Marc A. Hillmyer *Macromolecules* 38 (9) (2005) 4038-4039
10. Huiming Mao, Pedro L. Arrechea, Travis S. Bailey, Bret J. S. Johnson, M.A. Hillmyer *Faraday Discussions of the Chemical Society* 128 (2005) 149-162
11. Johanna H. Wolf, Marc A. Hillmyer *Langmuir* 19 (2003) 6553-6560

Amra Tihic

Address:	DTU-Building 229/206-2800 Kgs. Lyngby
Phone:	+45 4525 2863
Fax:	+45 4525 2800
e-mail:	amt@kt.dtu.dk
www:	http://www.ivc-sep.dtu.dk
Supervisors:	Georgios M. Kontogeorgis Nicolas von Solms Michael L. Michelsen
Ph.D. Study	
Started:	May 2005
To be completed:	June 2008

Advanced Thermodynamic Tools for Computer-Aided Product Design

Abstract

The simplified perturbed-chain statistical associating fluid theory (PC-SAFT) is applied to phase equilibria of binary systems that include a variety of non-associating compounds. Pure-component parameters of compounds that are not available in the literature are estimated by correlating vapor-pressure and liquid-density data. 143 new PC-SAFT parameters are estimated for different families of nonassociating compounds (polynuclear aromatics, sulfides, cyclo- and fluorinated- hydrocarbons, etc.). Simplified PC-SAFT is able to successfully predict vapor-liquid equilibria for nonassociating systems. In a few cases, a small binary interaction parameter k_{ij} is needed for the satisfactory correlation of the experimental data.

Introduction

An efficient development of complex "soft" products such as polymers – paints, detergents, pharmaceuticals, and food ingredients requires the ability to find the molecular structures with the requested functionality and without undesirable side effects for the health or the environment. Both types of properties are related to the physical properties (thermodynamics) of the molecules and the mixtures involved. Predicting the product properties based on molecular structure is referred to as Computer-Aided Product Design. This type of modeling represents a challenge due to the complexity of molecules, the presence of various types of intermolecular forces (polarity, hydrogen bonding, etc.) and the frequent coexistence of many phases at equilibrium e.g. vapor-liquid-liquid or solid-liquid-liquid.

In the early 1990's the theory of Wertheim emerged from statistical thermodynamics. This method has been implemented into a new generation of engineering equations of state (EoS) such as CPA (Cubic-Plus-Association) and SAFT (Statistical Associating Fluid Theory).

The model development of the PC-SAFT EoS is described in detail by Gross and Sadowski [1], while the main equations of the simplified PC-SAFT are given by von Solms *et al*. [2].

Specific Objectives

The model parameters are typically estimated from vapor pressure and liquid density data over extended temperature ranges. This has been possible for small complex compounds for which such data are readily available. However for more complex compounds such as polymers, pharmaceuticals and pesticides extensive vapor pressures and liquid densities are not available and in many cases they can not be measured at all. As mentioned, this limits the applicability of the models.

The suggested solution to this problem is to develop a group contribution scheme for estimating the parameters of these EoS from low molecular weight compounds for which data is available and then extrapolate to complex molecules. However, to be able to do this, it is necessary to have an extensive PC-SAFT parameter table.

Results and discussion

This section presents modeling results for vapor-liquid equilibria of binary nonassociating systems obtained with the simplified PC-SAFT.

Figure 1 shows the binary phase diagram for the system methane-hexadecane. This relative asymmetric system is well correlated with kij=0.013.

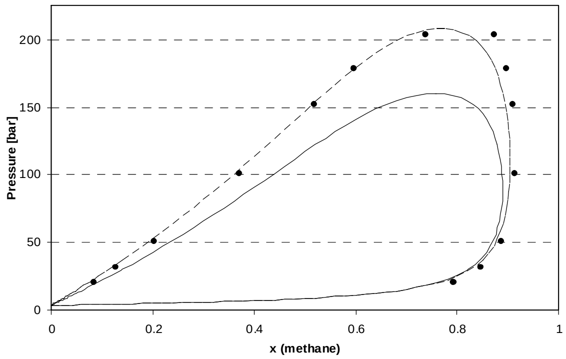

Figure 1. VLE correlations for C1-C16 at 623.15K, where symbols represent experimental data [3], and lines correspond to the correlations from simplified PC-SAFT with k*ij*=0. 013.

The solubility of nitrogen in octacosane is studied by simplified PC-SAFT using a single value of the interaction parameter kij=0.095. Figure 2 shows that the model represents very well the experimental data [4]. A trend of increasing solubility of nitrogen with increasing temperature and pressure is shown as well.

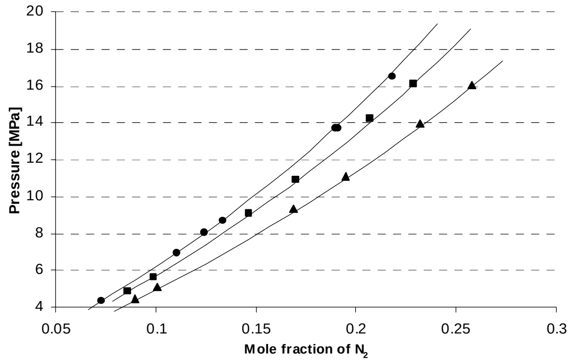

Figure 2. Solubility of nitrogen in octacosane at 323.2K [circles], 373.2K [squares] and 423.3K [triangles]. Lines correspond to the simplified PC-SAFT where k_{ij}=0.095.

One way to test the reliability of newly estimated PC-SAFT parameter is by predicting vapor-liquid equilibria at various conditions. Perfluoroalkanes is an important family of compounds with many applications. Figure 3 show the good agreement achieved between experimental data and simplified PC-SAFT estimations using new pure compound parameters for two perfluorohexane systems. The occurrence and location of the azeotrope are well captured by the model. These results show that the simplified PC-SAFT model allows the phase behavior of alkanes and perfluoroalkanes to be quantitatively estimated with the use of a single binary interaction parameter.

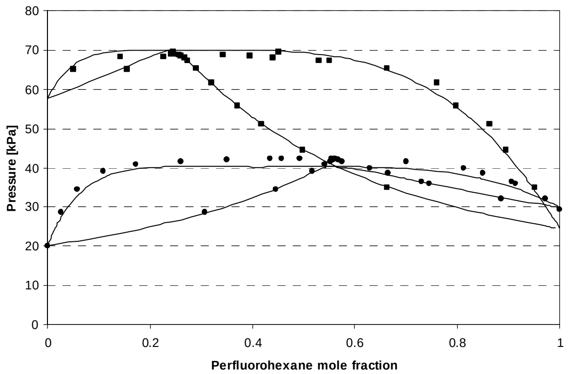

Figure 3. Vapor pressure of perfluorohexane + pentane (squares) at 293.15K and perfluorohexane + hexane (circles) at 298.65K, where symbols represent experimental data [5], and lines correspond to the correlations from simplified PC-SAFT with k_{ij}=0. 077.

Conclusions

So far, work in the project demonstrates that good agreement is obtained for light gases-heavy alkanes systems using a constant value of the binary interaction parameters.

The latest investigations justify the capability of simplified PC-SAFT in describing asymmetric systems.

Simplified PC-SAFT can successfully represent binary mixtures of alkanes and perfluoroalkanes by adjusting a temperature-independent interaction parameter. The same is true with binary mixtures of gases and perfluoroalkanes.

Generally satisfactory estimations of tested binary systems using newly estimated parameters (with or without k*ij*) are obtained.

Acknowledgments

The authors are grateful to the Danish Technical Research Council (STVF) for financial support of this work as part of a grant entitled "Advanced Thermodynamic Tools for Computer-Aided Product Design".

References

1. J. Gross, and G. Sadowski, Ind. Eng. Chem. Res. 40 (2001) 1244-1260
2. N. von Solms, M.L. Michelsen, and G.M. Kontogeorgios, Ind. Eng. Chem. Res. 42 (2003) 1098
3. H.M. Lin, H.M. Sebastian, K.C. Chao, J. Chem. Eng. Data 15 (1970) 82-91
4. J. Tong, W. Gao, R.L. Robinson, and K.A.M. Gasem, J. Chem. Eng. Data 44 (1999) 784-787
5. C. Duce, M.T. Tiné, L. Lepori, and E. Matteoli, Fluid Phase Equilibria 199 (2002) 197-212

Sylvain Verdier
Address: DTU - Building 229 – 2800 Lyngby
Phone: +45 4525 28 77
Fax: +45 4588 2258
e-mail: syv@kt.dtu.dk
www: http://www.ivc-sep.kt.dtu.dk

Supervisors: Erling H. Stenby (ehs@kt.dtu.dk)
Simon I. Andersen (sia@topsoe.dk)

Ph.D. Study
Started: May 2003
To be completed: May 2006

Experimental Study and Modelling of Asphaltene Precipitation Caused by Gas Injection

Abstract

The issues about asphaltenes are as wide and complex as the different aspects of science it deals with: colloidal science, surface phenomena, analytical techniques, chemistry, modelling of phase behaviour, thermodynamics, kinetics and characterization of a complex fluid. This work is an attempt to understand and describe a few of these aspects.

Introduction

Amongst the solid deposits occurring in the oil industry, asphaltenes might be the most studied and the less understood issue. The problems due to this heavy and polar fraction of petroleum are found in the reservoirs, in the wells, in the tubing or during the refinery processes. The colloidal behaviour of asphaltenes in crude oil, the lack of knowledge about its structure, the complexity of the aggregation, flocculation and precipitation processes - without mentioning the deposition - make this topic quite complex and interesting.

During the Enhanced Oil Recovery process, gas is injected in order to decrease the viscosity of the oil or to push it towards the well, whether it is miscible or not. However, this injection clearly modifies the composition and the conditions of the oil and asphaltenes have the tendency to flocculate and precipitate during such modifications.

There is no predictive tool so far since models are descriptive at the best. The technical solutions are expensive (injection solvent, cleaning pipes). Getting bottom-holes sample is quite expensive and their representation is often subject to debate. Thus, studying asphaltene precipitation during gas injection and trying to get more knowledge about asphaltene stability seemed relevant.

Specific Objectives

The objectives of this work were quite simple in appearance:

1. Study asphaltene precipitation in presence of gas (CO_2 for instance)
2. Identify, if any, the effects of pressure and temperature on the stability of recombined oils
3. Bring input about asphaltene precipitation by means of calorimetry
4. Measure input parameters used for the modelling of the asphaltene phase behaviour (namely the solubility parameters of oils and asphaltenes)
5. Test a model taking into account the aggregation based on a cubic equations

Results and Discussion

1. The asphaltene Phase Envelope (APE)

Accurate determination of the asphaltene phase envelope is closer to utopia than to reality. Uncertainties about such measurements have many origins, especially related to:

- *The sample*: how long has it been stored? In which conditions? How representative is it of the oil in the field?
- *The technique*: does it determine the **flocculation** (aggregation of asphaltenes) or the **precipitation** (when buoyancy forces can overcome Brownian forces - when particles are larger than $1\,\mu m$ [1] - agglomerates can settle out of solution)? How sensitive is it? When working with high pressure and live oils, is the sample flashed when filling the PVT cell? How is the cell cleaned?
- *The kinetics*: is the equilibrium reached?

In the literature, APE's are scarce but can be found though ([2-4] for instance). On these curves, the precipitation curve, as well as the bubble point, are present. Sometimes, the re-dissolution curve is plotted (low pressure at which asphaltenes go back to solution).

In this work, a novel high-pressure cell – developed at and by the Laboratoire des Fluides Complexes, Université de Pau, France - was used for the determination of the APE curves of two fluids [5]. The main advantages of this cell are: its small volume (from 2.6 to 13 mL), its absence of dead volume, the isobaric transfer of the gas, the isobaric filtration (used to check whether or not asphaltenes are precipitated).

The two fluids under investigation are respectively from Venezuela and Middle-East and both have asphaltene problems in fields. The filters have a $0.5\ \mu m$ pore size. The whole set-up is fully described in [6].

Figure 1 shows the influence of temperature on the onset of precipitation for the Venezuelan crude oil. Here, temperature tends to destabilize the asphaltenes since less CO_2 is required when temperature is increased. The same effect was seen in literature with CO_2 [7].

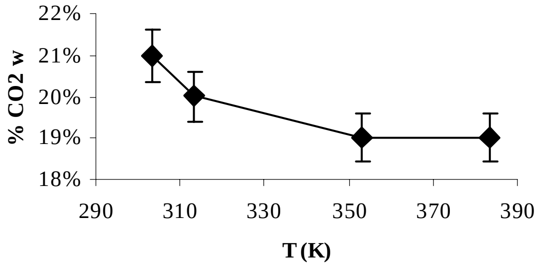

Figure 1: Influence of temperature on the onset (Venezuelan crude oil at 20 MPa with 19% CO2)

Figure 2 shows an APE determined for the crude oil from Middle-East.

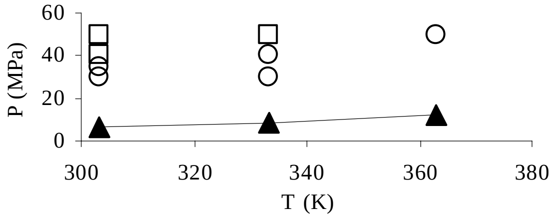

Figure 2: Asphaltene Phase Envelope of the Middle-East crude oil (18% CO_2)

(□, no precipitated asphaltenes; ○, precipitated asphaltenes; ▲, bubble point)

In this case again, asphaltene precipitate when temperature is increased. Thus, this technique enables a fast determination of asphaltene phase envelope. However, the kinetic effects are still to be determined. An optical device enabling the measurement of refractive index by reflection has been developed for this very cell [8] and, combined with the filtration technique, it will render these experiments even more reliable.

2. Temperature and pressure effects

The issue about asphaltene stability is our major concern. Asphaltene can precipitate during temperature, pressure or composition variations as said previously.

Literature abounds in the effects of temperature: they can be stabilizing or destabilizing [9]. There is no clear explanation but one could think about the effect of temperature on sterically stabilised colloids [10]. In this case, enthalpy stabilised colloids flocculate on heating while entropy stabilised ones on cooling. Resins are believed to adsorb on asphaltenes and peptize them, hence helping them to stay in solution. This could be an option.

The effect of pressure is more consensual since it is now agreed that asphaltenes precipitate by pressure depletion, i.e. that pressure has a stabilising effect [11-12].

The Le Châtelier's principle can help explaining those effects. Henri Le Châtelier stated that "every change of one of the factors of an equilibrium occasions a rearrangement of the system in such a direction that the factor in question experiences a change in a sense opposite to the original change" [13].

The equilibrium we are interested in is the following one:

$$Asphaltene(solution) \rightleftharpoons Asphaltene(precipitated)$$

If pressure is increased, the position of equilibrium will move so that the pressure is reduced again, i.e. the number of molecules is decreased or the volume is reduced. Experimentally, it is seen that solubility of asphaltenes in oil increases with increasing pressure. Thus, it means that the system decreases its volume when pressure is increased, i.e. the volume of the two-phase region is larger than the one of the one-phase region. To the authors' knowledge, there is no experimental evidence of a gain in volume during precipitation. However, by means of various EOS (CPA [14] and SAFT [15]), an increase up to 20 cm3/mole of asphaltene was calculated between the onset and the bubble point.

If temperature is increased, Le Châtelier's principle states that the position of equilibrium will move so that the temperature is reduced again. If the reaction is exothermic, the equilibrium will go to the left side when temperature is increased, i.e. asphaltenes will be more soluble. If not, the asphaltenes will be less soluble. As it was said previously, both stabilizing and destabilizing effects are found in the literature. Could it be that some asphaltene precipitations are exothermic and some others endothermic? Is it due to the solvent properties or to the asphaltenes themselves?

So, the Le Châtelier's principle relates the effect of pressure to molar volumes and the effect of temperature to the heat of precipitation. This tempting description of the problems needs experimental validation though.

3. Calorimetry and precipitation

The authors are not aware of any calorimetric evidence of heat of precipitation of asphaltenes except for one attempt made on a live oil [16]. In that study, a slight exothermic signal was observed during pressure depletion, though the signals are not that clear. Some interesting work has also been done with calorimetry and asphaltenes: exothermic heats of solution of asphaltenes in various solvents (from -20.2 up to -8.1 J/g) and endothermic peaks when temperature is increased by means of DSC [17] (various mixtures of crude oils with toluene and n-alkanes were studied). The last study concludes that the size of the endotherms might be linked to the ability of asphaltenes to precipitate.

One could intuitively believe that asphaltene precipitation should be exothermic since more bonds are created than broken but binding can be endothermic as well. Indeed, order/disorder transitions are endothermic since they are entropy-driven. For instance, examples of aggregation of polymers and surfactants [18] or polypeptides and proteins [19] are well described in literature, not to mention the sol-gel transitions. Experimental proofs are still needed to be able to conclude anything about asphaltenes though.

In this work, two different approaches were chosen:

- **Isothermal Titration Calorimetry**: this technique was used for asphaltenes in heptane-toluene solutions around the onset point. The experiments were carried at Kemiteknik.
- **PVT calorimeter**: a live oil sample was introduced in a PVT calorimeter at high pressure and both pressure and temperature were scanned. This set-up is located in the Laboratoire des Fluides Complexes (Pau)

The first method was tested on several varieties of asphaltenes and the same effects were detected. The experimental set-up is described in [20]. The procedure is simple: in the cell, a stable mixture toluene-n-heptane-asphaltene is mixed and n-heptane is injected until precipitation occurs. The onset was tested with another method, based on the absorbance of the solution [21]. As seen in figure 3, the onset is easily detected by the "noisy" variations around the heat signal due to dilution of toluene by n-heptane.

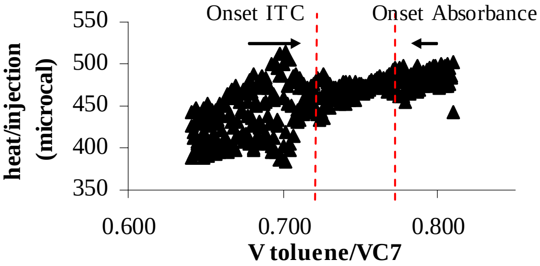

Figure 3:Calorimetric signal of the isothermal titration of an asphaltene solution

It is rather difficult to conclude of any exo- or endothermic precipitation though. Nonetheless, it seems to be the first calorimetric detection of asphaltene precipitation. The difference with the absorbance technique is probably due to the fact that the volume of the cell is constant (1.34 mL). Hence, when an injection is done, an equal volume flows over the top of the cell.

Other systems going through a phase transition were tested in order to qualify and understand a bit more asphaltene precipitation. The first model system is heptane-methanol, whose liquid/liquid equilibrium is well known. In many cases, asphaltene precipitation is modelled as a LLE so a similar heat signal could confirm this assumption. Figure 4 shows that the signal following the LLE is quite different.

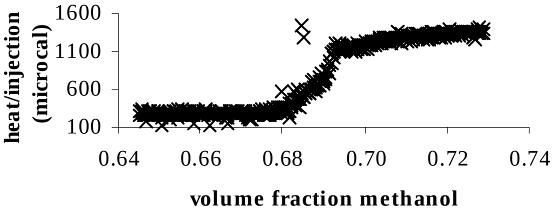

Figure 4: Calorimetric signal of the LLE heptane/methanol

The phase transition should happen for a volume fraction of methanol equal to 0.67 according to literature data. With this technique, it happens between 0.69 and 0.68. Other types of wellknown precipitations are currently investigated (AgCl(s), sterically stabilised colloids for instance). This should slightly lighten our knowledge about asphaltene precipitation.

The second technique with live oil gave interesting results as well. As seen in figure5, both calorimetric and volumetric signals were recorded during the scanning in temperature of the live oil. The pressure was kept constant at 80 MPa and the temperature going from 300 to 370 K.

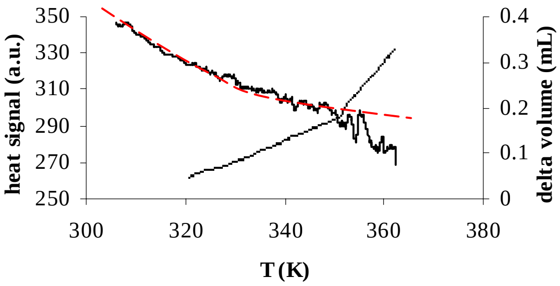

Figure 5: Calorimetric (curve going down) and volumetric (curve going up) signals obtained during the scanning in temperature of a live oil at 80 MPa

A continuous gain in volume was detected (0.1 mL for a total volume of 30 mL) - corresponding to change in thermal expansivity – as well as an exothermic signal. The observed phase transition is believed to be a precipitation and it causes changes in both thermal expansivity and heat capacity. Other concluding experiments were carried on and confirm this behaviour. A coming article will present these results.

4. Determination of solubility parameters

The phase behaviour of asphaltenic fluid has been modelled numerous times for the last twenty years: Flory-Huggins theory, Scatchard-Hildebrand, cubic EOS, SAFT, scaling equations, micellization models, and continuous thermodynamics to name a few of the attempts. But, as Porte at al. [22] state it, their capacities to predict the behaviour of asphaltenic fluids is generally poor. The failure of the modelling that has been done so far has many explanations:

- The lack of knowledge about asphaltene structure
- The difficulties lying in the fact that asphaltenes are a continuum of polar and heavy components
- The poor characterization of this fraction
- The approximations surrounding any characterization of a crude oil
- The difficulties surrounding any colloidal system
- The aggregation is said to be due to hydrogen bonding and the modelling of such bonds is difficult. Note that many properties of water cannot be modelled so far.

Thus, the engineer approach based on the solubility parameter seems to be rather satisfying, considering the number of unknowns and approximations.

For that matter, a different approach than the conventional one was used. Usually, the refractive index of the solution is measured and linked to the solubility parameter by a simple and linear relationship [23]. Indeed, the refractive index is only related to dispersion forces and is generally measured at ambient conditions. So, it was decided to measure the internal pressure, defined as:

$$\pi = \left(\frac{\partial U}{\partial V}\right)_T = T\left(\frac{\partial P}{\partial T}\right)_V - P = T\frac{\alpha_P}{\kappa_T} - P \qquad \textbf{Eq 1}$$

with U the internal energy, V the volume, T the temperature, P the pressure, α_P the thermal expansivity and κ_T the isothermal compressibility.

The relationship with the solubility parameter is as follows:

$$\delta^2 = \pi + \frac{A}{\rho} \qquad \textbf{Eq 2}$$

with ρ the density and A a constant.

The various derivations and relationships can be found in [24]. Thermal expansivity was determined by calorimetry measurements [25] within 2% uncertainty up to 30 MPa for pure compounds and isothermal compressibility by density measurements and derived with a modified Tait equation [24]. The uncertainty is within 3% for pure compounds. Thus, internal pressure was calculated and compared to solubility parameters from literature. The difference is within 1 $MPa^{1/2}$ for compounds without hydrogen bonds but much higher for ethanol for instance. Indeed, as mentioned by Bagley et al. [26], internal pressure only takes into account physical forces, i.e it can be represented as the sum of the polar and dispersion terms of the Hansen solubility parameter.

This method was applied to dead and live crude oils [27-28].

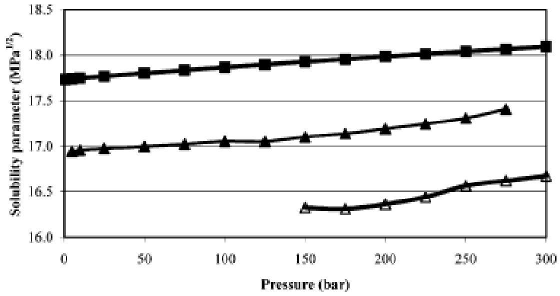

Figure 6: Solubility parameter of oil 1 at 303.15 K: (-Δ-) live oil 1, from internal pressure; (-▲-) dead oil 1, from internal pressure; and (-■-) dead oil 1, from the refractive index (from [28])

So, experimental determination of solubility parameters of live and dead oils can be performed as a function of pressure but the uncertainty (1 $MPa^{1/2}$ for pure compounds) is too high to enable a better modelling. Nonetheless, this work permitted a better definition of the solubility parameter and an alternative determination as well as the effects of pressure that have not been investigated in the literature.

The other task was the determination of the asphaltene's solubility parameter. So far, the techniques are based on miscibility [29], titration [21]), inverse gas chromatography [30] or correlations [31]. The method used here was already used for compounds of pharmaceutical importance [32]. The equation, based on the regular solution theory was slightly modified and is as follows:

$$\frac{\overline{V_{s2}} - V_{s2}^0}{\overline{V_{s2}}} = \frac{(\delta_1 - \delta_2)^2}{\pi_1} \qquad \textbf{Eq 3}$$

where $\overline{V_{s2}}$ is the partial specific volume of the solute, V_{s2}^0 its specific volume, δ_1 the solubility parameter of the solvent, π_1 its internal pressure and δ_2 the solubility parameter of the solute.

Density measurements were performed in order to determine the specific partial volumes of two asphaltenes in three different solvents (toluene, m-xylene and carbon disulfide). A molar mass of 1000 g/mol was assumed. Results are presented in table 1.

The values are within the expected range except for the solvent pair toluene/m-xylene. As it was explained in [33], the value of the internal pressure of toluene has a major impact on the results.

For the other solvent pairs, the following solubility parameters were found: 21.2 ± 0.3 $MPa^{1/2}$ for OLEO D and 22.4 ± 0.4 $MPa^{1/2}$ for A95 at 303.15 K and 0.1 MPa.

Solvents	**Solubility parameter ($MPa^{1/2}$)**		**Density (kg/m^3)**	
	OLEOD	**A 95**	**OLEOD**	**A 95**
Tol./m-xylene	28.2	28.7	1533	1657
Tol./CS2	**21.5**	**22.8**	**1092**	**1162**
CS2/m-xylene	**20.8**	**22.0**	**1088**	**1150**

Table 1: Solubility parameter and densities of the asphaltenes OLEO D and A 95 (303.15 K and 0.1 MPa)

As for the density, Rogel and Carbognani [34] measured the densities of 13 different asphaltenes at 298.15 K and they vary between 1.17 and 1.52 g/cm3. Thus, the values of 1.09 g/cm3 and 1.16 g/cm3 (respectively for OLEO D and A95) seem relevant, though slightly smaller.

Thus, experimental determination of solubility parameters for both oils and asphaltenes was succeeded.

5. A model for the aggregation

The idea is to establish a model able to describe and predict asphaltene precipitation, taking into account the association of asphaltene molecules into nano aggregates [35]. The precipitation occurs when the asphaltene phase is in equilibrium with the bulk phase (the crude oil). In spite of an often complex scheme and a large number of fitting parameters, most of models invoking association do not allow representation of the simple fact that the asphaltene nano-aggregates in terms of size are insensitive to dilution in good solvents or a change in solvent quality when the solution is far from the precipitation threshold. The description of the mechanism of nano-aggregation by these models depends on the balance between the energy of association in opposition to the dispersive term. Thus, in some cases, the aggregates tend to grow indefinitely or, in other cases, to disappear completely. The geometry of the nano-aggregates is very difficult to take into account by these models.

Regarding this difficulty, the description proposed in [22] seems to be an attractive alternative. This description is based on a simple idea: on one side, the forces involved in the colloidal aggregation and on the other side, those driving the precipitation are different in nature and strength. The aggregation is driven by strong specific forces and the size of the aggregates is limited for geometric reason; therefore the aggregates are insensitive to the quality of the apolar solvent. The precipitation is determined by the weaker and non-specific dispersion forces. Using this picture, any equation of state can be modified for the description of asphaltene dissolution – precipitation

These are the assumptions:

- Asphaltene molecules are associated into aggregates having an equal number of asphaltene molecules. This number, noted *N*, is called the aggregation number
- There can be several types of asphaltenes but every molecule has the same number of “binding sites” N_S
- The association energy per bonding is equal for any asphaltene molecule
- The number of free asphaltene molecules is very small compared to the number of associated asphaltene molecules.

Let us consider the following reaction:

$$\sum N_i \cdot molecules \Leftrightarrow aggregate$$

Therefore, we can write the relation between the concentration of associated molecules of asphaltenes and free molecule. The first case-scenario is the monodispersed asphaltene. In this case, we have:

$$(x_a^{free})^N / x^{agg} \approx K_m \qquad \textbf{Eq 4}$$

Km is the equilibrium constant of the reaction.

This relationship enables the link between free and aggregated asphaltenes.

In crude oils, asphaltenes are mainly aggregated. Thus, we have $x^{agg} \approx x_a$. The free asphaltene fraction is expressed by Eq5:

$$x_a^{free} \approx \left(K_m \cdot x_a\right)^{\frac{1}{N}} \qquad \textbf{Eq 5}$$

Let us focus on the fugacity calculations now.

$$\ln f_a^{agg}(x_a^{agg}) = \ln P + \ln \phi_a^{agg} + \ln x_a^{agg} \qquad \textbf{Eq 6}$$

where ϕ_a^{agg} is the apparent fugacity coefficient of the overall asphaltenes and x_a^{agg} is the molar fraction

As it was written earlier, asphaltenes are mainly aggregated. So,

$$x_a \approx x^{agg} \qquad \textbf{Eq 7}$$

However, the fugacity of aggregated asphaltenes can not be calculated directly from the EOS. Nonetheless, since asphaltene fugacities are equal, we have:

$$\begin{aligned}\ln \phi_a &= \ln \phi_a^{EOS} + \ln x_a^{free} - \ln x_a \\ &= \ln \phi_a^{EOS} + \left(\frac{1}{N} - 1\right)\ln x_a + \frac{1}{N}\ln K_m\end{aligned} \qquad \textbf{Eq 8}$$

In this description, once we consider that the number of free asphaltene molecules is very small compare to the number of associated asphaltene molecules, the constant value of the constant K_m plays no role in the phase separation calculation since the last term is the same both for the oil phase and for the asphaltene rich phase.

As for the fugacities of the other components, it can be written as:

$$\ln \phi_i = \ln \phi_i^{EOS} - \ln\left(1 - x_a + \frac{x_a}{N}\right) \qquad \textbf{Eq 9}$$

According to Eq 8

$$f_a = P \cdot \phi_a \cdot x_a$$

$$= P \cdot \phi_a^{EOS} \cdot x_a^{\frac{1}{N}} \cdot K_m^{\frac{1}{N}} \qquad \textbf{Eq 10}$$

If the value of the aggregation number N is large, the value of $x_a^{\frac{1}{N}}$ will be close to 1 and the value of the fugacity of asphaltene faction will not be sensitive to the dilution.

Promising preliminary results show that the quasi-independence of the dilution with regards to the onset of flocculation can be modelled, which was not possible with any classical approach.

Conclusions

The investigation of asphaltene phase behaviour is complex. This work aimed at better understanding and describing these phenomena related to asphaltene stability. The promising aspects will be further investigated.

Acknowledgements

The authors thank the staff of the Laboratoire des Fluides Complexes of the University of Pau as well as Honggang Zhou (Total).

References

1. K.A. Ferworn, W.Y. Svrcek, A.K. Mehortra, Ind. Eng. Chem. Res. 32 (1993), 955 – 959
2. A.K.M. Jamaluddin, , N. Joshi, F. Iwere, O. Gurpinar, An Investigation of Asphaltene Instability under Nitrogen Injection, Proceedings of the SPE International Petroleum Conference and Exhibition of Mexico, 2002, 427 - 436
3. A. Hammami, C.H. Phelps, T. Monger-McClure, T.M. Little, Energ. Fuel. 14 (2000) 14 – 18
4. E. Buenrostro-Gonzalez, C. Lira-Galeana, A Gil-Villegas., J. Wu, AIChE Journal 50 (2004) 2552 - 2570
5. H. Carrier, V. Lazzeri, H. Zhou, J.L. Daridon, An experimental approach to study pressure and temperature effect on asphaltene stability, presented at the Heavy Organics Deposition International Conference, November 14-19 2004, Los Cabos Baja California Sur, Mexico
6. S. Verdier, H. Carrier, S.I. Andersen, J.L. Daridon, to be submitted to Energ. Fuel.
7. R.O. Idem, H.H. Ibrahim, J. Pet. Sci. Eng. 35 (2002) 233 – 246
8. J. Castillo, C. Canelon, S. Acevedo, H. Carrier, J.L. Daridon. Submitted to Energ. Fuel.
9. S.I. Andersen, K.S. Birdi, Fuel Sci. Techn. Int. 8 (1990) 593 – 615
10. D.H. Napper, J. Colloid Interf. Sci. 58, 2 (1977) 390 - 407
11. G. Hotier, M. Robin, Oil Gas Sci. Technol. 38, 1 (1983) 101 – 120
12. C. Lhioreau, J. Briant, R. Tindy, Oil Gas Sci. Technol. 22, 5 (1967) 797 - 806
13. H.L. Le Chatelier, Ann. Mines 13, 2 (1888) 157
14. L. B. Knudsen, Modelling of asphaltene precipitation. Master's thesis, Technical University of Denmark, Department of Chemical Engineering, June 2001
15. A.A. Christensen, C. Hadsbjerg, P.C. Vestager Tybjerg, A study of the perturbed chain statistical associating fluid theory, Midterm Project, Technical University of Denmark, Department of Chemical Engineering, May 2005
16. C. Stachowiak, Viguié J.R., JPE Grolier, Rogalski M., Langmuir 21 (2005) 4821 – 4829
17. Y. Zhang, T. Takanohashi, S. Sato, T. Kondo, I. Saito, Energ. Fuel. 17 (2003) 101 – 106
18. S. Dai, K.C. Tam, J. Phys. Chem. B 105 (2001), 10759-10763
19. W. Dzwolak, R. Ravindra, J. Lendermann, R. Winter, Biochemistry 42 (2003) 11347-11355
20. D. Merino-Garcia, S.I. Andersen, Pet. Sci. Technol. 21, 3 (2003), 507 – 526
21. Andersen S.I., Energ. Fuel. 13 (1999) 315 – 322
22. G. Porte, H. Zhou, V. Lazzeri, Langmuir 19 (2003), 40 – 47
23. J.S. Buckley, Energ. Fuel. 13 (1999), 328 – 332
24. S. Verdier, S.I. Andersen, Fluid Phase Equilib. 231 (2005), 125 – 137
25. S. Verdier, S.I. Andersen, J. Chem. Eng. Data 48 (2003), 892 – 897
26. E.B. Bagley, T.P. Nelson, J.M. Scigliano, J.Paint Technol. 43 (1971), 35
27. Duong, D. Determination of Solubility Parameters for Crude Oils, Master's Thesis, Technical University of Denmark, 2004
28. S. Verdier, D. Duong, S.I. Andersen, Energ. Fuel. 19 (2005) 1225-1229
29. L. Lian, Fuel 73 (1994), 423 – 428
30. F. Mutelet, G. Ekulu, R. Solimando, M. Rogalski, Energ. Fuel. 18 (2004), 667 – 673
31. H. Laux, Erdöl Erdgas Kohle 108 (1992), 227 – 232
32. X. Liron, S. Cohen, J. Pharm. Sci. 72 (1983), 499 – 504
33. S. Verdier, F. Plantier, D. Bessières, S.I. Andersen, H. Carrier, Towardas asphaltene characterization by simple measurements, Proceedings of the 17th European Conference on Thermophysical Properties, Bratislava, September 2005
34. E. Rogel, L. Carbognani, Energ. Fuel. 17 (2003), 378 – 386
35. H. Zhou, G. Porte and V. Lazzeri, personnal communication

List of Publications

[6], [24], [25], [28], [33]

Hugo Edson Gonzalez Villalba
Address: CAPEC, Building 227, office 208
Phone: +45 4525 2986
Fax: +45 4593 2906
e-mail: heg@kt.dtu.dk
www: http://www.capec.kt.dtu.dk/People/phds

Supervisors: Rafiqul Gani
Jens Abilskov

Ph.D. Study
Started: October 2005
To be completed: September 2008

Development of Group Contribution^{Plus} Models for Properties of Organic Chemical Systems

Abstract
In product and process design involving chemical and pharmaceutical industries, it is necessary to have available, reliable and predictive property models supported by a large and reliable thermophysical data bank. This project focuses on developing new and better group contribution models for pure components and mixtures involving high-value chemicals and mixtures.

Introduction

Properties of chemicals play a very important role in the design of the chemical product and in the design of chemical processes that can manufacture them. In computer-aided model-based methods and tools for synthesis and design of the product-process, the applicability of the model and its reliability is governed by the property models used in the product-process model. In addition to reliability of the property models, another important need in product-process synthesis and design is that the models need to be predictive and fairly simple and easy to use. Group contribution (GC) based property models satisfy most of the above requirements and are therefore, routinely used in product-process synthesis and design. There are however some limitations, for example, they are not very reliable for complex chemicals or systems of complex chemicals; group parameters may not be available; not enough experimental data is available to develop a large set of group parameters; reliability is often dependent on how the chemical structure is represented by the groups. These limitations make the synthesis and design of high-value chemical products such as drugs, pesticides, structured polymers, etc., difficult with model-based methods since the necessary reliable property models are not available. Consequently, the current synthesis and design of these chemical products are based on the inefficient and time consuming approach of experiment-based trial and error, mainly for reasons of reliability.

Specific Objectives

The objective of the PhD-project is to develop a new class of group contribution^{plus} models, which addresses the limitations of the current GC-models so that industrially important chemical product-process synthesis and design problems can be solved through reliable and efficient model-based approaches. The "GC^{plus}" indicates that the developed models will use hybrid models that will combine the simplicity and the predictive nature of GC-models with the additional molecular structure based contributions that are needed to improve the property estimations and to significantly extend the application range [1]. The additional molecular structure based contributions will be generated through atom-bond interactions, through molecular modeling based descriptors, etc., and will be integrated to the new GC^{plus} model . The advantage of this hybrid approach would be that the model will be able to handle complex chemicals through additional correction terms to the original GC-term; the new model will be able to distinguish between a larger set of isomers than currently possible; the new model will be able to automatically generate new groups without the need for experimental data; and, the new model will be able to handle structured polymers (many high-value products are structured polymers).

Using the CAPEC property prediction package as a starting point, the new model will concentrate first on properties that are important in high-value chemical product design but are not currently available. For example, pKa, solvatochromic properties, diffusion coefficients and thermal conductivities of pure chemical compounds. Also, in the area of mixture properties, GC-based models are used in the prediction of phase equilibria and the objective here would be to extend the idea of automatic group parameter generation for the missing groups and their interactions so that the application range of the model can be increased without the need for new experimental data [2] (using atom-based interactions). The final objective of the project is to illustrate the scope and significance of the developed methods through case studies involving the synthesis and design of industrial chemical product-process.

Acknowledgements

Funding for Hugo E. Gonzalez Villalba through the National Council of Science and Technology (CONACyT) from Mexico is gratefully acknowledged.

References

1. Gani R., Harper P.M., Hostrup M. Automatic Creation of Missing Groups Through Connectivity Index for Pure-Component Property Prediction.
2. Le Bert B., Abilskov J., Gani R. Proceedings CAPEC annual meeting, Lyngby, Denmark, 2005.

Yanwei Wang
Address: DPC, Dept. of Chemical Engineering,
Building 423, Office 112, Technical
University of Denmark
Phone: +45 4525 6809
Fax: +45 4588 2161
e-mail: waya@kt.dtu.dk
www: http://www.student.dtu.dk/~s031488/

Supervisors: Ole Hassager
Flemming Yssing Hansen, KI
Guenther H.j. Peters, KI

Ph.D. Study
Started: August 2005
To be completed: August 2008

Equilibrium Molecular Dynamics Simulation of Linear Polymer Melt and Shear Viscosity of Lennard Jones Model Fluid

Abstract
The static properties of polymer chains in equilibrium melt state are studied by means of Molecular Dynamics. The distributions of the polymer end-to-end distance and radius of gyration obtained agree well with those for polymer chains following Gaussian statistics. The typical shape of a polymer chain in melt is not spherical symmetry, and this asphericity can be characterized by the eigenvalues of the radius of gyration tensor. In an equilibrium system, the polymer molecules have no preferred orientation, as one may expect.

Introduction

The aim of my Ph.D project is to obtain an understanding of the static, dynamic and rheological properties of entangled polymer melts from molecular level by means of Molecular Dynamics (MD) simulation. MD simulation can be used to study both equilibrium and non-equilibrium systems [1]. Besides, it can be easily implemented to study the tribology and rheology of nanoscopically confined molecules.

MD Simulation

A typical MD simulation includes four stages: initialization, relaxation, equilibration and production. After the initial setup of the simulation box, a preprocessing of it is often necessary in order to remove the overlapping in coordinates before the full simulation using the exact potential model takes over. For the MD simulation of entangled polymer melts, the equilibration process usually takes quite a long time if one follows the exact slow physical dynamics [2]. Until the system has reached thermodynamic equilibrium, one can start the production run, sampling desired static and dynamic properties of the system.

For a MD simulation to be reliable the inter-atomic interaction potential model should be accurate enough considering the physical origin; the equations of motion of the system should enable the sampling of the correct statistical ensemble average; the numerical integration scheme should be able to keep the important features of the dynamics.

Although the term “MD” simulation often refers to the classical Equilibrium Molecular Dynamics, MD simulation can also be further extended to the non-equilibrium regime, where an external field, force or flux is imposed onto the system. The system can often approach a non-equilibrium steady state in Non-Equilibrium Molecular Dynamics (NEMD).

EMD Simulation of Linear Polymer Melt

Simulation Details

The simulated system consists of 32 chains with 100 beads on each chain. The polymer chains are modeled as bead-spring chains. The beads interact with each other via the repulsive Weeks-Chandler-Andersen (WCA) potential, which corresponds to the usual LJ potential that is truncated at the minimum and shifted. The springs are represented by a finitely extendable nonlinear elastic (FENE) potential. The parameters for the spring potential are optimized in order to avoid any bond crossing [3]. Such a combination between the WCA potential and FENE potential is often called “Kremer-Grest Model”, which is commonly used to describe the interaction between polymer beads in a coarse-grained bead spring model.

The detailed simulation settings are listed in Table 1. Note that the density and temperature of the simulation box are given in reduced units. Such variables are introduced through the standard unit reduction method for LJ system.

Table 1: details for the polymer melt simulation

Number of chains	32
Number of beads on each chain	100
Potential model	Kremer-Grest model
Simulation Ensemble	NVT
Reduced Density of the system	0.85
Reduced Temperature	1.0
Thermostat	Nosé-Hoover
Integration scheme	Velocity verlet
Sampling scheme	Block analysis

Results and Discussion

A polymer chain in a good solvent tends to expand with respect to the ideal state, owing to the long range monomer-monomer repulsions. In polymer melt, it has been believed that the intra-chain excluded volume interactions are screened by the surrounding polymers, and the strong interpenetration of the chains suppresses the expansion of an individual chain [4].

Experimentally, the Gaussian behavior of polymer chains in melt state can be examined by Neutron scattering experiment. In MD simulations, since the molecular trajectory is exactly known at each time step, one can easily calculate all the desired structure properties.

In this simulation, properties such as the mean square end-to-end distance (higher order moments and distributions), the mean square radius of gyration (higher order moments and distributions) are calculated. Besides, eigenvalues of the inertia tensor, asphericity of the polymer chains and the chain orientations are also investigated. The calculated quantities are then compared with those following Gaussian statistics.

All the structure quantities obtained from the simulation of a well-equilibrated polymer melt agree well with those for polymer chains following Gaussian statistics. The shape of a polymer chain in the simulated system can be characterized by calculating the three eigenvalues of the radius of gyration tensor [5]. The typical shape of a polymer chain in melt is not spherical symmetry, and this shape anisotropy is of considerable scientific and technological importance, affecting a variety of polymer properties. Since the chains are aspherical, the molecular orientation is also studied. In a well equilibrated polymer melt system, the molecules have no preferred orientation, as one may expect.

The chain dynamics is also studied, and the results can be interpreted by the Rouse theory. For the system studied, polymer chains are not long enough to study “reptation dynamics”.

Conclusions

Molecular Dynamics method is used to study an equilibrated polymer melt system. Both static and dynamic properties can be obtained from the molecular trajectories in MD simulation.

As the next step, transport properties of polymer system are going to be investigated by means of NEMD. By modifying the boundary conditions, molecules under confined geometry (nanorheology) can also be studied. The entanglement dynamics of long chain polymer melt is also going to be studied through a systematic coarse-graining approach.

References

1. M.P. Allen, D.J. Tildesley, Computer Simulation of Liquids, Oxford Science Publications, Oxford, 1987.
2. R. Auhl, R. Everaers, G.S. Grest, K. Kremer S.J. Plimpton, J. Chem. Phys. 119 (24) (2003).
3. K. Kremer, G.S. Grest, J. Chem. Phys. 92 (8) (1990).
4. M. Doi, Introduction to Polymer Physics, Clarenton Press, Oxford, 1996
5. J. Rudnick, G. Gaspari, J. Phys. A: Math. Gen. 19 (191) (1986).

Yi Lin

Address: Building 229, room 230
Phone: +45 4525 2869
Fax: +45 4588 2258
e-mail: yil@kt.dtu.dk
www: http://www.kt.dtu.dk

Supervisor: Kaj Thomsen

Ph.D. Study
Started: September 2003
To be completed: September 2006

New Equation of State for Electrolytes

Abstract

The aim of the project is to develop a new equation of state for electrolytes over wide range of temperature and pressure, which is simple to implement. Several successful theories have been studied such as Poisson-Boltzmann equation theory, Integral Equation theories, Perturbation theories and Fluctuation theory from the literature about the electrolyte solution. The equation of state (EOS) from Mayer, Sandler and Wood has been studied in details and implemented. Based on the performances of Mayer, Sandler and Wood's (MSW) equation of state, improvement has been made and new equations of states for electrolytes were introduced: the simplified Debye-Hückel (DH) Electrolyte EOS, the modified MSW EOS and the Cubic Plus Association electrolyte EOS. The MSW EOS and the simplified DH Electrolyte EOS have been applied to multi-component system and SLE computations have been carried out. Later these equations will be applied to a new test system for further study.

Introduction

Oil and Gas production in the North Sea involves transporting complex mixtures of oil, gas and formation water over large distances. Crude oil and natural gas consist mainly of hydrocarbons of varying molecular size, acetic acid and carbon dioxide and various amounts of dissolved minerals such as sodium chloride, calcium, barium, strontium sulfate and carbonate. In order to avoid problems such as clogging of pipes due to the formation of gas hydrates, wax, minerals or other solids, it is necessary to be able to predict the phase behavior of such mixtures. To avoid the formation of gas hydrates, additives like methanol or MEG (Mono Ethylene Glycol) can be added to the gas-oil-water mixture. Salts and acetic acid will however accumulate in the water/MEG phase and with time minerals will precipitate from this phase. Some acetic acid and carbon dioxide will remain in the gas phase where it will cause corrosion in connection with condensation in the top part of the pipe. Today it is possible to perform equilibrium calculations for complex mixtures of hydrocarbons and various production chemicals. It is also possible to separately perform equilibrium calculations with aqueous solutions of minerals and non-electrolytes, usually done by use of an activity coefficient model. Activity coefficient models however lack the ability to describe the gas phase properties and need to be combined with cubic equations of state in order to describe such properties. In order to describe the phase behavior of complex mixtures of oil, gas, water, and minerals, the activity coefficient model approach can be expanded to encompass a proper description of the gas phase or the cubic equation of state can be expanded to encompass a proper description of the liquid phase. The second approach is chosen and the challenge addressed in this project is to develop an equation of state that also includes components such as minerals and sour gases.

Simplified Debye-Hückel Electrolyte EOS

The expression for the total change in Helmholtz free energy to form the electrolyte system can be expressed as follows:

$$A(T,V,\mathbf{n}) - A^{IGM}(T,V,\mathbf{n}) = \Delta A^{SRK} + \Delta A^{sDH}$$

where $\mathbf{n}$ is the vector of the number of moles of each component of the mixture, and A^{IGM} is the Helmholtz free energy of an ideal mixture. ΔA^{sDH} is the truncated simplified Debye-Hückel term often seen in thermodynamic textbooks.

Myers, Sandler and Wood Electrolyte EOS

Myers and Sandler's Electrolyte equation of state is intended to be developed for the systems more general than just containing hydrocarbons, water and salt and over wide ranges of temperature, pressure and composition. Use the property of a state function; we get the expression for the total change in Helmholtz free energy to form the electrolyte system:

$$A(T,V,\ \mathbf{n}) - A^{IGM}(T,V,\ \mathbf{n}) = \Delta A^{Born}_{dis} + \Delta A^{PR} + \Delta A^{Born}_{chg} + \Delta A^{sMSA}$$

.

The Electrolyte CPA EOS

It is of our interest in this project to extend the CPA equation to electrolyte systems. Wu and Prausnitz's equation of state is an example of electrolyte CPA based on PR EOS and they use the complete MSA term in their model to count for the long range ion-ion interaction. Here we would like to have a SRK based CPA EOS plus a simplified MSA term and the empirical SR2 term used in Fürst's electrolyte EOS. The newly developed EOS in this project have the following form in Helmholtz free energy:

$$A(T,V,\ \mathbf{n}) - A^{IGM}(T,V,\ \mathbf{n}) = \Delta A^{SRK} + \Delta A^{Association} + \Delta A^{sMSA\_Fürst} + \Delta A^{SR2} + \Delta A^{Born}_{dis} + \Delta A^{Born}_{chg}$$

Modified Myers, Sandler and Wood Electrolyte EOS

This last equation of state is developed simply for the purpose of comparison. The modified EOS of Myers, Sandler and Wood for electrolyte can be expressed in terms of Helmholtz free energy as follows:

$$A(T,V,\ \mathbf{n}) - A^{IGM}(T,V,\ \mathbf{n}) = \Delta A^{PR} + \Delta A^{sMSA\ \ Fürst} + \Delta A^{Born}_{dis} + \Delta A^{Born}_{chg} + \Delta A^{SR2}$$

Terms used in the Electrolyte EOS

Peng-Robinson term The Peng-Robinson term is given by

$$\Delta A^{PR}(T,V,\mathbf{n}) = \frac{an}{2\sqrt{2}b}\ln\left(\frac{v+c+(1-\sqrt{2})b}{v+c+(1+\sqrt{2})b}\right) + nRT\ln\left(\frac{v}{v+c-b}\right)$$

In this term, a volume translation parameters c has been introduced here for the Peng-Robinson EoS.

Cubic Plus Association term The CPA EOS for pure compounds has the following general form expressed in the compressibility factor form not the Helmholtz free energy form:

$$\begin{aligned} Z &= Z^{SRK} + Z^{assoc}, \\ Z^{SRK} &= \frac{V}{V-b} - \frac{a}{RT(V+b)}, \\ Z^{assoc} &= -\frac{1}{2}\left(1+\rho\frac{\partial \ln g(\rho)}{\partial\rho}\right)\sum_i x_i \sum_{A_i}(1-X_{\acute{A}_i}). \end{aligned} \qquad (0.1)$$

where $a = a_0\left(1+c_1\left(1-\sqrt{T_r}\right)\right)$,

ρ is the molar density of the mixture.

x_i is the superficial (apparent) mole fraction of the component *i* in the mixture.

X_{A_i} is the mole fraction of the molecule *i* not bonded at site A, also known as the monomer mole fraction and is defined as:

$$X_{A_i} = \left(1+\rho\sum_j \sum_{B_j} x_j X_{B_j}\Delta^{A_iB_j}\right)^{-1} \qquad (0.2)$$

and X_{A_i} is calculated by solving equation (0.2).

The association strength parameter is defined as:

$$\Delta^{A_iB_j} = g(\rho)\left[\exp(\frac{\varepsilon^{A_iB_j}}{RT})-1\right]b_{ij}\beta^{A_iB_j}$$

$\Delta^{A_iB_j}$ is the association strength between two association sites belonging in two different molecules, where $\varepsilon^{A_iB_j}$ and $\beta^{A_iB_j}$ are the association energy and volume of interaction between site A of the molecule *i* and site B of the molecule *j*, respectively.

Born contribution The free energy required to discharge ions in vacuum is calculated by the equation proposed by Born.

$$\Delta A^{Born}_{dis}(T,V,\mathbf{n}) = -\frac{N_A e^2}{4\pi\varepsilon_0}\sum_{ions}\frac{n_i Z_i^2}{\sigma_i}$$

The free energy required to charge an ion in a medium of electric constant ε is calculated by the equation proposed by Born.

$$\Delta A^{Born}_{chg}(T,V,\mathbf{n}) = \frac{N_A e^2}{4\pi\varepsilon_0\varepsilon}\sum_{ions}\frac{n_i Z_i^2}{\sigma_i}$$

The Born equation provides a means of calculating salvation free energies of ions in water. Born contribution has no effect on the ion activity coefficients but affect the water activity.

SR2 contribution The short-range ionic term is given as

$$F_{SR2} = \frac{A_{SR2}-A^0}{RT} = -\sum_k\sum_l\frac{n_k n_l W_{kl}}{V(1-\varepsilon_3)} \triangleq \frac{W}{V(1-\varepsilon_3)} \qquad (0.3)$$

and
$$\varepsilon_3 = \frac{N_A\pi}{6}\sum_k\frac{n_k\sigma_k^3}{V} \qquad (0.4)$$

where k is over all species. This term is the same as that in Fürst's EOS. The physical meaning of ε_3 is similar to packing fraction of various ions in the system. Two types of parameters appear in the above equations: they are interaction parameters W_{kl} and the ion diameters σ_k.

Simplified MSA term The additional Helmholtz free energy change due to the Coulomb interaction between ions is calculated through the simplified mean spherical approximation (sMSA). It is derived under the assumption that all ions have the same average diameter σ. The average diameter σ can be calculated through various mixing rules and here the conventional linear mixing rule has been adopted. The expression of the Helmoholtz free energy is given by:

$$A^{Coul} = -\frac{2\Gamma^3 RTV}{3\pi N_A \varepsilon_0 \varepsilon}\left\{1+\frac{3}{2}\Gamma\sigma\right\},$$

$$\Gamma = \frac{1}{2\sigma}\left[\sqrt{1+2\sigma\kappa}-1\right], \qquad \text{where } \kappa = \left(\frac{e^2 N_A^2}{\varepsilon\varepsilon_0 RTV}\sum_{ions} n_i Z_i^2\right)^{1/2}$$

$$\text{where } \sigma_i = \sigma_i^{(1)} + \sigma_i^{(2)}/T, \qquad \sigma = \sum_{ions} n_i\sigma_i \Big/ \sum_{ions} n_i$$

Γ is the MSA screening parameters and κ is the Debey screening length. e is the electronic charge, k is the Boltzmann's constant, ε is the relative permittivity of the medium, ε_0 is the vacuum permittivity, z_i is the valence and σ_i is the diameter of species i, where $\sigma_i^{(1)}$ and $\sigma_i^{(2)}$ are fitted constant which are different for different salt. T is the absolute temperature, ρ_i is the number density of species i. Here a mixing rule is needed for the average ion diameter σ. The Uematsu and Frank model has been used to calculated the relative permittivity of the medium ε for pure water.

MSA term from Renon and Fürst The additional Helmholtz free energy change due to the Coulomb interaction between ions can also be calculated through the simplified MSA implicit expression from Renon in Helmoholtz free energy:

$$A^r(T,V,n) = -\frac{e^2 N_A}{4\pi\varepsilon_0\varepsilon}\left(\Gamma\sum_i \frac{n_i z_i^2}{1+\Gamma\sigma_i}\right) + \frac{V\Gamma^3}{3\pi}kT$$

where

$$4\Gamma^2 = \frac{e^2 N_A{}^2}{\varepsilon_0 \varepsilon RT}\sum_i \frac{n_i}{V}\left[\frac{z_i}{1+\Gamma\sigma_i}\right]^2$$

The symbols are as in above simplified MSA.

The above simplified MSA equation from Renon and Fürst reduces to the simplified common ion-size solution of MSA used by Mayer et. al. as the assumption, that all ions have the same average diameter σ,is applied.

The Computation Results

The MSW EOS and electrolyte DH EOS were fitted to experimental data of a multi-component testing system (H_2O, Na^+, H^+, Cl^-, SO_4^{2-}, OH^-) for aqueous electrolyte solutions at 25 °C and 1 bar. The equation does well in correlating activity coefficients osmotic coefficients, densities over the wide range of concentration. In the following Fig. 1, the solid-liquid equilibrium calculations were presented for both equations graphically.

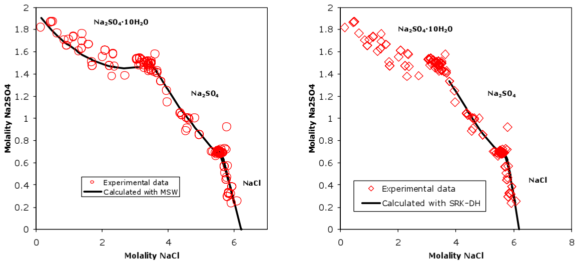

Figure 1 Plot of SLE phase diagrams for multi-component system generated by MSW EOS and electrolyte DH EOS.

In the following figures, the computational results and the original experimental data points are provided for comparison. It can be seen that the correlated curves agrees with the experimental results. A more comprehensive application to mixed-salt systems will be given in the future. The selected test system for future study is H_2O, Na^+, Ca^{2+}, Cl^-, SO_4^{2-}, CO_3^{2-}, HCO^{3-}, CO_2 and Glycol.

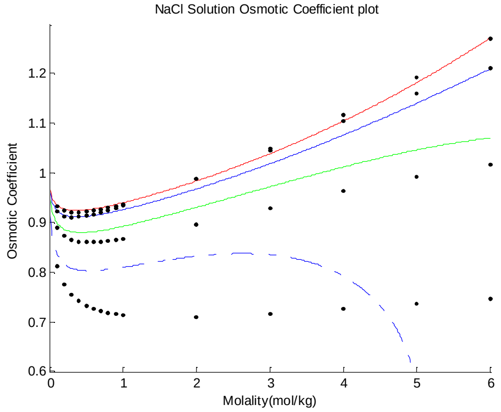

Figure 2 **The computation results of the osmotic coefficient of aqueous NaCl solution from electrolyte CPA EOS . The red solid line, blue solid line, green solid line and the blue dashed line are the values at 25°C, 100°C, 200°C, 300°C respectively. The red line are correlated to experimental data at 25°C and others are predictions based on parameters obtained at 25°C .**

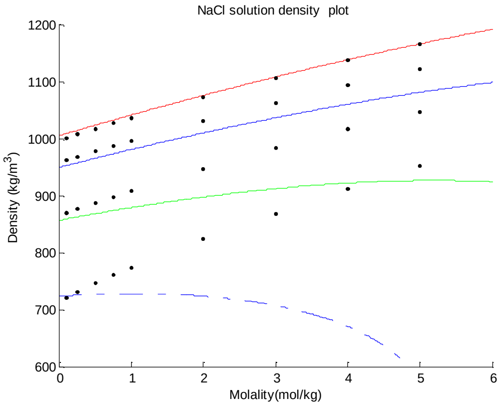

Figure 3 **The density of aqueous NaCl solution from electrolyte CPA EOS. The red solid line, blue solid line, green solid line and the blue dashed line are the calculated values at 25°C, 100°C, 200°C, 300°C respectively. The red line are correlated to experimental data at 25°C and others are predictions based on parameters obtained at 25°C .**

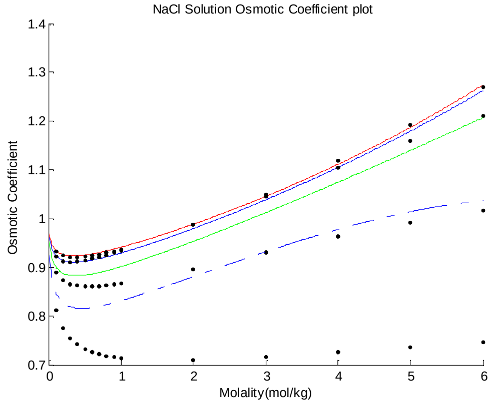

Figure 4 The computation results of the osmotic coefficient of aqueous NaCl solution from the modified MSW EOS. The red solid line, blue solid line, green solid line and the blue dashed line are the values at 25°C, 100°C, 200°C, 300°C respectively. The red line are correlated to experimental data at 25°C and others are predictions based on parameters obtained at 25°C .

Conclusion

The computation results of the SLE for multi-component system from the simplified MSA and the Electrolyte Debye-Hückel EOS are very close. It shows that it is possible to develop an EOS for multiple electrolytes over wide ranges of temperature and pressure. The density, mean ionic activity coefficient and osmotic coefficient calculation from Modified MWS EOS and the electrolyte CPA EOS agree well with the reported experimental values from literature.

References

[1] Loehe, J.R.; Donohue, M.D. “Recent advances in modeling thermodynamic properties of Aqueous Strong Electrolyte Systems”, *AIChE Journal*, 43, (1997), 180-195.

[2] Friedman H.L.. ”Electrolyte solutions at equilibrium”, *Ann. Rev. Phys. Chem.*, 32, (1981), 179-204.

[3] McQuarrie D. A. “Statistical Mechanics”, HARPER & ROW Publishers, 1976.

[4] Kaj Thomsen; “Mixture with Electrolytes”, IVC-SEP Ph. D. Summer School August 14, 2003

[5] Debye P.; Hückel E. ”Zur Theorie der Elektrolyte. I. Gefrierpunktserniedrigung und verwandte Erscheinungen”, *Physikalische Zeitschrift*, 24, (1923), 185-206.

[6] Zareen Abbas, Magnus Gunnarsson, Elisabet Ahlberg, and Sture Nordholm. “Corrected Debye-Hückel Theory of Salt Solutions: Size Asymmetry and Effective Diameters”, *J. Phys. Chem. B* 2002, 106, 1403-1420.

[7] Blum L.. “Mean Spherical model for asymmetric electrolytes I. Method of solution”, *Molecular Physics*. Vol. 30, No.5, 1529-1535, 1975.

[8] Blum, L.; Høye J.S.. ”Mean Spherical Model for Asymmetric Electrolytes. 2. Thermodynamic Properties and the pair Correlation Function”, *Journal of Physical Chemistry*, 81(13), 1311-1316, 1977.

[9] Wei D.; Blum L.. “Internal Energy in the Mean Spherical Approximation As Compared to Debye-Hückle Theory”. *Journal of Physical Chemistry,*.91: 4342-4343, 1987.

[10] Jin G., Donohue M. D.. "An equation of state for electrolyte solutions. 1. Aqueous systems containing strong electrolytes”, *Ind. Eng. Chem. Res.* 27,1073-1084, 1988.

[11] Jin G. and Donohue M.D.. “An Equaiton of State for Electrolyte Solutions. 3. Aqueous Solutions Containing Multiple Salts”, *Ind. Eng. Chem. Res.* 30, (1991), 240-248.

[12] Wu, J. and Prausnitz, J.M.. “Phase Equilibirum for systems Containing Hydrocarbons, Water and Salt: An Extended

Peng-Robinson Equation of State" , *Ind. Eng. Chem. Res.* 37, (1998), 1634-1643.

[13] Myers, J.A., Sandler, S. I. and Wood R. H.. "An Equation of State for Electrolyte Solutions Covering Wide Range of Temperature, Pressure and Composition", *Ind. Eng. Chem. Res.* 41, (2002), 3282-3297.

[14] Dimitrios P. Tassios. Applied Chemical Engineering Thermodynamics, Springer-Verlag; Germany, 1993.

[15] Planche H., Renon H.. "Mean Spherical Approximation applied to a simple but non-primitive model of interaction for electrolyte solutions and polar substances", *J. Phys. Chem.*, 5, (1981), 3924-3929.

[16] Fürst W., Renon H.."Representation of Excess Properties of Electrolyte Solutions Using a New Equation of State", *AIChE Journal*, 39, (1993), 335-343.

[17] Kaj Thomsen, Ph. D. thesis, "Aqueous electrolytes: model parameters and process simulation", Technical University of Denmark, Denmark, 1997.

[18] Breil M. P., Ph D. Thesis. "Thermodynamics, Experimental, and Modelling of Aqueous Electrolyte and Amino Acid Solutinos", Technical University of Denmark, Denmark, 2001.

[19] Zuo J. Y., Zhang D. and Fürst W.. "Predicting LLE in Mixed-Solvent Electrolyte Systems by an Eletrolyte EOS", *AIChE Journal*, 46, (2000), 2318-2328.

[20] Prausnitz, J. M.; Lichtenthaler, R. N.; de Azevedo, E. G.; Molecular Thermodynamics of Fluid-Phase Equilibria (Third Edition)", Prentice Hall International Series in the Physical and Chemical Engineering Sciences; USA, 1999.

Ayten Yilmaz

Address: CHEC Dept. of Chemical Engineering,
Building 229, Office 118
Technical University of Denmark
Phone: +45 4525 2920
Fax: +45 4588 2258
e-mail: ayt@kt.dtu.dk
www: http://www.chec.dtu.dk

Supervisors: Peter Glarborg
Hans Livbjerg

Ph.D. Study
Started: August 2005
To be completed: September 2008

Particle Formation During Natural Gas Combustion at Domestic Appliances

Abstract

The contribution of the home environment and other life style factors in the pathogenesis of allergic disease has attracted much attention, particularly the role of indoor pollution from gas cooking appliances via nitrogen dioxide (NO_2) and carbon-monoxide (CO) emissions. A recent hypothesis is that the epidemiological associations between illness and nitrogen dioxide may be the consequence of confounding by particle numbers. In this PhD study, the particle formation during natural gas combustion at the domestic appliances will be investigated. The work involves determination of the particle size distribution and the chemical composition of the particles together with the total amount of particles formed. Once the particles have been identified, the mechanism of formation of the particles will be studied and a model for particle formation during gas combustion will be developed.

Introduction

The contribution of the home environment and other life style factors in the pathogenesis of allergic disease has attracted much attention, particularly the role of indoor pollution from gas cooking appliances and its association with asthma-like symptoms. In particular, natural gas is recognized as one of the most important cooking fuels for domestic gas burners in developed countries [1].

Seaton and Dennekamp [2] brought recently the hypothesis that the epidemiological associations between illness and nitrogen dioxide may be the consequence of confounding by particle numbers. When particles are measured as mass the greatest contribution comes from the largest particles, but the greatest number of particles by far are the submicron ones. These ultrafine particles are generated, as is NO, by the combustion process, and therefore the two pollutants (ultrafine particles and NO_2) are likely to correlate closely. Dennekamp et al [3] carried out cooking experiments with the gas cooker and the electric cooker, comparing the effects of the two cooking fuels. They reported that while the gas rings were burning, the particles grew up to a peak of about 50-70 nm.

The EUROPART group [4] - a European interdisciplinary group of researchers- assessed the relevance of particle mass, surface area or number concentration as risk indicators for health effects in non-industrial buildings by reviewing papers identified in Medline, Toxline and OSH. They concluded that there is inadequate scientific evidence that airborne, indoor particulate mass or number concentrations can be used as generally acceptable risk indicators of health effects in non-industrial buildings.

Many residential gas appliances, eg., cooking ranges and ovens, employ laminar jet flames. In these applications, the fuel stream is usually partially premixed with air, which is essential to provide non-sooting operation [5]. The primary aeration, which is typically 40 – 60 percent of the stoichiometric air requirement, makes the flames short and prevents soot formation, resulting in the familiar blue flame. The maximum amount of air that can be added is limited by safety considerations. Current design practices rely heavily on the art and craft of experienced burner designers; however recent concern with indoor air quality and pollutant emissions -particularly emissions of nitrogen dioxide (NO_2) and carbon-monoxide (CO) have resulted in the use of more sophisticated design methods [6].

There are several studies available in literature reporting the effects of cook-top burner design and operation factors (such as cap material, cap size, port shape, port size, port spacing, central secondary aeration, flame inserts, load height, load height to flame length ratio, thermal input, etc) on the gaseous emissions (NOx, CO and hydrocarbon emissions) from the natural gas fired cook-top burners [7,8,9]. However these studies do not provide any correlations for particulate matter or soot emissions.

Gas composition is particularly a vital parameter affecting burner performance. It is known that using the same gas stove to burn natural gas with various heating values other than the intended fuel is inappropriate and hazardous due to the possible occurrence of incomplete combustion (i.e. a increase of CO emissions and/or soot formation) lift-off, flashback and inadequate heat input Hence, the inter-changeability of gaseous fuel is of great significance. Ko and Lin [6] studied the CO emissions and efficiency of a domestic gas stove burning natural gases with various compositions. They concluded that if a burner is to be used with a gas of higher heating value instead of the intended lower heating value, the performance of the burner can be significantly improved by adjusting (1) the gas pressure, (2) the primary aeration, (3) the thermal input and (4) the heating height.

Specific Objectives

The objective of this PhD study is to provide new results on particle formation during natural gas combustion at the domestic appliances. Gas cookers are the main focus of the work.

The particle size distribution and the chemical composition of the particles will be determined together with the total amount of particles formed and the accompanying gaseous emissions (CO, NOx, SO_2).

Once the particles have been identified, a model for their formation in gas combustion will be developed.

Future work

Together with the continued literature search, experiments will be performed to determine the size range of the particles formed.

Depending on the nature of the particles, the project may focus on the precursor chemistry (formation and conversion of PAH prior to soot inception; formation of SO3 as the limiting step in sulfuric acid formation) or on nucleation and particle growth. The heat transfer characteristics of the flame may also be part of the study.

Once the particles have been identified, a model for their formation in gas combustion will be developed.

Acknowledgements

Special thanks to Per Gravers Kristensen and Danish Gas Technology Center (DGC) for supporting the project.

References

1. A.J. Chauhan, Clinical and Experimental Allergy, 29 (1999), 1009–1013.
2. A. Seaton, M. Dennekamp, Thorax, 58 (2003), 1012-1015.
3. M Dennekamp, S Howartha, C A J Dickb, J W Cherriea, K Donaldsonb, A Seaton, Occup. Environ. Med, 58 (2001), 511-516.
4. T.Schneider, J.Sundell, W.Bischof et al, Indoor Air, 13 (2003), 38-48.
5. S. R. Turns, An Introduction to Combustion Concepts and Applications, McGraw Hill 2000, p. 305.
6. Y.C Ko, T.H. Lin, Energy Conversion and Management 44 (2003) 3001-3014.
7. R. Junus, J. F. Stubington, G. D.Sergeant, Intern. Journal of Environmental Studies, 45 (1994), 101-121.
8. J.F. Stubington, G. Beashel, T. Murphy, R. Junus, P.J. Ashman and G.D. Sergeant, Journal of Institute of Energy, 67(1994), 143-155.
9. C. R. Shaddix, J. R. Harrington, K. C. Smyth, Combustion and Flame, 99 (1994), 723-732.

Jacob Zeuthen
Address: DTU, building 206, room 264
Phone: +45 4525 2964
Fax: -
e-mail: jz@kt.dtu.dk
www: http://www.aerosol.kt.dtu.dk

Supervisors: Hans Livbjerg
Peter Glarborg
Flemming Frandsen

Ph.D. Study
Started: October 2003
To be completed: November 2006

Laboratory Investigation of Formation of Aerosols and Chemical Reactions in Flue Gas from Biomass- and Waste-Combustion

Abstract

The aim with this project is to investigate the formation of aerosol particles and deposits during combustion of the so-called CO_2-neutral fuels, biomass and waste. The kinetics of the chemical reactions leading to the formation of these particles and deposits, and the phase transitions involved, are studied. In general, combustion aerosols should be avoided due to their harmful behavior in the environment. Particles from combustion of bio-fuels are particularly harmful due to their sticky and corrosive behavior in process equipment.

This project involves experiments performed in a tubular furnace and also CFD (computational fluid dynamics) simulations using Fluent. The focus is on developing a quantitative model based on experiments and simulations. The quantitative model can be used for design and control of Danish power plants using biomass and waste combustion in the future.

Introduction

Straw, some sorts of wood, and various kinds of waste contain considerable amounts of volatile inorganic salts, in particular the chlorides of sodium, potassium and zinc, which evaporate during combustion. When the flue gas cools down after combustion the inorganic vapors condense and form aerosol particles and deposits on walls and super heater tubes. This phenomenon is much more pronounced for bio-fuels than for other fuels. Dealing with the problems caused by deposition of salts in the process equipment increases the cost of 'CO_2-neutral' combustion considerable. The aerosol particles and the deposits have previously been studied intensively by field-studies and the chemical compositions of these have been found. However, the proposed qualitative models for the chemical reactions involved are not clear and are contradictory. Also, no quantitative models have been developed. Field-data are influenced by a highly varying chemistry of the fuel and by complicated distributions of residence times, temperatures and flow-patterns. Therefore it is not possible to develop quantitative models based on these data.

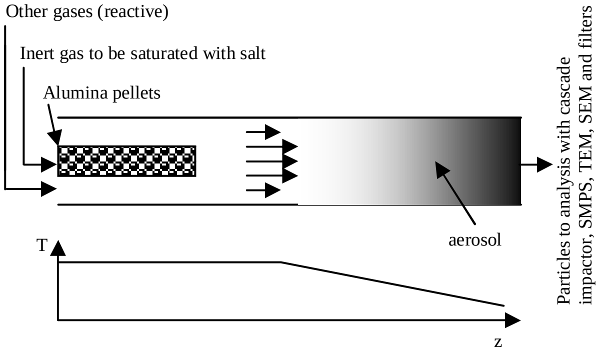

Figure 1: *Schematic drawing of the tubular furnace. Gas enters the reactor in one end. An inert gas is led through a packing of pellets to be saturated with a volatile salt. The salt concentration of the gas is adjusted by changing the temperature of this part of the reactor. A temperature profile is applied on the reactor and particles are formed in the cooling zone by nucleation. The aerosol leaving the reactor can be studied by using a cascade impactor, SMPS (Scanning Mobility Particle Seizer), SEM (Scanning Electron Microscopy), TEM (Transmission Electron Microscopy) and other methods.*

In order to set up a quantitative model the important reactions involving the key chemical components must be studied separately. In this project a bench-scale tubular furnace with well-defined flue gas flow, temperature and gas-composition is used to establish a qualitative as well as a quantitative model for the formation of particles and deposits.

Figure 2: *Experimental setup. To the left the SMPS system is placed and to the right the tubular furnace is seen.*

Experimental work

For the experimental work a 173 cm long tubular furnace (Ø=25 mm) with laminar flow is used (see figure 1 and 2). It is possible to control the temperature up to ~1200 ºC in nine separate axial sections along the flue gas flow direction. In the first part of the reactor an inner tube is placed. In this inner tube a flow of inert nitrogen passes pellets of inert alumina impregnated with the salt to be volatilized (e.g. NaCl or KCl). The nitrogen becomes saturated and by changing the temperature of the pellets it is possible to adjust the salt-concentration in the gas (see figure 3). Other reactive gases (SO_2, H_2O, NO and O_2/air) enter the reactor on the outside of the salt-containing alumina pipe. The temperature is kept constant in the first part of the reactor and is then decreased in the flow direction after a given length. Using this technique, it is possible to study effects of different temperature gradients, flow velocities and chemical compositions on the formation of particles and deposits. It is also possible to introduce particle seeds with the inlet gas to study the effect of foreign seeds in the flue gas. These will serve as nucleation sites for further growth of inorganic materials and may serve to suppress homogeneous nucleation. Homogeneous nucleation leads to sub-micron particles (D_p<1μm), which are the most harmful particles for the environment, spreading over larger distances and with harmful impact on the human lungs. These particles are also more difficult to separate from the flue gas.

Homogeneous nucleation

Particles can be formed directly from a gas phase if the super-saturation is sufficiently high. This can happen by either cooling or chemical reaction. In homogeneous nucleation, particles are formed in very high concentrations. The concentration depends on the properties of the nucleating compound and on the temperature at which it nucleates. When nucleation takes place at higher temperatures the diffusion coefficient will be higher and the resulting particle concentration will be lower. However, the particles formed will be larger, since they are growing faster due to the higher diffusion coefficient. This is investigated in the tubular furnace. Different temperature profiles and nucleation of different salts are investigated. By

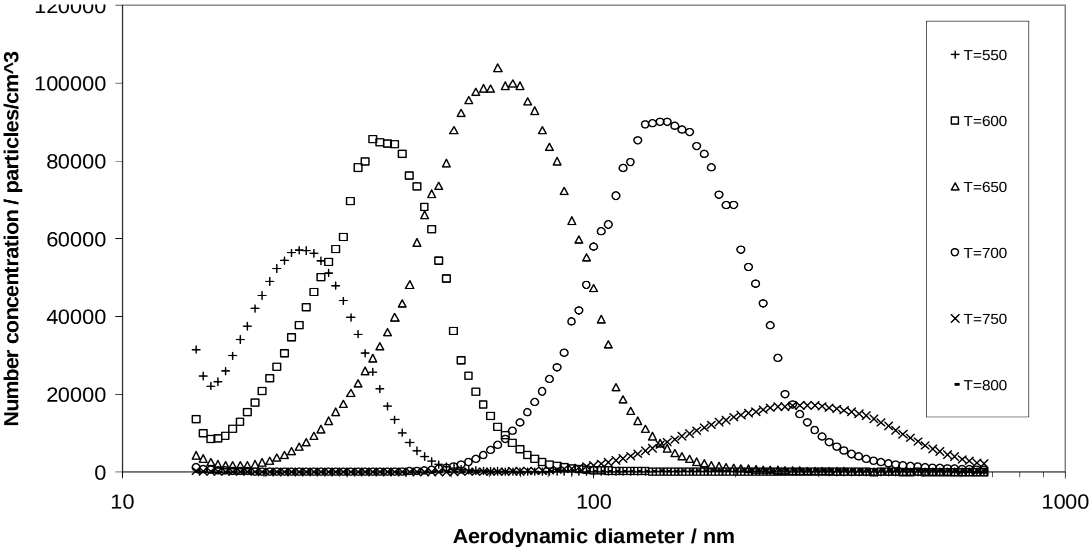

Figure 3: *Size distribution of pure KCl-particles from experiments with homogeneous nucleation in a tubular furnace. The temperature of the saturation zone with alumina pellets impregnated with the salt is varied to obtain different concentrations of $KCl_{(g)}$. With increasing temperature the concentration of $KCl_{(g)}$ is increased and the average particle diameter increases, because the temperature where nucleation takes place is higher. However, while the mass of particles formed will keep increasing with higher temperature the number of particles formed is highest at some given temperature. Above this temperature coagulation of the small particles with the larger ones will dominate.*

introducing seeds to the experiments, it is also found that suppression of homogeneous nucleation occurs by the presence of a particle concentration around 10^5 $1/Ncm^3$. If sulphation of the potassium chloride is applied, the suppression is not possible. The sulphation of KCl and KOH is given by the reactions:

$$2KCl + SO_2 + H_2O + ½O_2 \rightarrow K_2SO_4 + 2HCl$$

$$2KOH + SO_2 + ½O_2 \rightarrow K_2SO_4 + H_2O$$

This could indicate that potassium sulphate (and not potassium chloride) is the nucleating compound in the system.

Mechanism for aerosol formation

Before developing a model for aerosol formation during biomass combustion the mechanism of the initial nucleation leading to particle formation has been investigated. To determine how particles are nucleated two approaches have been used. In the first approach the aerosol is filtered from the gas phase at high temperature (>800ºC). This prevents the most volatile compound from nucleating. The hot filtration showed potassium sulphate condensation at temperatures where potassium chloride was only in gas phase (see figure 4).

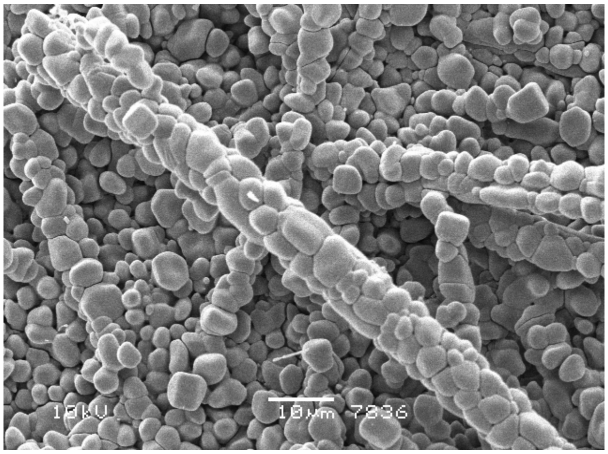

Figure 4: *SEM micrograph of potassium sulphate ´filtered´ from the synthetic flue gas.*

However, the deposits on the filter showed particles with diameters larger than 5 µm. Since these are larger than the aerosol particles, a growth on the filter must take place. This can happen by either sintering of small particles or by heterogeneous condensation. To find out whether small particles hits the surface and then sinter with the existing deposits or if the deposits are due to a heterogeneous catalytic reaction a slide to be used for quench cooling of the filter has been made.

By quench cooling the filters, small particles on top of the deposits has been observed (see figure 5). These could indicate that potassium sulphate is the nucleating component.

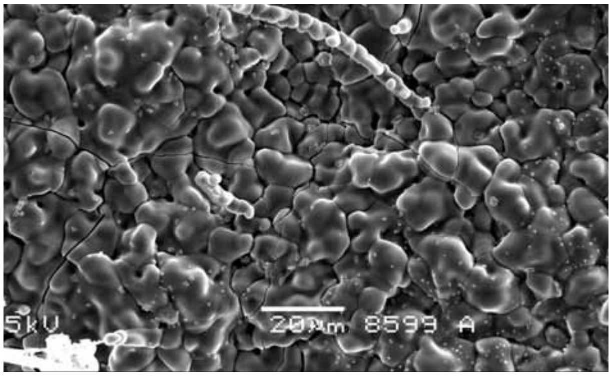

Figure 5: *SEM micrograph of quench-cooled potassium sulphate substrate ´filtered´ from the gas phase in a experiment with sulphation of KCl. Small particles are observed on top of the big filter cake.*

Another technique developed is a ´hot impactor´. In this probe the flue gas hits a plate with high velocity causing particles (if any) to be caught by impaction. Thus, if deposits at the impaction plate are observed, the existence of particles at high temperatures can be proved. The two techniques are shown on figure 6.

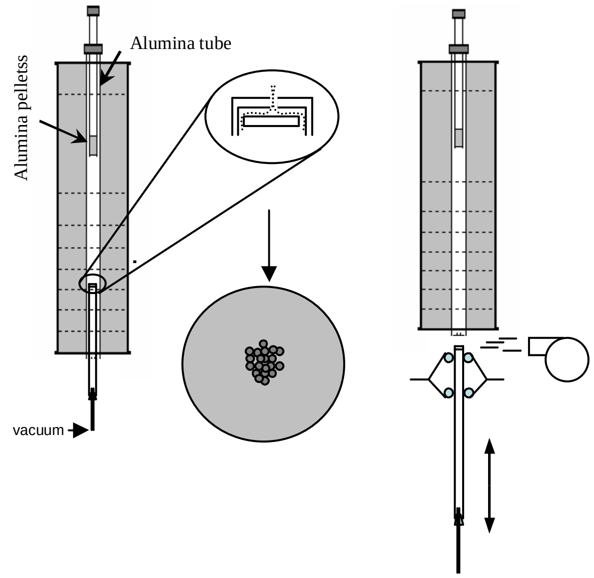

Figure 6: *Experiments for investigating the aerosol formation mechanism. To the left is shown the ´hot impactor´ inserted into a tubular furnace. If particles are present in the gas phase (at high temperatures) they will impact on the impaction plate. To the right is shown the hot filter with a slide that allows fast extraction of the filter and subsequently quench-cooling.*

These experiments showed existence of potassium sulphate particles at 760ºC. It was possible to form the sulphate from either KCl or KOH. The chemical composition was verified by EDX. The mechanism for particle formation in a flue gas from straw combustion is then a two step formation. First chlorides react with sulfur dioxide, oxygen and water to form gas phase sulphate. The sulphate nucleates to form very small particles in high concentrations with a large surface area. The remaining gas phase sulphate is depleted by heterogen condensation on the small particles. By further cooling the remaining chloride is condensed onto the sulphate particles. In principle the solid chloride can react with sulfur dioxide to form sulphates but this reaction is very slow. In figure 7 a SEM micrograph of sulphate particles from the hot impactor is shown.

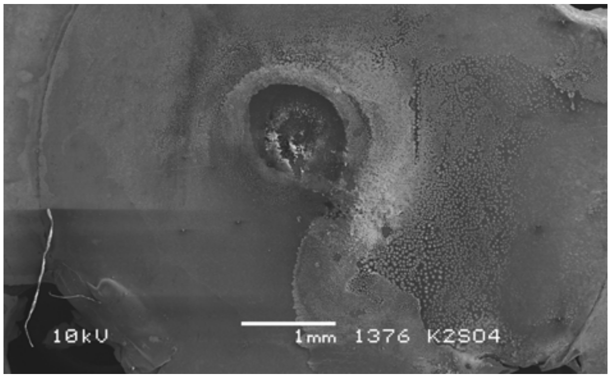

Figure 7: *SEM micrograph of potassium sulphate partic-les deposited on platinum in the hot impactor.*

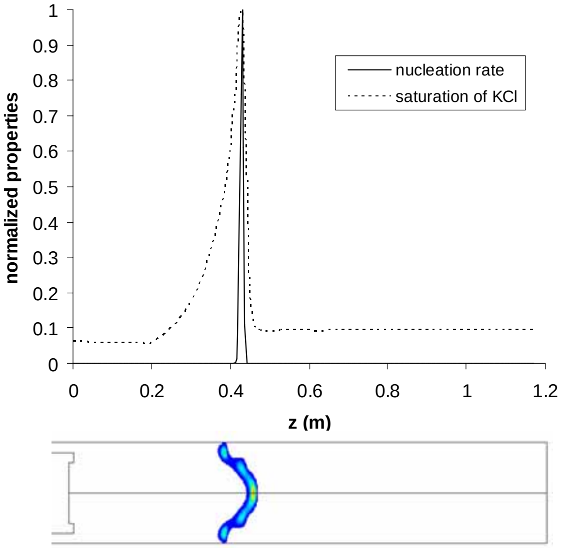

Figure 8: *Normalized saturation ratio and nucleation rate of KCl as a function of the distance from the inlet of the LFAC. It is seen that the saturation ratio increases as the gas moves downstream and cools down. At some point the super saturation is so high that particles are formed in the gas phase. The nucleation rate increases very rapidly at this point. The new particles deplete the gas phase by vapor condensation and the nucleation dies out fast as the saturation drops to unity. The contour plot show the nucleation rate in a case where the maximum nucleation rate appears in the center of the reactor.*

Modeling

A mathematical model has been used to describe the experiments performed. The model is a CFD post processing stream tube model. The simulations of aerosol dynamics in the LFAC are performed in cooperation with the Technical Research Centre of Finland. Simulations in 1D and 2D have been applied to 1 component nucleation with satisfying results. It is the intention to develop the model further to account for chemical equilibrium and reaction. The sulphation reaction will be studied and it is the intention to simulate nucleation of sulphate using the model. A few key parameters from the simulations of one component nucleation are shown in figure 8.

Field measurements

A measuring campaign at a full scale power plant firing straw has been carried out at Avedøre Power Plant (AVV2). In the 2½ weeks measuring campaign, experiments with different additives where performed and the effects on temperature, deposits, emissions, particles loads, and aerosols where done. The Aerosol Laboratory performed aerosol measurements and total dust samplings in the flue gas upstream from the bag house filter. The Aerosol measurements were carried out using a gas ejector for diluting and cooling the flue gas. When the flue gas is diluted, coagulation is minimized and furthermore, by changing the dilution rate, the concentration can be optimized for the sampling method used. The flue gas leaving the gas ejector is conditioned in a gas conditioner to remove moisture. By measuring the CO_2 concentration in the diluted flue gas and in a non-diluted, filtered flue gas, the dilution rate is found, and saved by data-logging. The temperature and the concentration of NO are also logged, since these also may influence the formation of submicron particles. The aerosol is characterized by cascade impactor and SEM/EDX. The total dust samplings are made on a filter from Haldor Topsøe which samples the flue gas iso-kinetically. These filter measurements are used to find total dust load and chemical composition of the solid fraction of the flue gas. The measuring campaign was carried out by E2, RISØ, Vattenfall, Force and The Department of Chemical Engineering, DTU. The main conclusion was that all sorbents except for chalk lowered the load of sub micron particles in the flue gas. The mass size distributions are shown in figure 9.

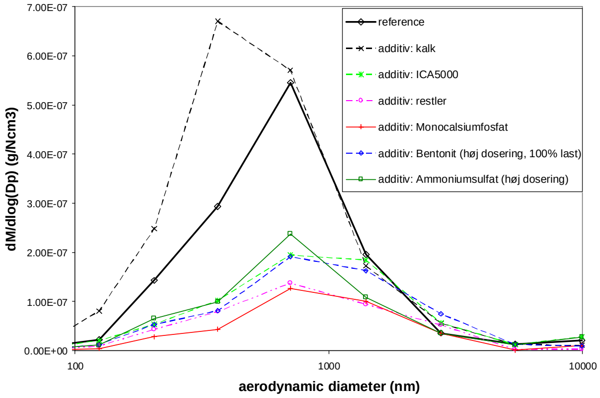

Figure 9: *Mass size distributions from field measure-ments with sorbents measured by cascade impactor.*